



THE LATE QUATERNARY HISTORY OF THE SOUTH ASIAN MONSOON

DANIEL GEBREGIORGIS

2016

PHD THESIS

The late Quaternary history of the South Asian monsoon

Die spätquartäre Entwicklung des Südasiatischen Monsuns

Dissertation
zur Erlangung des akademischen Grades
Dr. rer. nat.

der Mathematisch-Naturwissenschaftlichen Fakultät
der Christian-Albrechts-Universität zu Kiel

vorgelegt von

Daniel Gebregiorgis

Kiel, 2016

1. Gutachter und Betreuer:
2. Gutachter:

Prof. Dr. Martin Frank
Prof. Dr. Wolfgang Khunt

Eingereicht am:
Datum der Disputation:
Zum Druck genehmigt:

27. October, 2016

Erklärung

Hiermit erkläre ich gemäß § 8, dass ich die vorliegende Abhandlung, abgesehen von der Beratung durch meinen Betreuer, nach Inhalt und Form selbstständig erarbeitet habe und keine anderen, als die von mir aufgeführten Quellen und Hilfsmittel verwendet wurden. Diese Arbeit ist unter Einhaltung der Regeln guter wissenschaftlicher Praxis der Deutschen Forschungsgemeinschaft entstanden und wurde weder in Auszügen noch in ganzer Form an einer anderen Stelle im Rahmen eines Prüfungsverfahrens eingereicht.

Teile dieser Arbeit sind bereits in Fachzeitschriften veröffentlicht, wurden zur Veröffentlichung eingereicht oder sind in Vorbereitung, eingereicht zu werden.

Kiel, den 15.09.2016

Daniel Gebregiorgis

CONTENTS	X
CONTENTS	
ABSTRACT	I
ZUSAMMENFASSUNG	V
ABBREVIATIONS	VII
I. INTRODUCTION	1
I.1 RESEARCH BACKGROUND AND MOTIVATION	1
I.2 MONSOON THEORY	3
I.3 THE SOUTH ASIAN MONSOON SYSTEM	4
I.4 PRESENT AND PAST FORCING MECHANISMS OF THE SOUTH ASIAN	7
I.5 PALEO-MONSOON PROXIES	10
I.6 RESEARCH QUESTIONS AND THESIS OUTLINE	14
REFERENCES	15
II. EXPERIMENTAL DESIGN	23
II.1 PALEOCLIMATE TIMESERIES ANALYSIS	24
III. PUBLICATIONS AND MANUSCRIPTS	27
DECLARATION OF MY CONTRIBUTION TO THE FOLLOWING CHAPTERS	27
CHAPTER I:	29
ASTRONOMICAL FORCING OF SOUTH ASIAN MONSOON PRECIPITATION OVER THE PAST ~1MILLION YEARS	
CHAPTER II:	51
ORBITAL FORCING OF SOUTH ASIAN MONSOON INFERRED FROM ANDAMAN SEA X-RAY FLUORESCENCE CORE SCANNING RECORDS	
CHAPTER III:	77
ORBITAL VARIATIONS OF THE MIXED LAYER AND THERMOCLINE OVER THE PAST ~1 MILLION YEARS	
CHAPTER IV:	97
SOUTH ASIAN MONSOON VARIABILITY DURING THE LAST ~54 KYRS INFERRED FROM SURFACE WATER SALINITY AND RIVER RUNOFF PROXIES	
IV. SUMMARY AND OUTLOOK	133
APPENDIX	141
ACKNOWLEDGMENT	159
CURRICULUM VITAE	161

Abstract

The Indian summer or South Asian monsoon (SAM) is a major component of the global climate system that dominates weather patterns and impacts the livelihood of billions of people across the subcontinent. Despite significant improvements over the past decade, the SAM remains difficult to predict and to model. This is directly related to the fact that instrumental records of monsoon precipitation at most date back few centuries. Consequently, the need to generate proxy records of monsoon precipitation and analysis of paleoclimate data is crucial to understand the various forcing mechanism of the monsoon on different timescales.

In this thesis, the link between interhemispheric insolation changes and monsoon precipitation is explored and a working hypothesis is provided. High-resolution paleoclimate datasets have been generated from three sediment cores in the Andaman Sea. I develop potential proxies of SAM precipitation and perform paleoclimate time series analysis to better understand orbital and sub-orbital forcing mechanisms of the monsoon. The first continuous long-term high resolution records of monsoon precipitation based on paired Mg/Ca and $\delta^{18}\text{O}$ analyses of near surface dwelling planktonic foraminifera are presented, from which I estimate sea surface temperature (SST) and seawater $\delta^{18}\text{O}$ ($\delta^{18}\text{O}_{\text{sw}}$). In addition, monsoon intensity changes are evaluated using proxies such as Ba/Ca, x-ray fluorescence (XRF) Ti/Ca, and Si/Al, which have been associated with the monsoon via different causal linkages

Chapters I and II of this study provide direct evidence for the orbital forcing mechanism of the monsoon and fill in a fundamental gap and lack of consensus in how the monsoon has responded to insolation forcing. Reconstructed $\delta^{18}\text{O}_{\text{sw}}$, as well as XRF Si/Al records show that that the phasing and timing of SAM precipitation has been driven by distinct factors operating over a range of orbital frequency bands. In the precession band, the seasonal cross-hemispheric thermal/pressure contrast determines the timing and pace of SAM precipitation and accounts for ~25 to 30 %

of the total variance contained in the $\delta^{18}\text{O}_{\text{sw}}$ and Si/Al records. A large fraction of the variance in these records is dominated by heterodyne frequencies of the primary orbital periods, which indicates that monsoon dynamics of different forcing mechanisms have been predominantly non-linear. Taken together our records provide direct and clear evidence that precession driven variability in the Bay of Bengal is consistent with that observed in the Arabian Sea. Our records also suggest that obliquity forcing plays a more important role in monsoon intensification than previously considered. This has mainly been a consequence of enhanced cross-hemispheric atmospheric moisture flux due to decreased obliquity forcing resulting in Northern Hemisphere (NH) cooling and Southern Hemisphere (SH) warming.

Chapters III and IV of this study deal with the forcing mechanisms driving upper ocean stratification of the northern Indian Ocean on orbital and sub-orbital time scales. I use the ecological habitats of different planktonic foraminiferal species to reconstruct freshwater-induced stratification based on paired Mg/Ca and $\delta^{18}\text{O}$ analysis. The difference between mixed and thermocline layer $\delta^{18}\text{O}_{\text{sw}}$ ($\Delta\delta^{18}\text{O}_{\text{sw}}$) and temperature (ΔT) is used as a proxy for upper ocean stratification and thermocline depth respectively. On orbital time scales, mixed layer $\delta^{18}\text{O}_{\text{sw}}$ ($\delta^{18}\text{O}_{\text{ML}}$) and thermocline layer $\delta^{18}\text{O}_{\text{sw}}$ ($\delta^{18}\text{O}_{\text{TL}}$) data document a mean lag of ~ 9 kyrs with respect to maximum NH insolation (P min) in the precession band and indicate the prevalence of monsoonal forcing triggered by enhanced cross-equatorial transport of latent heat rather than a direct NH insolation response. Phase relationships between $\delta^{18}\text{O}_{\text{ML}}$ and $\delta^{18}\text{O}_{\text{TL}}$ over the obliquity band also reveal that a common monsoonal forcing controls freshening of the mixed layer and the thermocline waters and is triggered by poleward moisture flux in response to intensified intra-hemispheric temperature gradient over this frequency band. A closer look at upper ocean stratification changes during the last ~ 54 kyrs, however, suggests a more complex relationship between upper ocean stratification and monsoonal forcing. Upper stratification remained relatively stable during the last ~ 54 kyrs despite gradual strengthening of the monsoon beginning at ~ 18 kyrs and peak monsoon strength intervals during the mid-Holocene as inferred from Ba/Ca records.

Zusammenfassung

Der indische oder Südasiatische Monsun (SAM) ist eine wichtige Komponente des globalen Klimasystems, das das Wettergeschehen und somit die Existenzgrundlage von Milliarden Menschen innerhalb des Subkontinents kontrolliert. Trotz signifikanter Verbesserungen während der letzten Dekade bleibt es schwierig, den SAM vorherzusagen und zu modellieren. Dies liegt hauptsächlich an der Tatsache, dass instrumentelle Aufzeichnungen des Monsunniederschlags bestenfalls einige Jahrhunderte zurückreichen. Folglich gibt es den klaren Bedarf, den Monsunniederschlag anhand von Proxydaten zu rekonstruieren und die Analyse von Paläoklima-Daten ist entscheidend, um die verschiedenen Mechanismen die den Monsun über lange Zeitskalen antreiben, zu verstehen.

Im Rahmen dieser Dissertation wird die Verbindung zwischen der Veränderung von interhemisphärischer Insolationsintensität und Monsunniederschlag untersucht. Hochauflösende paläoklimatische Datenreihen wurden für drei Sedimentkerne aus der Andamansee generiert. Die Analyse der Proxy-Indikatoren für SAM Niederschlag resultierten in paläoklimatischen Zeitserienanalysen, die es möglich machen, orbitale und suborbitale Steuerungsmechanismen des Monsuns besser zu verstehen. Ich präsentiere die ersten langfristigen Aufzeichnungen des Monsunniederschlags basierend auf $d^{18}O$ Werten des Meerwassers ($d^{18}O_{sw}$), die aus kombinierten Mg/Ca (Oberflächenwassertemperaturen) und $d^{18}O$ Analysen von Foraminiferen, die in den oberen Wasserschichten leben, rekonstruiert wurden. Zusätzlich wurden die Veränderungen der Monsunintensität dadurch untersucht, dass weiteren Proxy-Indikatoren wie Ba/Ca, XRF Ti/Ca und Si/Al einbezogen wurden, die über unterschiedliche kausale Zusammenhänge mit dem Monsun assoziiert waren.

Kapitel I und II dieser Arbeit erbringen den direkten Nachweis für orbitale Antriebmechanismen des Monsuns und füllen fundamentale Lücken unseres Verständnisses darüber, wie der Monsun auf Änderungen der Insolation reagiert

hat. Rekonstruktionen von $d^{18}O_{sw}$ sowie XRF Si/Al Aufzeichnungen zeigen, dass die gemittelten Variationen des SAM Niederschlags von Faktoren in den orbitalen Frequenzbändern gesteuert wurden. Im Präzessionsband bestimmten saisonale Hemisphären-übergreifende Wärme- und Druckunterschiede das Timing und die Geschwindigkeit von Änderungen des SAM-Niederschlags und trugen ungefähr 25 bis 30% zur gesamten Varianz der $d^{18}O_{sw}$ und Si/Al Rekonstruktionen bei. Der Großteil der Varianz ist jedoch in überlagernden Frequenzen enthalten und zeigt an, dass die Monsundynamik nicht-linear gesteuert wurde. Insgesamt liefern meine Rekonstruktionen direkte und eindeutige Nachweise dafür, dass die Präzessionsgetriebene Variabilität im Golf von Bengalen mit Beobachtungen aus der Arabischen See übereinstimmt. Meine Rekonstruktionen zeigen außerdem, dass Obliquitätssteuerung eine wichtigere Rolle für die Monsunintensivierung gespielt hat, als bisher angenommen. Dies wird hauptsächlich einem verstärkten Hemisphären-übergreifenden, atmosphärischen Feuchtigkeitsaustausch bei niedriger Obliquität zugeschrieben, wobei sich gleichzeitig die Nordhemisphäre abkühlte und die Südhemisphäre erwärmte.

Kapitel III und IV dieser Arbeit beschäftigen sich mit den Antriebsmechanismen der Stratifizierung des Oberflächenozeans auf orbitalen und suborbitalen Zeitskalen. Ich nutze für diese Untersuchungen die ökologischen Habitate von verschiedenen planktonischen Foraminiferenarten um basierend auf Mg/Ca und $d^{18}O$ Analysen Süßwasser-induzierte Stratifizierung zu rekonstruieren. Der Unterschied zwischen dem $d^{18}O_{sw}$ ($D^{18}O_{sw}$) und der rekonstruierten Temperatur (DT) wird als Proxy für Oberflächenstratifizierung und Thermoklintiefe genutzt. Auf orbitalen Skalen dokumentieren die Daten, dass die Hauptänderungen der $d^{18}O_{sw}$ ($d^{18}O_{ML}$)-Signaturen der durchmischten Schicht und des Thermoklinen $d^{18}O_{sw}$ ($d^{18}O_{TL}$)-Signals einen durchschnittlichen zeitlichen Versatz von ungefähr 9000 Jahren haben, was der maximale nordhemisphärischen Insolation (P min) in der Präzession entspricht. Dies legt eine dominierende Kontrolle durch die Monsunschwankungen anstatt einer direkten Reaktion auf die NH Insolation nahe. Die Phasenbeziehung zwischen $d^{18}O_{ML}$ und $d^{18}O_{TL}$ über der Obliquity zeigt die Kontrolle durch den

Monsun. Die genauere Betrachtung der Veränderung der Stratifizierung der Ozeanoberfläche während der letzten 54000 Jahre zeigt ebenso einen komplexeren Zusammenhang zwischen der Stratifizierung des Ozeanoberflächens und der Monsunsteuerung. Die Stratifizierung des Ozeanoberflächens während der letzten 54000 Jahre war relativ stabil trotz einer graduellen Verstärkung des Monsuns vor ungefähr 18000 Jahren und Maxima der Monsunintensität während des Mittleren Holozäns, die aus Ba/Ca Variationen abgeleitet wurden.

Abbreviations

SAM	South Asian monsoon
SST	Sea surface temperatures
ITCZ	Inter-tropical convergence zone
ENSO	El Niño–Southern Oscillation
IOD	Indian Ocean dipole
AMOC	Atlantic Meridional Overturning Circulation
NH	Northern Hemisphere
SH	Southern Hemisphere
XRF	X-ray fluorescence
ETP	Eccentricity, tilt and precession
SSIO	Southern Subtropical Indian Ocean

I. Introduction

I.1 Motivation

The South Asian summer monsoon (SAM) is one of the oldest known climatic phenomena on Earth that directly impacts the livelihood of one third of humanity. The South Asian monsoon region roughly covers the area 70°E-110°E, 10°N-30°N and comprises most or all parts of the present day territories of India, Pakistan, Sri Lanka, Bangladesh, Bhutan, Nepal, Myanmar, Laos, Thailand and parts of mainland China. The summer monsoon accounts for as much as 75 percent of the annual rainfall over most parts of the region (e.g. Dhar and Nandargi, 2003) and is a major factor in the South Asian economy (e.g. Barker et al., 1985). It provides vital water resources for agriculture and hydroelectric power generation while also posing significant risk to human life through flooding. Significant fluctuations in summer monsoon variability often bring great damage to the region. Recent evidence from quantitative reconstruction of Holocene climate change points out that the development and collapse of civilizations in both South and East Asia have been controlled to a large extent by monsoon intensity changes*.

The monsoon is, however, hard to predict and to model, and its future evolution in a changing global climate is mostly unknown and remains a severe test even for the most advanced coupled ocean-atmosphere general circulation models (e.g. Flato et al., 2013). Identified biases in simulated summer monsoon precipitation include systematic overestimation of precipitation over the equatorial Indian Ocean and underestimation of precipitation over the Indian subcontinent (Johnson et al., 2016 and references therein). Our incomplete understanding of the monsoon is in part due to scarcity of detailed records of past monsoon precipitation on different timescales. For instance, to date our understanding of the low frequency variability of the South Asian monsoon heavily relies on proxy records of wind strength and

* Clift, Peter D., and R. Alan Plumb. *The Asian monsoon: causes, history and effects*. Vol. 270. Cambridge: Cambridge University Press, 2008, pp-199.

the associated upwelling in the Arabian Sea (e.g. Caley et al., 2011; Clemens et al. 1991, 1996, 2008; Schulz et al., 1998; Ziegler et al., 2010) while very little is known about the variability of monsoon precipitation both on land and over the ocean. The few paleo-records generated from the Bay of Bengal and Andaman Sea rarely extend beyond the last 100 kyrs (e.g. Gebregiorgis et al., 2016; Rashid et al., 2007, Kudrass et al., 2001). Quantifying the response of the monsoon to changes in future regional and global climates requires a thorough understanding of the natural variability in the climate system across timescales. For instance, vital insights into the dynamics of monsoon climate and its driving mechanisms, presently lacking, can be gained through analysis of paleoclimate time series on Milankovitch timescales* (Fig 1.1). Paleoclimate time series analysis on these time scales allows us to examine, for example, the relationships between solar radiation arriving at the top of the atmosphere and monsoon climate. This provides a conceptual framework for understanding future monsoonal changes in light of assumed global warming and response mechanisms. This work is primarily motivated by the lack of understanding of how the monsoon responds to the most basic boundary conditions related to insolation changes, imperative in achieving a better understanding of future monsoon evolution.

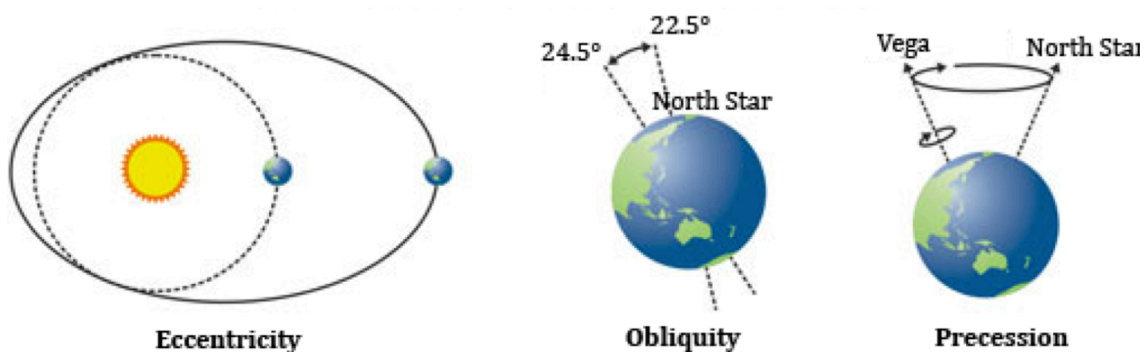


Fig 1.1. Schematic illustration of the three main orbital periods (Milankovitch cycles). Figure available at <http://www.functionspace.com/>

* Milutin Milankovitch proposed in the early twentieth century that changes in the intensity of solar radiation received at the Earth's Atmosphere and subsequent changes in Earth's climate are driven by three elements of Earth-Sun geometry namely: eccentricity, obliquity and precession.

I.2 Monsoon theory

Classical monsoon theory was first formulated in the 17th century and defines the monsoon as a massive convectonal system produced by differential seasonal heating of continental and oceanic areas*. Per this definition, the monsoon is treated as a giant sea breeze that is fundamentally driven by differences in the heat capacities of land and the ocean, and ensuing temperature differences between warmer land and cooler ocean surfaces (Fig 1.2). Although the classical monsoon view has not been out-rightly rejected, it's known for several decades now that monsoon circulation is more complex and also spatially non-uniform (e.g. Webster, 1987). Webster (1987) first provided a conceptual model of the monsoon building on the models of Halley (1686) and Hadley (1735) as a seasonal moist sea breeze modified by the Coriolis force.

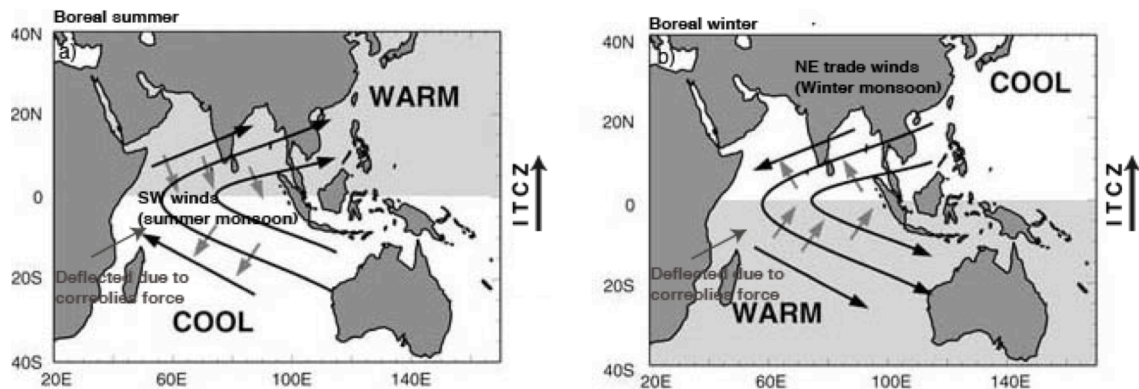


Fig 1.2. Classical view of the monsoon within the context of the SAM. Figure modified from Loschnigg and Webster (2000).

Monsoon circulation in both hemispheres is characterized by seasonal migration of the solar zenith angle, which leads to annual migration of the equatorial trough and the Inter Tropical Convergence Zone (ITCZ) north and south of the equator (Fig 1.3). In the overall scheme of the monsoon, the differential sensible heating of the land and ocean, and tropospheric latent heating determines the strength of the monsoon (e.g. Webster et al., 1998; Chou, 2003). The evolution of the regional monsoons is primarily dependent on the distribution of land and ocean, which alters the net

* English astronomer and mathematician Edmond Halley in 1686 defined the monsoon as resulting from thermal contrasts between continents and oceans due to their differential heating dependent on seasonal march of the sun.

ocean heat transport and is subject to large temperature gradients between the land and ocean surfaces (e.g. Webster et al., 1998). Besides differential heating leading to large temperature gradients, the development of the monsoon is also directly influenced by several other factors, such as orography, the shape of the continents and circulation in the upper troposphere (e.g. Dirmeyer et al., 1998; Fasullo et al., 2003; Li and Yanai, 1996; Sato et al., 2007). Geological evidence suggests that the age of inception of the Asian monsoon was linked to the uplift of the Tibetan Plateau and highlights the important role of orography despite the lack of consensus on the precise age of inception (e.g. see Clift et al., 2008 and Betzler et al., 2016).

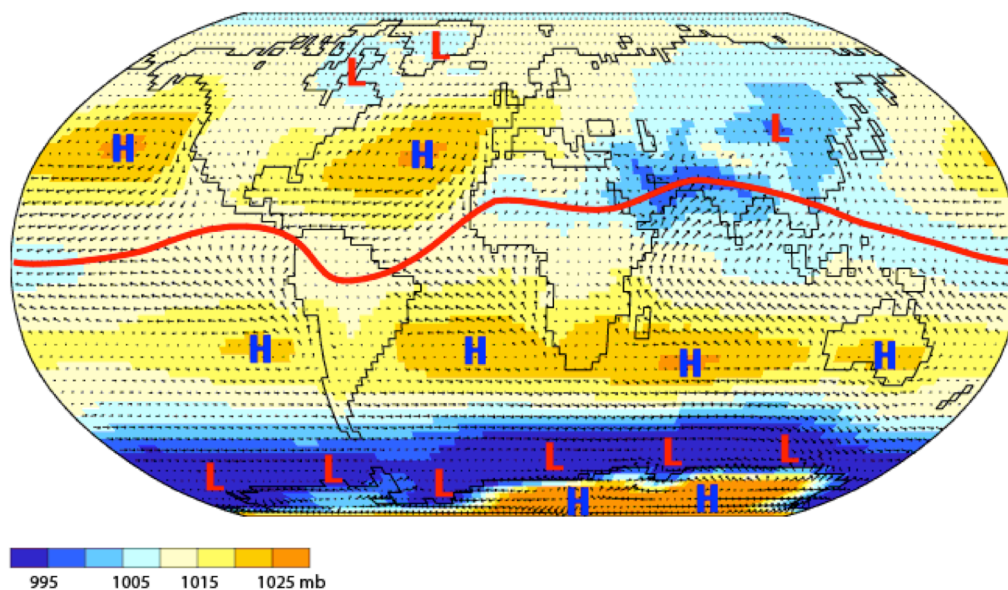


Fig 1.3. Mean July prevailing surface winds and centers of atmospheric pressure, 1959-1997 schematic representation of the ITCZ. Figure in its present form from Pidwirny (2006) and originally from lab section of environmental research group, University of Oregon. Available at <http://www.physicalgeography.net/fundamentals/7p.html>.

I.3 The South Asian Monsoon system

The South Asian monsoon is a major component of the global climate system and dominates weather patterns across the subcontinent. The southwesterly monsoon winds bring abundant moisture from the warm waters of the tropical ocean to the Asian continent during boreal summer and displays a remarkably consistent annual cycle. The amount of seasonal rainfall delivered by the monsoon winds, however,

differs from one year to the other. At the most basic level, the SAM is driven by increased solar heating of continental land relative to adjoining oceans, which drives a large-scale meridional surface temperature gradient (Li and Yanai, 1996), following a gradual sensible heating of the Asian land mass during late spring. This forms a low-pressure zone over Tibet and triggers a north–south pressure gradient prompting a cross-equatorial surface flow as schematically illustrated in Fig 5.

The mean surface elevation of the Tibetan Plateau is over 4.5 km above sea level and plays a significant role in the development of the regional climate system (e.g. Hahn and Manabe 1975; Manabe and Broccoli 1990; Kutzbach et al. 1989). The Tibetan plateau has been widely considered to drive the Asian monsoon via increased sensible and latent heat fluxes prevailing over the eastern and western Plateau, respectively (e.g. Luo and Yanai, 1984; Webster et al., 1998; Wu and Zhang, 1998; Yanai and Wu, 2006). The determinative role the Tibetan plateau plays is also due to the fact that sensible and latent heat fluxes from Tibetan plateau reach a higher altitude and the atmosphere above the plateau is heated more strongly than its surroundings (Fig 1.4) (e.g. Turner and Annamalai, 2012). The Tibetan Plateau and the Himalayan mountain complex ensure that heating during spring is not confined to the surface but also extends to a significant altitude in the troposphere (e.g. Chou, 2003; Fasullo and Webster, 2003, Li and Yanai, 1996). Lower densities of the atmosphere at these sites also mean that distinct radiative processes significantly alter the thermal dynamics and influence atmospheric circulation to a large extent (e.g., Smith and Shi, 1992; Shi and Smith, 1992).

The intense solar heating during boreal spring and summer provides the necessary thermodynamic conditions and enhances poleward convection of moisture coherent with the seasonal migration of the ITCZ (Prive and Plumb, 2007). The northward migration of convection and its interaction with circulation leads to a positive feedback and triggers a deeper monsoon trough, which ultimately enhances the cross-equatorial flow in the lower troposphere. The meridionally oriented East African Highlands at the same time act as a mechanical barrier deflecting the low-

level cross-equatorial flow towards the south Asian continent and forms the low-level westerly jet directed by the Earth's rotation (e.g. Hoskins and Rodwell, 1995; Slingo et al., 2005)

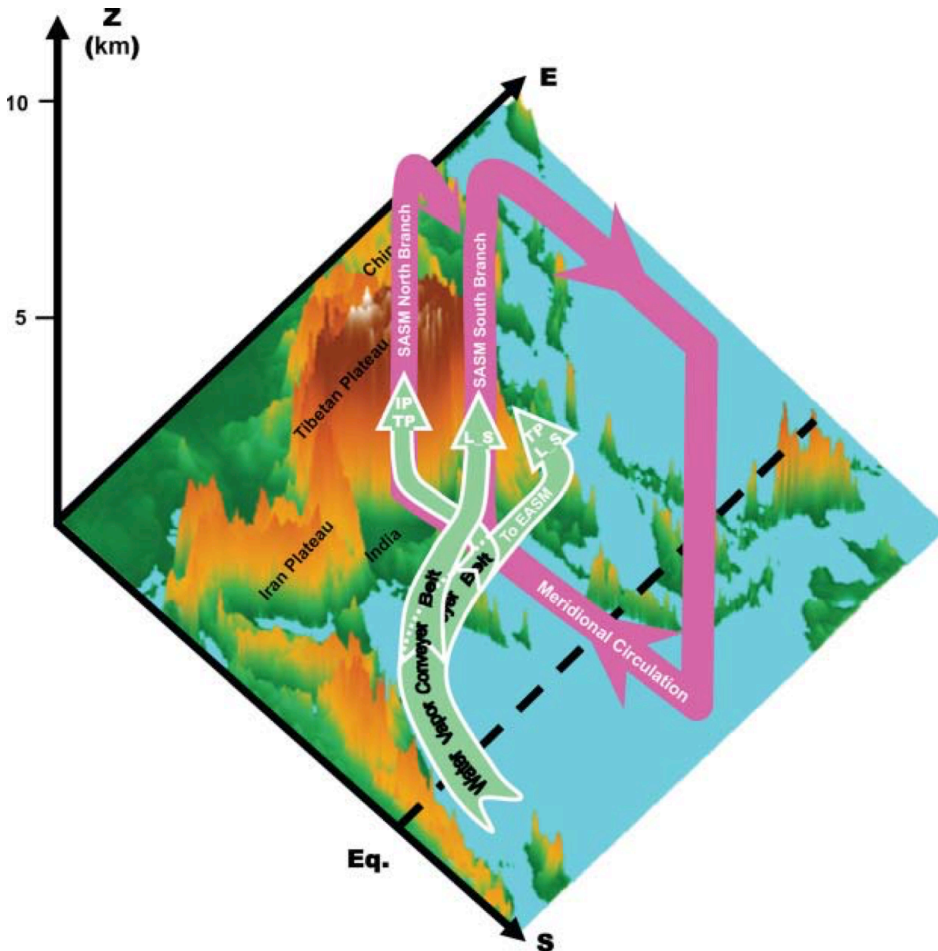


Fig 1.4. Schematic diagram showing the basic structure of the SAM. For the southern branch, water vapor along the conveyor belt is lifted up due mainly to land-sea thermal contrast in the tropics; for the northern branch the water vapor is drawn away from the conveyor belt northward toward the foothills and slopes of the Tibetan Plateau (TP), and is uplifted to produce heavy precipitation; the rest of the water vapor is transported northeastward to sustain the East Asian summer monsoon, which is controlled by the land-sea thermal contrast as well as thermal forcing of the TP. (Figure and figure caption after Wu et al., 2012)

In the following section a detailed description of the forcing mechanisms of the South Asian monsoon on different timescales is provided. In this context, the basis for interpreting the paleo-monsoon signal imprinted in various geological archives

is highlighted. At the same time a brief summary of several well-established proxies of the monsoon is provided.

I.4 Present and past forcing mechanisms of the South Asian Monsoon

A crucial step forward for better understanding of the SAM and its future evolution requires extensive analysis of observational and proxy data, and in retrospect a detailed understanding of monsoon variability on different timescales. The SAM has exhibited pronounced variability on time scales ranging from intraseasonal and interannual to decadal and longer (e.g., Webster et al. 1998; Gadgil, 2003; Turner and Annamalai 2012; Schneider et al. 2014). The interannual variability of SAM is particularly well documented and is strongly linked to sea surface temperature (SST) changes in the tropical oceans and associated phenomena such as the El Niño–Southern Oscillation (ENSO; e.g., Pant and Parthasarathy 1981; Rasmusson and Carpenter 1982; Meehl, 1987; Webster and Yang, 1992) and the Indian Ocean dipole (IOD; e.g., Ashok et al., 2001; Cherchi and Navarra, 2013). Historically, above/below average SAM precipitation has been closely related to phases of strong El Niño/La Niña conditions (Fig 1.5), which is due to variations of the regional Hadley and Walker circulation anomalies (e.g. Krishnamurthy and Goswami, 2000). However, this relationship appears to have weakened significantly in the course of global warming (Mani et al., 2009; Wang et al., 2015) despite high ENSO variability during the most recent decades (Li et al., 2013). Although considerably weaker compared to the ENSO forcing, land processes such as snow cover changes on the Tibetan Plateau and Eurasia have influenced the interannual variability of the SAM (Dickson, 1984; Hahn and Shukla, 1976; Kumar et al., 1999). On decadal to centennial timescales, the monsoon has varied in coherence with temperature fluctuations in northern high latitudes, which implies a dominant northern hemisphere insolation forcing (Fleitmann et al., 2003). It's not clear, however, whether the solar insolation–monsoon relationship is driven by direct (e.g. Shindell et al., 2001) or indirect forcing mechanisms via the monsoon–Eurasian snow cover link (e.g. Neff et al., 2001).

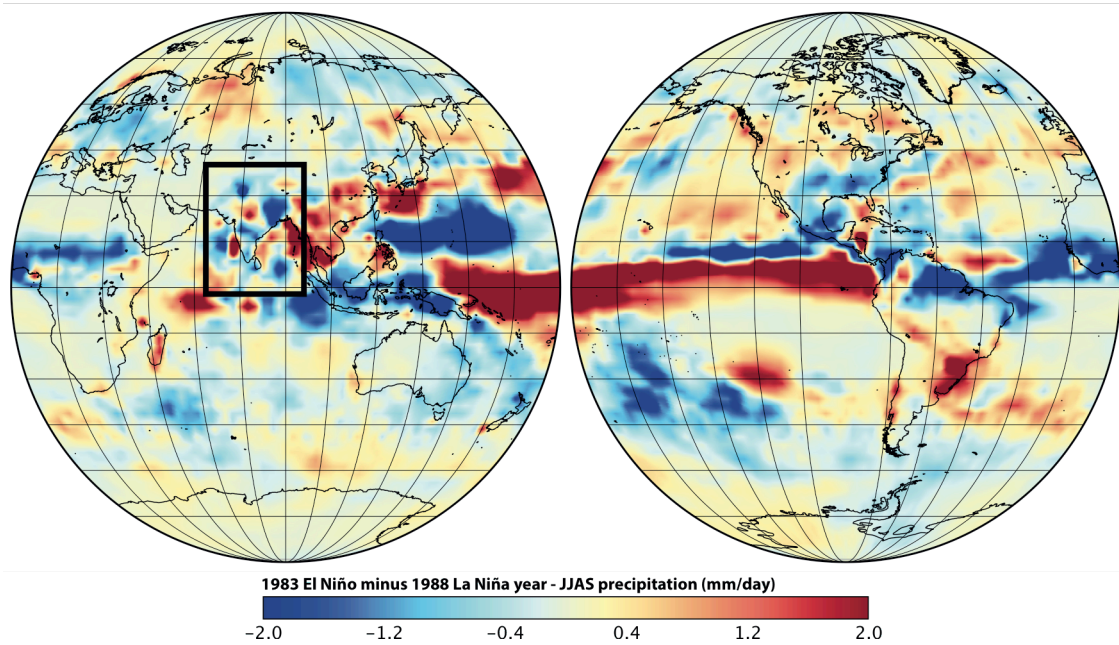


Fig 1.5. Global precipitation composite mean: strong El Niño (1983) minus a strong La Niña (1988) years showing increased precipitation over the Indian subcontinent during La Niña. Precipitation data from NOAA.

On millennial time scales, the SAM has exhibited variability that has been closely linked to abrupt climate change in the north Atlantic region (e.g. Overpeck et al., 1996; Schulz et al., 1998) associated with the Atlantic meridional overturning circulation (AMOC) (e.g. McManus et al., 1999). The AMOC is a major component of global heat transport across both hemispheres and plays a vital role in regulating the mean position of the ITCZ, and thus also affects the tropical monsoon systems. For instance, a weakening of the AMOC can cause cool North Atlantic SSTs and trigger a southward migration of the ITCZ via anomalous warming/cooling (SH warming in case of weak AMOC) of one hemisphere with respect to the other (e.g. Broccoli et al., 2006; Vellinga and Wood, 2008; Zhang and Delworth, 2008). Strengthening or weakening of the AMOC, thus, triggers a shift in the mean position of the ITCZ towards the warming hemisphere and influences monsoon dynamics across both hemispheres (Mohtadi et al., 2016 and references therein). This is particularly evident during periods of abrupt warming or cooling of the Northern

Atlantic region such as the Heinrich and Dansgaard–Oeschger events of the last glacial period. These alternating stadial (cold) and interstadial (warm) phases are well documented in several palaeo-monsoon records from both hemispheres and were physically linked to the monsoon via variations in the AMOC and its associated heat transport (Mohtadi et al., 2016 and references therein).

On orbital timescales, changes in Earth’s precession wobble, tilt of Earth’s axis or obliquity, and Earth’s eccentricity have largely controlled the temporal and spatial distribution of insolation received at both hemispheres (Fig 1.6) and consequently influences SAM dynamics both in space and time. The Earth’s precessional cycle has two components: axial precession and elliptical precession and occurs on periods of roughly 19 kyrs and 23 kyrs. The precession cycle profoundly influences the seasonal cycle of incoming solar radiation and its distribution across the hemispheres, and can have detrimental effects on monsoon intensity. During periods of precession minima, monsoon rainfall is generally characterized by increased intensity in the Northern Hemisphere (NH) as the perihelion occurs during the boreal summer and is reduced in the Southern Hemisphere (SH). It’s widely regarded that this is due to a stronger land–sea thermal gradient triggered by increased warming of NH land enhancing moisture transport during boreal summer (Merlis et al., 2013). On the other hand, changes in obliquity occur on a characteristic timescale of 41 kyrs and affect the seasonality of incoming solar radiation across both hemispheres. Obliquity-induced changes exert substantial effects on the strength of monsoon systems by triggering changes in the moisture transport pathways on glacial–interglacial timescales (Mohtadi et al., 2016). Recent studies have suggested that obliquity forcing of the monsoon is facilitated via interhemispheric insolation gradients (e.g. Bosmans et al., 2015; Mantsis et al., 2014) and contributes directly to monsoon intensity changes. Orbital eccentricity linked to 100 Kyr glacial–interglacial climate cycles has, however, limited influence in seasonal or mean annual insolation and it remains unclear whether glacial–interglacial variability is an extension of precession or obliquity forcing.

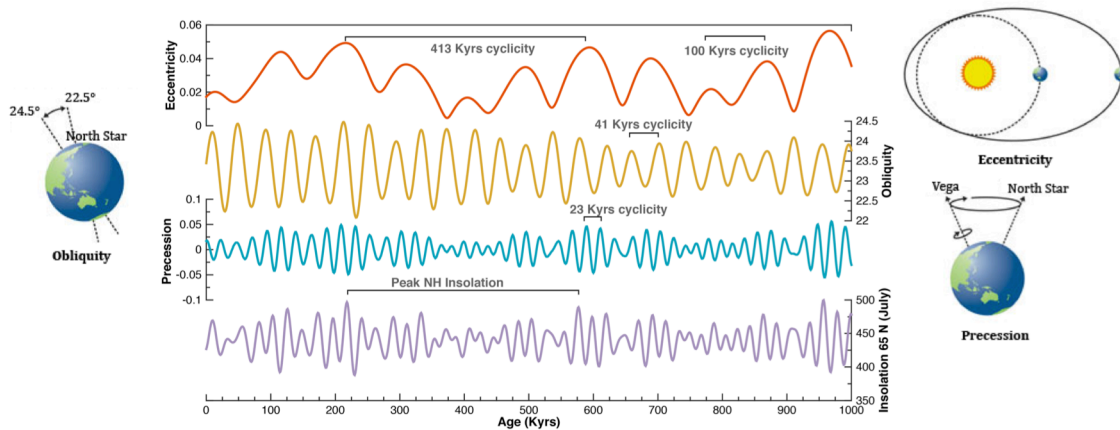


Fig 1.6. Eccentricity, precession, and obliquity cycles of the Earth, which are the three basic drivers of solar insolation and also the global monsoon climate. Data from Berger, 1999.

I.5 Paleo-monsoon proxies

Much of our understanding of present day climate variability is based on instrumental records at most dating back few centuries (e.g. Sontakke et al., 2008). Information regarding past climate variability beyond the instrumental record comes from the use of proxy indicators that are connected to the climate system via distinct physical or chemical pathways. Proxy evidence imprinted in natural archives such as ice cores, trees, speleothems, corals, ocean and lake sediments can be used to provide detailed information on global and regional climate variability ranging from annual to tectonic timescales. This can be achieved through quantitative and qualitative techniques and reconstruction of a range of climatic parameters (e.g. among others air and sea temperatures, precipitation, sea-level changes, past atmospheric compositions, past ice-sheet extent and thickness, variations in solar activity, and ocean chemistry). However, interpretation of a given proxy record can be complicated due to presence of high noise to signal ratio, and possible distortion of the imprinted climate signal and necessities careful calibration and validation steps.

Paleo-monsoon proxies are typically divided into wind-based and rain-based proxies, contingent to the ways in which they are connected to the climate system (Wang et al., 2015) (Table 1). Frequently enlisted wind-based monsoon proxies include eolian dust and foraminiferal abundance among others and are applied in distinct atmospheric and oceanography settings. Eolian dust proxies have been extensively used to estimate changes in the strength of atmospheric circulation and dust source regions as well as changes in atmospheric transport pathways and scavenging mechanisms (e.g. Clemens and Prell, 1990; De Angelis et al., 1987; Petit et al., 1990; Rea et al., 1985; Sirocko et al., 1991). Within the monsoon context, interpretation of eolian flux and grain size proxies is primarily based on the core assumption that stronger monsoon winds control the variability of the eolian fraction supplied to the sediments. Employing census counts of planktic foraminiferal species to trace past monsoon variability, on the other hand, relies on the assumption that seasonally reversing strong summer monsoon winds promote blooming of distinct upwelling indicator species such as *Globigerina bulloides* and *Neogloboquadrina dutertrei*. Support for the direct application of these proxies as monsoon indicators is provided in modern observations from the Arabian Sea (e.g. Clemens, 1998; Curry et al., 1992), although the interpretations may not always be unambiguous.

On the other hand, the rain-based proxies are directly linked to the monsoon via hydrological pathways and typically include paired Mg/Ca- $\delta^{18}\text{O}$ proxies of sea surface salinity (SSS), speleothem $\delta^{18}\text{O}$, XRF based proxies and to some extent Ba/Ca serving as river runoff proxies. Over recent decades, there has been an increase in the use of rain-based monsoon proxies thanks to significant advances in analytical techniques and measurement capabilities. For example, elemental ratios such as Ti/Al and K/Si obtained via nondestructive X-ray fluorescence analyses have been applied with great practical success to explore variability in monsoon precipitation at a very high time resolution (e.g. Tian et al., 2011). This is based on the assumption that some elements are enriched rather than others during periods of intense monsoon regimes and is also true for Ba/Ca river runoff proxies. Monsoon intensity

changes can also be directly inferred from the oxygen isotope composition ($\delta^{18}\text{O}$) of calcite from planktonic foraminifera, which is a function of both surface temperature and seawater $\delta^{18}\text{O}$ –itself an indicator of global ice volume and salinity (Shackleton, 1974). The salinity signal can be extracted by correcting for the temperature using magnesium/calcium (Mg/Ca) measurements on the same foraminiferal tests (e.g. Elderfield and Ganssen, 2000). The global ice volume effect, on the other hand, is accounted for typically using a global sea level record (e.g. Rohling et al., 2014; Waelbroeck et al., 2002). Speleothem $\delta^{18}\text{O}$ records from the Asian continent, on the other hand, are often directly applied as indicators of summer monsoon intensity (e.g. Cheng et al., 2016; Kathayat et al., 2016; Wang et al., 2008) despite lingering uncertainty with regard to application of these proxy records for example arising from changes in moisture sources (e.g. Clemens et al., 2010; Maher and Thompson, 2012). Table 1 provides an extensive summary of the widely used wind-based and rain-based proxies in the Asian monsoon domain.

Table 1.1. Summary of paleo-monsoon proxies. Table modified after Wang et al. (2015)

Wind based Proxies	Features and processes	Proxies	Archive
	Wind transport	Eolian dust	Loess, ice core
		Wind-borne pollen	Lacustrine and marine sediments
	Wind-driven upwelling	Upwelling-indicative phytoplankton and zooplankton <i>e.g. Globigerina bulloides</i>	Marine sediments
		Benthic foraminifera indicative of high carbon flux	
	Wind-induced structure of surface ocean	Geochemical proxies indicative of high productivity e.g., C_{org} , opal, Ba, Cd/Ca, etc.	
		Horizontal SST gradient	
Thermocline depth based on microfossils			
Rain-based Proxies	River runoff	Sea surface salinity based on $\delta^{18}O$ and Ba/Ca	
		Laminated deposits due to water column stratification	
		Sapropel deposits (Mediterranean)	
	Precipitation	Lake level	Lacustrine deposits
		Lake salinity based on microfossils and isotopes	Lake salinity based on microfossils and isotopes
		Pollen-based vegetation, charcoal	Pollen-based vegetation, charcoal
		Speleothem $\delta^{18}O$, trace elements, GDGT-based proxies	Cave speleothem
		Atmospheric CH_4 % and $\delta^{18}O_{atm}$	Ice-core air bubble
		^{10}Be , $\delta^{13}C_{org}$	Loess deposits
	Weathering and pedogenesis	Clay minerals	Marine, lacustrine and loess deposits
		Chemical weathering indices	
		Magnetic susceptibility	
		Pedogenesis indices, e.g., FeD/FeT	

I.6 Research questions and thesis outline

The principal objective of this project is to generate the first long-term paleoclimate record from the major monsoon moisture sink region in the Andaman Sea and gain fundamental understanding into various forcing mechanisms of SAM precipitation on orbital and sub-orbital timescales. More specifically, the following objectives and research questions (RQ) were directly addressed in the following chapters.

RQ I: Have periods of weaker/stronger monsoon precipitation been coupled to documented weakening/strengthening of monsoon winds over the Arabian Sea?

RQ II: What are the potential forcing mechanisms of monsoon precipitation both on land and over the ocean?

RQ III: Has monsoon precipitation been the only forcing mechanism driving upper ocean stratification changes in the Andaman Sea and Bay of Bengal over orbital time scales?

RQ IV: What controlled monsoon spatial variability/uniformity during the last deglaciation?

Chapter I:

Presents the first orbital scale monsoon precipitation proxy record for the last ~1 million years from a major moisture sink region of the SAM precipitation. Here we address the fundamental divergence in opinion and lack of understanding that has long persisted in how the monsoon has responded to changes in basic boundary conditions, such as interhemispheric insolation and global ice volume.

Chapter II:

Here I present ultra high-resolution proxy records of the monsoon obtained by non-destructive x-ray fluorescence (XRF) core scanning. The aim is to assess the response mechanism of the SAM precipitation to adjustments in the precession, obliquity and eccentricity cycles following Chapter I and further exploring independent proxies of the monsoon.

Chapter III:

Here, I utilize the depth habitat preferences of different foraminiferal species and present long term mixed layer and thermocline (for the first time here) temperature and seawater $\delta^{18}\text{O}$ records. The main objective of this study is to understand the feedback mechanisms and interactions between the mixed layer and the thermocline on orbital time scales.

Chapter IV:

Here, I utilize the depth habitat preferences of different foraminiferal species to investigate the freshwater-induced stratification in the Andaman Sea and assess changes in riverine runoff and monsoon intensity spanning the last ~54 kyrs.

References

- Altabet, M.A., Higginson, M.J. and Murray, D.W., 2002. The effect of millennial-scale changes in Arabian Sea denitrification on atmospheric CO₂. *Nature*, 415(6868): 159-162.
- Ashok, K., Guan, Z. and Yamagata, T., 2001. Impact of the Indian Ocean dipole on the relationship between the Indian monsoon rainfall and ENSO. *Geophysical Research Letters*, 28(23): 4499-4502.
- Barker, R., Herdt, R.W. and Rose, B., 1985. The rice economy of Asia, 2. *Int. Rice Res. Inst.*
- Betzler, C., Eberli, G.P., Kroon, D., Wright, J.D., Swart, P.K., Nath, B.N., Alvarez-Zarikian, C.A., Alonso-García, M., Bialik, O.M. and Blättler, C.L., 2016. The abrupt onset of the modern South Asian Monsoon winds. *Scientific Reports*, 6.
- Bosmans, J., Hilgen, F., Tüenter, E. and Lourens, L., 2015. Obliquity forcing of low-latitude climate. *Climate of the Past*, 11(10): 1335-1346.
- Broccoli, A.J., Dahl, K.A. and Stouffer, R.J., 2006. Response of the ITCZ to Northern Hemisphere cooling. *Geophysical Research Letters*, 33(1).
- Caley, T., Malaizé, B., Zaragosi, S., Rossignol, L., Bourget, J., Eynaud, F., Martinez, P., Giraudeau, J., Charlier, K. and Ellouz-Zimmermann, N., 2011. New Arabian Sea records help decipher orbital timing of Indo-Asian monsoon. *Earth and Planetary Science Letters*, 308(3): 433-444.
- Cheng, H., Edwards, R.L., Sinha, A., Spötl, C., Yi, L., Chen, S., Kelly, M., Kathayat, G., Wang, X. and Li, X., 2016. The Asian monsoon over the past 640,000 years and ice age terminations. *Nature*, 534(7609): 640-646.
- Cherchi, A. and Navarra, A., 2013. Influence of ENSO and of the Indian Ocean Dipole on the Indian summer monsoon variability. *Climate dynamics*, 41(1): 81-103.

- Chou, C., 2003. Land–sea heating contrast in an idealized Asian summer monsoon. *Climate Dynamics*, 21(1): 11-25.
- Clemens, S.C., 1998. Dust response to seasonal atmospheric forcing: Proxy evaluation and calibration. *Paleoceanography*, 13(5): 471-490.
- Clemens, S.C., Murray, D.W. and Prell, W.L., 1996. Nonstationary phase of the Plio-Pleistocene Asian monsoon. *Science*, 274(5289): 943.
- Clemens, S.C. and Prell, W.L., 1990. Late Pleistocene variability of Arabian Sea summer monsoon winds and continental aridity: Eolian records from the lithogenic component of deep-sea sediments. *Paleoceanography*, 5(2): 109-145.
- Clemens, S., Prell, W., Murray, D., Shimmield, G. and Weedon, G., 1991. Forcing mechanisms of the Indian Ocean monsoon. *Nature*, 353(6346): 720-725.
- Clemens, S.C., Prell, W.L. and Sun, Y., 2010. Orbital-scale timing and mechanisms driving Late Pleistocene Indo-Asian summer monsoons: Reinterpreting cave speleothem $\delta^{18}\text{O}$. *Paleoceanography*, 25(4).
- Clift, P.D., Hodges, K.V., Heslop, D., Hannigan, R., Van Long, H. and Calves, G., 2008. Correlation of Himalayan exhumation rates and Asian monsoon intensity. *Nature Geoscience*, 1(12): 875-880.
- Curry, W., Ostermann, D., Guptha, M. and Ittekkot, V., 1992. Foraminiferal production and monsoonal upwelling in the Arabian Sea: evidence from sediment traps. *Geological Society, London, Special Publications*, 64(1): 93-106.
- De Angelis, M., Barkov, N. and Petrov, V., 1987. Aerosol concentrations over the last climatic cycle (160 kyr) from an Antarctic ice core. *Nature*, 325(6102): 318-321.
- Dhar, O. and Nandargi, S., 2003. Hydrometeorological aspects of floods in India. *Natural Hazards*, 28(1): 1-33.
- Dickson, R.R., 1984. Eurasian snow cover versus Indian monsoon rainfall—An extension of the Hahn-Shukla results. *Journal of Climate and Applied Meteorology*, 23(1): 171-173.
- Dirmeyer, P.A., 1998. Land-sea geometry and its effect on monsoon circulations. *Journal of Geophysical Research: Atmospheres*, 103(D10): 11555-11572.
- Elderfield, H. and Ganssen, G., 2000. Past temperature and $\delta^{18}\text{O}$ of surface ocean waters inferred from foraminiferal Mg/Ca ratios. *Nature*, 405(6785): 442-445.
- Fasullo, J. and Webster, P., 2003. A hydrological definition of Indian monsoon onset and withdrawal. *Journal of Climate*, 16(19): 3200-3211.
- Flato, G., Marotzke, J., Abiodun, B., Braconnot, P., Chou, S.C., Collins, W.J., Cox, P., Driouech, F., Emori, S. and Eyring, V., 2013. Evaluation of Climate Models. In: *Climate Change 2013: The Physical Science Basis. Contribution of Working Group I to the Fifth Assessment Report of the Intergovernmental Panel on Climate Change*. *Climate Change 2013*, 5: 741-866.
- Fleitmann, D., Burns, S.J., Mudelsee, M., Neff, U., Kramers, J., Mangini, A. and Matter, A., 2003. Holocene forcing of the Indian monsoon recorded in a stalagmite from southern Oman. *Science*, 300(5626): 1737-1739.

- Gadgil, S., 2003. The Indian monsoon and its variability. *Annual Review of Earth and Planetary Sciences*, 31(1): 429-467.
- Gebregiorgis, D., Hathorne, E., Sijinkumar, A., Nath, B.N., Nürnberg, D. and Frank, M., 2016. South Asian summer monsoon variability during the last~ 54 kyrs inferred from surface water salinity and river run off proxies. *Quaternary Science Reviews*, 138: 6-15.
- Hadley, G., 1735. Concerning the cause of the general trade-winds: By Geo. Hadley, Esq; FRS. *Philosophical Transactions*, 39(436-444): 58-62.
- Hahn, D.G. and Manabe, S., 1975. The role of mountains in the south Asian monsoon circulation. *Journal of the Atmospheric Sciences*, 32(8): 1515-1541.
- Hahn, D.G. and Shukla, J., 1976. An apparent relationship between Eurasian snow cover and Indian monsoon rainfall. *Journal of Atmospheric Sciences*, 33: 2461-2462.
- Halley, E., 1686. An Historical Account of the Trade Winds, and Monsoons, Observable in the Seas between and Near the Tropicks, with an Attempt to Assign the Phisical Cause of the Said Winds, By E. Halley. *Philosophical transactions*, 16(179-191): 153-168.
- Hoskins, B.J. and Rodwell, M.J., 1995. A model of the Asian summer monsoon. Part I: The global scale. *Journal of the atmospheric sciences*, 52(9): 1329-1340.
- Johnson, S.J., Levine, R.C., Turner, A.G., Martin, G.M., Woolnough, S.J., Schiemann, R., Mizielinski, M.S., Roberts, M.J., Vidale, P.L. and Demory, M.-E., 2016. The resolution sensitivity of the South Asian monsoon and Indo-Pacific in a global 0.35° AGCM. *Climate Dynamics*, 46(3-4): 807-831.
- Kathayat, G., Cheng, H., Sinha, A., Spötl, C., Edwards, R.L., Zhang, H., Li, X., Yi, L., Ning, Y. and Cai, Y., 2016. Indian monsoon variability on millennial-orbital timescales. *Scientific reports*, 6.
- Krishnamurthy, V. and Goswami, B., 2000. Indian monsoon-ENSO relationship on interdecadal timescale. *Journal of Climate*, 13(3): 579-595.
- Kudrass, H., Hofmann, A., Dose, H., Emeis, K. and Erlenkeuser, H., 2001. Modulation and amplification of climatic changes in the Northern Hemisphere by the Indian summer monsoon during the past 80 ky. *Geology*, 29(1): 63-66.
- Kumar, K.K., Rajagopalan, B. and Cane, M.A., 1999. On the weakening relationship between the Indian monsoon and ENSO. *Science*, 284(5423): 2156-2159.
- Kutzbach, J. and Gallimore, R., 1989. Pangaeen climates: megamonsoons of the megacontinent. *Journal of Geophysical Research: Atmospheres*, 94(D3): 3341-3357.
- Kutzbach, J.E., 1981. Monsoon climate of the early Holocene: climate experiment with the earth's orbital parameters for 9000 years ago. *Science*, 214(4516): 59-61.
- Li, C. and Yanai, M., 1996. The onset and interannual variability of the Asian summer monsoon in relation to land-sea thermal contrast. *Journal of Climate*, 9(2): 358-375.
- Li, J., Xie, S.-P., Cook, E.R., Morales, M.S., Christie, D.A., Johnson, N.C., Chen, F., D'Arrigo, R., Fowler, A.M. and Gou, X., 2013. El Niño modulations over the past seven centuries. *Nature Climate Change*, 3(9): 822-826.

- Luo, H. and Yanai, M., 1984. The large-scale circulation and heat sources over the Tibetan Plateau and surrounding areas during the early summer of 1979. Part II: Heat and moisture budgets. *Monthly Weather Review*, 112(5): 966-989.
- Maher, B.A. and Thompson, R., 2012. Oxygen isotopes from Chinese caves: records not of monsoon rainfall but of circulation regime. *Journal of Quaternary Science*, 27(6): 615-624.
- Manabe, S. and Broccoli, A., 1990. Mountains and arid climates of middle latitudes. *Science*, 247(4939): 192-195.
- Mani, N.J., Suhas, E. and Goswami, B., 2009. Can global warming make Indian monsoon weather less predictable? *Geophysical Research Letters*, 36(8).
- Mantsis, D.F., Lintner, B.R., Broccoli, A.J., Erb, M.P., Clement, A.C. and Park, H.-S., 2014. The response of large-scale circulation to obliquity-induced changes in meridional heating gradients. *Journal of Climate*, 27(14): 5504-5516.
- McManus, J.F., Oppo, D.W. and Cullen, J.L., 1999. A 0.5-million-year record of millennial-scale climate variability in the North Atlantic. *Science*, 283(5404): 971-975.
- Meehl, G.A., 1987. The annual cycle and interannual variability in the tropical Pacific and Indian Ocean regions. *Monthly Weather Review*, 115(1): 27-50.
- Merlis, T.M., Schneider, T., Bordoni, S. and Eisenman, I., 2013. The tropical precipitation response to orbital precession. *Journal of Climate*, 26(6): 2010-2021.
- Mohtadi, M., Prange, M. and Steinke, S., 2016. Palaeoclimatic insights into forcing and response of monsoon rainfall. *Nature*, 533(7602): 191-199.
- Neff, U., Burns, S., Mangini, A., Mudelsee, M., Fleitmann, D. and Matter, A., 2001. Strong coherence between solar variability and the monsoon in Oman between 9 and 6 kyr ago. *Nature*, 411(6835): 290-293.
- Overpeck, J., Anderson, D., Trumbore, S. and Prell, W., 1996. The southwest Indian Monsoon over the last 18 000 years. *Climate Dynamics*, 12(3): 213-225.
- Pant, G. and Parthasarathy, S.B., 1981. Some aspects of an association between the Southern Oscillation and Indian summer monsoon. *Archives for meteorology, geophysics, and bioclimatology, Series B*, 29(3): 245-252.
- Petit, J.-R., Jouzel, J., Mounier, L., Korotkevich, Y.S. and Kotliakov, V., 1990. Palaeoclimatological and chronological implications of the Vostok core dust record. *Nature*, 343: 56-58.
- Pidwirny, M., 2006. "Global Scale Circulation of the Atmosphere". *Fundamentals of Physical Geography, 2nd Edition*. Date Viewed: July, 2016. <http://www.physicalgeography.net/fundamentals/7p.html>
- Privé, N.C. and Plumb, R.A., 2007. Monsoon dynamics with interactive forcing. Part I: Axisymmetric studies. *Journal of the atmospheric sciences*, 64(5): 1417-1430.
- Rashid, H., Flower, B., Poore, R. and Quinn, T., 2007. A ~ 25ka Indian Ocean monsoon variability record from the Andaman Sea. *Quaternary Science Reviews*, 26(19): 2586-2597.

- Rasmusson, E.M. and Carpenter, T.H., 1982. Variations in tropical sea surface temperature and surface wind fields associated with the Southern Oscillation/El Niño. *Monthly Weather Review*, 110(5): 354-384.
- Rea, D.K., Leinen, M. and Janecek, T.R., 1985. Geologic approach to the long-term history of atmospheric circulation. *Science*, 227(4688): 721-725.
- Rohling, E., Foster, G.L., Grant, K., Marino, G., Roberts, A., Tamisiea, M.E. and Williams, F., 2014. Sea-level and deep-sea-temperature variability over the past 5.3 million years. *Nature*, 508(7497): 477-482.
- Sato, T. and Kimura, F., 2007. How does the Tibetan Plateau affect the transition of Indian monsoon rainfall? *Monthly Weather Review*, 135(5): 2006-2015.
- Schneider, U., Becker, A., Finger, P., Meyer-Christoffer, A., Ziese, M. and Rudolf, B., 2014. GPCP's new land surface precipitation climatology based on quality-controlled in situ data and its role in quantifying the global water cycle. *Theoretical and Applied Climatology*, 115(1-2): 15-40.
- Schulz, H., von Rad, U. and Erlenkeuser, H., 1998. Correlation between Arabian Sea and Greenland climate oscillations of the past 110,000 years. *Nature*, 393(6680): 54-57.
- Shackleton, N., 1974. Attainment of isotopic equilibrium between ocean water and the benthonic foraminifera genus *Uvigerina*: isotopic changes in the ocean during the last glacial.
- Shi, L. and Smith, E.A., 1992. Surface forcing of the infrared cooling profile over the Tibetan Plateau. Part II: Cooling-rate variation over large-scale plateau domain during summer monsoon transition. *Journal of the atmospheric sciences*, 49(10): 823-844.
- Shindell, D.T., Schmidt, G.A., Mann, M.E., Rind, D. and Waple, A., 2001. Solar forcing of regional climate change during the Maunder Minimum. *Science*, 294(5549): 2149-2152.
- Sirocko, F., Sarnthein, M., Lange, H. and Erlenkeuser, H., 1991. Atmospheric summer circulation and coastal upwelling in the Arabian Sea during the Holocene and the last glaciation. *Quaternary Research*, 36(1): 72-93.
- Slingo, J., Spencer, H., Hoskins, B., Berrisford, P. and Black, E., 2005. The meteorology of the Western Indian Ocean, and the influence of the East African Highlands. *Philosophical Transactions of the Royal Society of London A: Mathematical, Physical and Engineering Sciences*, 363(1826): 25-42.
- Smith, E.A. and Shi, L., 1992. Surface forcing of the infrared cooling profile over the Tibetan plateau. Part I: Influence of relative longwave radiative heating at high altitude. *Journal of the atmospheric sciences*, 49(10): 805-822.
- Sontakke, N., Singh, N. and Singh, H., 2008. Instrumental period rainfall series of the Indian region (AD 1813—2005): revised reconstruction, update and analysis. *The Holocene*, 18(7): 1055-1066.
- Tian, J., Xie, X., Ma, W., Jin, H. and Wang, P., 2011. X-ray fluorescence core scanning records of chemical weathering and monsoon evolution over the past 5 Myr in the southern South China Sea. *Paleoceanography*, 26(4).
- Turner, A.G. and Annamalai, H., 2012. Climate change and the South Asian summer monsoon. *Nature Climate Change*, 2(8): 587-595.

- Vellinga, M. and Wood, R.A., 2008. Impacts of thermohaline circulation shutdown in the twenty-first century. *Climatic Change*, 91(1-2): 43-63.
- Waelbroeck, C., Labeyrie, L., Michel, E., Duplessy, J.C., McManus, J., Lambeck, K., Balbon, E. and Labracherie, M., 2002. Sea-level and deep water temperature changes derived from benthic foraminifera isotopic records. *Quaternary Science Reviews*, 21(1): 295-305.
- Wahl, E.R. and Morrill, C., 2010. Toward understanding and predicting monsoon patterns. *Science*, 328(5977): 437-438.
- Wang, B., Xiang, B., Li, J., Webster, P.J., Rajeevan, M.N., Liu, J. and Ha, K.-J., 2015. Rethinking Indian monsoon rainfall prediction in the context of recent global warming. *Nature communications*, 6.
- Wang, Y., Cheng, H., Edwards, R.L., Kong, X., Shao, X., Chen, S., Wu, J., Jiang, X., Wang, X. and An, Z., 2008. Millennial-and orbital-scale changes in the East Asian monsoon over the past 224,000 years. *Nature*, 451(7182): 1090-1093.
- Webster, P.J., 1987. The elementary monsoon. *Monsoons*. Wiley, New York: 3-32.
- Webster, P.J., Magana, V.O., Palmer, T., Shukla, J., Tomas, R., Yanai, M. and Yasunari, T., 1998. Monsoons: Processes, predictability, and the prospects for prediction. *Journal of Geophysical Research: Oceans*, 103(C7): 14451-14510.
- Webster, P.J. and Yang, S., 1992. Monsoon and ENSO: Selectively interactive systems. *Quarterly Journal of the Royal Meteorological Society*, 118(507): 877-926.
- Wu, G., Liu, Y., He, B., Bao, Q., Duan, A. and Jin, F.-F., 2012. Thermal controls on the Asian summer monsoon. *Scientific Reports*, 2: 404.
- Wu, G. and Zhang, Y., 1998. Tibetan Plateau forcing and the timing of the monsoon onset over South Asia and the South China Sea. *Monthly weather review*, 126(4): 913-927.
- Yanai, M. and Wu, G.-X., 2006. Effects of the tibetan plateau, *The Asian Monsoon*. Springer, pp. 513-549.
- Zhang, R. and Delworth, T.L., 2005. Simulated tropical response to a substantial weakening of the Atlantic thermohaline circulation. *Journal of Climate*, 18(12): 1853-1860.
- Ziegler, M., Lourens, L.J., Tuenter, E., Hilgen, F., Reichert, G.J. and Weber, N., 2010. Precession phasing offset between Indian summer monsoon and Arabian Sea productivity linked to changes in Atlantic overturning circulation. *Paleoceanography*, 25(3).

II. Experimental design

The methods and materials used in this dissertation are presented in detail in the subsequent chapters and are based on previously well-established methodologies. A detailed description of the methods is provided in chapters I (Material and methods, and supplement material), II (section 2.3), and IV (section 2.2 and 2.3). Here, a brief overview of the experimental design, and statistical framework is provided. Data presented in this thesis were generated from three Andaman Sea sediment cores obtained during three expeditions: the Indian National Gas Hydrate Program (NGHP) expedition in 2006, the 168th cruise of ORV Sagar Kanya in 2008, and IODP expedition 353 in 2014. This work is part of larger collaborative projects between the GEOMAR Helmholtz Centre for Ocean Research Kiel and several other institutes, which will be listed in full in future publications.

The experimental design is divided into four stages. Different approaches were chosen to generate high-resolution proxy records of the monsoon and are discussed in detailed in the following chapters.

- (1)** The first stage involved sampling of a long sediment core from NGHP site 17 at roughly similar intervals for discrete measurements. A total of ~700 samples were taken from this sediment core. Four planktic (*Globigerinoides sacculifer* and *Neogloboquadrina dutertrei*) and benthic (*Cibicidoides wuellerstorfi* and *Cibicidoides mundulus*) foraminiferal species were picked based on their habitat depth. Here, on average >50 specimens per sample for the planktic species (except for samples from SK168, see chapter 6) and ~3 to 5 specimens for the benthic species were picked to obtain a representative geochemical signature.
- (2)** The second stage involved thorough cleaning of foraminiferal samples for Mg/Ca measurements following well established cleaning procedures (e.g. Boyle, 1981). Mg/Ca measurements were performed using an Agilent 7500-CX inductively coupled plasma mass

spectrometer (OC-ICP-MS)/ICP OES (VARIAN 720-ES). The $\delta^{18}\text{O}$ measurements were performed using a MAT 253 mass spectrometer coupled with a Kiel IV Carbonate device (Thermo Scientific). For details of the Mg/Ca cleaning steps followed, see (Gebregiorgis et al., 2016) and section 3 of chapter 6.

- (3)** The third stage involved generating ultra high resolution XRF data through non-destructive techniques using an Avaatech X-ray fluorescence core scanner. Detailed description of this method and developed proxies are given in chapter 2.
- (4)** The final stage consisted robust statistical analysis of the proxy records generated following **(2)** and **(3)** as discussed below.

II.1 Paleoclimate timeseries analysis

Cross-spectral analysis is often used to quantify and estimate the relationship between two variables in the time domain as a function of frequency and is expressed in terms of coherency and phase spectrum. Coherency is a measure of how well two time series co-vary over a frequency band when the phase difference is set to zero. Cross-spectral analysis is employed here to identify common variability between two time series and quantify phase relationships with respect to the primary orbital frequency bands (e.g. over precession, obliquity or eccentricity bands). Phase estimates over a specific frequency band indicate temporal (lead/lag) relationships between two time series and are given in degrees. In subsequent chapters, cross-spectral results (i.e. coherence and phase relationships) are summarized in phase wheels. For example, if we consider that time series B lags a reference insolation index time series A by 5 kyrs with respect to precession minima and obliquity maxima, this is synonymous to a $\sim 79^\circ$ (i.e. $5 \text{ kyrs}/23 \text{ kyrs} * 360^\circ$) and $\sim 44^\circ$ (i.e. $5 \text{ kyrs}/41 \text{ kyrs} * 360^\circ$) lag over the two frequency bands respectively (Fig 2.1). A statistically significant coherence would thus indicate the presence of a strong linear relationship between time series A and B and a plausible direct causal link can be established given that a physical link between the two is anticipated.

Coherence estimates and phase relationships, then, allow us to establish causal links between potential forcing mechanisms, such as orbital insolation forcing and proxies of the monsoon or other variables.

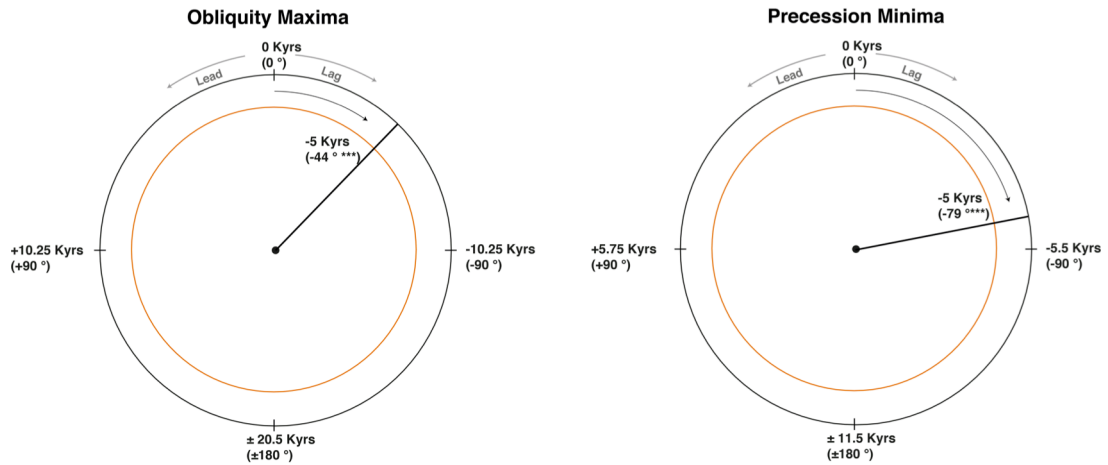


Fig 2.1. In this hypothetical phase wheel representation, the 12 o'clock position represents maximum Milankovitch forcing, and phase lags increase in the clockwise direction. Vector length (from circle centre to middle of arc represents the degree of coherence, and the associated arc denotes the estimated phase error. Red circles mark 80% coherence.

III. Publications and manuscripts

Declaration of my contribution to the following chapters:

Chapter I:

Astronomical forcing of South Asian monsoon precipitation over the past ~1 million years

D. Gebregiorgis, E.C. Hathorne, L. Giosan, S. Clemens, D. Nürnberg and M. Frank
Manuscript to be submitted to Nature.

Statement:

Ed Hathorne, in collaboration with Liviu Giosan and Martin Frank, wrote and submitted the proposal to the DFG, through which this PhD project was funded (DFG, grant HA 5751/3-1). Ed Hathorne and I planned the experiment and sampling of sediment material. Ingmar Schindlbeck, Imke Bruhn and Julia Langer helped picking foraminiferal samples. I did the Mg/Ca cleaning and trace metal /Ca measurements on Agilent 7500cs ICP-MS under the guidance of Ed Hathorne. I did the Mg/Ca measurements on ICP OES (VARIAN 720-ES) under the guidance of Nadine Ghere. I did all stable isotope measurements with generous hand from Fynn Wulf and Sebastian Fessler. I preformed paleoclimate timeseries analysis and wrote the manuscript. All co-authors helped revising this manuscript.

Chapter II:

Orbital forcing of South Asian monsoon inferred from Andaman Sea X-ray fluorescence core scanning records

D. Gebregiorgis, E.C. Hathorne, L. Giosan, D. Nürnberg, A. Plass, M. Frank, S.C Clemens and Exp. 353 Scientists
Manuscript to be submitted to EPSL.

Statement:

I designed the study together with Ed Hathorne. I generated the XRF data from core U1448 together with Ed Hathorne and Anna Plass. Liviu Giosan generated XRF data for NGHP 17. I analyzed the XRF data from both cores, performed paleoclimate timeseries analysis and wrote the manuscript. Martin Frank and Ed Hathorne helped improving the manuscript.

Chapter III:

Orbital variations in the mixed layer and thermocline over the past ~1 million years

D. Gebregiorgis, E.C. Hathorne, D. Nürnberg, S., Clemens, L. Giosan and M. Frank¹

Manuscript to be submitted to GRL.

Statement:

Ed Hathorne and I planned the experiment and sampling of sediment material. I did the Mg/Ca cleaning. I did the Mg/Ca measurements on Agilent 7500cs ICP-MS under the guidance of Ed Hathorne. I did the Mg/Ca measurements on ICP OES (VARIAN 720-ES) under the guidance of Nadine Ghere. I did all stable isotope measurements with generous hand from Fynn Wulf and Sebastian Fessler. I performed paleoclimate timeseries analysis and wrote the manuscript. Ed Hathorne helped revising this manuscript.

Chapter IV:

South Asian summer monsoon variability during the last ~54 kyrs inferred from surface water salinity and river runoff proxies

D. Gebregiorgis, E.C. Hathorne, A.V. SijinKumar, B. Nagender Nath, D. Nürnberg, and M. Frank

Quaternary Science Reviews 138: 6–15, doi: 10.1016/j.quascirev.2016.02.012

Statement:

Ed Hathorne and I planned the experiment. I did the Mg/Ca cleaning and trace metal /Ca measurements on Agilent 7500cs ICP-MS under the guidance of Ed Hathorne. I did the stable isotope measurements with help from Fynn Wulf. I performed the analyses and wrote the manuscript. All co-authors reviewed and gave feedbacks on earlier versions of the manuscript prior to submission and during the revision process. Two anonymous reviews helped to improve this paper.

Chapter I

Astronomical forcing of South Asian monsoon precipitation over the past ~1 million years

D. Gebregiorgis¹, E.C. Hathorne¹, L. Giosan², S. Clemens², D. Nürnberg¹, and M. Frank¹

¹*GEOMAR Helmholtz Centre for Ocean Research Kiel, Wischhofstraße 1-3, 24148 Kiel, Germany*

²*Woods Hole Oceanographic Institution, Woods Hole, Massachusetts, USA, USA*

³*Earth, Environmental, and Planetary Sciences, Brown University, Providence, RI, U.S.A.*

Abstract *

The Indian summer or south Asian monsoon (SAM) precipitation is vitally important for billions of people yet its controlling mechanisms on orbital (> 1000 yr) time scales are still poorly understood (Mohtadi et al., 2016). Absolutely dated speleothem records from China (Cheng et al., 2009; Cheng et al., 2016; Wang et al., 2008; Wang et al., 2001) record a mixed signal of the amount of precipitation and moisture sources (Clemens et al., 2010; Maher and Thompson, 2012) while records of monsoon wind induced upwelling in the Arabian Sea may not have been directly related to monsoon rainfall (Ziegler et al., 2010). The core convective region of the SAM is over the Bay of Bengal and Andaman Sea but no record of surface seawater conditions prior 80,000 years ago exists for this region. Here we reconstruct surface seawater temperature and oxygen isotope compositions in the Andaman Sea over the past one million years with measurements of near surface dwelling planktonic foraminifera. Our records show that summer monsoon precipitation peaked ~9 kyrs after the NH insolation maximum in the precession band, in phase with productivity changes in the Arabian Sea. Nonetheless, the precession band accounts for only a small component (~30 %) of the total variance of $\delta^{18}\text{O}_{\text{sw}}$ and can thus not be considered the primary forcing mechanism driving the monsoon system and tropical climate change. We propose that obliquity forcing has played a much larger role than previously assumed and in ways fundamentally different from precession forcing of the monsoon via enhanced cross-hemispheric atmospheric moisture flux.

* Manuscript to be submitted to *Nature*

At present, over 3 billion people live in the region influenced by the South Asian monsoon (SAM) and their number is estimated to increase to over 5 billion by 2050 (Lutz and Samir, 2011). The SAM supplies the precipitation essential for food supply of the people of south Asia, while also posing a risk to human life through flooding. The conventional view of the SAM is that it's primarily driven by interhemispheric temperature/pressure differences between the Asian continent (particularly over the southern Tibetan Plateau) and the southern Indian Ocean (e.g. Webster et al., 1998), although the role of the Tibetan plateau summer warming has been challenged recently (e.g. Boos and Kuang, 2010). One characteristic feature of the SAM is that it exhibits a remarkably consistent annual cycle. Historically, the SAM changes were considered to have been under the direct influence of ENSO, with above/below average SAM precipitation occurring during phases of strong El Niño/La Niña conditions. However, in the course of global warming this relationship has become markedly less clear (Mani et al., 2009; Wang et al., 2015) and how the monsoon responds directly to external forcing remains uncertain. It is not surprising then that even simulating the basic aspects of the SAM remains a severe test for the most advanced coupled ocean-atmosphere general circulation models (Flato et al., 2013). Paleoclimate timeseries analysis on orbital timescales provides a unique opportunity to examine monsoon sensitivity to external insolation forcing, where Earth's precession, obliquity and eccentricity cycles modulate the distribution of global and regional solar radiation and can be accurately calculated going back several millions of years (Berger and Loutre, 1991). A better understanding of monsoon evolution on various timescales greatly enhances understanding of the monsoon system and its sensitivities, and also affects the performance of climate models (Mohtadi et al., 2016).

Previous studies of summer monsoon variability mainly relied on wind-based proxies from the Arabian Sea. Interpretation of these proxies is based on the core assumption that seasonally reversing strong summer monsoon winds promote upwelling-driven production of distinct plankton species (Anderson and Prell, 1993;

Naidu and Malmgren, 1996). Lithogenic grain size proxies, on the other hand, are directly linked via the transport capacity of the summer monsoon winds (e.g. Clemens et al., 1991). Several of these records indicate a consistent time lag of ~8 kyrs between peak Northern Hemisphere summer insolation and peak monsoon intensity at the precession cycle (e.g. Caley et al., 2011; Clemens et al., 1991). This is in direct contrast to the absolutely dated speleothem records from China, frequently cited as proxies of summer monsoon precipitation, which exhibit a time lag of only 3 kyrs with respect to Northern Hemisphere peak summer insolation (Cheng et al., 2009; Cheng et al., 2016; Wang et al., 2008; Wang et al., 2001). However, the validity of both the wind-based and speleothem $\delta^{18}\text{O}$ proxies have been questioned due to significant orbital-scale interferences by other processes not directly related to the monsoon (e.g. Ziegler et al., 2010, Clemens et al., 2010; Maher and Thompson, 2012). Consequently, there is a fundamental divergence in opinion and lack of understanding in how the monsoon responds to changes of the most basic boundary conditions, such as insolation and global ice volume. This basic lack of understanding is directly related to the fact that no record of surface seawater conditions longer than the past 80,000 years exists from the core convective region of the summer monsoon over the Bay of Bengal and Andaman Sea.

Here, we combine Mg/Ca measurements (a proxy for the temperature prevailing during calcification) and $\delta^{18}\text{O}$ analyses of mixed-layer dwelling planktic foraminifera *G. sacculifer* from the Andaman Sea basin at site 17 (NGHP 17) to produce the first continuous orbital scale monsoon precipitation record for the last ~1 million years. The oxygen-isotopic composition of planktonic foraminifera is a function of calcification temperature and of ambient seawater $\delta^{18}\text{O}$ ($\delta^{18}\text{O}_{\text{sw}}$). The Mg/Ca ratio of planktonic foraminiferal calcite is essentially a function of calcification temperature and has the unique advantage of being an independent temperature proxy that is measured on the same shells as for $\delta^{18}\text{O}$. Paired Mg/Ca- $\delta^{18}\text{O}$ measurements therefore allow the reconstruction of temperature and seawater $\delta^{18}\text{O}_{\text{sw}}$ signals for any given time in the past. In the Bay of Bengal and the Andaman Sea the strength of the SAM governs the sea-surface conditions. The net

annual surface precipitation gain (i.e. precipitation plus runoff minus evaporation) within the Bay of Bengal and Andaman Sea is on average $152 \times 10^{10} \text{ m}^3$ and is primarily due to intense freshening of the surface ocean from direct precipitation and runoff from the Irrawaddy and Salween river basins during the summer monsoon season (Varkey et al., 1996). This is also clearly reflected in the monsoon driven seasonal climatology of net fresh water flux (precipitation minus evaporation) in the Andaman Sea (Fig 1). We therefore infer that any observed changes in our proxy records were solely a function of summer monsoon precipitation and can be used to unambiguously unravel insolation forcing mechanisms of the SAM over the last ~ 1 million years.

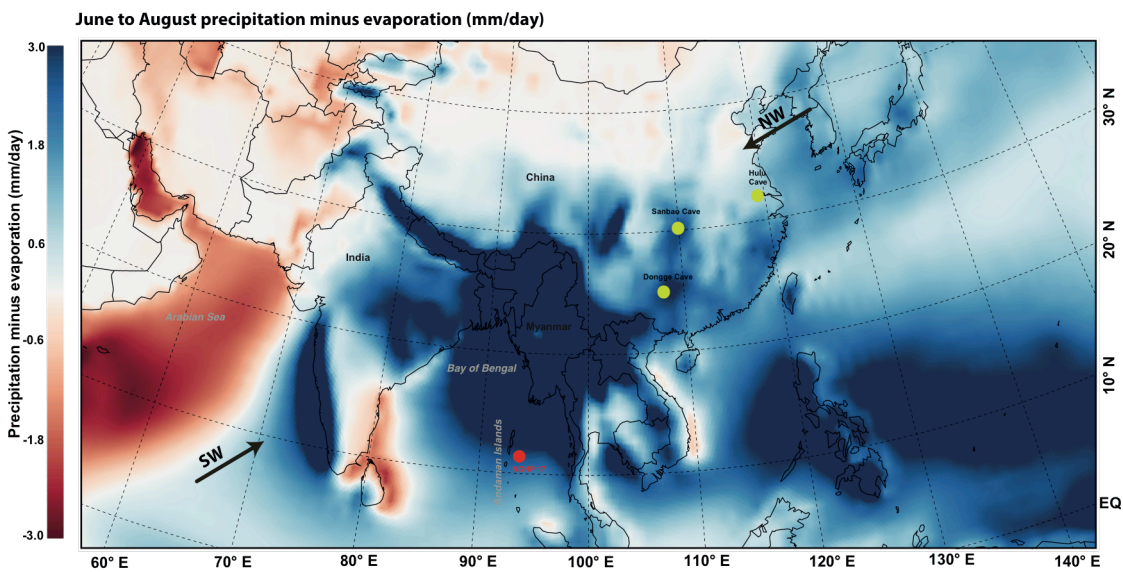


Fig 1. Summer net precipitation flux (precipitation minus evaporation) (mm/day) in the Asian monsoon domain for the period 1979-2015 (precipitation and evaporation data from ERA-Interim global reanalysis dataset). NGHP17 core site is shown in red filled circle. Filled green circles show cave locations in the East Asian monsoon region (Cheng et al., 2016).

The temporal evolution of SST, $\delta^{18}\text{O}$ and $\delta^{18}\text{O}_{\text{sw}}$ records from NGHP 17 over the past ~ 1 million years are shown in Fig. 2. Reconstructed SST, $\delta^{18}\text{O}$ and $\delta^{18}\text{O}_{\text{sw}}$ document large, persistent shifts in surface temperature and salinity indicating sensitivity to orbital forcing. The SST and $\delta^{18}\text{O}$ records are dominated by pronounced ~ 100 Kyr

eccentricity, 41 Kyr obliquity and ~ 23 Kyr precession cycles, with increasing spectral power in that order ($>90\%$ CI). Cross-spectral analyses with respect to eccentricity, obliquity and precession (ETP) (Berger, 1999) indicate that SST and $\delta^{18}\text{O}$ records are highly coherent ($>95\%$ CI) over the precession band and to lesser extent over the obliquity band ($>80\%$ CI). Similar to the SST records, the $\delta^{18}\text{O}_{\text{SW}}$ power spectrum shows a statistically significant signal in the precession, obliquity and eccentricity bands ($>80\%$ CI) (Fig 3). However, cross-spectral analysis of $\delta^{18}\text{O}_{\text{SW}}$ with respect to ETP reveals a strong coherency ($>95\%$) only in the precession band despite the fact that more variance in the proxy record is contained in the obliquity and eccentricity frequency bands. Precession related variance in both $\delta^{18}\text{O}_{\text{SW}}$ and SST records accounts for at most ($\sim 30\%$) of the total variance in the records and provides the clearest evidence that precession forcing cannot be considered the primary mechanism driving the monsoon system and tropical climate change. This proves that the forcing mechanisms of the monsoon are far more complex and the link between insolation forcing due to variation of Earth's orbit and monsoon climate cannot be assumed to be linear as consequence of internal climate processes (Clemens et al., 1991). The prevalence of distinct spectral peaks at ~ 178 kyrs and in particular ~ 30 kyrs in the $\delta^{18}\text{O}_{\text{SW}}$ record, likely representing heterodynes of the primary orbital periods, provide additional evidence demonstrating that the response of monsoon climate has been strongly non-linear and sensitive to a combined insolation (precession and obliquity driven) and ice volume (eccentricity driven) forcing ($1/100+1/41 = \mathbf{1/29}$ or $1/100 + 1/23 = \mathbf{1/30}$). Thus, in order to establish causal links between orbital forcing and summer monsoon precipitation, we need to consider phase relationships between the proxies with respect to ETP (Fig 4). Here, we compare SST and $\delta^{18}\text{O}_{\text{SW}}$ records in an effort to understand the link between tropical SST in the Bay of Bengal and monsoon precipitation. The phasings between two Arabian monsoon stacks hereafter denoted AS1 (Clemens and Prell, 2003) and AS2 (Caley et al., 2011), and a recently published composite cave $\delta^{18}\text{O}$ record from China (Cheng et al., 2016) are compared to validate these proxy records of the monsoon.

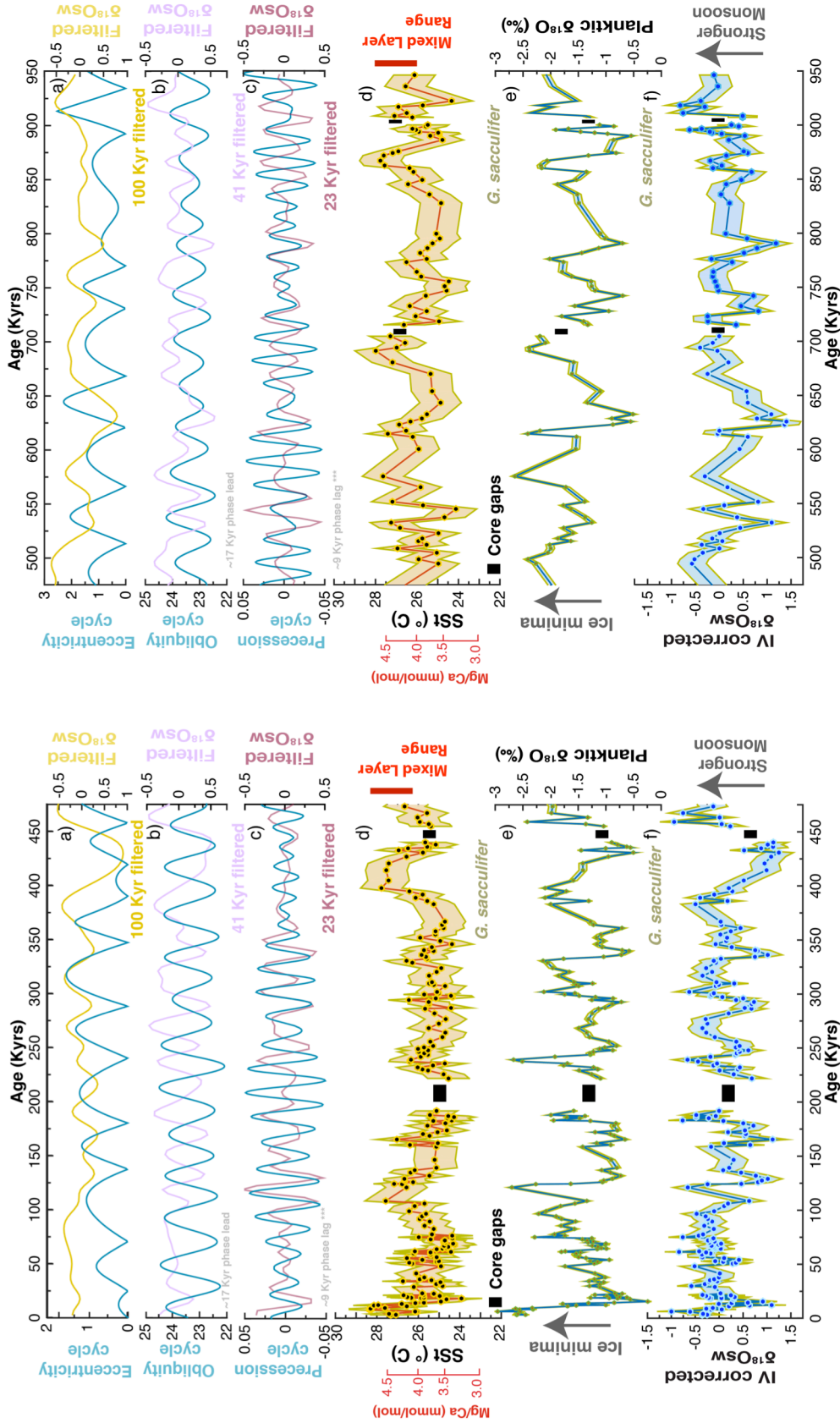


Fig 1. a) Comparison of 100 Kyr obliquity (Berger, 1999) (blue) and 100 Kyr filtered $\delta^{18}\text{Osw}$; b) Comparison of 23 Kyr precession (Berger, 1999) (blue) and 23 Kyr filtered $\delta^{18}\text{Osw}$; c) Comparison of 41 Kyr obliquity (Berger, 1999) (blue) and 41 Kyr filtered $\delta^{18}\text{Osw}$; d) Reconstructed SST at site 17; e) Oxygen isotope ratios of foraminifera *G. sacculifer*; f) Ice volume corrected $\delta^{18}\text{Osw}$. Envelopes in d and f show 1 σ -error (see methods). Also shown $\delta^{18}\text{Osw}$ phase lags with respect to the three main orbital frequencies (***denotes 95% CI).

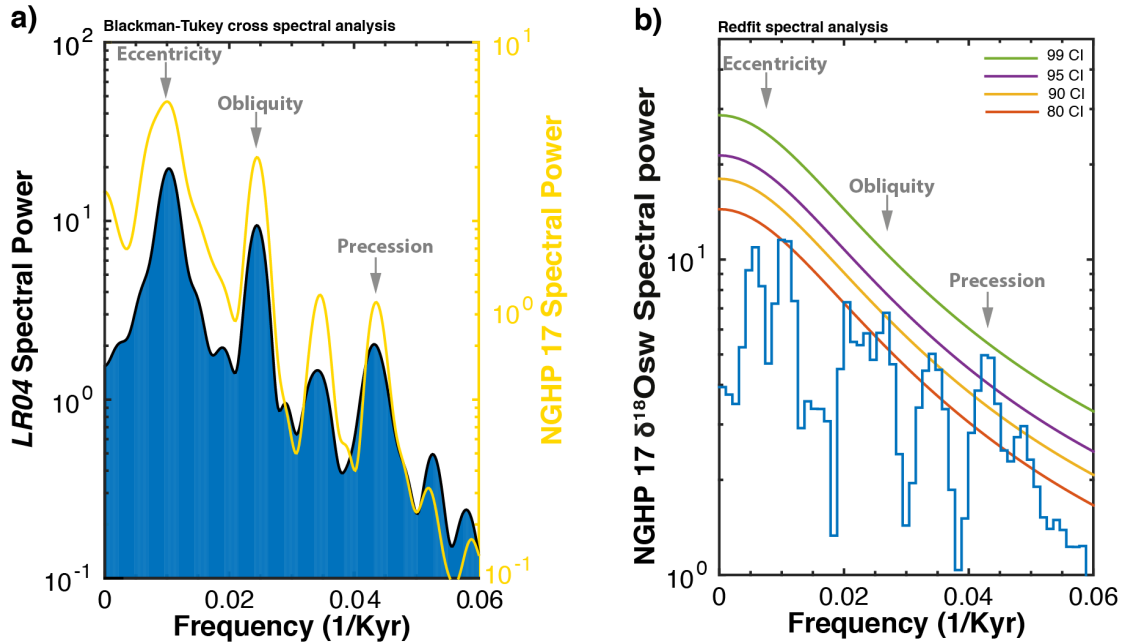


Fig 3 a) Blackman-Tukey cross spectral analysis of LR04 (Lisiecki and Raymo, 2005) tuned NGHP 17 benthic isotope stratigraphy indicating strong coherence at the three main orbital frequencies (95% CI). b) Spectral analysis (Redfit, Schulz and Mudelsee, 2002) of Ice volume corrected $\delta^{18}\text{O}_{\text{sw}}$. Spectral analyses were performed on unevenly spaced time series with an oversampling factor of 3 and a Hanning window to define spectral peaks.

Fig. 4 summarizes coherence and phase relationships between Site 17 records and ETP in the precession and obliquity bands. SST and $\delta^{18}\text{O}_{\text{sw}}$ indicate that both records are highly coherent with respect to ETP in the precession band. However, the two records are out of phase. Reconstructed $\delta^{18}\text{O}_{\text{sw}}$ show a lag of ~ 9 kyrs ($-148^\circ/360^\circ * 23$ kyrs) behind NH insolation while the SST records are indistinguishably in phase ($-13^\circ/360^\circ * 23$ kyrs) with maximum NH insolation in the precession band (Fig 3.4). This ~ 9 kyr lag between Andaman Sea SST and $\delta^{18}\text{O}_{\text{sw}}$ proves that direct NH summer insolation did not set the timing and strength of summer monsoon precipitation in the precession band and demonstrates that the monsoon is rather driven by internal processes occurring within the climate system. A zero-phase fast physical response would have otherwise led to instant maxima in summer monsoon precipitation broadly in phase with SST changes. Within error, reconstructed $\delta^{18}\text{O}_{\text{sw}}$ are in phase with both AS1 and AS2, while showing a similar phasing offset of ~ 3 to ~ 5 kyr with respect to minimum ice volume and Chinese cave $\delta^{18}\text{O}$ records. The Asian summer monsoon is traditionally divided in to two large

regional subsystems: the South Asian monsoon (SAM) and the East Asian monsoon (EAM). Both SAM and EAM receive a significant proportion of their annual rainfall during June to September and May to September respectively. The Indian Ocean is the dominant source of moisture for both during the respective periods (Wang, 2006) despite differences in interannual variability arising from the different land-ocean configurations. A reasonable degree of coherence between SAM and EAM is thus, anticipated within the broader Asian monsoon over a range of timescales. Based on this understanding, we argue that precession dominated composite cave $\delta^{18}\text{O}$ records from China (Cheng et al., 2016) cannot be interpreted as proxies of pure summer monsoon precipitation. On the other hand, a strong coupling between basin-scale monsoon winds over the Arabian Sea and monsoon precipitation imply that cross-equatorial transport of latent heat and ice-volume are the primary mechanisms driving changes of the monsoon circulation over the precession band (e.g. Clemens et al., 1991), which accounts for 30% of the total variance in $\delta^{18}\text{O}_{\text{sw}}$.

In the obliquity band, reconstructed $\delta^{18}\text{O}_{\text{sw}}$ leads maximum obliquity (maximum latent heat export) and SST by ~ 19 kyrs ($166^\circ/360^\circ * 41$ kyrs) and ~ 21 kyrs ($179^\circ/360^\circ * 41$ kyrs) respectively. This is indirect contrast with previous timing estimates of summer monsoon maxima in the Arabian Sea records (Caley et al., 2011; Clemens et al., 1991; Clemens and Prell, 2003). The $\delta^{18}\text{O}_{\text{sw}}$ lag appears close to ice volume maxima and sensible heat minima, which leads/lags obliquity maxima/minima by ~ 14 and 6 kyrs. This nearly 180° degree out of phase relationship between monsoon precipitation and maximum obliquity indicates that neither decreased ice volume nor increased latent heat export following obliquity maxima set the phasing of strong monsoon precipitation at this location over this frequency band. We propose that the obliquity forcing plays a vital role in monsoon intensification through enhanced cross-hemispheric atmospheric moisture fluxes as obliquity decreases and the NH cools and the SH warms. Support for this hypothesis is also found in Vostok deuterium-excess records (Vimeux et al., 1999), which are assumed to reflect changes in the poleward atmospheric moisture fluxes, which were high during glacial inception and decreased obliquity. This demonstrates that

basin scale winds over the Arabian Sea have been decoupled from continental precipitation over this frequency band and requires reinterpretation of the obliquity forcing of the wind-based proxies from the Arabian Sea. This is also consistent with the view that pacing of the monsoon has more likely been driven by interhemispheric moisture transport rather than enhanced southwesterly winds. It's also likely that tropical forcing may have played a dominant role through asymmetric heating of the tropics leading to a permanent La Niña like state and strengthening of the Walker circulation, which would have brought low pressure zones closer to the Indian subcontinent.

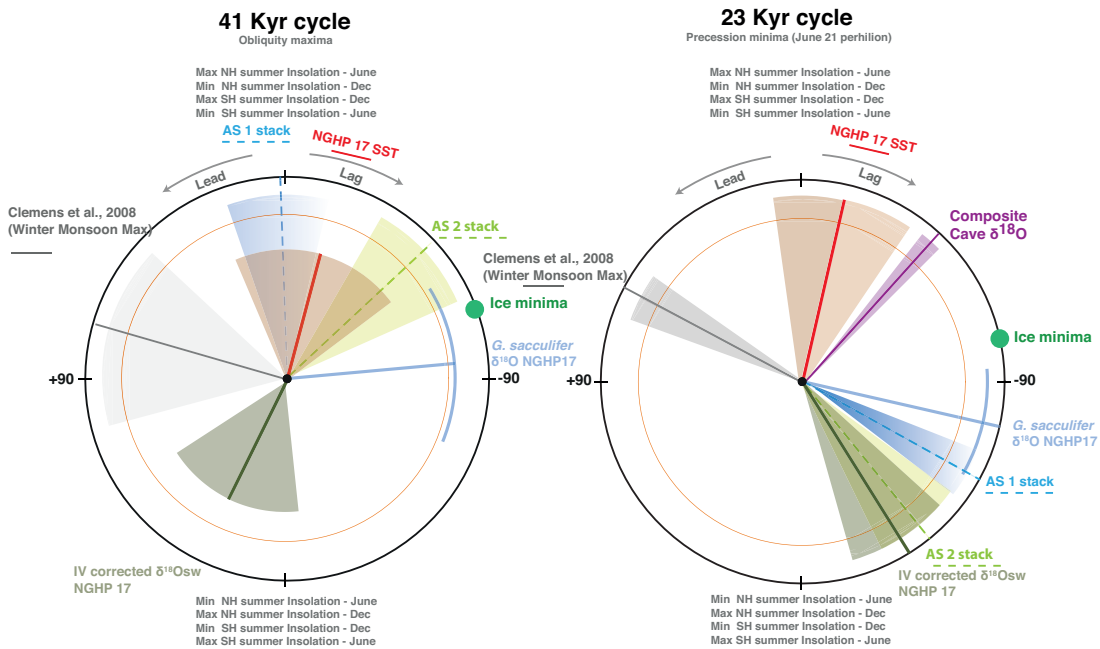


Fig. 4. Phase wheels summarizing Asian monsoon response to insolation forcing at the orbital obliquity (41 kyrs) and precession (23 kyrs) periods during early to late Pleistocene. The precession index is defined as $\Delta \epsilon \sin \omega$ where ω is the longitude of the perihelion measured from the moving vernal point and ϵ is the eccentricity of Earth's orbit around the Sun (Berger and Loutre, 1997; Laskar et al., 1993). Obliquity is the axial tilt of Earth's rotation axis with respect to the orbital plane. In the phase wheel representation the 12 o'clock position is set to precession minima (P min; $\omega = 90^\circ$, 21st June perihelion) and obliquity maxima (O max), respectively. Negative/Positive phases are measured in the clockwise/anticlockwise direction and represent phase lags/leads relative to P min or O max. Published records plotted (with shaded phase estimate errors) are the Arabian Sea summer monsoon stacks AS1 and AS2, the Chinese cave $\delta^{18}O$ composite (Cheng et al., 2016), and winter and summer monsoon maxima (Clemens et al., 2008) and IV corrected $\delta^{18}O_{sw}$ from NGHP 17 (this study). All other records are coherent with respect to ETP at the 95% confidence level except $\delta^{18}O_{sw}$ of NGHP 17 which shows weaker coherence ($< 80\%$ CI) at the obliquity period. Orange circle denotes 80% coherence. 95% and 80% confidence intervals for coherence are 0.79 and 0.64 with bandwidth 0.00423175. Interpolated time interval is 3.5 kyrs and is from 3 to 951 kyrs.

In summary, our records provide compelling evidence that precession driven variability in the Bay of Bengal is consistent with that observed in the Arabian Sea, implying cross-equatorial transport of latent heat as primary mechanisms driving changes of the monsoon circulation at this frequency. We propose that obliquity forcing via cross-hemispheric atmospheric moisture fluxes has played a much more important role in monsoon intensification given that the NH cools and the SH warms when obliquity decreases. This is fundamentally different from the mechanisms of precessional forcing of the monsoon. In view of these results, the role of atmospheric moisture flux triggered by hemispheric insolation gradients and the feedback processes need to be examined in the future using transient model simulations. At the same time, speleothem $\delta^{18}\text{O}$ records from the East Asian and South Asian monsoon domains cannot be interpreted as standalone proxies of summer monsoon precipitation.

Material and Methods

In 2006, the Indian National Gas Hydrate Program (NGHP) used the IODP vessel JOIDES Resolution to core Site 17 in a water depth of 1356 m in the Andaman Sea. The site was cored to about 700 m below seafloor. In particular, the upper 118 m of foraminifera rich nanno-fossil ooze was continuously APC cored with excellent recovery. Here we present data for the upper ~ 50 m of the core. The age model of Site 17 is constructed based on correlation of benthic *C. wuellerstorfi*/*C. mundulus* $\delta^{18}\text{O}$ records (Figure supplement 1a) to the LR04 global benthic $\delta^{18}\text{O}$ stack (Lisiecki and Raymo, 2005) using Analyseries (Paillard et al., 1996). This was achieved by aligning notable features from the benthic $\delta^{18}\text{O}$ record, which shows 1.75 ‰ glacial-interglacial variability during ~ 100 kyr cycles (supplement Figure 1). For the upper section of the core, the age model was further controlled by five ^{14}C dates converted to conventional ages and the identification of the youngest Toba ash layer (Ali et al., 2015). The AMS ^{14}C ages were corrected for marine reservoir ages that were determined locally (Southon et al., 2002). Foraminiferal stable isotope analysis was performed at GEOMAR, Kiel, using a MAT 253 mass spectrometer coupled with a Kiel IV Carbonate device system (Thermo Scientific). Mg/Ca ratios were measured

with an Agilent 7500cs ICP-MS (for samples up to 22 m depth) and ICP OES (VARIAN 720-ES) (for samples below 22 m depth). For details of the Mg/Ca cleaning steps followed, see Gebregiorgis et al. (2016) and the supplementary material. Seawater $\delta^{18}\text{O}$ ($\delta^{18}\text{O}_{\text{SW}}$) was calculated using the $\delta^{18}\text{O}$ - temperature calibration of (Bemis et al., 1998) and was corrected for global ice volume following (Rohling et al., 2014). $\delta^{18}\text{O}_{\text{SW}}$ values were converted to Vienna Standard Mean Ocean Water (VSMOW) by adding 0.27‰. Uncertainties in $\delta^{18}\text{O}_{\text{SW}}$ and SST were estimated by propagating maximum possible analytical errors of the $\delta^{18}\text{O}$ and Mg/Ca measurements, calibration equations for both temperature and the $\delta^{18}\text{O}_{\text{SW}}$ and the global ice volume corrections ($\pm 0.09\text{‰}$). Uncertainties in the age model are quantified based on phasing offsets between NGHP 17 benthic record and LR04 (see supplement material). Spectral analyses were performed on unevenly distributed time series using REDFIT (Schulz and Mudelsee, 2002). Coherence and phase analysis were performed using the Arand software package (Howell, 2001).

References

- Ali, S., Hathorne, E.C., Frank, M., Gebregiorgis, D., Statterger, K., Stumpf, R., Kutterolf, S., Johnson, J.E. and Giosan, L., 2015. South Asian monsoon history over the past 60 kyr recorded by radiogenic isotopes and clay mineral assemblages in the Andaman Sea. *Geochemistry, Geophysics, Geosystems*, 16(2): 505-521.
- Anderson, D.M. and Prell, W.L., 1993. A 300 kyr record of upwelling off Oman during the late Quaternary: evidence of the Asian southwest monsoon. *Paleoceanography*, 8(2): 193-208.
- Bemis, E., Spero, H.J., Bijma, J. and Lea, D.W., 1998. Reevaluation of the oxygen isotopic composition of planktonic foraminifera: Experimental results and revised paleotemperature equations. *Paleoceanography*, 13(2): 150-160.
- Berger, A., 1999. Parameters of the Earth's orbit for the last 5 Million years in 1 kyr resolution. *PANGAEA*, doi, 10.
- Berger, A. and Loutre, M.-F., 1991. Insolation values for the climate of the last 10 million years. *Quaternary Science Reviews*, 10(4): 297-317.
- Berger, A. and Loutre, M.-F., 1997. Intertropical latitudes and precessional and half-precessional cycles. *Science*, 278(5342): 1476-1478.
- Boos, W.R. and Kuang, Z., 2010. Dominant control of the South Asian monsoon by orographic insulation versus plateau heating. *Nature*, 463(7278): 218-222.
- Caley, T., Malaizé, B., Zaragosi, S., Rossignol, L., Bourget, J., Eynaud, F., Martinez, P., Giraudeau, J., Charlier, K. and Ellouzi-Zimmermann, N., 2011. New Arabian Sea

- records help decipher orbital timing of Indo-Asian monsoon. *Earth and Planetary Science Letters*, 308(3): 433-444.
- Cheng, H., Edwards, R.L., Broecker, W.S., Denton, G.H., Kong, X., Wang, Y., Zhang, R. and Wang, X., 2009. Ice age terminations. *science*, 326(5950): 248-252.
- Cheng, H., Edwards, R.L., Sinha, A., Spötl, C., Yi, L., Chen, S., Kelly, M., Kathayat, G., Wang, X. and Li, X., 2016. The Asian monsoon over the past 640,000 years and ice age terminations. *Nature*, 534(7609): 640-646.
- Clemens, S., Prell, W., Murray, D., Shimmield, G. and Weedon, G., 1991. Forcing mechanisms of the Indian Ocean monsoon. *Nature*, 353(6346): 720-725.
- Clemens, S.C. and Prell, W.L., 2003. A 350,000 year summer-monsoon multi-proxy stack from the Owen Ridge, Northern Arabian Sea. *Marine Geology*, 201(1): 35-51.
- Clemens, S.C., Prell, W.L. and Sun, Y., 2010. Orbital-scale timing and mechanisms driving Late Pleistocene Indo-Asian summer monsoons: Reinterpreting cave speleothem $\delta^{18}\text{O}$. *Paleoceanography*, 25(4).
- Clemens, S.C., Prell, W.L., Sun, Y., Liu, Z. and Chen, G., 2008. Southern Hemisphere forcing of Pliocene $\delta^{18}\text{O}$ and the evolution of Indo - Asian monsoons. *Paleoceanography*, 23(4).
- Flato, G., Marotzke, J., Abiodun, B., Braconnot, P., Chou, S.C., Collins, W., Cox, P., Driouech, F., Emori, S. and Eyring, V., 2013. Evaluation of climate models, *Climate change 2013: the physical science basis. Contribution of Working Group I to the Fifth Assessment Report of the Intergovernmental Panel on Climate Change*. Cambridge University Press, pp. 741-866.
- Howell, P., 2001. ARAND Time Series and Spectral Analysis Package for the Macintosh, in IGBP PAGES/World Data Center for Paleoclimatology Data Contribution, edited. NOAA/NGDC Paleoclimatology Program, Boulder, CO.
- Laskar, J., Joutel, F. and Boudin, F., 1993. Orbital, precessional, and insolation quantities for the Earth from -20 Myr to + 10 Myr. *Astronomy and Astrophysics*, 270: 522-533.
- Lisiecki, L.E. and Raymo, M.E., 2005. A Pliocene - Pleistocene stack of 57 globally distributed benthic $\delta^{18}\text{O}$ records. *Paleoceanography*, 20(1).
- Lutz, W. and Samir, K., 2011. Global human capital: Integrating education and population. *Science*, 333(6042): 587-592.
- Maher, B.A. and Thompson, R., 2012. Oxygen isotopes from Chinese caves: records not of monsoon rainfall but of circulation regime. *Journal of Quaternary Science*, 27(6): 615-624.
- Mani, N.J., Suhas, E. and Goswami, B., 2009. Can global warming make Indian monsoon weather less predictable? *Geophysical Research Letters*, 36(8).
- Mohtadi, M., Prange, M. and Steinke, S., 2016. Palaeoclimatic insights into forcing and response of monsoon rainfall. *Nature*, 533(7602): 191-199.
- Naidu, P.D. and Malmgren, B.A., 1996. A high-resolution record of late Quaternary upwelling along the Oman Margin, Arabian Sea based on planktonic foraminifera. *Paleoceanography*, 11(1): 129-140.
- Paillard, D., Labeyrie, L. and Yiou, P., 1996. Macintosh program performs time-series analysis. *Eos, Transactions American Geophysical Union*, 77(39): 379-379.

- Rohling, E., Foster, G.L., Grant, K., Marino, G., Roberts, A., Tamisiea, M.E. and Williams, F., 2014. Sea-level and deep-sea-temperature variability over the past 5.3 million years. *Nature*, 508(7497): 477-482.
- Schulz, M. and Mudelsee, M., 2002. REDFIT: estimating red-noise spectra directly from unevenly spaced paleoclimatic time series. *Computers & Geosciences*, 28(3): 421-426.
- Southon, J., Kashgarian, M., Fontugne, M., Metivier, B. and Yim, W.W., 2002. Marine reservoir corrections for the Indian Ocean and Southeast Asia. *Radiocarbon*, 44(1): 167-180.
- Varkey, M., Murty, V. and Suryanarayana, A., 1996. Physical oceanography of the Bay of Bengal and Andaman Sea.
- Vimeux, F., Masson, V., Jouzel, J., Stievenard, M. and Petit, J., 1999. Glacial–interglacial changes in ocean surface conditions in the Southern Hemisphere. *Nature*, 398(6726): 410-413.
- Wang, B., 2006. The asian monsoon. Springer Science & Business Media.
- Wang, B., Xiang, B., Li, J., Webster, P.J., Rajeevan, M.N., Liu, J. and Ha, K.-J., 2015. Rethinking Indian monsoon rainfall prediction in the context of recent global warming. *Nature communications*, 6.
- Wang, Y., Cheng, H., Edwards, R.L., Kong, X., Shao, X., Chen, S., Wu, J., Jiang, X., Wang, X. and An, Z., 2008. Millennial-and orbital-scale changes in the East Asian monsoon over the past 224,000 years. *Nature*, 451(7182): 1090-1093.
- Wang, Y.-J., Cheng, H., Edwards, R.L., An, Z., Wu, J., Shen, C.-C. and Dorale, J.A., 2001. A high-resolution absolute-dated late Pleistocene monsoon record from Hulu Cave, China. *Science*, 294(5550): 2345-2348.
- Webster, P.J., Magana, V.O., Palmer, T., Shukla, J., Tomas, R., Yanai, M. and Yasunari, T., 1998. Monsoons: Processes, predictability, and the prospects for prediction. *Journal of Geophysical Research: Oceans*, 103(C7): 14451-14510.
- Ziegler, M., Lourens, L.J., Tuenter, E., Hilgen, F., Reichert, G.J. and Weber, N., 2010. Precession phasing offset between Indian summer monsoon and Arabian Sea productivity linked to changes in Atlantic overturning circulation. *Paleoceanography*, 25(3).

Supplement material

Astronomical forcing of South Asian monsoon precipitation over the past ~1 million years

D. Gebregiorgis¹, E.C. Hathorne¹, L. Giosan², S. Clemens³, D. Nürnberg¹, and M. Frank¹

¹*GEOMAR Helmholtz Centre for Ocean Research Kiel, Wischhofstraße 1-3, 24148 Kiel, Germany*

²*Woods Hole Oceanographic Institution, Woods Hole, Massachusetts, USA, USA*

³*Earth, Environmental, and Planetary Sciences, Brown University, Providence, RI, U.S.A.*

Core material and sample preparation

Site 17 was cored to about 700 m below seafloor while the focus here is solely on the upper ~50 m of the core section for which there is a benthic stable isotope stratigraphy. Missing portions of the core identified in Figure 1 are due to the fact that only a single hole was cored during this expedition. Nevertheless, the APC section down to ~50 m represents the last 1 million years and provides a resolution significant enough to interpret orbital time scale variations. The shallow water depth at the site is well above the modern average calcium carbonate compensation depth (CCD) in the Indian Ocean (Kolla et al., 1976) and the effect of calcite dissolution is negligible at this site. Core lithologies categorized based on smear slides include clay-sized (70-100%) grains, silt-sized grains (up to 30%) and other minor lithologies (volcanic ashes, iron sulfide-rich zones, organic-rich intervals and non-biogenic pyrite). The total biogenic component of the sediment mainly consists of calcareous nannofossils and make up 52% to 97% of the total sediment grains.

Foraminifera samples from NGHP 17 were collected, and analyzed every 10 cm down to 25 m and every 25 cm for the remaining of the core. On average ~50-60 specimens per sample were considered enough to obtain a representative geochemical signature and were picked from a constant size fraction to avoid possible size dependent biases (e.g. Elderfield et al., 2002; Ni et al., 2007). Specimens of *G. sacculifer* were picked from the 315-400 μm size fraction and gently cracked between glass slides before being mixed and split for paired analysis of

Mg/Ca and stable isotopes. Cracked samples were cleaned for Mg/Ca analysis following a full reductive cleaning method (Boyle, 1981). Initially, samples were repeatedly rinsed with ultra sonication in distilled water (18.2 m Ω) followed by ethanol (analytical grade) to ensure clay removal. Samples were then inspected under a binocular to ensure samples were free of obvious sediment or detrital contamination. Next, samples were treated with ammonium citrate/hydrazine solution at 82°C for 30 mins and placed in the ultrasonic bath three times (one minute each) to maintain contact between reagents and sample. Samples were then rinsed multiple times with distilled water and transferred to new acid leached vials. To remove organic matter, samples were then treated with oxidizing NaOH/H₂O₂ solution at 82°C for 20 mins. Before final dissolution, a weak acid leach with 100 μ L 0.001 M HNO₃ was applied and followed by two rinses with distilled water. Assisted by sonication for 25 minutes, samples were finally dissolved in 0.075 M nitric acid (HNO₃) (500 μ L), centrifuged (4 mins at 13400 rpm) and 400 μ L of supernatant from each sample was transferred to new acid leached vials.

Age model and oxygen isotope stratigraphy of NGHP17

The age model of Site 17 is constructed by aligning notable features from the benthic $\delta^{18}\text{O}$ record, which shows 1.75 ‰ glacial-interglacial ~100 kyrs cycles, with equivalent features in the LR04 global benthic $\delta^{18}\text{O}$ stack (Lisiecki and Raymo, 2005) (Fig 1). *C. wuellerstorfi* and *C. mundulus* are epibenthic foraminiferal species, and $\delta^{18}\text{O}$ values were adjusted to equilibrium by adding 0.64 following (Schackleton et al., 1984). The mean sedimentation rate remained constant throughout the studied period and is on average ~5 cm/kyr (Figure supplement 1b). The upper 25 m was sampled at a resolution of 10 cms while the remaining core section was sampled at a resolution of 20 cms. Our sampling strategy thus represents a time slice of on average 2 to 4 kyrs.

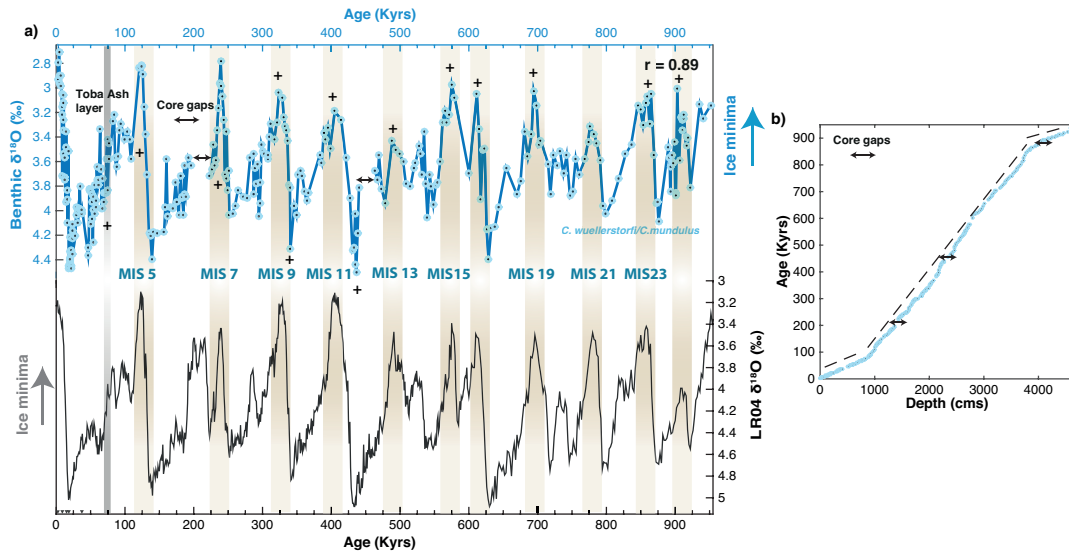


Figure supplement 1. a) Correlation of our benthic (*C. wuellerstorfi* / *C. mundulus*) $\delta^{18}O$ record (dark green) and the LR04 benthic foraminiferal $\delta^{18}O$ stack (Lisiecki and Raymo, 2005). Major Tie points are shown in cross; b) Age depth model for NGHP 17 indicating a near linear sedimentation rate.

To investigate whether this tuning approach is robust, we performed spectral and evolutionary spectra wavelet analysis of NGHP 17 benthic record on age and depth domains (Figure supplement 2). Spectral analysis of NGHP 17 benthic record on depth domain reveals strong power spectra at 0.002, 0.005 and 0.007 m/cycle and to a lesser extent at 0.003 and 0.006 m/cycle. These periodicities have a nearly precise 1:1.5:4 frequency ratios, which demonstrate the presence of Milankovitch-related periodicities in the depth domain coherent with the age domain. The absence of a strong shift in the depth domain wave bands also confirms that sedimentation rates largely remained constant. As a result, we find the tuning approach appropriate for constructing the NGHP 17 stratigraphy. The accuracy of the age model depends on the accuracy of the LR04 benthic stack. Consequently, phasing offsets between NGHP 17 benthic record and LR04 are used to quantify age model uncertainties. The phase error associated with our age model is $\sim\pm 2.2$ kyr for the 100 kyr-eccentricity cycle, $\sim\pm 1.1$ kyr for the 41 kyr-obliquity cycle and $\sim\pm 0.5$ kyr for the 23 kyr-precession cycle (Figure supplement 3).

Astronomical forcing of SAM

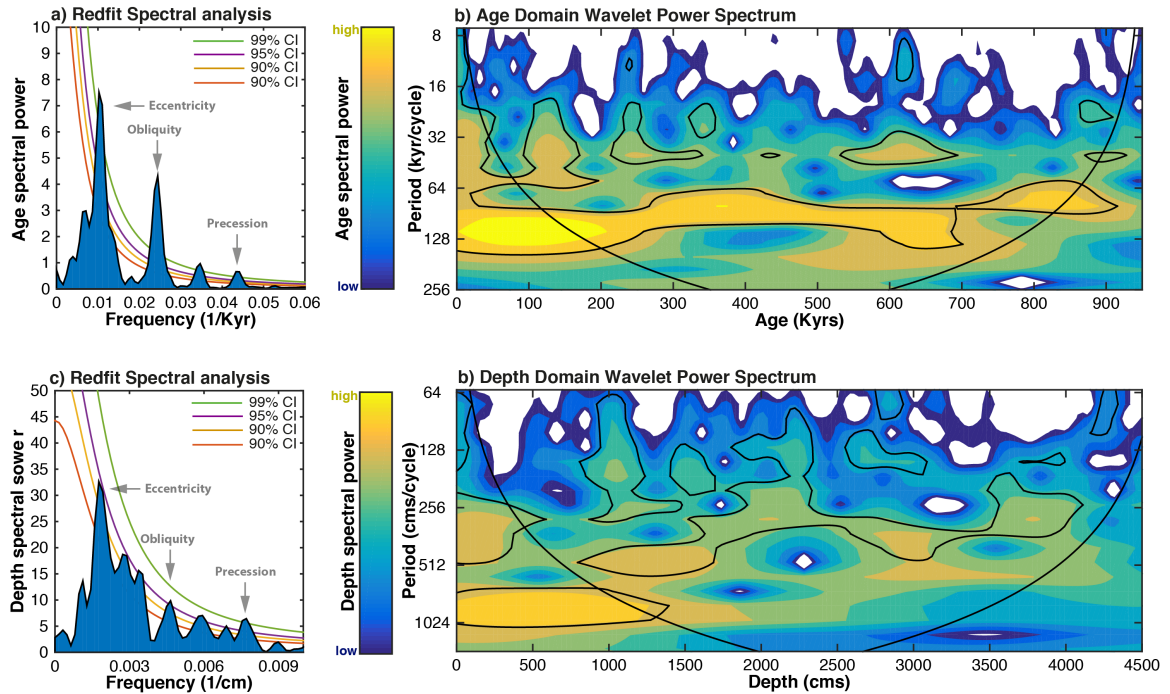


Figure supplement 2. a) Redfit spectral analysis of LR04 tuned Site 17 benthic isotope stratigraphy showing strong periodicity at frequencies corresponding to the three main orbital periods (95% CI). b) Continuous wavelet transform of NGHP 17 benthic isotope stratigraphy; c) Redfit spectral analysis (Schulz and Mudelsee, 2002) NGHP 17 benthic record on depth domain showing strong power spectra at 0.002, 0.005 and 0.007 m/cycle (95% CI); d) Continuous wavelet transform of NGHP 17 benthic records on depth domain. Black line contours in b) and d) represent 90% confidence level. Evolutionary wavelet spectrum is computed using the Matlab codes of Torrence and Compo (Torrence and Compo, 1998) and available at (paos.colorado.edu/research/wavelets/).

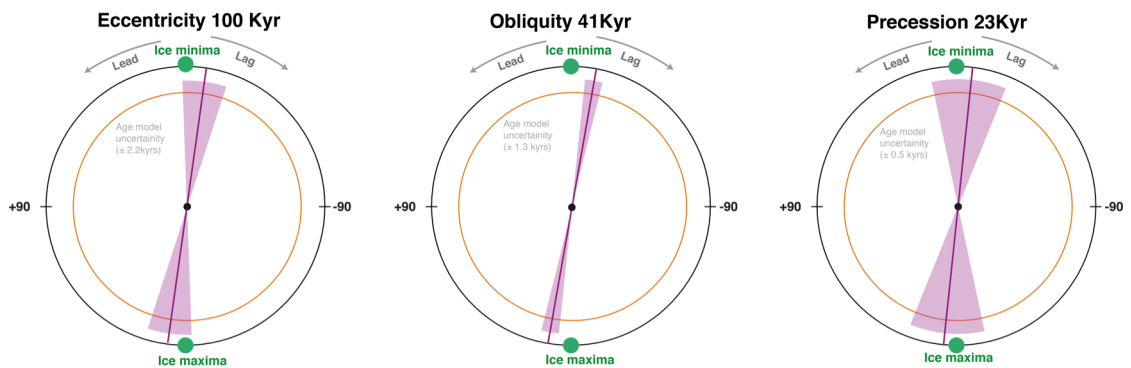


Figure supplement 3. Phase wheels summarizing age model uncertainties with respect to LR04. Ice

Foraminiferal isotopic and elemental analysis

Foraminiferal stable isotope analysis was performed at GEOMAR, Kiel, using a MAT 253 mass spectrometer coupled with a Kiel IV Carbonate device system (Thermo Scientific). Results were referenced to the NBS19 standard and are reported on the VPDB scale. Analytical errors calculated based on multiple measurements of an in house standard (SHK Bremen) were $\pm 0.05\text{‰}$ (1σ) for $\delta^{18}\text{O}$. Mg/Ca ratios were measured with an Agilent 7500cs ICP-MS (for samples up to 22 m depth) and ICP OES (VARIAN 720-ES) (for samples below 22 m depth) both housed at GEOMAR Kiel. Precision error estimated for both instruments is based on replicate measurements of ECRM752-1 standard and are on average $< \pm 0.1$ mmol/mol (1σ). To exclude biases due to possible clay contamination, we have carefully monitored Al/Ca, Fe/Ca and Mn/Ca ratios (Barker et al., 2003). For the data set presented here no systematic relationship exists between Al/Ca (or Fe/Ca) and Mg/Ca ratios and we exclude the possibility of clay contamination. However, Al/Ca values in some 16 samples were relatively higher and these data were excluded from further interpretations.

Uncertainties in $\delta^{18}\text{O}_{\text{sw}}$ and SST are estimated by propagating errors introduced by the $\delta^{18}\text{O}$ and Mg/Ca measurements, calibration equations for both temperature and the $\delta^{18}\text{O}_{\text{sw}}$. Uncertainties in SST and $\delta^{18}\text{O}_{\text{sw}}$ are on average ~ 1 °C and $\sim 0.3\text{‰}$ respectively. For the SST and $\delta^{18}\text{O}_{\text{sw}}$ estimate, the following equations after Mohtadi et al. (2014) were used to propagate the errors.

SST calibration and error propagation

SSTs were calculated by using the multispecies equation of (Anand et al., 2003)

which is given as follows: $\frac{\text{Mg}}{\text{Ca}} = be^{aT}$, where, $b = 0.38 \pm 0.02$ mmol/mol; $a = 0.090 \pm$

0.003 °C⁻¹

Errors associated with SST are estimated by propagating the errors in a, b, and Mg/Ca measurement errors and is given as:

$$\sigma_T^2 = \left(\frac{\partial T}{\partial a}\sigma_a\right)^2 + \left(\frac{\partial T}{\partial b}\sigma_b\right)^2 + \left(\frac{\partial T}{\partial \text{Mg/Ca}}\sigma_{\text{Mg/Ca}}\right)^2$$

Where $\frac{\partial T}{\partial a} = -\frac{1}{a^2}\ln\left(\frac{\text{Mg/Ca}}{b}\right)$, $\frac{\partial T}{\partial b} = -\frac{1}{ab}$, and $\frac{\partial T}{\partial \text{Mg/Ca}} = \frac{1}{a}\frac{1}{\text{Mg/Ca}}$

$\delta^{18}\text{O}_{\text{sw}}$ and error propagation

$\delta^{18}\text{O}_{\text{sw}}$ were calculated by using the $\delta^{18}\text{O}$ -paleotemperature equation of Bemis et al., (1998) which is given as follows:

$$T = a + b (\delta^{18}\text{O}_{\text{calcite}} - \delta^{18}\text{O}_{\text{seawater}}),$$

Where $a = 16.5 \pm 0.2^\circ\text{C}$; $b = -4.80 \pm 0.16^\circ\text{C}$ and T is estimated from Mg/Ca measurements as shown above:

Errors associated with $\delta^{18}\text{O}_{\text{sw}}$ are estimated by propagating the errors in a, b, T and $\delta^{18}\text{O}$ measurement errors by assuming no covariance among the errors and is given as:

$$\sigma_{\delta^{18}\text{O}_{\text{sw}}}^2 = \left(\frac{\partial \delta^{18}\text{O}_{\text{sw}}}{\partial T}\sigma_T\right)^2 + \left(\frac{\partial \delta^{18}\text{O}_{\text{sw}}}{\partial a}\sigma_a\right)^2 + \left(\frac{\partial \delta^{18}\text{O}_{\text{sw}}}{\partial b}\sigma_b\right)^2 + \left(\frac{\partial \delta^{18}\text{O}_{\text{sw}}}{\partial \delta^{18}\text{O}_{\text{calcite}}}\sigma_{\delta^{18}\text{O}_{\text{calcite}}}\right)^2$$

Where, $\frac{\partial \delta^{18}\text{O}_{\text{sw}}}{\partial T} = -\frac{1}{b}$, $\frac{\partial \delta^{18}\text{O}_{\text{sw}}}{\partial a} = \frac{1}{b}$, $\frac{\partial \delta^{18}\text{O}_{\text{sw}}}{\partial b} = \frac{T}{b^2} - \frac{a}{b^2}$, and $\frac{\partial \delta^{18}\text{O}_{\text{sw}}}{\partial \delta^{18}\text{O}_{\text{calcite}}} = 1$

References

- Anand, P., Elderfield, H. and Conte, M.H., 2003. Calibration of Mg/Ca thermometry in planktonic foraminifera from a sediment trap time series. *Paleoceanography*, 18(2).
- Barker, S., Greaves, M. and Elderfield, H., 2003. A study of cleaning procedures used for foraminiferal Mg/Ca paleothermometry. *Geochemistry, Geophysics, Geosystems*, 4(9).
- Bemis, E., Spero, H.J., Bijma, J. and Lea, D.W., 1998. Reevaluation of the oxygen isotopic composition of planktonic foraminifera: Experimental results and revised paleotemperature equations. *Paleoceanography*, 13(2): 150-160.
- Boyle, E.A., 1981. Cadmium, zinc, copper, and barium in foraminifera tests. *Earth and Planetary Science Letters*, 53(1): 11-35.
- Elderfield, H., Vautravers, M. and Cooper, M., 2002. The relationship between shell size and Mg/Ca, Sr/Ca, $\delta^{18}\text{O}$, and $\delta^{13}\text{C}$ of species of planktonic foraminifera. *Geochemistry, Geophysics, Geosystems*, 3(8): 1-13.
- Kolla, V., Bé, A.W. and Biscaye, P.E., 1976. Calcium carbonate distribution in the surface sediments of the Indian Ocean. *Journal of Geophysical Research*, 81(15): 2605-2616.
- Mohtadi, M., Prange, M., Oppo, D.W., De Pol-Holz, R., Merkel, U., Zhang, X., Steinke, S. and Luckge, A., 2014. North Atlantic forcing of tropical Indian Ocean climate. *Nature*, 509(7498): 76-80.
- Ni, Y., Foster, G.L., Bailey, T., Elliott, T., Schmidt, D.N., Pearson, P., Haley, B. and Coath, C., 2007. A core top assessment of proxies for the ocean carbonate system in surface - dwelling foraminifers. *Paleoceanography*, 22(3).
- Paillard, D., Labeyrie, L. and Yiou, P., 1996. Macintosh program performs time-series analysis. *Eos, Transactions American Geophysical Union*, 77(39): 379-379.
- Schulz, M. and Mudelsee, M., 2002. REDFIT: estimating red-noise spectra directly from unevenly spaced paleoclimatic time series. *Computers & Geosciences*, 28(3): 421-426.
- Torrence, C. and Compo, G.P., 1998. A practical guide to wavelet analysis. *Bulletin of the American Meteorological society*, 79(1): 61-78.

Chapter II

Orbital forcing of South Asian monsoon inferred from Andaman Sea X-ray fluorescence core scanning records

D. Gebregiorgis¹, E.C. Hathorne¹, L. Giosan², D. Nürnberg¹, A. Plass¹, M. Frank¹, S.C Clemens³ and Exp. 353 Scientists

¹*GEOMAR Helmholtz Centre for Ocean Research Kiel, Wischhofstraße 1-3, 24148 Kiel, Germany*

²*Woods Hole Oceanographic Institution, Woods Hole, USA*

³*Department of Geological Sciences, Brown University, Providence, RI, USA*

Abstract*

The orbital forcing of the Asian summer monsoon and its response mechanisms have been explored intensively over the last three decades. Yet, there is still a fundamental lack of understanding in how the monsoon responds to changes of the basic boundary conditions and changes in insolation in both hemispheres leading to discrepant interpretations. This lack of consensus is due to the proxies for different processes used to interpret the paleo-monsoon and the lack of long-term high-resolution proxy records from regions of major monsoon rainfall. Here we try to reconcile the existing divergence in opinion utilizing new scanning x-ray fluorescence (XRF) data with a spatial resolution of 1cm. We use Ti/Ca ratios to reconstruct terrigenous material fluxes versus marine productivity, while Si/Al ratios are used as direct tracers of changes in monsoon intensity due to their reflection of weathering regime. The Ti/Ca record is essentially 180° out of phase with respect to maximum sea level at both precession and obliquity bands indicating the prevalence of a dominant sea level related variance in the proxy record. The Si/Al record (minima in Si/Al ratios), in contrast show a lag of ~12 kyrs with respect to NH insolation and is in phase with maximum SH insolation in the precession band. Consistent with earlier findings the precession phasing of the Si/Al record suggests that increased latent and sensible heating, and a net latent heat transport from Southern Subtropical Indian Ocean (SSIO) control the strength and

* Manuscript to be submitted to *EPSL*

timing of the monsoon. Our results suggest that obliquity forcing plays a more important role in controlling the pace of the summer monsoon through enhanced cross-hemispheric atmospheric moisture supply following obliquity minima, which is fundamentally different from the precession pacing of the monsoon, which has been mainly controlled by interhemispheric moisture transport. In addition, apparent lack of NH coupled millennial scale variability in this high resolution XRF data suggest that either these proxies take more time to respond to precipitation changes or SAM precipitation is not sensitive to Northern Hemisphere millennial scale climate variability.

1. Introduction

Reconstructions of past monsoon intensity are mainly based on proxy records of discrete sample analyses obtained using destructive techniques such as ICP-MS (e.g. Gebregiorgis et al., 2016; Rashid et al., 2007; Kudrass et al., 2001) and other conventional techniques such foraminiferal species abundance (e.g. Clemens et al., 1991). X-ray fluorescence (XRF) core scanning provides high-resolution non-destructive elemental records and is extensively used to investigate abrupt climate changes otherwise difficult to resolve using the conventional methods. Recently, for example, high-resolution riverine runoff and dust proxy data from XRF measurements have provided precise quantitative estimates of spatial and temporal shifting points of the Australian monsoon during the last deglaciation (Kuhnt et al., 2015). Other studies have also used elemental ratios to reconstruct past climates over a range of timescales (Clift et al., 2008; Haug et al., 2001; Mohtadi et al., 2011; Ziegler et al., 2010). Changes in the abundances of major elements occurring in marine sediments such as Ca, Fe, Sr, K and Ti are used as indicators of past environmental changes (Rothwell, 2015). For example, Ti/Ca and Fe/Ca ratios are often used to reconstruct marine versus terrigenous sedimentation near continental margins (Bender et al., 2013; Burone et al., 2013; Govin et al., 2012). Other widely applied proxies include ratios of K/Al and Ti/Al, which are used as indicators of

chemical and physical weathering processes on orbital and longer time scales (Clift et al., 2008; Tian et al., 2011; Wei et al., 2006).

On orbital time scales climatic changes in low latitudes are primarily modulated by changes in the tilt of Earth's axis (obliquity) and wobbling of Earth's spin axis (precession). The Earth's precessional cycle controls the seasonal cycle of incoming solar radiation while changes in Earth's obliquity influence its distribution in space and time. The mechanisms by which these orbital parameters pace the Asian monsoon and its response time, however, are still widely debated (Mohtadi et al., 2016). Past inferences regarding orbital and sub-orbital variability of the South Asian monsoon (SAM) are based on numerous marine sediment records from the Arabian Sea in particular (e.g. Caley et al., 2011; Clemens et al., 1991; Clemens et al., 1996; Clemens et al., 2008; Sarkar et al., 2000; Schulz et al., 1998; Ziegler et al., 2010) and the equatorial Indian Ocean (e.g. Bolton et al., 2013). Only short-term paleomonsoon records have, however so far been generated from the Bay of Bengal and Andaman Sea (e.g. Kudrass et al., 2001; Rashid et al., 2007; Rashid et al., 2011; Gebregiorgis et al., 2016) and our understanding of the long-term evolution of the SAM within the broader Asian monsoon remains incomplete. For instance, several paleomonsoon records from the Arabian Sea indicate significantly longer (8-9 kyrs) phase lags between northern hemisphere (NH) peak summer insolation and monsoon driven maximum productivity recorded in the Arabian Sea (e.g. Caley et al., 2011; Clemens and Prell, 2003). In contrast, high-resolution speleothem records from China (Sanbao and Hulu caves) lag maximum NH summer insolation by 2.9 kyrs over the precession band (e.g. Wang et al., 2008). Fundamental differences in the geological records of the monsoon are due to the lack of long-term records of monsoon precipitation from major moisture sink regions such as the Bay of Bengal and Andaman Sea. In this regard, XRF based terrigenous and weathering proxies have the potential to be used as direct proxies of the monsoon precipitation on land.

Here we use new long sediment cores recovered in the Andaman Sea (Integrated Ocean Drilling Program Expedition 353, National Gas Hydrate Program 17) to examine the past variability of monsoon precipitation on the Indian sub-continent.

We utilize data obtained by nondestructive x-ray fluorescence (XRF) core scanning at a spatial resolution of 1cm corresponding to a resolution of 150-200 hundreds of years. The main objective of this study is to assess potentials and pitfalls in using XRF based proxies of the monsoon, and better understand the response of the South Asian monsoon climate to adjustments in the precession, obliquity and eccentricity cycles. We perform spectral analysis to identify significant cyclicity and, employ coherence and phase analysis with respect to eccentricity, tilt or obliquity and precession (ETP) to examine different forcing mechanisms of the monsoon. The astronomical index ETP is calculated based on numerical solutions of the Lagrangian and the Polsson equations of the Earth-Moon system (Berger and Laoutre, 1991; Berger, 1999). Particular attention is given to the Si/Al ratio, which is used as tracer of monsoon intensity, whereas the Ti/Ca ratio is analyzed to trace changes in terrigenous versus marine productivity. These data provide new insights into the role of orbital forcing mechanisms driving late Quaternary low latitude paleoclimatic and paleocenographic changes.

2. Materials and Methods

2.1 Provenance and Andaman Sea sediment source regions

The Andaman Sea receives more than 360 million tonnes of sediments annually from the Indo-Burman Ranges and surrounding regions through major river systems of Myanmar mainly the Irrawaddy and Salween (Awasthi et al., 2014; Meade, 1996). The Irrawaddy and Salween system constitutes up to 50% of the total suspended and dissolved material flux from the Himalayas and Tibet delivered annually to the ocean (Chapman et al., 2015). The catchment rocks of the Irrawaddy include Cretaceous to mid-Cenozoic flysch of the western Indo-Burman Ranges, Eocene-Miocene-Quaternary sediments of the Myanmar Central Basin, as well as Late Precambrian, and Cretaceous-Eocene metamorphic, basic, ultrabasic rocks of the Himalayan syntaxis in southeastern Tibet (Fig 1) (Bender, 1983; Curray, 2005; Najman, 2006; Socquet and Pubellier, 2005). The Salween mainly drains the magmatic rock of the northern Lhasa block and Precambrian to Tertiary

sedimentary and metamorphic rocks of the Shan Plateau and Sibumashau block (Bender, 1983).

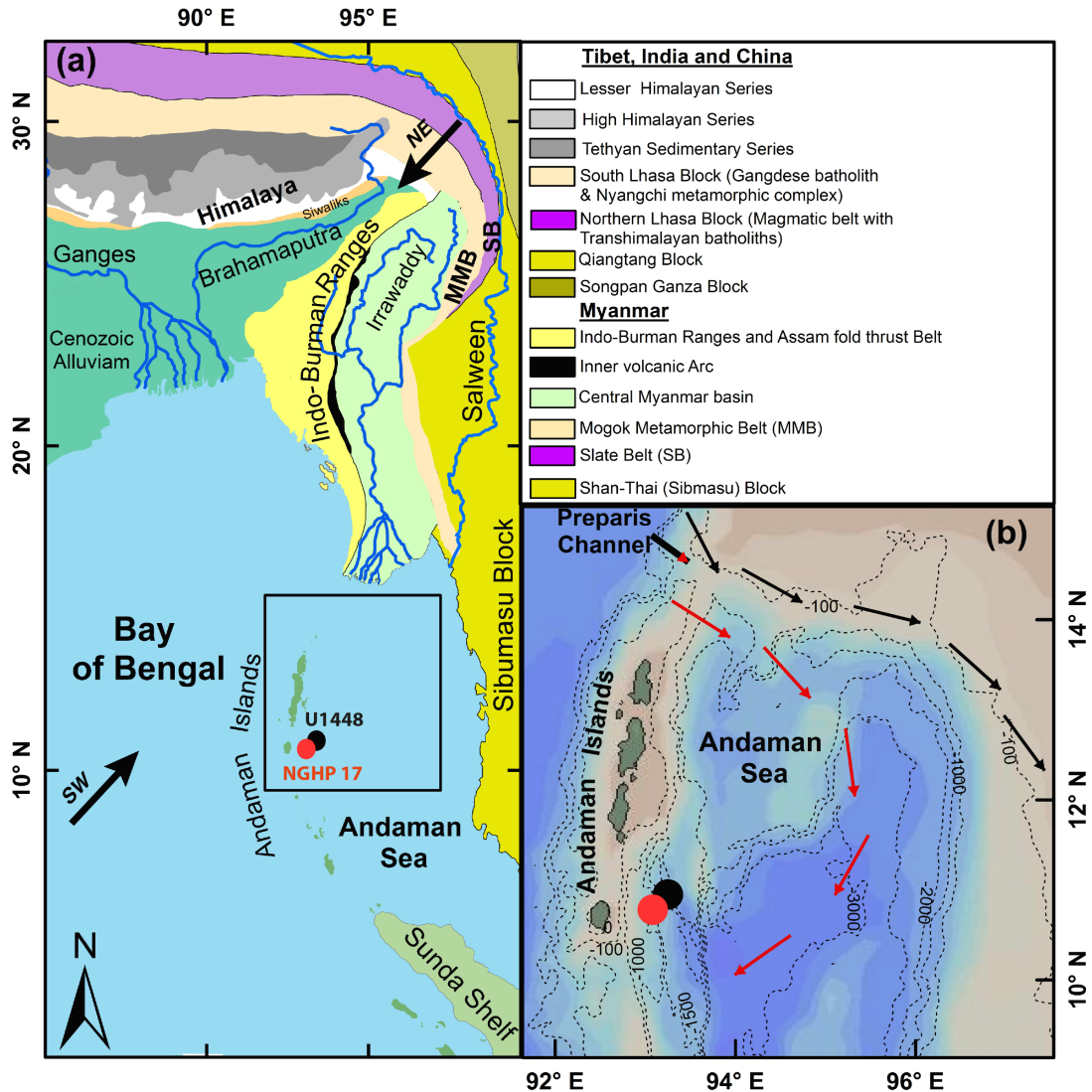


Fig 1. (a) General geological map of the Andaman Sea sediment source regions modified after Awasthi et al. [2014], Robinson et al. [2014], and Garcon et al. [2013]. (b) Schematic bathymetric map of the Andaman Sea. Colored dots show location of the two core sites (NGHP17 and U1448) in the Andaman Sea. Also shown are directions of surface currents during the summer monsoon (black) and winter monsoon (red) periods (Rizal et al., 2012).

Most of the sediments from the Indo-Burman-Arakan (IBA) mountain ranges are supplied to the Andaman Sea through eastward-moving surface currents during the summer monsoon (Rodolfo, 1969). Sedimentary rocks of the IBA ranges derived from Basaltic source rocks are composed of highly weatherable material (Awasthi et

al., 2014). A substantial load of suspended material is also delivered to the eastern Bay of Bengal and the Andaman Sea during peak monsoon seasons through SW monsoonal surface currents (Awasthi et al., 2014). Other potential sediment supply sources include the Andaman-Nicobar ridges, which are mostly made up of mafic and ultramafic rocks of the Cretaceous ophiolite sequence, and sedimentary rocks derived from the flysch deposits. This indicates that sediments deposited in the Andaman Sea are dominated by influx from the Indo-Burman Ranges and Central Myanmar basin and provide important archives to investigate past changes in SAM intensity and weathering from a region of intense monsoon precipitation (Ali et al., 2015; Colin et al., 1999; Damodararao et al., 2016).

2.2 Core description and age model

Sediment core NGHP17 (Lat 10°45.190' N; Long 93°6.70' E) was retrieved in 2006 in a water depth of 1356 m in the Andaman Sea using the IODP vessel JOIDES Resolution (Fig 1). The site was cored to over 700 m depth and preserves a late Miocene to recent stratigraphy. Core U1448 is located 44 km offshore Little Andaman Island (~20 km from site 17) and was retrieved from a water depth 1097 m using the same vessel by IODP EXP 353 (Fig 1). Site 17 core lithologies are determined from smear slides and primarily include clay-sized (70-100%) grains and minor amounts of silt-sized grains (up to 30%). Other minor lithologies consist of volcanic ashes and non-biogenic pyrite, or iron sulfide-rich or organic-rich intervals. The total biogenic component of the sediment is predominantly comprised of calcareous nannofossils and make up 52% to 97% of the total sediment grains (Collett et al., 2008). Core U1448 has a similar lithology and is primarily composed of hemipelagic clays with a significant biogenic component. The upper 180 m of the core is composed of Late to early Pleistocene greenish gray clay and abundant calcareous nannofossils with varying proportions of nannofossils and foraminifers, and clayey nannofossil ooze (Clemens et al., 2016).

The age model of Site 17 is based on correlation of benthic *C. wuellerstorfi* $\delta^{18}\text{O}$ to the LR04 global benthic $\delta^{18}\text{O}$ stack (Lisiecki and Raymo, 2005). For the upper

section of the core, the age model was further controlled by five ^{14}C dates converted to conventional ages following (Southon et al., 2002) and the youngest Toba ash layer (Ali et al., 2015). Tuning of our high-resolution benthic records to the LR04 age model results in an average linear sedimentation rate of ~ 5 cm/kyr for site 17. The age model for Site U1448 was constructed on the basis of oxygen isotope stratigraphy of site 17 and tuning of the Ti/Ca data from site 17 and U1448. Ti/Ca data from both cores consistently maintain high signal-noise ratios, which allow a clear cross-site correlation (see section 3.1). XRF ages between tie points are linearly interpolated and each continuous core sections were reduced to a frequency of 1/kyrs using a cubic spline model prior to tuning. The primary aim is to provide a continuous high-resolution time series representing the Andaman Sea by filling the few sediment gaps identified in the Site 17 core, which are due to the fact that only a single hole was cored during this expedition and prior sampling of sediment material. A 1 cm sampling resolution thus represents a time slice of on average ~ 200 years. Age model uncertainties are quantified based on coherency analysis and are discussed below (see section 3.1).

2.3 XRF core scanning and proxies of SAM precipitation

X-ray fluorescence (XRF) scanning was performed using a Cox Analytical ITRAX and Avaatech X-ray fluorescence core scanners at WHOI (NGHP 17) and University of Kiel. Details of this methods and analytical capabilities of the ITRAX and Avaatech multi-function core scanners are described here (Croudace et al., 2006) and here (Richter et al., 2006) respectively. XRF scans were made using a molybdenum tube set at 10 and 30 kV and 25 mA with counting times of 10 to 30 s. These two settings provided analyses of 13 elements (K, Ca, Ti, V, Cr, Mn, Fe, Cu, Zn, Br, Rb, Sr and Zr). Of all the 13 elements, Ca is the most abundant with a mean response rate of $\sim 360,000$ counts per second (cps). The response rates of the elements K, Ti, Si, Al elements range from $\sim 40,000$ to $\sim 10,000$ cps in that order and is well above the nominal sensitivity of the instrument. All cores were measured after careful

cleaning and scratching off 1–2 mm of sediment and covering of the core surface with SPEXCerti Ultralene® foil. Except the upper ~1.5m of the core for site 17 (measured at a step size of 1mm), all measurements were performed at a step size of 4mm (site 17) and 1 cm (U1448). The XRF core scans were made on sediments between depths of 0.01 and ~100 m and results of a total ~6300 measurements are presented here. Analytical precision was estimated through repeat spot measurements of in-house standards and is better than 0.05 cps (2σ) for all elements. Raw spectroscopic data were processed and converted to element counts using Iterative Least square software (WIN AXIL Batch) package. This program uses peak integration results as initial element intensities and employs a goodness of fit parameter (chi-square). The measured element intensities depend on concentrations of the elements as well as matrix effects, physical properties, the sample geometry, and machine hardware settings. In order to remove these artifacts element intensities are presented as log ratios of two elements and can be directly interpreted as the relative concentrations of these elements (Weltje and Tjallingii, 2008).

We use elemental ratios linked to terrigenous detrital input (K/Ca, Fe/Ca, Ti/Ca) and clay versus sand (e.g. sand) influx (Si/Al) to examine imprinted paleoceanographic and paleoclimatic signals in Andaman Sea sediments over the late Quaternary. Preliminary comparisons between K/Ca, Fe/Ca and Ti/Ca show very similar patterns and only results from Ti/Ca analysis are presented here for clarity. We use Ti/Ca ratios to trace changes in terrigenous input versus marine productivity. This is based on the assumption that Ti contents in marine sediments are directly linked to terrigenous (siliciclastic) sediment influx from the continent while Ca intensities reflect changes in the carbonate content of the sediment and local marine productivity of CaCO_3 producing plankton (Peterson et al., 2000). We use Si/Al ratios as a measure of monsoon strength changes independent of fluctuations in oceanic biogenic carbonate. A key assumption of this proxy is that clays are generally rich in Al and sands in Si (Clift et al., 2014) given that there is minimal biogenic opal production. As a consequence, we assume that the clay versus

sand content in the sediment is directly related to physical and chemical weathering processes, which are dependent on the strength of the monsoon. Thus its assumed that increased/decreased summer monsoon relatively increases/decreases chemical/physical weathering and increases/decreases clay/sand fraction flux to the sediment. This particular proxy offers the opportunity to single out the land-based paleoclimatic signals from paleoceanographic changes in the deeper ocean.

2.4 Power spectral and coherence analysis

Spectral analyses of the XRF records are performed on an evenly distributed time series using REDFIT (Schulz and Mudelsee, 2002). We use the Arand software package (Howell, 2001) to perform coherence and phase analysis with respect to ETP on the same evenly distributed timeseries. For visual inference, a Gaussian filter is used to extract precession and obliquity components from the Ti/Ca and Si/Al records (Fig 2b and c) (Paillard et al., 1996). The central frequencies of the filter for precession, obliquity and 100 Kyr eccentricity cycles are 0.0435 cycles/1kyr, 0.024 cycles/1kyr and 0.01 cycles/1kyr respectively. The evolutionary wavelet spectrum is computed using the Matlab codes of Torrence and Compo (Torrence and Compo, 1998) and is available at paos.colorado.edu/research/wavelets/.

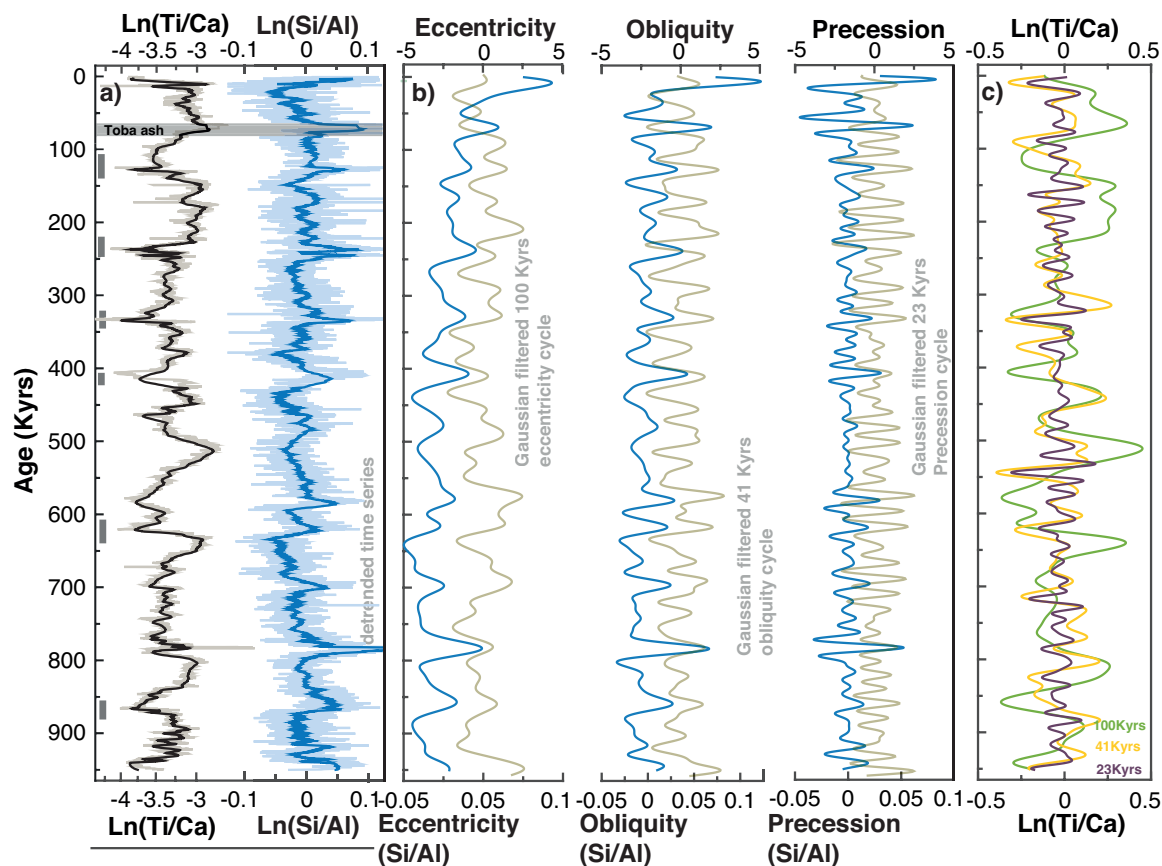


Fig 2. a) Log ratios of XRF Ti/Ca and Si/Al records from U1448. All time series are linear detrended for identical time windows to avoid patterns that are not intrinsic to the timeseries. b) Comparison of filtered eccentricity, obliquity and precession (Berger, 1999) (light green) with identical frequency filtered components of the Si/Al record. c) Eccentricity, obliquity and precession filtered components of the Ti/Ca record. Gray bars in (a) show peak interglacial periods identified from the Ti/Ca record.

3. Results and Discussions

3.1 Uncertainties in Site U1448 stratigraphy and construction of composite section

The accuracy of site U1448 stratigraphy is dependent on the stratigraphy of site 17, which is mainly constructed on the basis of the LR04 benthic stack (Lisiecki and Raymo, 2005). This tuning strategy is considered suitable to construct the stratigraphy of site 17 after performing depth domain spectral and wavelet analysis (see Chapter I for more details). Strong coherence between NGHP 17 benthic isotope records and LR04 stack is attained at all three main orbital frequencies (> 95% CI) (Fig3a). This is also true for the Ti/Ca data from site 17 and U1448, which clearly shows strong coherence at the same frequency bands (> 95% CI) (Fig 3b).

Ti/Ca data from site 17 show distinct cyclicity within the co-varying age and depth domains and allow the clearest cross-hole correlation (Fig 4a). Coherency is consistently high (> 95%) in all periods corresponding to the main orbital frequencies and translates in to smaller age model uncertainty. The accuracy of the Ti/Ca based age model is verified on statistical grounds by quantifying phasing offsets at the main orbital frequencies and is given for the three main orbital periods (Fig 4b). Age model uncertainties associated with site U1448 stratigraphy (taking in to account uncertainties in NGHP 17 stratigraphy) are $\sim\pm 3$ kyrs for the 100 Kyr- eccentricity cycle, $\sim\pm 3$ kyrs for the 41 kyr- obliquity cycle and $\sim\pm 1$ kyrs for the 23 kyrs- precession cycle. Significant (> 90%) coherence also occurs at half-precession and half-obliquity cycles. The Ti/Ca based age model, thus, is suitable to assess low frequency variability and orbital phase relationships with reasonable accuracy.

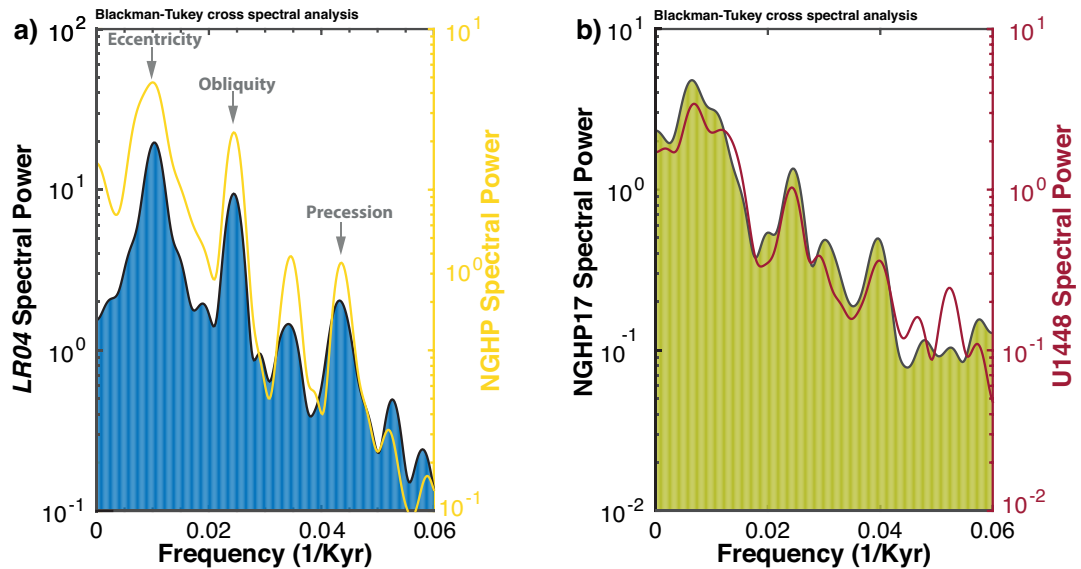


Fig 3. a) Blackman-Tukey cross-spectral analysis of LR04 tuned NGHP 17 benthic isotope stratigraphy indicating strong coherency at the three main orbital frequencies (95% CI). b) Blackman-Tukey cross-spectral analysis of Ti/Ca records from NGHP 17 and U1448 similarly indicating strong coherence over the same frequency bands.

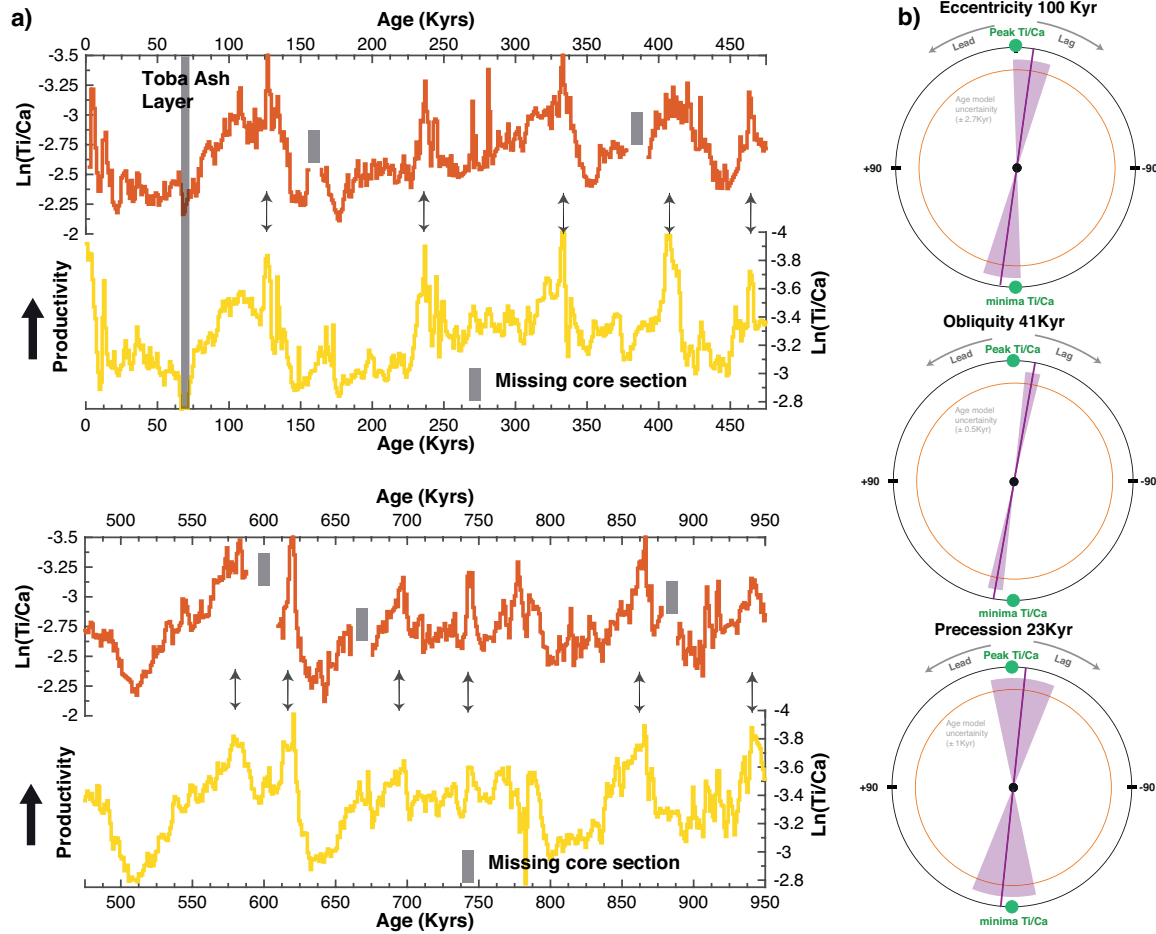


Figure 4) a) Scanning XRF measurements of Ti/Ca for NGHP17 and U1448. The age model for the U1448 site record was derived by splicing the Ti/Ca records for both cores and transferring the benthic $\delta^{18}O$ record of NGHP17 onto the new composite depth. Solid lines represent interpolated time interval $\Delta t=1\text{Kyr}$. b) Phase wheels summarizing age model uncertainties with respect to NGHP 17 Ti/Ca record excluding uncertainties in NGHP 17 age model.

3.2. Statistical analysis of XRF proxies for the summer monsoon strength

Terrigenous supply versus marine productivity at NGHP 17 is estimated using XRF-derived ratio of titanium (Ti) versus calcium (Ca). Ti/Ca is widely used proxy for fluvial supplied material (e.g. Jennerjahn et al., 2004; Toucanne et al., 2009). Assuming this holds true at Site 17, higher/lower Ti/Ca values would imply the prevalence of a stronger/weaker monsoon consistent with the Si/Al record. The Ti/Ca power spectrum shows statistically significant signal at eccentricity (~ 100 yrs) and obliquity (~ 41 yrs) frequency bands ($>90\%$ CI) and explain a high percentage of the total variance ($>60\%$) in the Ti/Ca record. To a lesser extent, the

Ti/Ca power spectrum document significant signal at precession frequency band (~23 kyrs) and reveals a unique ~166 kyrs cycle (>80% CI). Continuous wavelet transform of the Ti/Ca similarly indicate that strong spectral power is consistently concentrated at frequency bands mainly corresponding to orbital eccentricity and to a lesser extent obliquity (Fig 5b). This might indicate that potential forcing mechanisms driving terrigenous material flux are directly related to external radiation forcing over eccentricity and obliquity bands. However, one should also take note that insolation changes related to the ~100 kyrs eccentricity are very small and suggests that other processes unrelated to the monsoon likely influence the Ti/Ca record (see below) and phase relationships at the two frequencies should be carefully examined. The Si/Al record is one alternative approach considered here to assess the monsoon related variance. This proxy is used as an indicator to examine changes in the relative proportion of the ratio of quartz sand (rich in Si) and clay (rich in Al). Thus, high/low Si/Al values suggest increased/decreased proportion of sand in the sediment and weakened/intensified monsoon regime. The Si/Al record is dominated by significant obliquity (>90% CI) and ~100 kyrs glacial/interglacial variability (>80% CI). However, the Si/Al record does not show a consistent evolutionary pattern through out the studied period (Fig 5d).

Table1. Coherency and Phase relationships relative to *orbital parameters (ETP)*

<i>Andaman Sea records</i>	<i>Precession Coherency (23kyrs)</i>	<i>Precession Phase</i>	<i>Obliquity Coherency (41kyrs)</i>	<i>Obliquity Phase</i>	<i>Eccentricity Coherency (100kyrs)</i>	<i>Eccentricity Phase</i>
<i>U1448 Ti/Ca¹</i>	0.77***	+140°	0.91***	+122°	0.62	+153°
<i>U1448 Si/Al²</i>	0.63	+175°	0.51	+137°	0.54	-170°
<i>NGHP Vs U1448 (Ti/Ca)³</i>	0.86***	-10°	0.90***	+10°	0.90***	+10°
<i>NGHP $\delta^{18}O_{benthic}$ VS LR04⁴</i>	0.84***	-6°	0.99***	-10°	0.93***	-8.5°

Test statistic for non-zero coherency at the 80% and 95% level ^{1,2,3,4} are 0.68 and 0.83 respectively. Negative phase indicates a lag of the proxy record relative to ETP and positive phase indicates a lead. ** and *** represent significance at the 80% and 95% levels respectively.

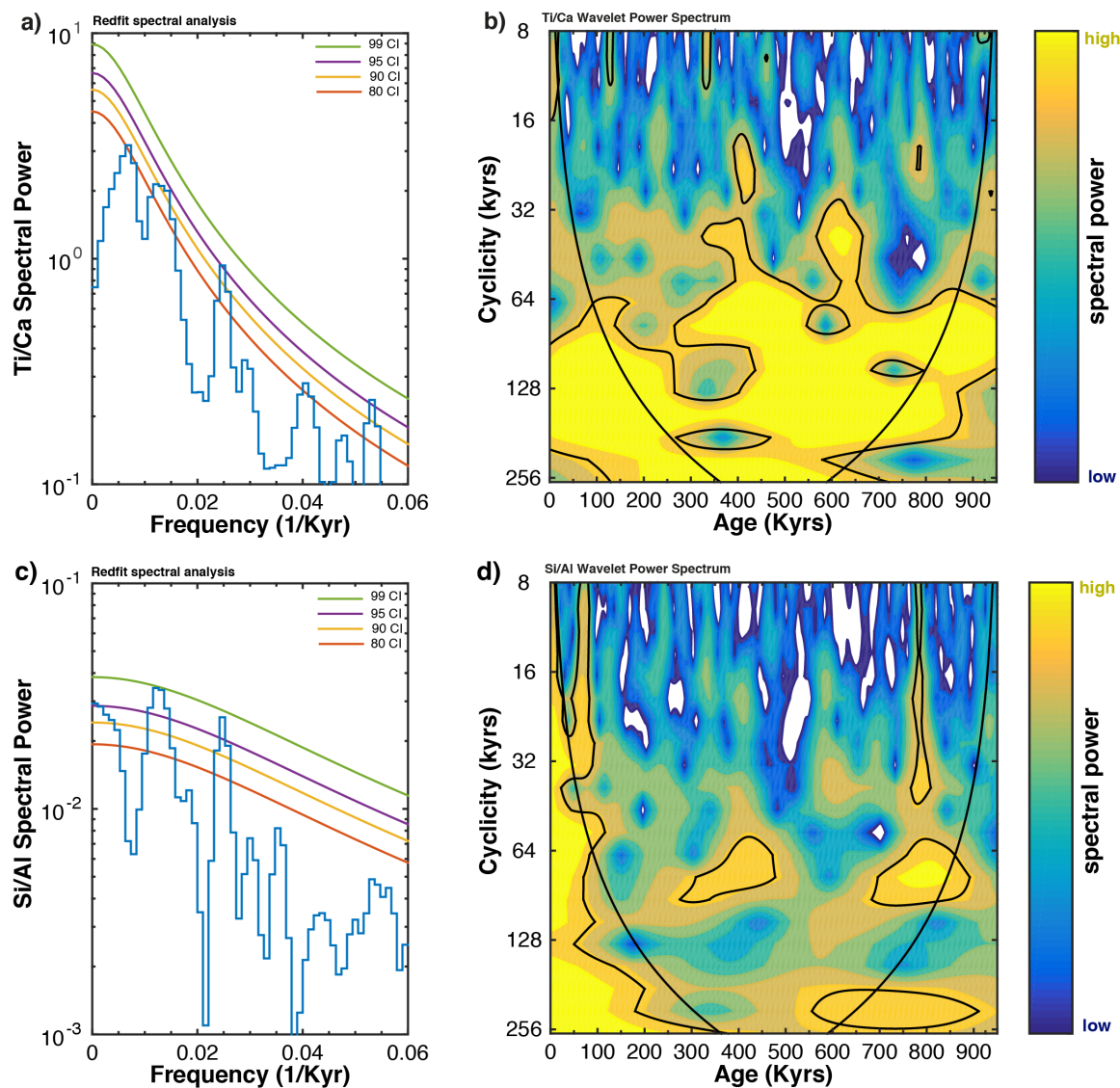


Figure 5 a) Redfit spectral analysis of U1448 Ti/Ca record showing strong periodicity at frequencies corresponding to the three main orbital periods (80% CI). b) Continuous wavelet transform of the Ti/Ca record; c) Redfit spectral analysis U1448 Ti/Ca record showing strong power at frequencies corresponding to the orbital eccentricity and obliquity (95% CI). d) Continuous wavelet transform of the Si/Al record. Black line contours in b) and d) represent 80% confidence level.

Fig. 6 summarizes coherence and phase relationships between the XRF proxy records with respect to ETP at the precession and obliquity cycles. Only precession and obliquity phase wheels are presented here taking in to account limited role of direct eccentricity forcing and relatively better coherency is achieved over these frequency bands. Cross-spectral analyses indicate that Ti/Ca records are highly

coherent with ETP at the precession and obliquity bands (>95% CI) (Table 1). Coherency between Ti/Ca and ETP over the eccentricity band, however, is considerably lower. The Ti/Ca record lead minimum precession and maximum obliquity (maximum latent heat export) by ~ 14 kyrs ($122^\circ/360^\circ * 41$ kyrs) and ~ 10 kyrs ($140^\circ/360^\circ * 41$ kyrs) respectively. Taken at face value longer precession and obliquity related leads indicate that terrigenous flux in the Andaman Sea are completely decoupled from NH insolation changes. However, it's likely that the terrigenous signal is diluted by the Ca-signal. It's also likely that high XRF Ti/Ca ratios during peak glacial and interglacial periods could be as much driven by sea level fluctuations via increased mixing of water masses and enhanced local marine productivity taking in to account that the Ti/Ca record is not susceptible to carbonate dissolution at this location (Kolla et al., 1975). To test whether this holds true, we have determined sea level related marine productivity variance by estimating the phasing of peak sea level points from a recently published global sea level stack (Rohling et al., 2014). The Ti/Ca record is essentially 180° out of phase with respect to high sea level points at the precession and obliquity bands and is compatible with a direct sea level related response. Cross-spectral analyses between Si/Al and Ti/Ca records, however, indicate significant coherency at all frequencies corresponding to the three main orbital periods (>80% CI) and in particular at the obliquity and eccentricity bands (>95% CI). This suggests that monsoon related variance is likely contained in the Ti/Ca, records and a link between local marine productivity and monsoon intensity might be speculated. This complicates a direct interpretation of terrigenous proxies such as Ti/Ca or Fe/Ca as monsoon tracers. Relatively stronger coherency between the Si/Al record and ETP is attained over the precession band than obliquity or eccentricity bands. The Si/Al record lead NH insolation maxima by ~ 12 kyrs ($175^\circ/360^\circ * 23$ kyrs) and is in phase with maximum SH insolation over the precession band. A similar phasing is also recorded for the obliquity band where minimum Si/Al values (maximum monsoon intensity) lead/lag maximum NH/SH summer insolation by ~ 16 kyrs ($137^\circ/360^\circ * 41$ kyrs) and ~ 5 kyrs ($-43^\circ/360^\circ * 41$ kyrs) respectively. This highlights the role of SH forcing of the monsoon via internal processes occurring within the climate system and

compliments recent findings based on $\delta^{18}\text{O}_{\text{sw}}$ records from the Andaman Sea (Gebregiorgis et al., in prep, Chapter I). Otherwise a dominant NH control would have forced a closer phasing of summer monsoon precipitation near precession minima and obliquity maxima (Fig 6). However, weaker coherency over both precession and obliquity as well as eccentricity frequency bands suggest a strongly non-linear relationship exists between insolation forcing and SAM climate.

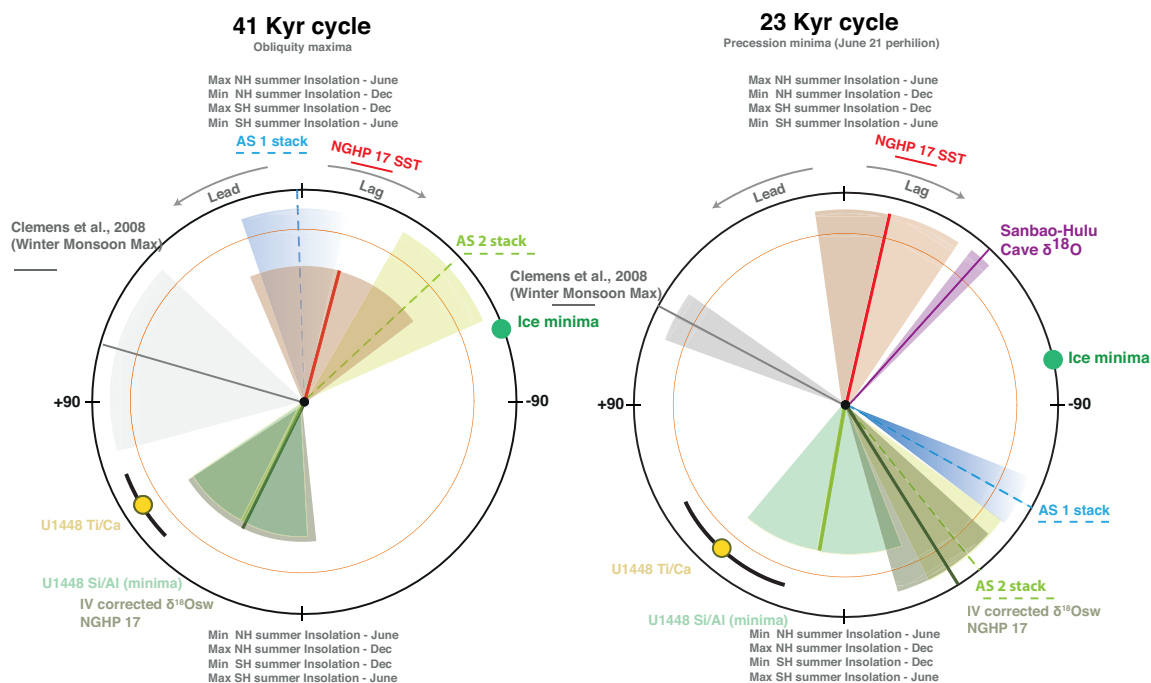


Fig. 6. Phase wheels summarizing Asian monsoon response to insolation forcing at the orbital obliquity (41 kyrs) and precession (23 kyrs) periods during early to late Pleistocene. The precession index is defined as $\Delta \epsilon \sin \omega$ where ω is the longitude of the perihelion measured from the moving vernal point and ϵ is the eccentricity of Earth's orbit around the Sun (Berger and Loutre, 1997; Laskar et al., 1993). Obliquity is the axial tilt of Earth's rotation axis with respect to the orbital plane. In the phase wheel representation the 12 o'clock position is set to precession minima (P min; $\omega = 90^\circ$, 21st June perihelion) and obliquity maxima (O max), respectively. Negative/Positive phases are measured in the clockwise/anticlockwise direction and represent phase lags/leads relative to P min or O max. Published records plotted (with shaded phase estimate errors) are the Arabian Sea summer monsoon stacks AS1 and AS2, the Chinese Sanbao-Hulu cave $\delta^{18}\text{O}$ composite (Cheng et al., 2009), and winter and summer monsoon maxima (Clemens et al., 2008). Obliquity and precession phasing of XRF records of Ti/Ca and Si/Al is shown in light orange and green. Also shown IV corrected $\delta^{18}\text{O}_{\text{sw}}$ from NGHP 17 (Gebregiorgis et al., in prep). Orange circle denotes 80% coherency. 95% and 80 confidence intervals for coherency are 0.82 and 0.68 with bandwidth 0.0038. Interpolated time interval is 1 kyrs and is from 3 to 951 kyrs.

3.3 Orbital coherence and phase relationships with in the broader Asian Summer monsoon system

Our understanding of the Quaternary evolution of the SAM mainly relies on wind-based proxies (e.g. the abundances of pollen, foraminifera and eolian dust grains) from the Arabian Sea (e.g. Caley et al., 2011; Clemens et al., 1991; Clemens et al., 1996; Clemens et al., 2008; Sarkar et al., 2000; Schulz et al., 1998; Ziegler et al., 2010). Much of our knowledge about the long-term variability of the East Asian summer monsoon, on the other hand, comes from high-resolution terrestrial records from mainland China (e.g. cave calcite deposits and loess–paleosol sequences) and the South China Sea (e.g. Cheng et al., 2016; Ding et al., 1994; Wang et al., 1999). Reconstructions of past climate conditions from terrestrial and marine archives are derived from paleoclimatology proxies, which provide estimates of past climate change over a range of timescales. These proxies are directly or indirectly connected to the climate system via different pathways. For example, wind-based proxies from the Arabian Sea are extensively used as indicators of summer monsoon strength on the assumption that seasonally reversing monsoon winds are known to promote blooming of distinct fauna and transport considerable amount of dust along the way. Similar assumptions are provided for the use of grain size proxies in loess deposits, which indicate the relative wind strength of the dust-bearing Asian winter monsoon (e.g. Porter and Zhisheng, 1995; Xiao et al., 1995). Widely cited high resolution oxygen isotopic composition of cave calcite deposits, on the other hand, are linked to Asian summer monsoon precipitation based on the assumption that the oxygen isotopic composition of cave calcites is a function of precipitation amount. Others have disputed the core assumptions of several of the proxies outlined above. For example, it was suggested that signals recorded in the wind-based productivity proxies from the Arabian are predominantly controlled by physical and biological processes unrelated to the monsoon (Ruddiman, 2006; Ziegler et al., 2010). Oxygen isotope records from cave calcites, on the other hand, appear susceptible to changes in winter temperature and moisture source (Clemens et al., 2010; Maher and Thompson, 2012). Noting these proxy limitations, we put

forward a multiproxy specific frequency analysis approach. Focus is on peak variance among different monsoon related proxies at major orbital frequency bands where significant changes are expected and proxy signals are recorded beyond dispute.

Circumstantial evidence points that the Si/Al record is predominantly controlled by fluctuations in summer monsoon intensity. Precession phasing of the Si/Al record show a response time lag of ~12 kyrs with respect to NH summer insolation (Fig. 6). This is some ~3 kyrs later than previous precession related timing of the summer monsoon estimated from Arabian Sea proxies and also recently validated (Gebregiorgis et al., in prep and Chapter I). However, this discrepancy can be reconciled taking in to account that XRF proxies of the monsoon likely take more time to respond to precipitation changes and is underlined by the fact that millennial scale variability is lacking in these records. Dansgaard-Oeschger (D-O) like millennial variability has been observed in paleo-salinity and paleo-productivity reconstructions in the northern Bay of Bengal (e.g. Kudrass et al., 2001) and the Arabian Sea (e.g. Zeigler et al., 2010) but such is not apparent in the high resolution XRF data from the Andaman Sea. This indicates either these proxies take more time to respond to precipitation changes or precipitation in the Irrawaddy catchment is not sensitive to Northern Hemisphere millennial scale climate variability. Examining the Holocene to LGM record suggests the former is likely as the XRF records appear to show a consistent lag of ~2 to 3 kyrs during phases major intensification of the southwest monsoon inferred from a Ba/Ca and $\delta^{18}\text{O}_{\text{sw}}$ records from a nearby core (Fig 7) (Gebregiorgis et al., 2016). Oxygen isotopic composition of cave calcite deposits from East Asia are frequently used as proxies of summer precipitation, on the other hand, show relatively shorter time lag of ~3 kyrs with respect to Northern Hemisphere peak summer insolation (Cheng et al., 2009; Wang et al., 2008; Wang et al., 2001). Our conservative estimates indicates a larger ~9 kyr phase difference between the Si/Al record presented here and the cave calcite. A similar orbital phasing between the two Asian monsoon subsystems is anticipated taking in to account modern monsoon climatology and that the Southern Indian Ocean is a

common moisture source (Wang, 2006). The much longer phase difference between these two records, thus, is likely due to proxy limitations and demands re-interpretation of the proxy records (Clemens et al., 2010). Clemens et al. (2010) re-analyzed the heterodyne frequencies of the primary orbital cycles in the cave $\delta^{18}\text{O}$ spectrum and demonstrated that common variance is contained in both Arabian Sea and cave $\delta^{18}\text{O}$ summer monsoon records. By subtracting this variance from the cave $\delta^{18}\text{O}$ records, Clemens et al. 2010 showed that the residual time series is highly coherent and in phase with Arabian Sea summer monsoon proxies over the precession band. The ~ 3 kyrs precession related time lag observed in the cave $\delta^{18}\text{O}$ records, thus, reflects a combined summer and winter monsoon forcing. It stands out that the precession related ~ 8 kyrs time lag between NH insolation maxima and monsoon maxima, resulted from increased latent and sensible (direct) heating, and a net latent heat transport from Southern Subtropical Indian Ocean (SSIO) (Clemens et al., 1991). It should be stressed however, that precession related variability in both Ti/Ca and Si/Al records at most account for ~ 25 and $\sim 30\%$ of the total variance in these records respectively and cannot be considered a primary driving force.

In the Obliquity band, the Si/Al record leads maximum obliquity (latent heat maxima) by ~ 19 kyrs ($169^\circ/360^\circ * 41$ kyrs) and is in polar contrast with the previous timing estimate of summer monsoon maxima from the Arabian Sea (Caley et al., 2011; Clemens et al., 1991; Clemens and Prell, 2003). The Si/Al record is nearly 180° degree out of phase with respect to maximum obliquity, like $\delta^{18}\text{O}_{\text{sw}}$ records from the same Andaman Sea sediments (Gebregiorgis et al., in prep, Chapter I). Over all, coherent obliquity phasing of these proxies, as fundamentally different as they are, suggest that increased cross-equatorial moisture flux, triggered by intensified intra-hemispheric insolation and temperature gradient following obliquity minima, is likely the main driver of intensified summer monsoon at this frequency band. This is also consistent with earlier suggestions that atmospheric poleward moisture flux intensifies during glacial inception and periods of decreased obliquity (Vimeux et al., 1999).

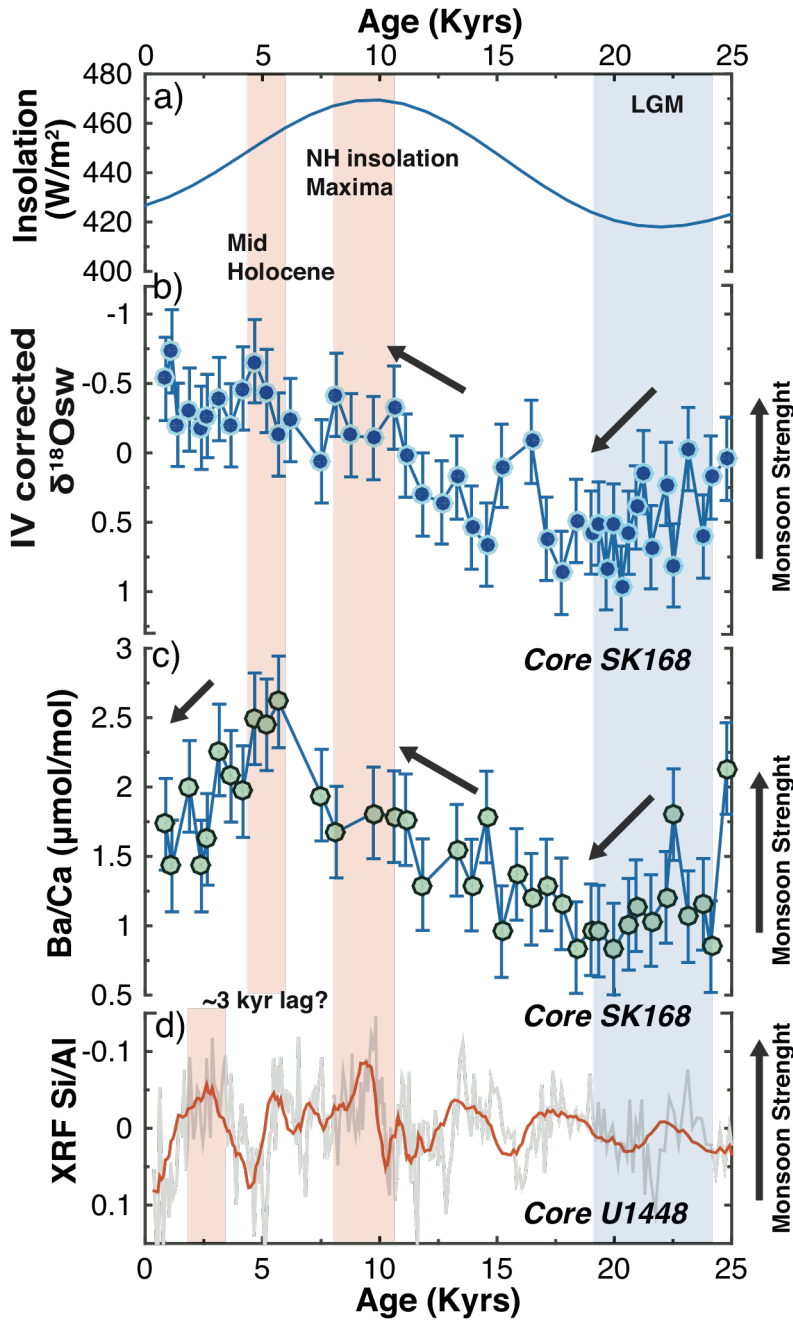


Fig 7. XRF Si/Al record in comparison with recently published records of $\delta^{18}O_{sw}$ and Ba/Ca records (Gebregiorgis et al., 2016); a) Insolation (mid-.July) (W/m^2) at 65 N (Berger, 1999); b) $\delta^{18}O_{sw}$ calculated using the calibration equation of Bemis et al. (1998) and corrected for global ice volume using (Waelbroeck et al., 2002); c) Ba/Ca ratios derived from mixed layer species *G. sacculifer*; d) Detrended Si/Al timeseries from U1448.

4. Conclusions

Analysis of high resolution XRF records from Andaman sea marine sediments show that summer monsoon precipitation peaked ~8-11 kyrs after NH insolation over the precession band and is broadly consistent with earlier findings. Over the precession band, it was previously suggested that a net latent heat transport from Southern Subtropical Indian Ocean (SSIO) triggered by increased latent and sensible (direct) heating control the strength and timing of the monsoon. The precession phasing of Ti/Ca and Si/Al appears consistent with recently generated $\delta^{18}\text{O}_{\text{sw}}$ records from the Andaman Sea (Gebregiorgis et al., in prep). However, precession related variability in both Ti/Ca and Si/Al appears muted and only accounts for ~25 and ~30% of the total variability in the records and indicate minimal precession forcing. Our results suggest that obliquity forcing plays a dominant role in controlling the pace of the summer monsoon in ways that are fundamentally different than precession pacing of the monsoon. We provide first evidence that obliquity controls the pace of the summer monsoon precipitation through enhanced cross-hemispherical atmospheric moisture following obliquity minima in line with recent $\delta^{18}\text{O}_{\text{sw}}$ records from the same Andaman Sea sediments.

References

- Ali, S., Hathorne, E.C., Frank, M., Gebregiorgis, D., Statterger, K., Stumpf, R., Kutterolf, S., Johnson, J.E. and Giosan, L., 2015. South Asian monsoon history over the past 60 kyr recorded by radiogenic isotopes and clay mineral assemblages in the Andaman Sea. *Geochemistry, Geophysics, Geosystems*, 16(2): 505-521.
- Awasthi, N., Ray, J.S., Singh, A.K., Band, S.T. and Rai, V.K., 2014. Provenance of the Late Quaternary sediments in the Andaman Sea: Implications for monsoon variability and ocean circulation. *Geochemistry, Geophysics, Geosystems*, 15(10): 3890-3906.
- Bender, F.K., 1983. *Geology of Burma*, 16. Gebrüder Borntraeger Verlagsbuchhandlung, Science Publishers.
- Bender, V.B., Hanebuth, T.J. and Chiessi, C.M., 2013. Holocene shifts of the subtropical shelf front off Southeastern South America controlled by high and low latitude atmospheric forcings. *Paleoceanography*, 28(3): 481-490.
- Berger, A. and Loutre, M.-F., 1991. Insolation values for the climate of the last 10 million years. *Quaternary Science Reviews*, 10(4): 297-317.
- Berger, A., 1999. Parameters of the Earth's orbit for the last 5 Million years in 1 kyr resolution. PANGAEA, doi, 10.
- Berger, A. and Loutre, M.-F., 1997. Intertropical latitudes and precessional and half-precessional cycles. *Science*, 278(5342): 1476-1478.
- Bolton, C.T., Chang, L., Clemens, S.C., Kodama, K., Ikehara, M., Medina-Elizalde, M., Paterson, G.A., Roberts, A.P., Rohling, E.J. and Yamamoto, Y., 2013. A 500,000 year record of Indian summer monsoon dynamics recorded by eastern equatorial Indian Ocean upper water-column structure. *Quaternary Science Reviews*, 77: 167-180.
- Burone, L., Ortega, L., Franco-Fraguas, P., Mahiques, M., García-Rodríguez, F., Venturini, N., Marin, Y., Brugnoli, E., Nagai, R. and Muniz, P., 2013. A multiproxy study between the Río de la Plata and the adjacent South-western Atlantic inner shelf to assess the sediment footprint of river vs. marine influence. *Continental shelf research*, 55: 141-154.
- Caley, T., Malaizé, B., Zaragosi, S., Rossignol, L., Bourget, J., Eynaud, F., Martinez, P., Giraudeau, J., Charlier, K. and Ellouz-Zimmermann, N., 2011. New Arabian Sea records help decipher orbital timing of Indo-Asian monsoon. *Earth and Planetary Science Letters*, 308(3): 433-444.
- Cheng, H., Edwards, R.L., Broecker, W.S., Denton, G.H., Kong, X., Wang, Y., Zhang, R. and Wang, X., 2009. Ice age terminations. *science*, 326(5950): 248-252.
- Cheng, H., Edwards, R.L., Sinha, A., Spötl, C., Yi, L., Chen, S., Kelly, M., Kathayat, G., Wang, X. and Li, X., 2016. The Asian monsoon over the past 640,000 years and ice age terminations. *Nature*, 534(7609): 640-646.
- Clemens, S., Prell, W., Murray, D., Shimmield, G. and Weedon, G., 1991. Forcing mechanisms of the Indian Ocean monsoon. *Nature*, 353(6346): 720-725.
- Clemens, S.C., Murray, D.W. and Prell, W.L., 1996. Nonstationary phase of the Plio-Pleistocene Asian monsoon. *Science*, 274(5289): 943-948.

- Clemens, S.C. and Prell, W.L., 2003. A 350,000 year summer-monsoon multi-proxy stack from the Owen Ridge, Northern Arabian Sea. *Marine Geology*, 201(1): 35-51.
- Clemens, S.C., Prell, W.L. and Sun, Y., 2010. Orbital-scale timing and mechanisms driving Late Pleistocene Indo-Asian summer monsoons: Reinterpreting cave speleothem $\delta^{18}\text{O}$. *Paleoceanography*, 25(4).
- Clemens, S.C., Prell, W.L., Sun, Y., Liu, Z. and Chen, G., 2008. Southern Hemisphere forcing of Pliocene $\delta^{18}\text{O}$ and the evolution of Indo-Asian monsoons. *Paleoceanography*, 23(4).
- Clift, P.D., Hodges, K.V., Heslop, D., Hannigan, R., Van Long, H. and Calves, G., 2008. Correlation of Himalayan exhumation rates and Asian monsoon intensity. *Nature Geoscience*, 1(12): 875-880.
- Clift, P.D., Wan, S. and Blusztajn, J., 2014. Reconstructing chemical weathering, physical erosion and monsoon intensity since 25Ma in the northern South China Sea: A review of competing proxies. *Earth-Science Reviews*, 130: 86-102.
- Croudace, I.W., Rindby, A. and Rothwell, R.G., 2006. ITRAX: description and evaluation of a new multi-function X-ray core scanner. *Special publication-geological society of London*, 267: 51.
- Curry, J.R., 2005. Tectonics and history of the Andaman Sea region. *Journal of Asian Earth Sciences*, 25(1): 187-232.
- Ding, Z.-l., Yu, Z.-w., Rutter, N. and Liu, T., 1994. Towards an orbital time scale for Chinese loess deposits. *Quaternary Science Reviews*, 13(1): 39-70.
- Gebregiorgis, D., Hathorne, E.C., Sijinkumar, A., Nath, B.N., Nürnberg, D. and Frank, M., 2016. South Asian summer monsoon variability during the last~ 54 kyrs inferred from surface water salinity and river run off proxies. *Quaternary Science Reviews*, 138: 6-15.
- Govin, A., Holzwarth, U., Heslop, D., Ford Keeling, L., Zabel, M., Mulitza, S., Collins, J.A. and Chiessi, C.M., 2012. Distribution of major elements in Atlantic surface sediments (36 N–49 S): Imprint of terrigenous input and continental weathering. *Geochemistry, Geophysics, Geosystems*, 13(1).
- Haug, G.H., Hughen, K.A., Sigman, D.M., Peterson, L.C. and Röhl, U., 2001. Southward migration of the intertropical convergence zone through the Holocene. *Science*, 293(5533): 1304-1308.
- Kolla, V., Bé, A.W. and Biscaye, P.E., 1976. Calcium carbonate distribution in the surface sediments of the Indian Ocean. *Journal of Geophysical Research*, 81(15): 2605-2616.
- Kudrass, H., Hofmann, A., Doose, H., Emeis, K. and Erlenkeuser, H., 2001. Modulation and amplification of climatic changes in the Northern Hemisphere by the Indian summer monsoon during the past 80 ky. *Geology*, 29(1): 63-66.
- Kuhnt, W., Holbourn, A., Xu, J., Opdyke, B., De Deckker, P., Röhl, U. and Mudelsee, M., 2015. Southern Hemisphere control on Australian monsoon variability during the late deglaciation and Holocene. *Nature communications*, 6.
- Kutzbach, J., Liu, X., Liu, Z. and Chen, G., 2008. Simulation of the evolutionary response of global summer monsoons to orbital forcing over the past 280,000 years. *Climate Dynamics*, 30(6): 567-579.

- Laskar, J., Joutel, F. and Boudin, F., 1993. Orbital, precessional, and insolation quantities for the Earth from -20 Myr to + 10 Myr. *Astronomy and Astrophysics*, 270: 522-533.
- Lisiecki, L.E. and Raymo, M.E., 2005. A Pliocene-Pleistocene stack of 57 globally distributed benthic $\delta^{18}\text{O}$ records. *Paleoceanography*, 20(1).
- Maher, B.A. and Thompson, R., 2012. Oxygen isotopes from Chinese caves: records not of monsoon rainfall but of circulation regime. *Journal of Quaternary Science*, 27(6): 615-624.
- Meade, R.H., 1996. River-sediment inputs to major deltas. Sea-level rise and coastal subsidence. Kluwer, London: 63-85.
- Mohtadi, M., Oppo, D.W., Steinke, S., Stuut, J.-B.W., De Pol-Holz, R., Hebbeln, D. and Lückge, A., 2011. Glacial to Holocene swings of the Australian-Indonesian monsoon. *Nature Geoscience*, 4(8): 540-544.
- Mohtadi, M., Prange, M. and Steinke, S., 2016. Palaeoclimatic insights into forcing and response of monsoon rainfall. *Nature*, 533(7602): 191-199.
- Najman, Y., 2006. The detrital record of orogenesis: A review of approaches and techniques used in the Himalayan sedimentary basins. *Earth-Science Reviews*, 74(1): 1-72.
- Ólafsdóttir, K.B., Schulz, M. and Mudelsee, M., 2016. REDFIT-X: Cross-spectral analysis of unevenly spaced paleoclimate time series. *Computers & Geosciences*, 91: 11-18.
- Paillard, D., Labeyrie, L. and Yiou, P., 1996. Macintosh program performs time-series analysis. *Eos, Transactions American Geophysical Union*, 77(39): 379-379.
- Peterson, L.C., Haug, G.H., Hughen, K.A. and Röhl, U., 2000. Rapid changes in the hydrologic cycle of the tropical Atlantic during the last glacial. *Science*, 290(5498): 1947-1951.
- Porter, S.C. and Zhisheng, A., 1995. Correlation between climate events in the North Atlantic and China during the last glaciation.
- Rashid, H., England, E., Thompson, L. and Polyak, L., 2011. Late glacial to Holocene Indian summer monsoon variability based upon sediment. *Terr. Atmos. Ocean. Sci*, 22(2): 215-228.
- Rashid, H., Flower, B., Poore, R. and Quinn, T., 2007. A ~ 25ka Indian Ocean monsoon variability record from the Andaman Sea. *Quaternary Science Reviews*, 26(19): 2586-2597.
- Richter, T.O., Van der Gaast, S., Koster, B., Vaars, A., Gieles, R., de Stigter, H.C., De Haas, H. and van Weering, T.C., 2006. The Avaatech XRF Core Scanner: technical description and applications to NE Atlantic sediments. Geological Society, London, Special Publications, 267(1): 39-50.
- Rizal, S., Damm, P., Wahid, M.A., Sundermann, J., Ilhamsyah, Y. and Iskandar, T., 2012. General circulation in the Malacca Strait and Andaman Sea: a numerical model study. *American Journal of Environmental Sciences*, 8(5): 479.
- Robinson, R.A.J., Bird, M., Oo, N.W., Hoey, T., Aye, M.M., Higgitt, D., Lu, X., Swe, A., Tun, T. and Win, S.L., 2007. The Irrawaddy River sediment flux to the Indian Ocean: the original nineteenth-century data revisited. *The Journal of Geology*, 115(6): 629-640.

- Rodolfo, K.S., 1969. Sediments of the Andaman basin, northeastern Indian Ocean. *Marine Geology*, 7(5): 371-402.
- Rohling, E., Foster, G.L., Grant, K., Marino, G., Roberts, A., Tamisiea, M.E. and Williams, F., 2014. Sea-level and deep-sea-temperature variability over the past 5.3 million years. *Nature*, 508(7497): 477-482.
- Rothwell, R.G., 2015. Twenty years of XRF core scanning marine sediments: What do geochemical proxies tell us?, *Micro-XRF Studies of Sediment Cores*. Springer, pp. 25-102.
- Ruddiman, W.F., 2006. What is the timing of orbital-scale monsoon changes? *Quaternary Science Reviews*, 25(7): 657-658.
- Sarkar, A., Ramesh, R., Somayajulu, B., Agnihotri, R., Jull, A. and Burr, G., 2000. High resolution Holocene monsoon record from the eastern Arabian Sea. *Earth and Planetary Science Letters*, 177(3): 209-218.
- Schulz, H., von Rad, U., Erlenkeuser, H. and von Rad, U., 1998. Correlation between Arabian Sea and Greenland climate oscillations of the past 110,000 years. *Nature*, 393(6680): 54-57.
- Schulz, M. and Mudelsee, M., 2002. REDFIT: estimating red-noise spectra directly from unevenly spaced paleoclimatic time series. *Computers & Geosciences*, 28(3): 421-426.
- Socquet, A. and Pubellier, M., 2005. Cenozoic deformation in western Yunnan (China–Myanmar border). *Journal of Asian Earth Sciences*, 24(4): 495-515.
- Southon, J., Kashgarian, M., Fontugne, M., Metivier, B. and Yim, W.W., 2002. Marine reservoir corrections for the Indian Ocean and Southeast Asia. *Radiocarbon*, 44(1): 167-180.
- Tian, J., Xie, X., Ma, W., Jin, H. and Wang, P., 2011. X-ray fluorescence core scanning records of chemical weathering and monsoon evolution over the past 5 Myr in the southern South China Sea. *Paleoceanography*, 26(4).
- Torrence, C. and Compo, G.P., 1998. A practical guide to wavelet analysis. *Bulletin of the American Meteorological society*, 79(1): 61-78.
- Vimeux, F., Masson, V., Jouzel, J., Stievenard, M. and Petit, J., 1999. Glacial–interglacial changes in ocean surface conditions in the Southern Hemisphere. *Nature*, 398(6726): 410-413.
- Wang, B., 2006. *The asian monsoon*. Springer Science & Business Media.
- Wang, L., Sarnthein, M., Erlenkeuser, H., Grimalt, J., Grootes, P., Heilig, S., Ivanova, E., Kienast, M., Pelejero, C. and Pflaumann, U., 1999. East Asian monsoon climate during the Late Pleistocene: high-resolution sediment records from the South China Sea. *Marine Geology*, 156(1): 245-284.
- Wang, Y., Cheng, H., Edwards, R.L., Kong, X., Shao, X., Chen, S., Wu, J., Jiang, X., Wang, X. and An, Z., 2008. Millennial-and orbital-scale changes in the East Asian monsoon over the past 224,000 years. *Nature*, 451(7182): 1090-1093.
- Wang, Y.-J., Cheng, H., Edwards, R.L., An, Z., Wu, J., Shen, C.-C. and Dorale, J.A., 2001. A high-resolution absolute-dated late Pleistocene monsoon record from Hulu Cave, China. *Science*, 294(5550): 2345-2348.
- Wei, G., Li, X.H., Liu, Y., Shao, L. and Liang, X., 2006. Geochemical record of chemical weathering and monsoon climate change since the early Miocene in the South China Sea. *Paleoceanography*, 21(4).

- Weltje, G.J. and Tjallingii, R., 2008. Calibration of XRF core scanners for quantitative geochemical logging of sediment cores: theory and application. *Earth and Planetary Science Letters*, 274(3): 423-438.
- Xiao, J., Porter, S.C., An, Z., Kumai, H. and Yoshikawa, S., 1995. Grain size of quartz as an indicator of winter monsoon strength on the Loess Plateau of central China during the last 130,000 yr. *Quaternary Research*, 43(1): 22-29.
- Ziegler, M., Lourens, L.J., Tuenter, E., Hilgen, F., Reichert, G.J. and Weber, N., 2010. Precession phasing offset between Indian summer monsoon and Arabian Sea productivity linked to changes in Atlantic overturning circulation. *Paleoceanography*, 25(3).

Chapter III

Orbital variations of the mixed layer and thermocline over the past ~1 million years

D. Gebregiorgis¹, E.C. Hathorne¹, D. Nürnberg¹, S., Clemens², L. Giosan³, and M. Frank¹

¹*GEOMAR Helmholtz Centre for Ocean Research Kiel, Wischhofstraße 1-3, 24148 Kiel, Germany*

²*Earth, Environmental, and Planetary Sciences, Brown University, Providence, RI, U.S.A.*

³*Woods Hole Oceanographic Institution, Woods Hole, Massachusetts, USA, USA*

Abstract *

The forcing mechanisms driving the upper ocean salinity and thermal structures within the mixed layer and thermocline in the Andaman Sea are still poorly understood. We present the first long term mixed layer and thermocline temperatures, and $\delta^{18}\text{O}_{\text{sw}}$ records. Based on $\Delta\delta^{18}\text{O}_{\text{sw}}$ and ΔT gradients, we reconstruct the water column structure and thermocline layer depth changes in the Andaman Sea during the late Quaternary. We estimate phase relationships between mixed layer and thermocline $\delta^{18}\text{O}_{\text{sw}}$ records, hereafter ($\delta^{18}\text{O}_{\text{ML}}$ and $\delta^{18}\text{O}_{\text{TL}}$), and assess the degree of coupling between the mixed layer and thermocline at the precession, obliquity and eccentricity cycles. Both $\delta^{18}\text{O}_{\text{MW}}$ and $\delta^{18}\text{O}_{\text{TW}}$ document a mean lag of ~9 kyrs with respect to maximum NH insolation (P min) in the precession band similar to published phases of wind-based monsoon proxy records from the Arabian Sea and indicate a persistent ‘top-bottom’ propagation of salinity to depth. The prevalence of strong monsoonal forcing is also indicated by the similar phase relationship between thermocline depth changes and summer monsoon precipitation. However, much of the variability in $\delta^{18}\text{O}_{\text{ML}}$ and $\delta^{18}\text{O}_{\text{TL}}$ records is contained at other frequency bands such as the 41 kyrs obliquity and quasi eccentricity cycles between 90-120 kyrs as well as heterodyne frequencies of the primary orbital periods. The phase relationship between $\delta^{18}\text{O}_{\text{MW}}$ and $\delta^{18}\text{O}_{\text{TW}}$, and ETP over the obliquity band is sharply in contrast with precession timing where both $\delta^{18}\text{O}_{\text{MW}}$ and $\delta^{18}\text{O}_{\text{TW}}$ lead/lag maximum latent heat export and NH insolation respectively. Based on these phase relationships we propose that freshening of the

* Manuscript to be submitted to *GRL*

mixed layer and the thermocline waters is controlled by a common monsoonal forcing triggered by poleward moisture flux in response to intensified intra-hemispheric temperature gradient triggered by changes in Earth's obliquity. Despite the presence of dominant eccentricity related variance in both mixed layer and thermocline temperature and $\delta^{18}\text{O}_{\text{sw}}$ records, the degree of coherence between all records and orbital eccentricity is relatively not significant and a direct forcing mechanism cannot be identified.

1. Introduction

Dynamical interactions between the mixed layer and the thermocline underneath offer essential information on the processes of ocean heat storage in the upper ocean (Ramesh and Krishnan, 2005). A better understanding of processes operating within the deeper ocean, in particular, is critical because of the role of the thermocline as a potential conveyer of high latitude climate signals (e.g. Harper, 2000) and its potential role driving SST changes via vertical mixing (e.g. Chen et al., 1994; Girishkumar et al., 2013). Modern day upper ocean variability in the Andaman Sea and Bay of Bengal is characterized by a semi-annual cycle of mixed layer and thermocline depth variations and is intrinsic to seasonally reversing monsoonal circulations (e.g. Girishkumar et al., 2013; Rao and Sivakumar, 2003). The summer monsoon is characterized by heavy precipitation exceeding evaporation and deepening of the mixed layer due to a large supply of freshwater (Fig 1a), which also triggers significant temperature changes in the thermocline (Han et al., 2001). The winter monsoon is marked by increased evaporation, and a net heat loss from the ocean as well as shoaling of the mixed layer (Fig 1b). A detailed description of the different processes driving upper and deeper ocean thermal and salinity structures is provided in the following text (see section 2)

To date, numerous proxy records of South Asian monsoon climate have been generated, among the notable, from the Arabian Sea (Altabet et al., 1995; Altabet et al., 1999; Burns et al., 2003; Caley et al., 2011; Clemens et al., 1991; Clemens et al.,

1996; Clemens and Prell, 1990; Clemens and Prell, 2003; Govil and Naidu, 2010; Leuschner and Sirocko, 2003; Prell, 1984; Reichert et al., 1998; Schulz et al., 1998), and fewer records from the Bay of Bengal/Andaman Sea (Gebregiorgis et al., 2016; Kudrass et al., 2001; Rashid et al., 2007) and the equatorial Indian Ocean (Bassinot et al., 2011; Beaufort et al., 1997; Bolton et al., 2013). Thanks to these studies, substantial progress has been made in understanding orbital to sub-orbital insolation-forcing mechanisms of the summer monsoon: a primary force driving upper ocean variability in the Andaman Sea and Bay of Bengal. Yet, there is lack of consensus in the degree of coupling between monsoon precipitation and insolation changes in response to Earth's orbital adjustments (Ziegler et al., 2010). These discrepancies are due to the different natures of the proxies employed to interpret SAM precipitation changes and are addressed in a separate publication (Chapter I, Gebregiorgis et al., in prep). Equally important but far more poorly understood, however, are the impacts of monsoonal and NH/SH insolation forcing on the thermal and salinity structures of the deeper upper ocean enclosing the mixed layer and the thermocline. So far, only one study has looked into orbital-scale phase relationships between thermocline and surface-waters (Bolton et al., 2013). The aim of this study was to examine potential insolation forcing mechanisms that drive upper ocean stratification in the eastern equatorial Indian Ocean. To our knowledge, this has not been previously explored in other oceanographic settings falling under the direct influence of the summer monsoon.

Here, we utilize the depth habitat preferences of *Golobigerinoides sacculifer* (*G. sacculifer*) and *Neogloboquadrina dutertrei* (*N. dutertrei*) and present a long term mixed layer and thermocline (for the first time here) temperature ($SST_{Mg/Ca}$ and $TT_{Mg/Ca}$) and $\delta^{18}O_{sw}$ records from paired Mg/Ca and $\delta^{18}O$ measurements. Differences in surface and thermocline temperatures (ΔT) and $\delta^{18}O$ ($\Delta\delta^{18}O$) records are used to assess changes in upper ocean stratification and thermocline depth. The main objective of this study is to understand the feedback mechanisms within the mixed layer and the thermocline and the processes driving upper and deeper ocean salinity and thermal structures in the Andaman Sea. To achieve this goal, we

perform statistical analysis of paleoclimate timeseries and establish phase relationships between the mixed layer and the thermocline with respect to eccentricity, tilt and precession (ETP) (Berger, 1999) and potential forcing mechanisms driving upper ocean thermal and salinity structures are identified.

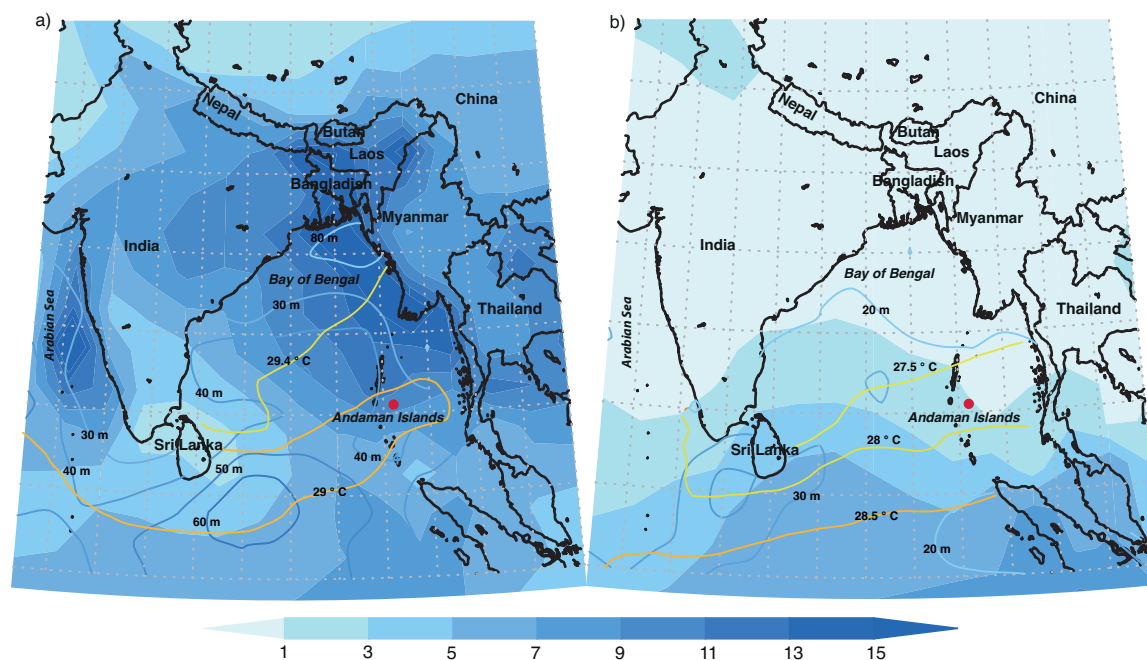


Fig. 1 Mean precipitation (mm/day) for JJAS and JFM (1979-2015) (GPCP data provided by the NOAA/OAR/ESRL PSD). Contour lines represent mixed layer depth (in meters) (de Boyer Montégut, et al., 2004) and SST ($^{\circ}$ C) variations during (a) SW summer monsoon and (b) NE winter monsoon. NGHP17 core site is shown in red filled circle.

2. Surface and deeper ocean processes in the Bay of Bengal and Andaman Sea

The Bay of Bengal and Andaman Sea form a unique semi-enclosed tropical basin over the northeastern Indian Ocean that experiences a dominant seasonal surface wind reversal during the boreal summer (June–September) and winter (November–February) seasons. The net annual surface water exchange (i.e. precipitation plus runoff minus evaporation) is primarily driven by intense freshening of the surface ocean during the summer monsoon season (Fig 1). This intense freshening of the upper ocean leads to a low salinity surface waters and strong stratification of the upper ocean. At the same time, the intense freshening suppresses vertical mixing and results in a shallow mixed layer (ML) (Fousiya et al., 2015 and references

therein), while the freshwater and thermal buoyancy fluxes strengthen stratification of the upper ocean (Prakash et al., 2012). The strong stratification of the upper ocean due to surface freshening and warming also prevents transport of cold subsurface water into the mixed layer while a weakening of stratification reinforces vertical nutrient supply and productivity (e.g. Doney, 2006). The freshwater forcing also exerts significant influence on SST patterns during the boreal winter and plays an important role in the coupled ocean-atmosphere interaction and broad-scale regional climate (Seo et al., 2009). On the other hand, the seasonal thermocline is influenced by physical processes such as wind-stress curl through the mechanism of Ekman pumping, geostrophic flow, and the radiation of Rossby waves from poleward propagating coastal Kelvin waves (e.g. Yu, 2003). The upward/downward movement of the thermocline plays an important role driving chlorophyll-*a* concentration and biological activities in the upper ocean by modulating the movement of nutrient rich thermocline water (Uz et al., 2001). In regions where the mean thermocline is shallow, variations of thermocline depth exerts considerable influence on SST bringing the colder thermocline water into the upper ocean through wind-induced upwelling, entrainment and mixing (Girishkumar et al., 2013) as schematically illustrated in Fig 2.

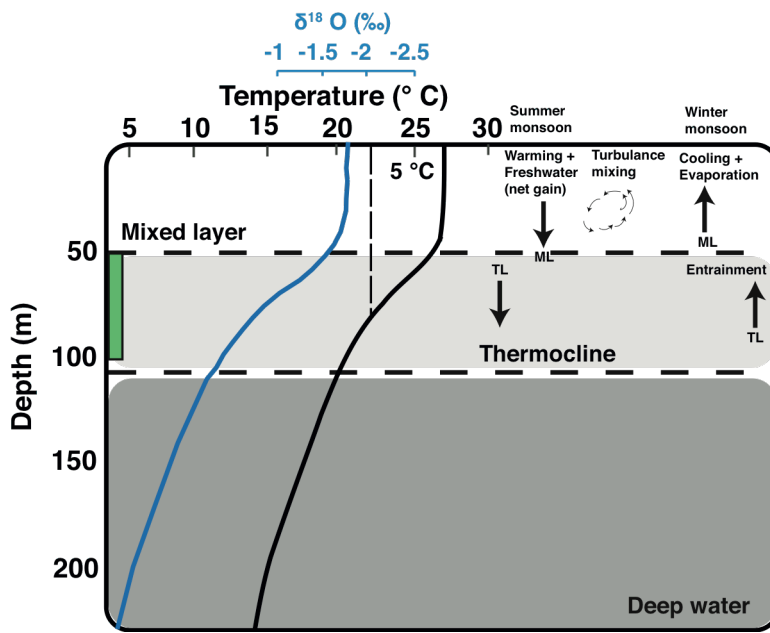


Figure 4. Schematic illustration of changes in upper ocean stratification. Modern depth profiles of temperature are for August from World Ocean Atlas 2013 (Levitus et al., 2013) while modern $\delta^{18}\text{O}$ values estimated from salinity and temperature data obtained from the Andaman Sea using Anand et al. (200) and Bemis et al. (1998). Green bar shows depth range of deep chlorophyll maximum (DCM) during May-June 1996 (Murty et al., 2000).

3. Material and methods

This study uses a unique long sediment core obtained by the IODP vessel *JOIDES* Resolution at core Site 17 in the Andaman Sea (Fig 1) in a water depth of 1356m. The sediment core was APC cored up to ~118m with excellent core recovery. Here we focus on the upper ~50 m of the core section for which there is a benthic stable isotope stratigraphy (see supplement). The age model of Site 17 is constructed based on correlation of benthic *C. wuellerstorfi*/*C. mundulus* $\delta^{18}\text{O}$ record (Figure supplement 1a) to the LR04 global benthic $\delta^{18}\text{O}$ stack (Lisiecki and Raymo, 2005) using Analyseries (Paillard et al., 1996) and is discussed in details elsewhere (Gebregiorgis et al., in prep and Chapter I of the present thesis). Age model uncertainties are estimated based on phasing offsets between NGHP 17 benthic record and LR04 and are given for the three main orbital periods ($\sim\pm 2.2$ kyrs for the 100 kyrs-eccentricity cycle, $\sim\pm 1.3$ kyrs for the 41 kyrs-obliquity cycle and $\sim\pm 0.5$ kyrs for the 23 kyrs-precession cycle).

Foraminiferal samples from NGHP 17 were collected at intervals of 10 cm up to 25 m and 25 cm for the remaining of the core. On average >50 specimens per sample were picked from the 315-400 μm size fraction to obtain a representative geochemical signature (e.g. sea Laepple and Huybers, 2013; Thirumalai et al., 2013). A constant 315-400 μm size fraction is maintained throughout the foraminifera picking process to minimize possible size dependent biases (e.g. Elderfield et al., 2002; Ni et al., 2007). Details of the cleaning steps followed are reported here (Gebregiorgis et al., 2016). Mg/Ca ratios were measured with an Agilent 7500cs ICP-MS for samples up to depth of 22 m and ICP OES (VARIAN 720-ES) for the remaining samples. Analytical error estimated for both instruments is based on repeated measurements of ECRM752-1 standard and is less than ± 0.1 mmol/mol (2σ). To check for possible clay contamination, we have carefully examined the relationship between Mg/Ca and, Al/Ca and Fe/Ca ratios (Barker et al., 2003). For the data set presented here, there is no systematic relationship between Al/Ca (or

Fe/Ca) and Mg/Ca ratios and the possibility of clay contamination in these records is negligible.

$\delta^{18}\text{O}$ measurements were carried out at GEOMAR, Kiel, using a MAT 253 mass spectrometer coupled with a Kiel IV Carbonate device system (Thermo Scientific). The results were calibrated to VPDB scale and were referenced to the NBS19 standard. Analytical errors were estimated based on repeated measurements of an in house standard (SHK Bremen) and were on average $\pm 0.05\text{‰}$ (1σ). Seawater $\delta^{18}\text{O}$ ($\delta^{18}\text{O}_{\text{sw}}$) was calculated using the $\delta^{18}\text{O}$ – temperature calibration equation of Bemis et al. (1998) and was corrected for global ice volume following Rohling et al. (2014). Uncertainties in $\delta^{18}\text{O}_{\text{sw}}$ and SSTs are calculated by propagating maximum possible errors introduced by the analytical measurements and temperature- $\delta^{18}\text{O}_{\text{sw}}$ calibration equations (e.g. Mohtadi et al., 2014). Estimated uncertainties in SST and $\delta^{18}\text{O}_{\text{sw}}$ reconstructions are on average 1 °C and 0.3‰ respectively.

Spectral analysis

To identify statistically significant periodicities, spectral analyses were performed using REDFIT (Schulz and Mudelsee, 2002). To avoid unintended artifacts generated by interpolation, spectral analyses were performed on unevenly time series. Spectral analyses were performed with an oversampling factor of 3 and a Hanning window was used to define spectral peaks. Coherence and phase lags between the records and also with respect to ETP (eccentricity, tilt or obliquity and precession) were performed using the Arand software package (Howell, 2001). For this purpose, paleoclimate time series were linearly interpolated to equal time intervals of 3.5 kyrs.

4. Results and discussion

4.1. Orbital coupling between changes in the mixed layer and thermocline

The temporal evolution of SST ($\text{SST}_{\text{Mg/Ca}}$) and thermocline temperatures ($\text{TT}_{\text{Mg/Ca}}$),

and $\delta^{18}\text{O}$ and Ice volume corrected mixed layer and thermocline $\delta^{18}\text{O}_{\text{sw}}$ values from the same samples are shown in Fig 2. Spectral analysis of $\text{SST}_{\text{Mg/Ca}}$ records indicate significant spectral power at the 23 Kyr precession, 41-Kyr obliquity and ~ 100 Kyr cycles. The $\text{TT}_{\text{Mg/Ca}}$ power spectrum, on the other hand, show significant ~ 100 Kyr and 41-Kyr cyclicity and a relatively muted variability over the precession band ($< 80\%$ CI) (Fig 3a). *G. sacculifer* and *N. dutertrei* $\delta^{18}\text{O}$ values show strong power at the three main orbital periods similar to *C. wuellerstorfi/C. mundulus* $\delta^{18}\text{O}$ but with discrete variability at higher frequencies. The $\delta^{18}\text{O}_{\text{sw}}$ power spectrum for both the mixed layer and thermocline ($\delta^{18}\text{O}_{\text{ML}}$ and $\delta^{18}\text{O}_{\text{TL}}$), however, only show strong power at the frequency band corresponding to Earth's precessional cycle ($> 95\%$ CI) (Fig 3b) despite the fact that precession related variance in both $\delta^{18}\text{O}_{\text{ML}}$ and $\delta^{18}\text{O}_{\text{TL}}$ accounts for at most 30% of the total variance in these records. Much of the variability in $\delta^{18}\text{O}_{\text{ML}}$ and $\delta^{18}\text{O}_{\text{TL}}$ records is contained at frequency bands such as the 41 Kyr obliquity and quasi eccentricity cycles between 90-120 kyrs (Fig 3b). Continuous wavelet transform of $\delta^{18}\text{O}_{\text{ML}}$ and $\delta^{18}\text{O}_{\text{TL}}$ also indicate that strong spectral power is relatively concentrated at these frequency bands (Fig 2c and d). The $\delta^{18}\text{O}_{\text{ML}}$ and $\delta^{18}\text{O}_{\text{TL}}$ records also contain heterodynes of the primary cycles and document common distinct spectral peaks between ~ 170 -190 kyrs, and at ~ 52 kyrs. The well identified ~ 52 kyrs cycle, in particular, represents the heterodyne of obliquity and precession cycles ($1/41 \pm 1/23 = 1/14.7$ and $1/52.4$) and suggests a combined insolation (precession and obliquity) forcing of the mixed layer and thermocline. More importantly, this demonstrates that the link between insolation forcing, and surface and thermocline variability are strongly non-linear. In order to establish causal links between insolation forcing and surface and thermocline variability, thus, we need to consider phase relationships between the two with respect to ETP. Here the degree of phasing between $\delta^{18}\text{O}_{\text{ML}}$ and $\delta^{18}\text{O}_{\text{TL}}$ as well as $\text{SST}_{\text{Mg/Ca}}$ and $\text{TT}_{\text{Mg/Ca}}$ with respect to ETP is considered in an effort to understand the coupling between the mixed layer and thermocline in the Andaman Sea.

Orbital variations in mixed layer and thermocline

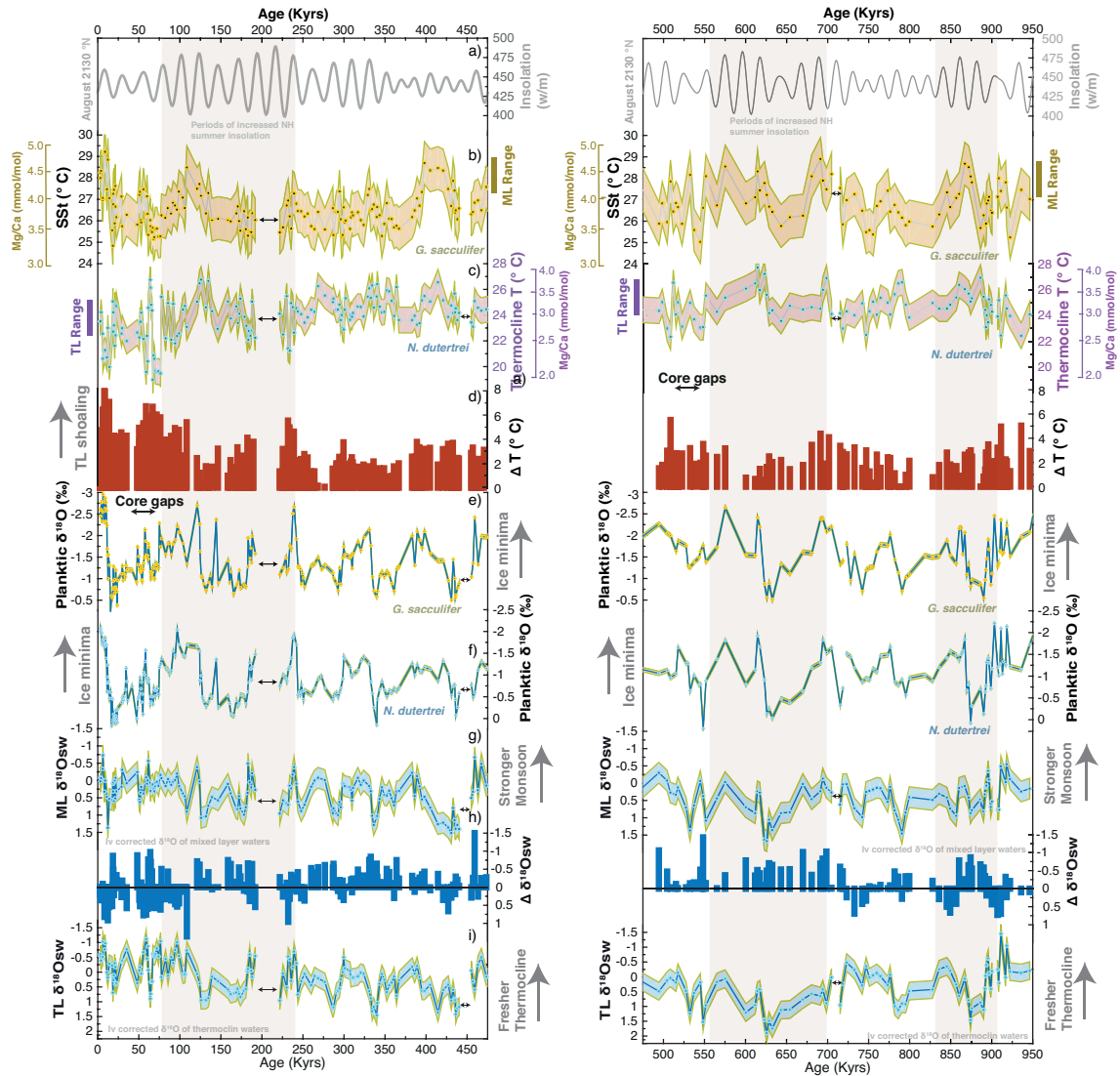


Fig. 3 a) August 21st Northern Hemisphere insolation at 30 °N (Laskar et al., 2004); b) Reconstructed SST ($SST_{Mg/Ca}$) at site 17; c) Reconstructed Thermocline temperatures ($TT_{Mg/Ca}$) at site 17; d) Gradients between $SST_{Mg/Ca}$ and $TT_{Mg/Ca}$; e) Oxygen isotope ratios of foraminifera *G. sacculifer*; f) Oxygen isotope ratios of foraminifera *N. dutertrei*; g) Ice volume corrected (Mixed layer) $\delta^{18}O_{ML}$ (VPDP Scale); h) Gradient between $\delta^{18}O_{ML}$ and $\delta^{18}O_{TL}$; i) Ice volume corrected (Thermocline layer) $\delta^{18}O_{TL}$ (VPDP Scale). Envelops in d and f show 1 σ -error.

Phase relationships and coherency between all records and ETP are shown in Fig 4. Phase estimates of $SST_{Mg/Ca}$ indicate that mixed layer temperature variations are highly coherent with respect to ETP over the precession band and are indistinguishably in phase ($-13^\circ/360^\circ * 23$ kyr) with maximum NH insolation (precession minima) (Fig 4). In contrast, $TT_{Mg/Ca}$ do not show uniform phasing over the precession band and appears to lead maximum NH insolation (Precession

minima) by ~ 9 kyrs ($146^\circ / 360^\circ * 23$). This clearly indicates that while SST changes in the Andaman Sea are primarily responsive to increased NH insolation following precession minima, only a small portion of this heat is transferred to the thermocline. A persistent downward diffusion of heat would have otherwise led to instant increase in thermocline temperatures and similar phasing between the mixed layer and the thermocline temperatures at this frequency band. Over the obliquity band where more variance in both temperature records is concentrated, $SST_{Mg/Ca}$ appears to lead $TT_{Mg/Ca}$ by ~ 2 kyrs, implying a persistent downward diffusion of heat and muted upward heat diffusion that would have been triggered by ventilation of the thermocline following changes in the Earth's orbital obliquity (Philander and Fedorov, 2003). Philander and Fedorov, (2003) proposed that, in a state of equilibrium, heat loss in the high latitudes should be balanced by heat gain elsewhere in low-latitudes through cross-equatorial heat transport via the shoaling of the tropical thermocline. In such scenario, periods of low obliquity (minimum NH summer insolation) for instance, are expected to excite a cross-equatorial transport of heat from the low latitudes where the ocean gains heat to high latitude where the ocean loses heat via enhanced thermocline circulations (Philander and Fedorov, 2003). However, there is no evidence of statistically significant coherence ($< 80\%$ CI) between the temperature records and ETP over the obliquity band. It might be speculated in this regard that processes that control the gain and losses of heat in regions of weaker offshore upwelling (e.g. Andaman Sea) are likely atmospheric in nature and intrinsic to monsoonal changes (see text below).

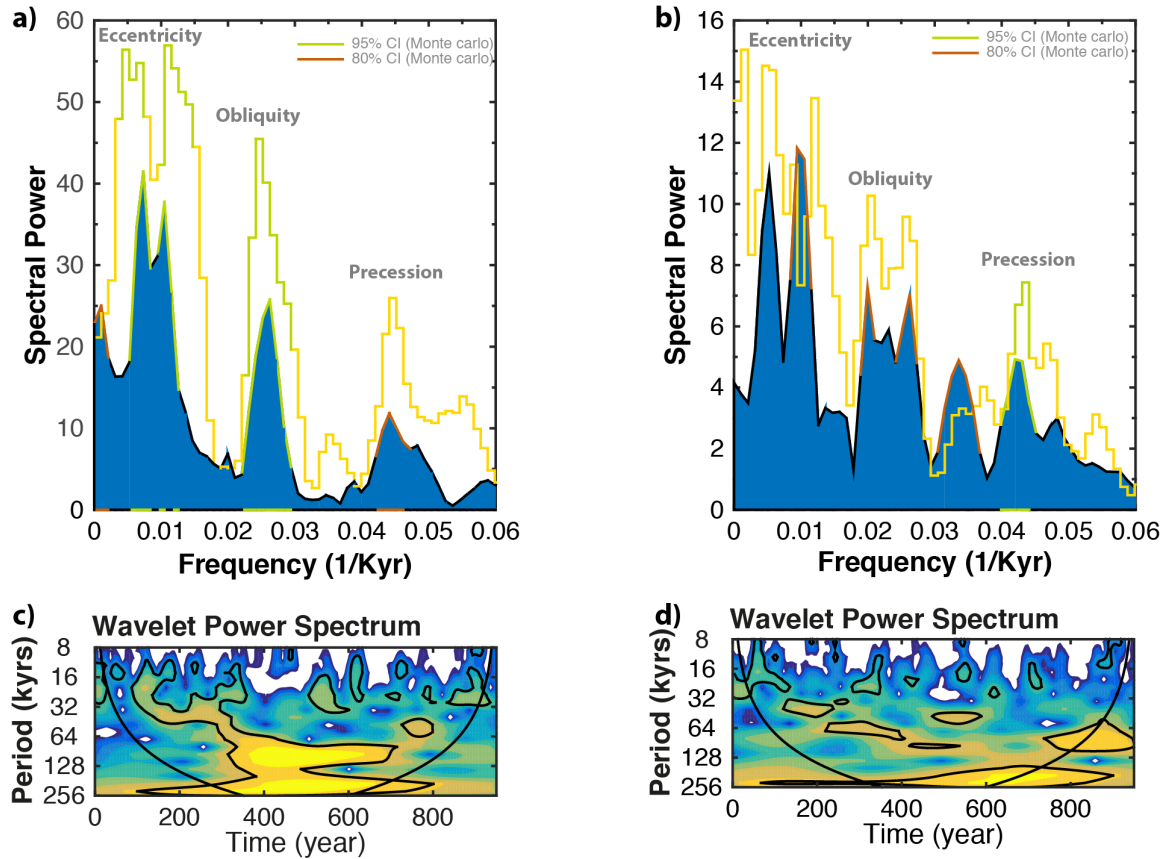


Fig 4. Redfit spectral analysis of a) SST_{Mg/Ca} (blue) and TT_{Mg/Ca} (yellow) records; b) Redfit spectral analysis Ice volume corrected $\delta^{18}O_{ML}$ (blue) and $\delta^{18}O_{TL}$ (yellow) records. Significant spectral powers at the 95% CI and 80% CI are shown in light green and brown respectively. c) Continuous wavelet transform of Ice volume corrected $\delta^{18}O_{MW}$. d) Continuous wavelet transform of Ice volume corrected $\delta^{18}O_{TL}$. Black contours in c) and d) represent 80% confidence level.

Reconstructed $\delta^{18}O_{MW}$ and $\delta^{18}O_{TW}$ show a lag of ~ 9 kyrs NH insolation over the precession band (Fig 3). The similar phasing between $\delta^{18}O_{MW}$ and $\delta^{18}O_{TW}$ indicates that Andaman Sea upper ocean salinity structure is primarily controlled by surface salinity changes. This indicates the prevalence of a top-down monsoonal control and consistent propagation of salinity to depth. Equally stronger signal registered in $\delta^{18}O_{TW}$ and the near constant phase lag of ~ 3 kyrs behind ice volume minima reaffirms the position that the variability and evolution of thermocline circulation in the Andaman Sea and Bay of Bengal are strongly dependent on the summer monsoon over the precession band. Consequently, intrinsic to increased sensible (direct) heating of the Asian topography (ice volume minima) and latent heat export

from the southern subtropical Indian Ocean (Clemens et al. 1991). The phase relationship between $\delta^{18}\text{O}_{\text{MW}}$ and $\delta^{18}\text{O}_{\text{TW}}$, and ETP over the obliquity band where more variance in both $\delta^{18}\text{O}_{\text{MW}}$ and $\delta^{18}\text{O}_{\text{TW}}$ is contained, however is sharply in contrast with precession timing where both $\delta^{18}\text{O}_{\text{MW}}$ and $\delta^{18}\text{O}_{\text{TW}}$ lead/lag maximum latent heat export (maximum at precession minima) and NH insolation respectively. Both $\delta^{18}\text{O}_{\text{MW}}$ and $\delta^{18}\text{O}_{\text{TW}}$ lead maximum obliquity (maximum latent heat export) and appear closer to ice volume maxima and sensible heat minima, which is $\sim 180^\circ$ out of phase with NH summer insolation over this frequency band. The phasing of $\delta^{18}\text{O}_{\text{MW}}$ and $\delta^{18}\text{O}_{\text{TW}}$ is virtually identical and demonstrates that thermocline changes are continuation of surface ocean variability in these settings at both precession and obliquity bands. Over the obliquity band, we propose that freshening of the mixed layer and the thermocline waters is primarily controlled by monsoon dynamics and is sensitive to a poleward moisture flux triggered by intensified intra-hemispheric temperature gradient at this frequency band. Despite the presence of dominant eccentricity related variance in these records the relatively lower degree of coherence between all records and orbital eccentricity indicates a far more complex relationship and prevalence of a non-linear eccentricity forcing of the mixed layer and thermocline.

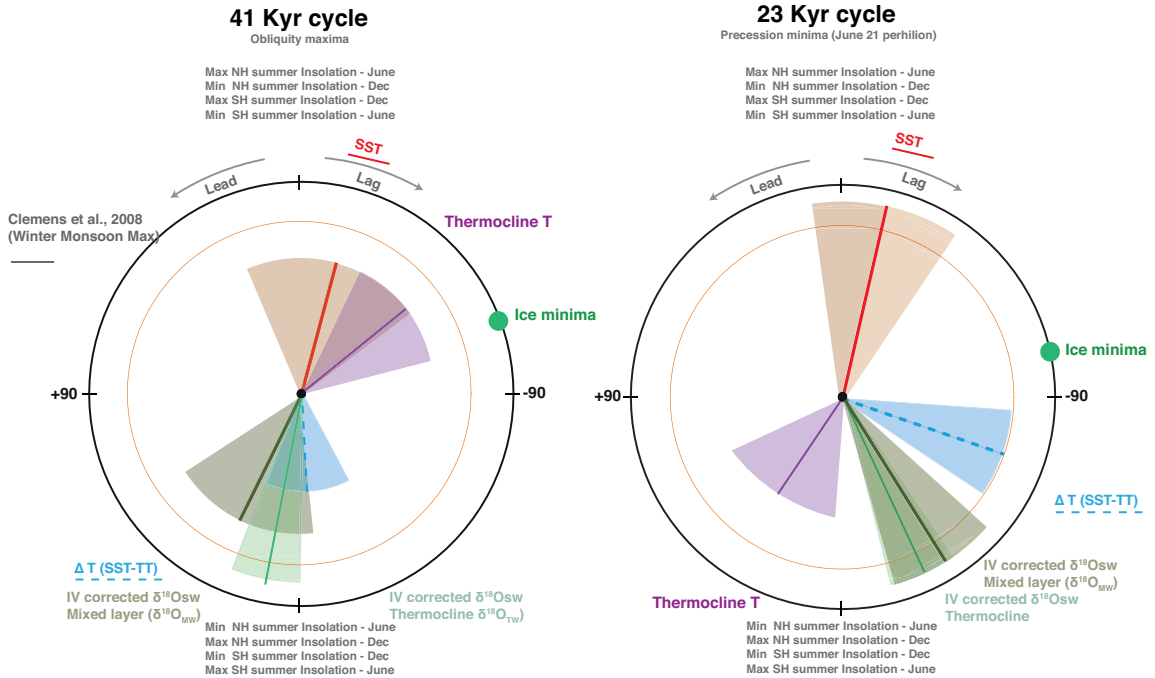


Fig. 5. Phase wheels summarizing Andaman Sea mixed layer and thermocline response to insolation forcing at the orbital obliquity (41 kyrs) and precession (23 kyrs) periods during early to late Pleistocene. The precession index is defined as $\Delta \varepsilon \sin \omega$ where ω is the longitude of the perihelion measured from the moving vernal point and ε is the eccentricity of Earth's orbit around the Sun (Berger and Loutre, 1997; Laskar et al., 1993). Obliquity is the axial tilt of Earth's rotation axis with respect to the orbital plane. In the phase wheel representation the 12 o'clock position is set to precession minima (P min; $\omega = 90^\circ$, 21st June perihelion) and obliquity maxima (O max), respectively. Negative/Positive phases are measured in the clockwise/anticlockwise direction and represent phase lags/leads relative to P min or O max. Orange circle denotes 80% coherence. Timeseries of $\Delta \delta^{18}O_{sw}$ show negligible coherence over both frequency bands and are not shown here. 95% and 80 confidence intervals for coherence are 0.79 and 0.64 with bandwidth 0.00423175. Interpolated time interval is 3.5 kyrs and is from 3 to 951 kyrs.

4.2 Thermocline depth and upper ocean salinity stratification changes

The $\Delta \delta^{18}O_{sw}$ and temperature gradient (ΔT) between mixed layer and thermocline dwelling planktic foraminifera are used as proxies for upper ocean stratification and thermocline depth changes. The $\Delta \delta^{18}O_{sw}$ is a function of local changes in $\delta^{18}O_{sw}$ of seawater given that the effect of temperature and global ice volume is corrected beforehand. A larger $\Delta \delta^{18}O_{sw}$ gradient implies a shallower thermocline and a stronger vertical temperature gradient (ΔT), while a small $\Delta \delta^{18}O_{sw}$ gradient indicates the presence of a deeper thermocline with relatively weak ΔT (Ravelo and Shackleton, 1995; Steinke et al., 2010; Steph et al., 2009). A sediment trap study

conducted in a transect in the Bay of Bengal (Fig. 1) show that the abundance of mixed layer dwelling planktonic foraminifera *G. sacculifer* is not biased towards a particular season (Guptha et al., 1997). This is also the case with the thermocline dwelling *N. dutertrei*, which is present throughout the year with a minor peak in abundance during the initiation of the summer monsoon (Cullen, 1981; Guptha et al., 1997). Thus, seasonal biases are not anticipated in these species and long-term changes in these records represent 'year round' surface and thermocline conditions. We assume the living depth of the two species likely remained similar to modern day observations although that cannot always be predicted (Field, 2004; Rohling et al., 2004).

Based on these assumptions, attempts are made to reconstruct thermocline depth changes and ocean salinity stratification over the past ~1 million years. The temporal evolution of ΔT and $\Delta\delta^{18}\text{O}_{\text{sw}}$ is shown in (Fig 2d and h). Spectral analysis of ΔT records indicate significant spectral power (> 80% CI) at 41-kyrs obliquity and ~100 kyrs eccentricity bands and at a non-primary frequency band corresponding to ~158 kyrs cycle (not shown here). However better coherency between ΔT and ETP is only achieved over the precession band. Phase relationships between ΔT time series and ETP over the precession band indicate that significant shoaling of thermocline occurs ~7 and ~3 kyrs behind NH insolation and maximum sensible heating (Ice volume minima) respectively. Phase differences between thermocline depth changes and summer monsoon precipitation are virtually indistinguishable and indicate that a stronger summer monsoon forcing, rather than direct NH insolation control the depth of the thermocline. Thus, shoaling/deepening of the thermocline primarily correspond to increased/decreased summer monsoon precipitation via increased/decreased subduction of warmer waters, which is similarly reflected in the modern climatology. However, it should also be noted that precession related variance only accounts for ~20% of the total variance in ΔT and weaker cross-spectral coherence of ΔT with orbital obliquity and eccentricity suggest that forcing mechanisms driving thermocline depth changes are strongly non-linear. On the other hand, $\Delta\delta^{18}\text{O}_{\text{sw}}$ time series show significant peaks (> 80%

CI) corresponding to the ~ 100 kyrs eccentricity and precession cycles and weaker spectral power at obliquity cycles ($< 80\%$ CI). The $\Delta\delta^{18}\text{O}_{\text{sw}}$ time series also shows distinct spectral peaks between ~ 170 - 190 kyrs, which likely represent the heterodyne frequencies of the primarily orbital periods and are also evident in $\delta^{18}\text{O}_{\text{ML}}$ and $\delta^{18}\text{O}_{\text{TL}}$ records and suggests a combined precession, obliquity and eccentricity related forcing. Weak coherence between the $\Delta\delta^{18}\text{O}_{\text{sw}}$ time series and ETP at all frequency bands, however, suggests a more complicated relationship between monsoon precipitation and upper ocean stratification. Maximum stratification appears to lag obliquity maxima by ~ 3 kyrs ($25^\circ/360^\circ * 41$ kyrs) although the $\Delta\delta^{18}\text{O}_{\text{sw}}$ time series is not significantly coherent over this frequency band or the precession band.

5. Conclusions

We present the first long term mixed layer and thermocline temperatures ($\text{SST}_{\text{Mg/Ca}}$ and $\text{TT}_{\text{Mg/Ca}}$) and $\delta^{18}\text{O}_{\text{sw}}$ records by using paired Mg/Ca and $\delta^{18}\text{O}$ measurements. Based on $\Delta\delta^{18}\text{O}_{\text{sw}}$ and ΔT gradients, we reconstruct the water column structure and thermocline water depth changes in the Andaman Sea during the late Quaternary to evaluate the coupling between mixed layer and thermocline processes on orbital time scales. Both $\delta^{18}\text{O}_{\text{MW}}$ and $\delta^{18}\text{O}_{\text{TW}}$ document a mean lag of ~ 9 kyrs with respect to maximum NH insolation (P min) in the precession band similar to published phases of wind-based monsoon proxy records from the Arabian Sea (e.g. Caley et al., 2011, Clemens et al., 2008) and demonstrates the prevalence of precession driven strong monsoonal forcing to depth. Over the same frequency band, significant shoaling of the thermocline also occurs ~ 9 kyrs behind NH insolation and in-phase with maximum summer monsoon precipitation. However, much of the variability in $\delta^{18}\text{O}_{\text{ML}}$ and $\delta^{18}\text{O}_{\text{TL}}$ records is contained at frequency bands such as the 41 kyrs obliquity and quasi eccentricity cycles between 90-120 kyrs and at heterodyne frequencies of the primary orbital periods (e.g. ~ 170 - 190 kyrs, and at ~ 52 kyrs). The phase relationship between $\delta^{18}\text{O}_{\text{MW}}$ and $\delta^{18}\text{O}_{\text{TW}}$, and ETP over the obliquity band is sharply in contrast with precession timing where both $\delta^{18}\text{O}_{\text{MW}}$ and $\delta^{18}\text{O}_{\text{TW}}$

lead/lag maximum latent heat export and NH insolation respectively. We propose that a common monsoonal forcing controls freshening of the mixed layer and the thermocline waters and is triggered by poleward moisture flux in response to intensified intra-hemispheric temperature gradient following obliquity minima. Despite the presence of dominant eccentricity related variance in these records, a relatively weaker degree of coherence between all records and orbital eccentricity demonstrates the prevalence of a non-linear eccentricity forcing of the mixed layer and thermocline.

References

- Altabet, M.A., Francois, R., Murray, D.W. and Prell, W.L., 1995. Climate-related variations in denitrification in the Arabian Sea from sediment $15\text{N}/14\text{N}$ ratios. *Nature*, 373(6514): 506-509.
- Altabet, M.A., Murray, D.W. and Prell, W.L., 1999. Climatically linked oscillations in Arabian Sea denitrification over the past 1 my: Implications for the marine N cycle. *Paleoceanography*, 14(6): 732-743.
- Barker, S., Greaves, M. and Elderfield, H., 2003. A study of cleaning procedures used for foraminiferal Mg/Ca paleothermometry. *Geochemistry, Geophysics, Geosystems*, 4(9).
- Bassinot, F., Marzin, C., Braconnot, P., Marti, O., Mathien-Blard, E., Lombard, F. and Bopp, L., 2011. Holocene evolution of summer winds and marine productivity in the tropical Indian Ocean in response to insolation forcing: data-model comparison. *Climate of the Past*, 7(3): 815-829.
- Beaufort, L., Lancelot, Y., Camberlin, P., Cayre, O., Vincent, E., Bassinot, F. and Labeyrie, L., 1997. Insolation cycles as a major control of equatorial Indian Ocean primary production. *Science*, 278(5342): 1451-1454.
- Bemis, E., Spero, H.J., Bijma, J. and Lea, D.W., 1998. Reevaluation of the oxygen isotopic composition of planktonic foraminifera: Experimental results and revised paleotemperature equations. *Paleoceanography*, 13(2): 150-160.
- Berger, A., 1999. Parameters of the Earth's orbit for the last 5 Million years in 1 kyr resolution. PANGAEA, doi, 10.
- Berger, A. and Loutre, M.-F., 1997. Intertropical latitudes and precessional and half-precessional cycles. *Science*, 278(5342): 1476-1478.
- Bolton, C.T., Chang, L., Clemens, S.C., Kodama, K., Ikehara, M., Medina-Elizalde, M., Paterson, G.A., Roberts, A.P., Rohling, E.J. and Yamamoto, Y., 2013. A 500,000 year record of Indian summer monsoon dynamics recorded by eastern equatorial Indian Ocean upper water-column structure. *Quaternary Science Reviews*, 77: 167-180.

- Burns, S.J., Fleitmann, D., Matter, A., Kramers, J. and Al-Subbary, A.A., 2003. Indian Ocean climate and an absolute chronology over Dansgaard/Oeschger events 9 to 13. *Science*, 301(5638): 1365-1367.
- Caley, T., Malaizé, B., Zaragosi, S., Rossignol, L., Bourget, J., Eynaud, F., Martinez, P., Giraudeau, J., Charlier, K. and Ellouz-Zimmermann, N., 2011. New Arabian Sea records help decipher orbital timing of Indo-Asian monsoon. *Earth and Planetary Science Letters*, 308(3): 433-444.
- Chen, D., Busalacchi, A.J. and Rothstein, L.M., 1994. The roles of vertical mixing, solar radiation, and wind stress in a model simulation of the sea surface temperature seasonal cycle in the tropical Pacific Ocean. *Journal of Geophysical Research: Oceans*, 99(C10): 20345-20359.
- Clemens, S., Prell, W., Murray, D., Shimmield, G. and Weedon, G., 1991. Forcing mechanisms of the Indian Ocean monsoon. *Nature*, 353(6346): 720-725.
- Clemens, S.C., Murray, D.W. and Prell, W.L., 1996. Nonstationary phase of the Plio-Pleistocene Asian monsoon. *Science*, 274(5289): 943.
- Clemens, S.C. and Prell, W.L., 1990. Late Pleistocene variability of Arabian Sea summer monsoon winds and continental aridity: Eolian records from the lithogenic component of deep - sea sediments. *Paleoceanography*, 5(2): 109-145.
- Clemens, S.C. and Prell, W.L., 2003. A 350,000 year summer-monsoon multi-proxy stack from the Owen Ridge, Northern Arabian Sea. *Marine Geology*, 201(1): 35-51.
- Cullen, J.L., 1981. Microfossil evidence for changing salinity patterns in the Bay of Bengal over the last 20 000 years. *Palaeogeography, Palaeoclimatology, Palaeoecology*, 35: 315-356.
- Doney, S.C., 2006. Oceanography: Plankton in a warmer world. *Nature*, 444(7120): 695-696.
- Elderfield, H., Vautravers, M. and Cooper, M., 2002. The relationship between shell size and Mg/Ca, Sr/Ca, $\delta^{18}\text{O}$, and $\delta^{13}\text{C}$ of species of planktonic foraminifera. *Geochemistry, Geophysics, Geosystems*, 3(8): 1-13.
- Field, D.B., 2004. Variability in vertical distributions of planktonic foraminifera in the California Current: Relationships to vertical ocean structure. *Paleoceanography*, 19(2).
- Fousiya, T., Parekh, A. and Gnanaseelan, C., 2015. Interannual variability of upper ocean stratification in Bay of Bengal: observational and modeling aspects. *Theoretical and Applied Climatology*: 1-17.
- Gebregiorgis, D., Hathorne, E.C., Sijinkumar, A., Nath, B.N., Nürnberg, D. and Frank, M., 2016. South Asian summer monsoon variability during the last~ 54 kyrs inferred from surface water salinity and river run off proxies. *Quaternary Science Reviews*, 138: 6-15.
- Girishkumar, M., Ravichandran, M. and Han, W., 2013. Observed intraseasonal thermocline variability in the Bay of Bengal. *Journal of Geophysical Research: Oceans*, 118(7): 3336-3349.

- Govil, P. and Naidu, P.D., 2010. Evaporation - precipitation changes in the eastern Arabian Sea for the last 68 ka: Implications on monsoon variability. *Paleoceanography*, 25(1).
- Guptha, M., Curry, W., Ittekkot, V. and Muralinath, A., 1997. Seasonal variation in the flux of planktic Foraminifera; sediment trap results from the Bay of Bengal, northern Indian Ocean. *The Journal of Foraminiferal Research*, 27(1): 5-19.
- Han, W., McCreary, J.P. and Kohler, K.E., 2001. Influence of precipitation minus evaporation and Bay of Bengal rivers on dynamics, thermodynamics, and mixed layer physics in the upper Indian Ocean. *Journal of Geophysical Research: Oceans*, 106(C4): 6895-6916.
- Harper, S., 2000. Thermocline ventilation and pathways of tropical-subtropical water mass exchange. *Tellus A*, 52(3): 330-345.
- Howell, P., 2001. ARAND Time Series and Spectral Analysis Package for the Macintosh, in IGBP PAGES/World Data Center for Paleoclimatology Data Contribution, edited. NOAA/NGDC Paleoclimatology Program, Boulder, CO.
- Kudrass, H., Hofmann, A., Doose, H., Emeis, K. and Erlenkeuser, H., 2001. Modulation and amplification of climatic changes in the Northern Hemisphere by the Indian summer monsoon during the past 80 ky. *Geology*, 29(1): 63-66.
- Laskar, J., Joutel, F. and Boudin, F., 1993. Orbital, precessional, and insolation quantities for the Earth from -20 Myr to + 10 Myr. *Astronomy and Astrophysics*, 270: 522-533.
- Laepple, T. and Huybers, P., 2013. Reconciling discrepancies between Uk37 and Mg/Ca reconstructions of Holocene marine temperature variability. *Earth and Planetary Science Letters*, 375: 418-429.
- Leuschner, D.C. and Sirocko, F., 2003. Orbital insolation forcing of the Indian Monsoon—a motor for global climate changes? *Palaeogeography, Palaeoclimatology, Palaeoecology*, 197(1): 83-95.
- Lisiecki, L.E. and Raymo, M.E., 2005. A Pliocene - Pleistocene stack of 57 globally distributed benthic $\delta^{18}O$ records. *Paleoceanography*, 20(1).
- Mohtadi, M., Prange, M., Oppo, D.W., De Pol-Holz, R., Merkel, U., Zhang, X., Steinke, S. and Luckge, A., 2014. North Atlantic forcing of tropical Indian Ocean climate. *Nature*, 509(7498): 76-80.
- Ni, Y., Foster, G.L., Bailey, T., Elliott, T., Schmidt, D.N., Pearson, P., Haley, B. and Coath, C., 2007. A core top assessment of proxies for the ocean carbonate system in surface - dwelling foraminifers. *Paleoceanography*, 22(3).
- Paillard, D., Labeyrie, L. and Yiou, P., 1996. Macintosh program performs time - series analysis. *Eos, Transactions American Geophysical Union*, 77(39): 379-379.
- Philander, S.G. and Fedorov, A.V., 2003. Role of tropics in changing the response to Milankovich forcing some three million years ago. *Paleoceanography*, 18(2).
- Prakash, S., Mahesh, C. and Mohan Gairola, R., 2012. Observed relationship between surface freshwater flux and salinity in the north Indian Ocean. *Atmospheric and Oceanic Science Letters*, 5(3): 163-169.

- Prell, L., 1984. Monsoonal climate of the Arabian Sea during the late Quaternary: a response to changing solar radiation, Milankovitch and climate: Understanding the response to astronomical forcing, pp. 349.
- Ramesh, K. and Krishnan, R., 2005. Coupling of mixed layer processes and thermocline variations in the Arabian Sea. *Journal of Geophysical Research: Oceans*, 110(C5).
- Rao, R. and Sivakumar, R., 2003. Seasonal variability of sea surface salinity and salt budget of the mixed layer of the north Indian Ocean. *Journal of Geophysical Research: Oceans*, 108(C1).
- Rashid, H., Flower, B., Poore, R. and Quinn, T., 2007. A~ 25ka Indian Ocean monsoon variability record from the Andaman Sea. *Quaternary Science Reviews*, 26(19): 2586-2597.
- Ravelo, A. and Shackleton, N., 1995. Evolution of surface water circulation in the east equatorial Pacific over the past 2.0 Ma: isotopic measurements from ODP Site 851, *Proceeding of the Ocean Drilling Program, Scientific Results*, pp. 50.
- Reichert, G.-J., Lourens, L. and Zachariasse, W., 1998. Temporal variability in the northern Arabian Sea Oxygen Minimum Zone (OMZ) during the last 225,000 years. *Paleoceanography*, 13(6): 607-621.
- Rohling, E., Foster, G.L., Grant, K., Marino, G., Roberts, A., Tamisiea, M.E. and Williams, F., 2014. Sea-level and deep-sea-temperature variability over the past 5.3 million years. *Nature*, 508(7497): 477-482.
- Rohling, E., Sprovieri, M., Cane, T., Casford, J., Cooke, S., Bouloubassi, I., Emeis, K., Schiebel, R., Rogerson, M. and Hayes, A., 2004. Reconstructing past planktic foraminiferal habitats using stable isotope data: a case history for Mediterranean sapropel S5. *Marine Micropaleontology*, 50(1): 89-123.
- Schulz, H., von Rad, U. and Erlenkeuser, H., 1998. Correlation between Arabian Sea and Greenland climate oscillations of the past 110,000 years. *Nature*, 393(6680): 54-57.
- Schulz, M. and Mudelsee, M., 2002. REDFIT: estimating red-noise spectra directly from unevenly spaced paleoclimatic time series. *Computers & Geosciences*, 28(3): 421-426.
- Seo, H., Xie, S.-P., Murtugudde, R., Jochum, M. and Miller, A.J., 2009. Seasonal effects of Indian Ocean freshwater forcing in a regional coupled model*. *Journal of Climate*, 22(24): 6577-6596.
- Steinke, S., Mohtadi, M., Groeneveld, J., Lin, L.C., Löwemark, L., Chen, M.T. and Rendle - Bühring, R., 2010. Reconstructing the southern South China Sea upper water column structure since the Last Glacial Maximum: Implications for the East Asian winter monsoon development. *Paleoceanography*, 25(2).
- Steph, S., Regenberg, M., Tiedemann, R., Mulitza, S. and Nürnberg, D., 2009. Stable isotopes of planktonic foraminifera from tropical Atlantic/Caribbean core-tops: Implications for reconstructing upper ocean stratification. *Marine Micropaleontology*, 71(1): 1-19.
- Thirumalai, K., Partin, J.W., Jackson, C.S. and Quinn, T.M., 2013. Statistical constraints on El Niño Southern Oscillation reconstructions using individual foraminifera: A sensitivity analysis. *Paleoceanography*, 28(3): 401-412.

- Uz, B.M., Yoder, J.A. and Osychny, V., 2001. Pumping of nutrients to ocean surface waters by the action of propagating planetary waves. *Nature*, 409(6820): 597-600.
- Yu, L., 2003. Variability of the depth of the 20 C isotherm along 6 N in the Bay of Bengal: Its response to remote and local forcing and its relation to satellite SSH variability. *Deep Sea Research Part II: Topical Studies in Oceanography*, 50(12): 2285-2304.
- Ziegler, M., Lourens, L.J., Tuenter, E., Hilgen, F., Reichert, G.J. and Weber, N., 2010. Precession phasing offset between Indian summer monsoon and Arabian Sea productivity linked to changes in Atlantic overturning circulation. *Paleoceanography*, 25(3).

Chapter IV

South Asian summer monsoon variability during the last ~54 kyrs inferred from surface water salinity and river runoff proxies

D. Gebregiorgis¹, E.C. Hathorne¹, A.V. SijinKumar², B. Nagender Nath³, D. Nürnberg¹, and M. Frank¹

¹GEOMAR Helmholtz Centre for Ocean Research Kiel, Wischhofstraße 1-3, 24148 Kiel, Germany

²Govt. College Kasaragod, Vidyannagar P.O, Kasaragod Dist., Kasaragod 671123, Kerala, India

³CSIR-National Institute of Oceanography, Dona Paula, Goa 403004, India

Abstract*

The past variability of the South Asian Monsoon is mostly known from records of wind strength over the Arabian Sea while high-resolution paleorecords from regions of strong monsoon precipitation are still lacking. Here, we present records of past monsoon variability obtained from sediment core SK 168/GC-1, which was collected at the Alcock Seamount complex in the Andaman Sea. We utilize the ecological habitats of different planktic foraminiferal species to reconstruct freshwater-induced stratification based on paired Mg/Ca and $\delta^{18}\text{O}$ analyses and to estimate seawater $\delta^{18}\text{O}$ ($\delta^{18}\text{O}_{\text{sw}}$). The difference between surface and thermocline temperatures (ΔT) and $\delta^{18}\text{O}_{\text{sw}}$ ($\Delta\delta^{18}\text{O}_{\text{sw}}$) is used to investigate changes in upper ocean stratification. Additionally, Ba/Ca in *G. sacculifer* tests is used as a direct proxy for riverine runoff and sea surface salinity (SSS) changes related to monsoon precipitation on land. Our $\Delta\delta^{18}\text{O}_{\text{sw}}$ time series reveals that upper ocean salinity stratification did not change significantly throughout the last glacial suggesting little influence of NH insolation changes. The strongest increase in temperature gradients between the mixed layer and the thermocline is recorded for the mid-Holocene and indicate the presence of a significantly shallower thermocline. In line with previous work, the $\delta^{18}\text{O}_{\text{sw}}$ and Ba/Ca records demonstrate that monsoon climate during the

* Published in Quaternary Science Reviews 138: 6–15,
Doi: 10.1016/j.quascirev.2016.02.012

LGM was characterized by a significantly weaker southwest monsoon circulation and strongly reduced runoff. Based on our data the South Asian Summer Monsoon (SAM) over the Irrawaddy strengthened gradually after the LGM beginning at ~18 ka. This is some 3 kyr before an increase of the Ba/Ca record from the Arabian Sea and indicates that South Asian Monsoon climate dynamics are more complex than the simple N-S displacement of the ITCZ as generally described for other regions. Minimum $\delta^{18}\text{O}_{\text{sw}}$ values recorded during the mid-Holocene are in phase with Ba/Ca marking a stronger monsoon precipitation, which is consistent with model simulations.

1. Introduction

The South Asian Summer Monsoon (SAM) is a dominant feature of the global monsoon circulation that directly affects the livelihood of over a billion people residing in the region. The SAM is part of the large scale Asian monsoon system and is primarily driven by seasonal changes in land-sea thermal contrast and the annual cycle of the angle of the solar zenith (Meehl, 1994; Trenberth et al., 2000; Wang and Ding, 2008 and Webster et al., 1998). The onset of the SAM during May and June is concurrent with the reversal of meridional temperature gradients in the upper troposphere over the Tibetan Plateau and regions to the south (Li and Yanai, 1996; Meehl, 1994; Wu and Zhang, 1998; Yanai et al., 1992). This reversal is the result of differential seasonal heating of the continent and surrounding oceans, which generates a strong pressure gradient leading to large-scale shifts in the position of the Intertropical Convergence Zone (ITCZ) and the initiation of the low level cross equatorial southwest monsoon wind circulation. Consequently, a landward tropospheric cyclonic flow coupled with a persistent deep atmospheric convection causes convergence of moisture fluxes on the Indian subcontinent (Chen, 2003; Lau et al., 2000; Randel and Park, 2006), with the Bay of Bengal/Andaman Sea and surrounding catchments being major moisture sinks (Yihui et al., 2004).

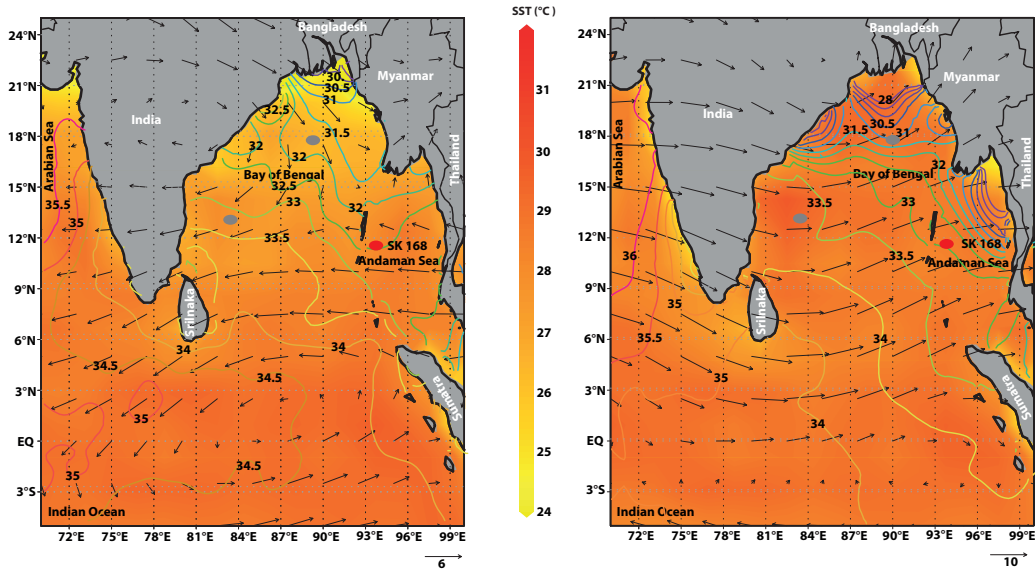


Figure 1. Winter (left) and summer (right) sea surface temperature distribution in the Indian Ocean and eastern Arabian Sea and the location of the sediment core studied (black dot). Winter and summer SST ranges are shown in color gradient. Contour lines represent annual sea surface salinities (SSS) in psu (Levitus et al., 2010). Black arrows indicate the atmospheric surface circulation pattern. Reference arrow given in m/s^{-1} .

The SAM has exhibited pronounced variability over a wide range of time scales. The roles of the El Niño Southern Oscillation (ENSO) (Pant and Parthasarathy, 1981; Rasmusson and Carpenter, 1983; Webster and Yang, 1992) and Eurasian snow cover (Dickson, 1984; Hahn and Shukla, 1976; Kumar et al., 1999) on the interannual fluctuations of the SAM have been widely documented. Other studies have highlighted the combined effects of changes in the North Atlantic Oscillation (NAO) and in the Southern Oscillation (SO) on seasonal monsoon patterns (Kakade and Dugam, 2000; Viswambharan and Mohanakumar, 2014). Decadal to centennial scale variations in monsoon precipitation have been in phase with temperature fluctuations in northern high latitudes (Fleitmann et al., 2003). Monsoonal changes on millennial to longer time-scales were principally driven by orbitally-induced changes in solar insolation prompting shifts in the mean position of the ITCZ (Fleitmann et al., 2007; Overpeck et al., 1996; Sirocko et al., 1993; Wang et al., 2005).

The past variability of the SAM has mostly been inferred from records of wind strength and the associated intensity of upwelling in the Arabian Sea (Caley et al., 2011; Clemens et al., 1991; Clemens et al., 1996; Clemens et al., 2008; Schulz et al.,

1998; Ziegler et al., 2010). Several studies from the Arabian Sea have documented that the intensity of the SAM was characterized by millennial scale variations superimposed on long-term glacial-interglacial variability (Overpeck et al., 1996; Schulz et al., 1998; von Rad et al., 1999). Other studies, mainly based on upwelling indices such as foraminifera (% *Globigerina bulloides*) and changes of eolian inputs, have argued that the strength and timing of the monsoon winds are primarily linked to the obliquity and precession of the Earth's orbit rather than long term glacial-interglacial variability (Clemens et al., 1991; Clemens et al., 1996; Clemens et al., 2010; Clemens et al., 2008). However, interpretations relying on the wind based proxies have been challenged as monsoonal precipitation over the subcontinent depends more on the moisture content of the interhemispheric monsoon winds and their transport pathways rather than wind strength (Ruddiman, 1997; Sarkar et al., 2000). It is also clear that the application of the occurrence of microfossils as upwelling indicators is sensitive to many environmental factors, some of which are possibly unrelated to the monsoon (Clemens and Prell, 2003 and Ziegler et al., 2010). As a result, considerable discrepancies with regard to the past variability of the SAM recorded by proxies from different regions remain unresolved. High-resolution proxy records from regions with strong monsoonal rainfall influence are therefore required to examine past changes of SAM intensity. In this regard, the Andaman Sea and the Bay of Bengal, where both monsoonal precipitation over the ocean and the continental runoff can be assessed, offer a unique prospect for understanding the past variability of the SAM. Despite this, relatively few studies have attempted to reconstruct SAM variability using proxy records of salinity in the Bay of Bengal (Govil and Divakar Naidu, 2011; Kudrass et al., 2001; Rashid et al., 2011) and in the Andaman Sea (Rashid et al., 2007). Kudrass et al. (2001) published a record of the SAM variability and sea surface salinity changes for the last 80 kyrs by combining $\delta^{18}\text{O}$ signatures of *Globigerinoides ruber* (*G. ruber*) and alkenone based temperature estimates. Similarly, paired $\delta^{18}\text{O}$ and Mg/Ca signals of planktonic foraminifera species were used to reconstruct seawater $\delta^{18}\text{O}$ ($\delta^{18}\text{O}_{\text{sw}}$) and to infer sea surface salinity (SSS) trends during the Last Glacial Maximum (LGM) and the deglaciation in the Bay of Bengal (Govil and Divakar Naidu, 2011; Rashid et al.,

2011) and the Andaman Sea (Rashid et al., 2007). More recently, however, a growing number of studies have used Ba/Ca ratios of planktic foraminiferal tests to infer past river water discharge and estimate SSS changes (e.g. Weldeab et al., 2007; Weldeab et al., 2014). This is based on the fact that riverine runoff is enriched in dissolved Ba relative to sea water (Bahr et al., 2013; Hall and Chan, 2004; Schmidt and Lynch-Stieglitz, 2011) and Ba incorporation into foraminiferal shells occurs in direct proportion to the corresponding seawater Ba concentration (Hönisch et al., 2011; Lea and Spero, 1992; Lea and Spero, 1994).

Here, we utilise the depth habitat preferences of different foraminifera species to investigate the freshwater-induced stratification in the Andaman Sea with paired Mg/Ca and $\delta^{18}\text{O}$ measurements on *Globigerinoides sacculifer* (*G. sacculifer*) and *Neogloboquadrina dutertrei* (*N. dutertrei*). These recorders of mixed layer and thermocline temperature ($\text{SST}_{\text{Mg/Ca}}$ and $\text{TT}_{\text{Mg/Ca}}$) and $\delta^{18}\text{O}$, respectively, are used to construct $\delta^{18}\text{O}_{\text{sw}}$ records, which approximate salinity at the respective water depth. The difference in surface and thermocline temperatures (ΔT) and $\delta^{18}\text{O}_{\text{sw}}$ ($\Delta\delta^{18}\text{O}_{\text{sw}}$) are used to infer changes in upper ocean stratification. Ba/Ca ratios of *G. sacculifer* tests are generated to assess changes in riverine runoff and provide the first such record for the Andaman Sea spanning the last ~54 kyr.

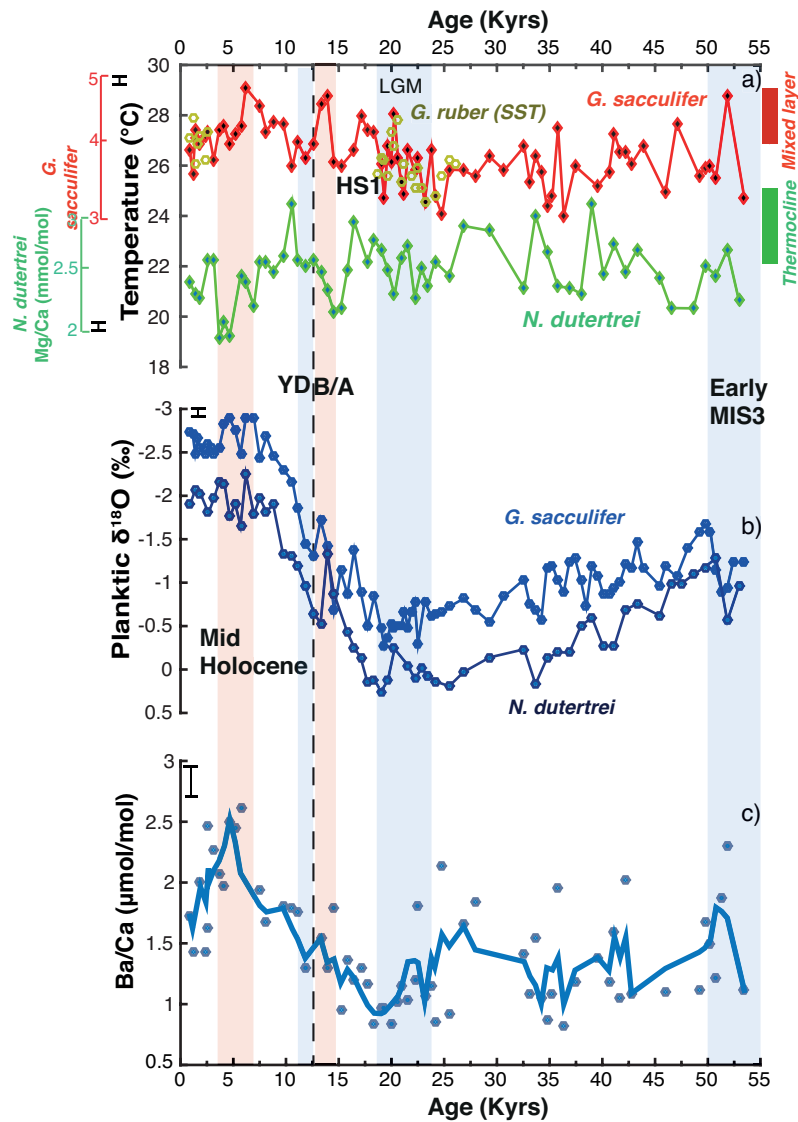


Figure 2.a) Mg/Ca-based temperature estimates for the thermocline dwelling *N. dutertrei* (green) and the mixed layer species *G. sacculifer* (red) over the last 55 kyrs. *G. ruber* SST_{Mg/Ca} estimates are given for LGM and late-Holocene time periods (yellow-green). The vertical bars show the range of annual SST (red) and thermocline temperatures (green) in the Andaman Sea (Antonov et al., 2010). 2 σ -error bars are based on repeated analysis (n=12) of the ECRM 752-1 standard (Greaves et al., 2008). b) Oxygen isotope ratios of foraminifera *G. sacculifer* (blue) and *N. dutertrei* (dark blue). c) Ba/Ca ratios of *G. sacculifer*. Solid line represent the 3-pt moving average. Younger Dryas (YD), Bølling-Allerød (B/A), Heinrich Stadial 1 (HS1) and last glacial maximum (LGM) are shaded based on stratigraphic boundaries defined by NGRIP (Andersen et al., 2006; Rasmussen et al., 2006). Early-MIS 3 shaded based on stratigraphic boundaries defined here (Liu et al., 2010).

2. Materials and methods

2.1. Oceanographic setting

The Andaman Sea is a marginal sea located in the northeastern corner of the Indian Ocean between the Malay Peninsula and the Andaman and Nicobar Islands. With a maximum water depth of 4200 m, it is connected with the Bay of Bengal and the Australasian Mediterranean Sea through several channels between the chain of the Andaman Islands and the Malacca Strait, respectively. The distribution of temperature and salinity with depth in the Andaman Sea is similar to that of the Bay of Bengal down to a depth of about 1000 m (Sarma and Narvekar, 2001). The Andaman Sea experiences strong seasonal variations in salinity due to abundant freshwater discharge from the Irrawaddy and Salween Rivers during the summer monsoon (Chapman et al., 2015). Distinct differences in deep sea temperature and salinity structure in the Andaman Sea are caused by the enclosed nature of the Andaman Basin and presence of several sills between the islands inhibiting deep water exchange between these two regions (Ramesh Babu and Sastry, 1976; Rao and Jayaraman, 1968; Sengupta et al., 1981). The Ganges–Meghna–Brahmaputra and Irrawaddy–Salween river systems on average discharge 1350 and 1000 km³ of freshwater annually to the Bay of Bengal and the Andaman Sea, respectively (Sengupta et al., 2006) thereby influencing mixed layer depth and salinity. In the Irrawaddy catchment, monsoon rains increase discharge from an average of ~12 km³/month during the winter and up to ~89 km³/month in the summer (Chapman et al., 2015). In the Andaman Sea, mean summer surface water salinity ranges between 28 and 33‰ (Zweng et al., 2013). The average near-surface temperature is 29 °C and is nearly homogenous in the mixed layer down to a depth of 50 m, below which stratification of the water masses restricts vertical mixing (Sarma and Narvekar, 2001; Uddin et al., 2014). The top of the thermocline varies seasonally between ~40 and ~60 m but is generally situated at a depth of ~50 m (Riser et al., 2008).

2.2. Core location and sample preparation

Sediment core SK 168/GC-1 (Lat. 11°42.463' N; Long. 94°29.606' E, water depth: 2064 m, core length: 4.20 m) was collected during the 168th cruise of ORV Sagar Kanya from the Alcock Seamount Complex in the Andaman Sea. A late Quaternary record of pteropod abundance and the $\delta^{18}\text{O}$ record from the surface dwelling planktic foraminiferal species *G. ruber* has previously been published (Sijinkumar et al., 2010). The age model from (Sijinkumar et al., 2010) was constructed with 5 Accelerator Mass Spectrometer (AMS) ^{14}C dates of planktic foraminiferal tests (mixed *G. ruber* and *G. sacculifer*). The AMS ^{14}C ages were uniformly corrected for a 460 year reservoir age following Butzin et al. (2005). The age model was further refined by correlating the oxygen isotope values of *G. ruber* with the stacked reference oxygen isotope curve of Martinson et al. (1987) and constant sedimentation rates were assumed between age tie points. The average sedimentation rate for the core is 7.79 cm/kyr with variations between ~3.65 and ~10.20 cm/kyr during the MIS3/MIS2 and the Pleistocene-Holocene transitions respectively (Sijinkumar et al., 2010). This provides an average temporal resolution of ~700 yrs for the upper 2 m of the core spanning the Holocene to the MIS3/MIS2 transition. Below this section the temporal resolution is ~1.3 kyrs. The accuracy of this age model has been confirmed by comparison to the recently published benthic foraminifera $\delta^{18}\text{O}$ data for ODP 758 (Bolton et al., 2013) (Supplement Fig 1). This is also in line with a new benthic foraminifera $\delta^{18}\text{O}$ data from core SK 168/GC-1 discussed in detail in a separate publication (Sijinkumar et al., 2016). Thus, the published age model for the core is employed without any modifications.

Foraminifera samples from the core section were collected, and analyzed every 5 cm down to 2 m and every 10 cm for the remaining 2.2 m of the core. The abundance of foraminiferal specimens was limited in these clay rich sediments, particularly for *G. sacculifer*, and 15–20 specimens available per sample and 10 specimens per sample in some 4 samples were considered enough to obtain a representative geochemical signature, although ideally this would be more (Laepplé and Huybers,

2013). For trace element analysis a constant and narrow size fraction of foraminifera is desired to avoid possible size dependent biases (e.g. Elderfield et al., 2002; Ni et al., 2007). Specimens of *G. sacculifer* and *N. dutertrei* were selected from the 315–400 μm size fraction and gently cracked between glass slides before being mixed and split for trace metal and stable isotopic analyses. For trace metal analysis the cracked sample was cleaned following a full reductive cleaning method (Boyle, 1981). Samples were initially repeatedly rinsed with sonication in distilled water (18.2 m Ω) and then ethanol (analytical grade) to ensure clay removal. Samples were then inspected under a binocular microscope to ensure they were free of obvious sediment contamination. Subsequently, samples were treated with ammonium citrate/hydrazine solution at 82 °C for 30 mins and sample racks were placed in the ultrasonic bath for 1 min every 10 mins to maintain contact between reagents and sample. Samples were rinsed multiple times with distilled water before being transferred to new acid leached vials. Samples were then treated with oxidizing NaOH/H₂O₂ solution at 82 °C for 20 mins to remove organic matter. After three more rinses with distilled water, a weak acid leach with 100 μL 0.001 M HNO₃ was applied and followed by two rinses with distilled water. Samples were dissolved in 0.075 M nitric acid (HNO₃) (500 μL) assisted by sonication for 25 mins. Finally samples were centrifuged for 4 mins at 13,400 rpm and 400 μL of supernatant was transferred to new acid leached vials and diluted for measurement.

2.3. Foraminiferal isotopic and elemental analysis

The $\delta^{18}\text{O}$ measurements were performed using a MAT 253 mass spectrometer coupled with a Kiel IV Carbonate device (Thermo Scientific). Results were referenced to the NBS19 standard and are given on the VPDB scale. The estimated analytical error for $\delta^{18}\text{O}$ measurements was 0.05‰ (1 σ) based on repeated measurements of an in house standard (SHK Bremen). Seawater $\delta^{18}\text{O}$ ($\delta^{18}\text{O}_{\text{sw}}$) was calculated using the calibration equation of Bemis et al. (1998) and was corrected for global ice volume following Waelbroeck et al. (2002). $\delta^{18}\text{O}_{\text{sw}}$ values were converted to Vienna Standard Mean Ocean Water (VSMOW) by adding 0.27‰ to

$\delta^{18}\text{O}_{\text{sw}}$. Uncertainties in $\delta^{18}\text{O}_{\text{sw}}$ are estimated by propagating the errors from the *G. sacculifer* and *N. dutertrei* $\delta^{18}\text{O}$ and Mg/Ca measurements (Mohtadi et al., 2014) and are on average 0.3‰.

Element/Ca ratios were measured with an Agilent 7500cs ICP-MS. In a first step Ca concentrations were measured using Sc as an internal standard and these data were used to dilute the samples to 10 ppm Ca for elemental analysis. Element/Ca ratios were calculated using intensity ratios (Rosenthal et al., 1999) that were calibrated using standards produced gravimetrically from single element solutions. The average Mg/Ca of carbonate reference material ECRM 752-1 (Greaves et al., 2008) measured during the course of the study was 3.83 ± 0.06 mmol/mol ($n = 12$, 1σ). Uncertainties in SST reconstructions are estimated by propagating the errors introduced by Mg/Ca measurements and the Mg/Ca-Temperature calibration equation and are on average 1 °C. $\text{SST}_{\text{Mg/Ca}}$ and $\text{TT}_{\text{Mg/Ca}}$ estimated from Mg/Ca data for *G. sacculifer* (*G. ruber*) and *N. dutertrei* are based on a species specific calibration equation obtained from North Atlantic (Anand et al., 2003). SSS was estimated from Ba/Ca ratios of *G. sacculifer* using a function based on sea water Ba (Ba_{sw}) concentrations and salinity data obtained from the Bay of Bengal (Singh et al., 2013) and a Ba/Ca_{sw}-foraminiferal calcite partition coefficient (D_{Ba}) of 0.19 (Lea and Boyle, 1991) (See supplement Fig 2).

Clay minerals are major sources of contamination for Mg/Ca analysis of foraminifera shells (Barker et al., 2003). To exclude such biases, aluminum (Al) and iron (Fe) concentrations were carefully monitored to identify the presence of clay contaminants. For the data set presented here there is no systematic relationship between Al/Ca (or Fe/Ca) and Mg/Ca ratios indicating the absence of clay contamination. However, Al/Ca values in 8 samples were higher than in all other samples and these data were excluded from further interpretation. In a similar manner, Ba/Ca values were compared with La/Ca values to check for barite contamination based on the idea that La is removed from sea water by barite formation (Garcia-Solsona et al., 2014). Ba/Ca ratios do not show a linear

relationship with La/Ca ratios. However, we assume that significantly elevated Ba/Ca values ($>3 \mu\text{mol/mol}$) in 9 samples are the result of barite contamination and were excluded from further interpretation.

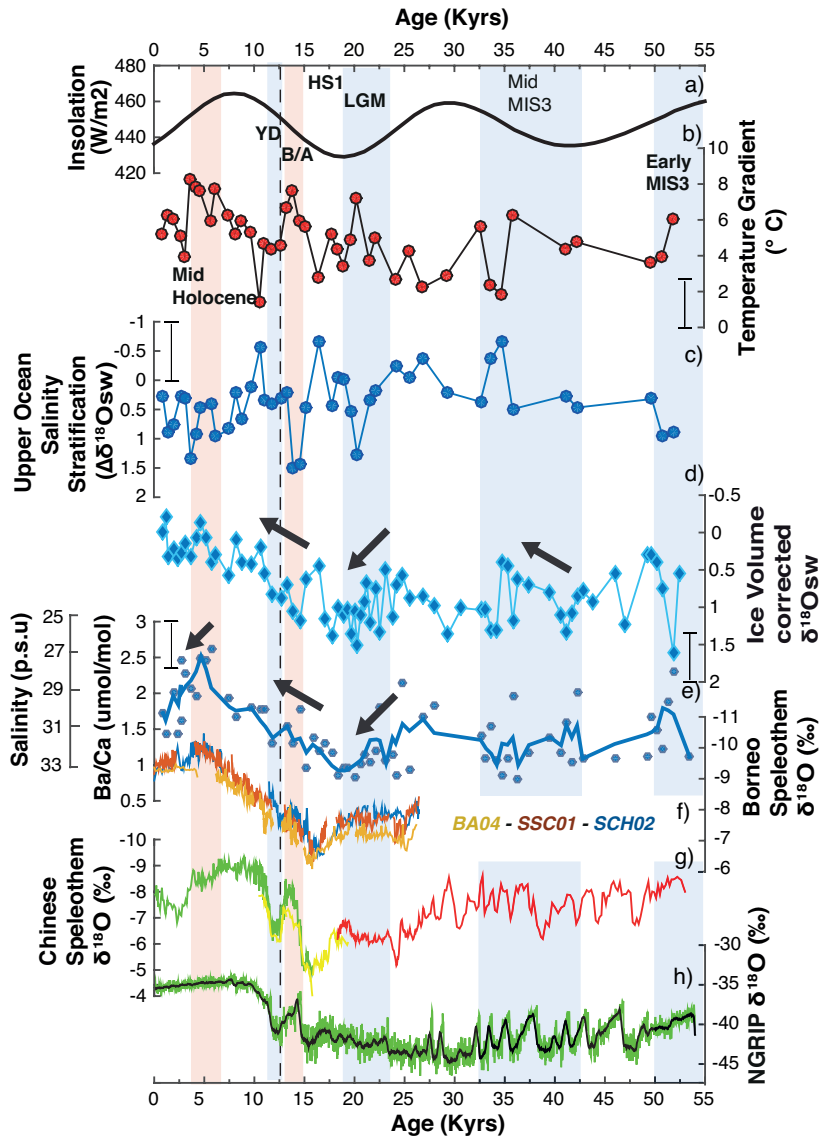


Figure 3. SK 168 records in comparison with high resolution east Asian and south-west monsoon proxies and Greenland ice core data: a) Insolation (August) (W/m^2) at 20°N (Laskar et al., 2004); b) Mixed layer and thermocline temperature gradient based on temperatures estimated from Mg/Ca ratios of *G. sacculifer* and of *N. dutertrei*. c) $\Delta\delta^{18}\text{O}$ record with maximum stratification plotted up. d) $\delta^{18}\text{O}_{\text{sw}}$ calculated using the temperature calibration equation for all species (Anand et al., 2003) and corrected for global ice volume using (Waelbroeck et al., 2002); e) Ba/Ca ratios derived from mixed layer species *G. sacculifer* and the estimated salinity estimate (see Supplement). f) High resolution oxygen isotopic data of stalagmites from Dongge cave (green), Hulu (PD) (yellow) and Hulu (MSD) (red) caves data plotted according to their independent timescales (Wang et al., 2001; Yuan et al., 2004); g) Greenland ice core $\delta^{18}\text{O}$ chronology (NGRIP) (Svensson et al., 2008). Solid line denotes 20-pts moving average.

3. Results

3.1. Sea surface temperatures and $\delta^{18}\text{O}$

Mg/Ca based estimates of SST ($\text{SST}_{\text{Mg/Ca}}$) and thermocline temperatures ($\text{TT}_{\text{Mg/Ca}}$) are shown in Fig. 2a. The SSTs range from ~29 °C to 24 °C whereas the thermocline temperatures range from 24.5 °C to 19 °C. Coldest SSTs are observed during MIS3 centered at 33–37 kyr and during the last glacial maximum (LGM). The average LGM SST of 25.8 °C in the Andaman Sea is similar to the late Holocene (defined here as the average of the top 15 cm of the core representing the last ~2.7 kyrs) within the margin of error. Thermocline temperatures also do not show a distinct trend during these two time intervals. Additional *G. ruber* measurements obtained from late Holocene and LGM samples reveal similar SST trends (Fig. 2a) and indicate no significant difference between the records of the two species (paired-samples *t*-test, $p < 0.01$). Although it is difficult to distinguish such small changes from the inherent noise in the records, the deglacial warming pattern appears to have two warming steps from the onset of the last glacial termination during Heinrich Stadial 1 (HS1), (~18–15 kyrs) and to the transition from Bolling/Allerod (B/A) (~15–12.9 kyrs) and Younger Dryas (YD) (~12.9–11.7 kyrs) (Fig. 2a). The start of deglacial warming in the Andaman Sea is hard to pinpoint but peak mixed layer temperatures ~28 °C are reached at the onset of the B/A. SST values gradually cooled to ~26 °C during the Younger Dryas (YD). After the YD values increase to a mid-Holocene maximum of ~29 °C before decreasing and remaining relatively constant at ~26 °C through the late Holocene.

G. sacculifer and *N. dutertrei* $\delta^{18}\text{O}$ values generally show synchronous patterns with lighter values during the mid-Holocene (~7–4 kyrs) and MIS3 (~27–54 kyrs) compared to the LGM (~23–19 kyrs) (Fig. 2b). *G. sacculifer* $\delta^{18}\text{O}$ values during MIS3 ranged from -1.7 to -0.5‰ and varied synchronously with the $\delta^{18}\text{O}$ values of *N. dutertrei*. Mean $\delta^{18}\text{O}$ values of *G. sacculifer* during the LGM progressively increased from -0.6‰ to -0.2‰ at around ~19 kyrs. The transition from the late glacial is marked by abrupt changes in $\delta^{18}\text{O}$ during the onset of the HS1 and the B/A.

The transition from the B/A to the YD is marked by a 0.5‰ increase in $\delta^{18}\text{O}$ values centered at ~12 kyr. Holocene $\delta^{18}\text{O}$ values gradually decreased and reached -2.9‰ for *G. sacculifer* and show a ~2‰ difference between the late glacial and mid-Holocene values. Late Holocene $\delta^{18}\text{O}$ values remained relatively constant and ranged between -2.5 and -2.7‰.

3.2. Ba/Ca ratios and seawater $\delta^{18}\text{O}$

Ba/Ca and $\delta^{18}\text{O}_{\text{sw}}$ records of Core SK 168 reveal distinct changes in monsoon precipitation above the Irrawaddy catchment during the last ~54 kyr (Fig. 2 and Fig. 3e). Peaks in Ba/Ca and surface *G. sacculifer* $\delta^{18}\text{O}$ ($\delta^{18}\text{O}_{\text{sw}}$) values are observed during the early part of the MIS3 and at the MIS3/2 transition centered at ~50 kyr and ~35 kyr, respectively. Ba/Ca gradually decreased from ~1.7 $\mu\text{mol/mol}$ during the MIS3/2 transition to ~1 $\mu\text{mol/mol}$ during the LGM which is equivalent to an SSS change from ~30 to 33‰. Minimum Ba/Ca values (0.86 $\mu\text{mol/mol}$) were recorded at ~19 ka. The deglacial transition is marked by a relatively abrupt decrease in $\delta^{18}\text{O}_{\text{sw}}$ values during the onset of HS1 and a gradual increase in Ba/Ca and $\delta^{18}\text{O}_{\text{sw}}$ values during the B/A. Ba/Ca values gradually increased from the LGM to the mid-Holocene reaching a maximum of 2.6 $\mu\text{mol/mol}$ corresponding to a salinity minimum of ~27‰. Peak $\delta^{18}\text{O}_{\text{sw}}$ values during the mid-Holocene centered around ~5 kyr were in phase with Ba/Ca peaks. Ba/Ca values during the late Holocene attained an average value of 1.7 $\mu\text{mol/mol}$ corresponding to an SSS estimate of ~30‰. This is in agreement with modern summer SSS values in this region of the Andaman Sea that range between 28 and 33‰ (Zweng et al., 2013).

3.3. Vertical temperature and $\delta^{18}\text{O}_{\text{sw}}$ ($\Delta\delta^{18}\text{O}_{\text{sw}}$) gradients

Changes in vertical temperature and $\delta^{18}\text{O}_{\text{sw}}$ gradients between the *G. sacculifer* and *N. dutertrei* ($\Delta\delta^{18}\text{O}_{\text{sw}}$) are considered a measure of the density gradient between the mixed layer and thermocline and are interpreted as a proxy for upper ocean stratification. The evolution of the $\Delta\delta^{18}\text{O}_{\text{sw}}$ and the temperature gradient between

the mixed layer and the thermocline are shown in Figs. 3b and c. The difference in measured $\delta^{18}\text{O}_{\text{sw}}$ between the two species ($\Delta\delta^{18}\text{O}_{\text{sw}}$) is on average 0.39‰ and ranges between -0.6 and 1.5‰, although the uncertainties associated with these calculations are $\pm 0.5\%$. The strongest increase in $\Delta\delta^{18}\text{O}_{\text{sw}}$ values is observed during the deglacial transition centered around the B/A. The temperature gradient between the mixed layer and the thermocline ranged between ~ 1.4 and 8.3 °C with large gradients during the deglacial transition, and the mid-Holocene. The temperature gradient during the mid-Holocene was on average ~ 7.5 °C while upper ocean density stratification remained fairly constant.

4. Discussion

4.1. Upper ocean stratification and monsoon intensity during the last glaciation

Given that the effect of global ice volume is cancelled out, the $\Delta\delta^{18}\text{O}_{\text{sw}}$ gradient between mixed layer and thermocline dwelling planktic foraminifera, a proxy for upper ocean stratification, is a function of local changes in $\delta^{18}\text{O}_{\text{sw}}$ of seawater. The application of the $\Delta\delta^{18}\text{O}_{\text{sw}}$ gradient to infer changes in surface water salinity stratification is dependent on the differential depth habitats of the studied foraminiferal species. Mixed layer dweller *G. sacculifer* has been observed to live and calcify within the upper 60 m of the water column (Fairbanks et al., 1982; Fairbanks et al., 1980), while *N. dutertrei* is generally most abundant in the thermocline (60–150 m) (Curry et al., 1983; Fairbanks et al., 1982). A sediment trap study conducted along a N-S transect in the Bay of Bengal (Fig 1) suggests that the abundance of mixed layer dwelling planktic foraminifera *G. sacculifer* does not change significantly with the seasons (Guptha et al., 1997). Thermocline dwelling *N. dutertrei* is also present throughout the year and exhibits a broad peak in abundance during the initiation of the summer monsoon, directly related to the low surface salinities associated with the monsoon (Cullen, 1981; Guptha et al., 1997). Thus, seasonal biases are most likely minimal in these species and observed long-term changes in $\delta^{18}\text{O}_{\text{sw}}$ largely reflect ‘year-round’ surface and thermocline conditions. However,

the assumption that the optimum living depth of a given species in the past has remained similar to modern day observations may not always be the case (Field, 2004; Rohling et al., 2004).

We interpret changes in the upper ocean stratification as a consequence of thermocline depth changes driven by strong wind-induced mixing and monsoon precipitation controlled upper ocean freshening, and vertical heat flux (Fig. 4). Thus, a larger/smaller ΔT gradient implies a shallower/deeper thermocline (Ravelo and Shackleton, 1995; Steinke et al., 2010; Steph et al., 2009), while $\Delta\delta^{18}O_{sw}$ minima indicates enhanced monsoon related salinity stratification. Relatively decreased temperature gradient between the mixed layer and the thermocline is recorded for the mid-MIS 3 (~35 kyrs) and indicate the presence of a deeper thermocline. However, our temperature corrected $\Delta\delta^{18}O_{sw}$ time series reveals that upper ocean salinity stratification did not change significantly when considering the uncertainties.

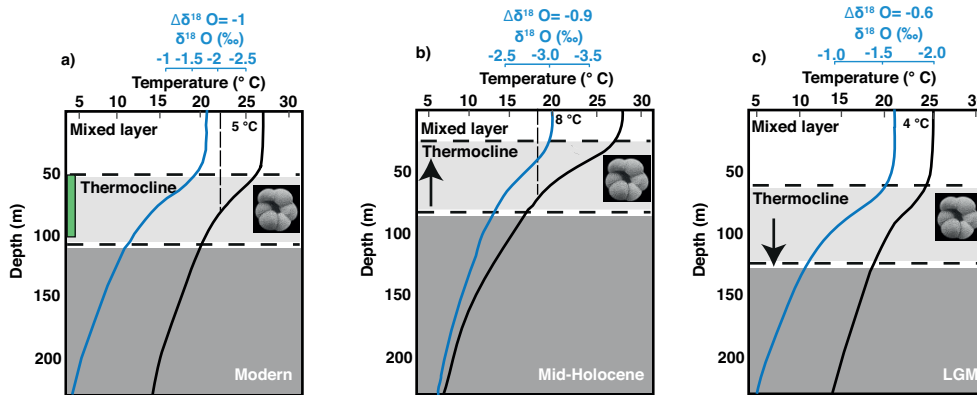


Figure 4. Schematic illustration of changes in upper ocean stratification inferred from sea surface and thermocline temperatures and $\delta^{18}O$ values. a) Modern depth profiles of temperature and $\delta^{18}O_{sw}$ for August from World Ocean Atlas 2013 (Levitus et al., 2013). Modern $\delta^{18}O_{sw}$ values estimated from salinity and temperature data obtained from the Andaman Sea using Anand et al. (2000) and Bemis et al. (1998). Green bar shows depth range of deep chlorophyll maximum (DCM) in the northern Indian Ocean during May-June 1996 (Murty et al., 2000). b) Reconstructed temperature and $\delta^{18}O_{sw}$ profiles for the mid-Holocene and c) the LGM. Mid to late-Holocene and LGM temperature and $\delta^{18}O$ estimates are based on the mixed layer species *G. sacculifer* and the thermocline dwelling *N. dutertrei*. White area = mixed layer; light gray area = thermocline.

The climate in the SAM region has generally been described as cool and dry during the LGM (e.g. Cullen, 1981; Kudrass et al., 2001), which is supported by our higher salinity estimates for the Andaman Sea (~33‰). The physical mechanism often invoked to explain this weak SAM during the LGM is increased snow accumulation on the Tibetan Plateau causing shifts in the mean position of the ITCZ (Kudrass et al., 2001; Overpeck et al., 1996; Sirocko et al., 1996). The northeast winter monsoon circulation likely remained strong during the LGM with prevailing high-pressure cells in the Tibetan plateau (Tibet High). This is in line with lower temperatures reported for the Tibetan Plateau (Shi, 2002) and Himalaya (Mark et al., 2005), which would have weakened the meridional thermal land–sea contrast. Thus part of the weakening in SAM rainfall can be explained by an increased influence of dry continental *air* masses entrained by the winter monsoon. Results from phases 2 and 3 of the Paleoclimate Modeling Inter-comparison Project (PMIP2 and 3) show that SAM precipitation was reduced in all models in the LGM experiments by as much as 1.7 mm/day due to changes in NH ice sheets extent (hence a strengthened Tibetan High) and atmospheric CO₂ concentration conditions (Braconnot et al., 2007). Modern meteorological data also support this interpretation and show that an increase of snow cover on the Tibetan Plateau strengthens the high pressure cell in winter and leads to a weakened Tibetan Low and a weaker summer monsoon in the following year (Fang et al., 1999 and references therein).

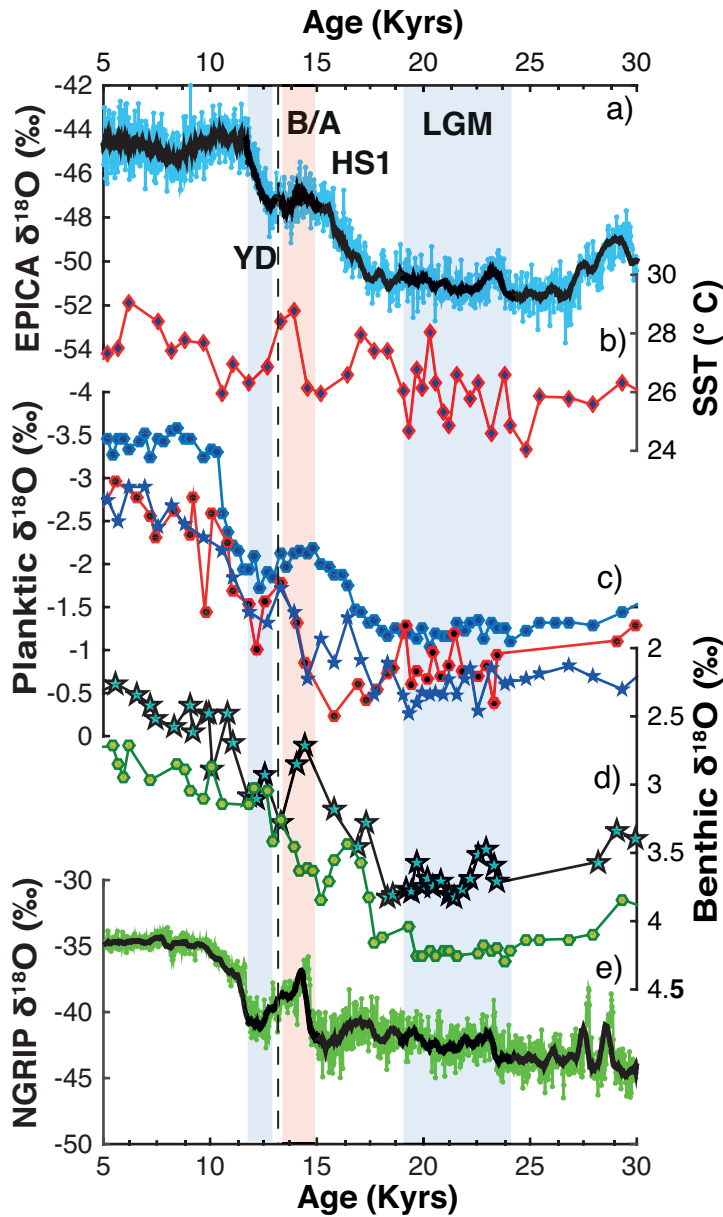


Figure 5. Deglacial SK168 proxy records in relation to changes in interhemispheric temperature and global ice volume. a) EPICA ice core $\delta^{18}\text{O}$ climate record (Barbante et al., 2006). b) $\text{SST}_{\text{Mg/Ca}}$ ($^{\circ}\text{C}$) derived from *G. sacculifer*. c) $\delta^{18}\text{O}$ of *G. ruber* (light blue), *G. sacculifer* (stars) and NGHP 17 *G. sacculifer* records from which the Andaman Sea (red). d) Benthic (*C. wuellerstorfi*/*C. mundulus*) $\delta^{18}\text{O}$ record from NGHP 17 (Ali et al., 2015). e) Greenland ice core $\delta^{18}\text{O}$ record (NGRIP) (Svensson et al., 2008). Solid line denotes 20-pt moving average. Shaded areas are based on stratigraphic boundaries according to (Andersen et al., 2006; Rasmussen et al., 2006).

4.2. The deglacial transition

The last deglaciation was punctuated by periods of Northern Hemisphere warming (B/A) and cooling (HS 1 and YD). Previous studies from the Bay of Bengal and the Arabian Sea indicate synchronous regional changes in deglacial warming and monsoon intensity remotely coupled to Greenland air temperature (Kudrass et al., 2001; Rashid et al., 2007; Schulz et al., 1998). Lighter $\delta^{18}\text{O}$ values in mixed layer dwelling planktic *G. sacculifer* marking the last deglaciation lag the changes of the surface dwelling planktic foraminifera (*G. ruber*) by ~2 kyr (Fig 5). This was also observed at ODP Site 758 in the southern Bay of Bengal (Bolton et al., 2013), and implies the slow propagation of salinity and temperature changes from surface to depth or a seasonal bias in one of the species. Deglacial Ba/Ca and $\delta^{18}\text{O}_{\text{sw}}$ trends are broadly synchronous and indicate a gradual monsoon strengthening with the exception of the HS1. *G. sacculifer* $\delta^{18}\text{O}_{\text{sw}}$ values indicate abrupt mixed layer freshening during HS1 consistent with other studies from the Arabian Sea that reported major intensification of the southwest monsoon around 15.5 ka (e.g. Naqvi and Fairbanks, 1996; Kessarkar et al., 2010) and appears to lead abrupt upper ocean salinity stratification changes recorded for the B/A. This is in contrast to the predominantly weak east Asian monsoon inferred for the Chinese speleothem records during HS1 (e.g. Wang et al., 2001). However, the gradual SAM strengthening observed in river runoff into the Andaman Sea began ~18 kyr, leading Ba/Ca increases in the Arabian Sea around the B/A (Saraswat et al., 2013) by ~2–3 kyr (Fig 6). Together these data demonstrate SAM climate dynamics are more complex than the simple N-S displacement of the ITCZ following insolation changes as described for other regions (e.g. Overpeck et al., 1996). The SAM appears to be strongly influenced by regional scale boundary conditions altering atmospheric convection as evident from Holocene model simulations (PMIP3, Braconnot et al., 2012, Fig. 7a and b) highlighting the importance of obtaining more SST records for this region.

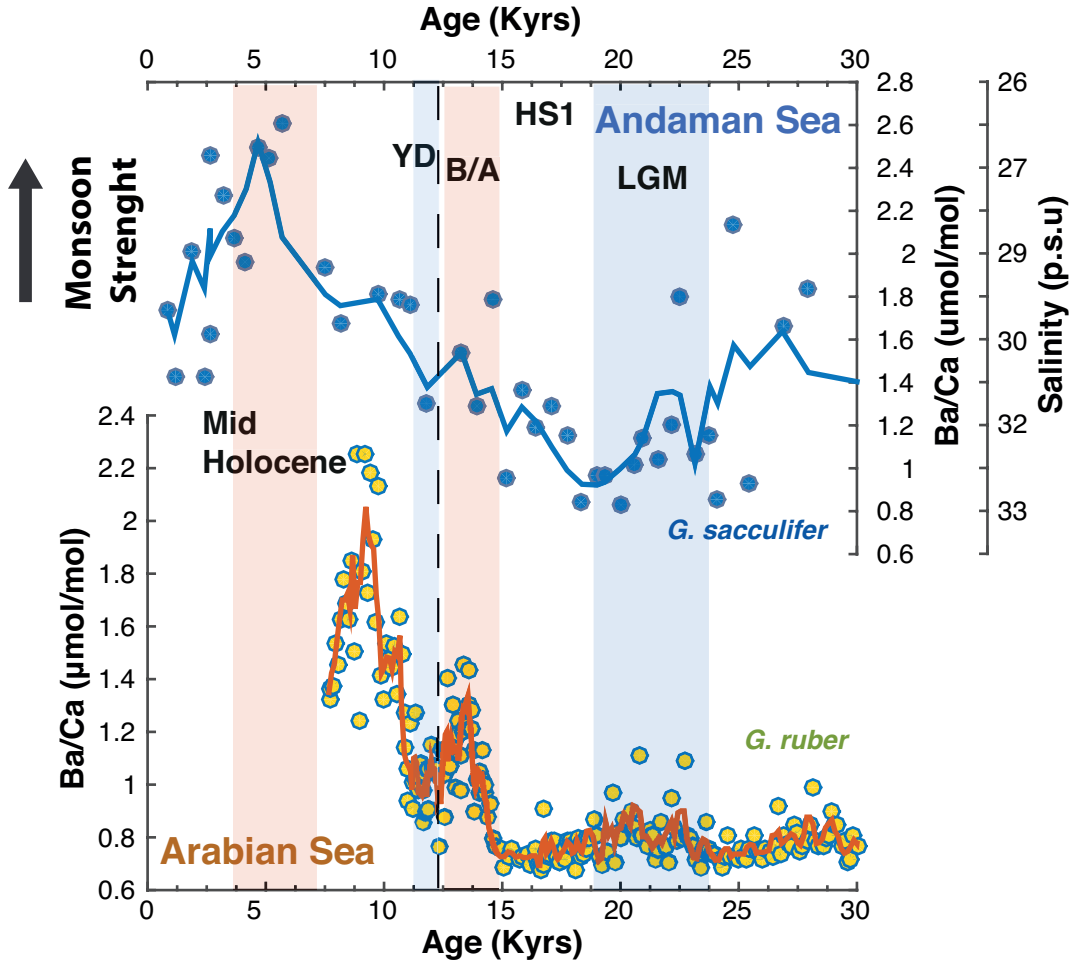


Figure 6. SK 168 Ba/Ca records of *G. sacculifer* in comparison with high resolution Ba/Ca records of *G. ruber* from the Arabian Sea (Saraswat et al., 2013). Solid lines denotes 3-pts running mean.

4.3. The Holocene

Upper ocean stratification changes during the Holocene are marked by a gradual increase in temperature gradient and shoaling of the thermocline from early to mid-Holocene in response to increased heating of the mixed layer. This is indicated by a sharp ΔT increase from $\sim 4^\circ$ to $\sim 8^\circ\text{C}$ from the early to the mid-Holocene while $\Delta\delta^{18}\text{O}_{\text{sw}}$ gradients are marked by increased variability but did not change significantly. In contrast, $\delta^{18}\text{O}_{\text{sw}}$ values and Ba/Ca values indicate a continued strengthening of summer monsoon intensity and maximum Irrawaddy River runoff during the early to mid-Holocene. Minimum $\delta^{18}\text{O}_{\text{sw}}$ values and maximum Ba/Ca

values recorded during the mid-Holocene mark the wettest period in the Andaman Sea of the past ~54 krs. A similar mid Holocene peak wetness was observed in speleothem records from northern Borneo, which has been linked to a southward shift in the mean position of the ITCZ thereby crossing the equatorial west Pacific ~5 kyr ago in response to precessional forcing (Partin et al., 2007). However, precessional forcing with a minimal lag would have resulted in the SAM maximum occurring considerably earlier between 10 and 8 kyrs as seen in several palaeo precipitation records from north of the Equator (e.g. Stott et al., 2004; Fleitmann et al., 2003). In contrast, our records indicate that SAM precipitation peaked during the mid-Holocene thus lagging the precession minimum (at 11.5 ka) and obliquity maxima (at 9.5 kyrs) by several kyrs. Clemens et al. (1991) and Clemens et al. (1996) proposed that this large time lag between maximum NH summer insolation and the timing of strengthened SAM was governed by interhemispheric transport of latent heat from the southern subtropical Indian Ocean. Thus a combined precession and obliquity forcing of the monsoon and latent heat export associated with the two orbital bands would have strengthened SAM precipitation sometime between 9.5 and 3.5 kyrs (Clemens and Prell, 2003). This hypothesis most likely explains the mid-Holocene pacing of the monsoon observed in our records, as well as in several other high-resolution Holocene records from northwest India and Tibet (Bryson and Swain, 1981; Swain et al., 1983; Gasse et al., 1991; Gasse and Van Campo, 1994), the Arabian Sea (Fleitmann et al., 2003; Neff et al., 2001; and Schulz et al., 1998), and records from other monsoon regions (Foerster et al., 2012; Weldeab et al., 2014), and results from the Paleoclimate Model Intercomparison Project (PMIP3, Braconnot et al., 2012). In particular, model output from the global climate model (MIROC-ESM) most competent in simulating the basic features of present day monsoon circulation (Sharmila et al., 2015) indicates mid-Holocene intensification of the SAM over the northern Indian subcontinent and Irrawaddy catchment (Fig. 7a and b). The late (4–2 ka) Holocene Ba/Ca data suggest reduction in riverine runoff while $\delta^{18}\text{O}_{\text{sw}}$ values remain stable potentially suggesting a difference in response over the oceans compared to the continent. The late Holocene weakening of the SAM possibly reflects the gradual retreat of the ITCZ in response to decreasing summer

insolation (Laskar et al., 2004) as also observed in terrestrial records from India (Bryson and Swain, 1981; Swain et al., 1983; Yadava and Ramesh, 2005).

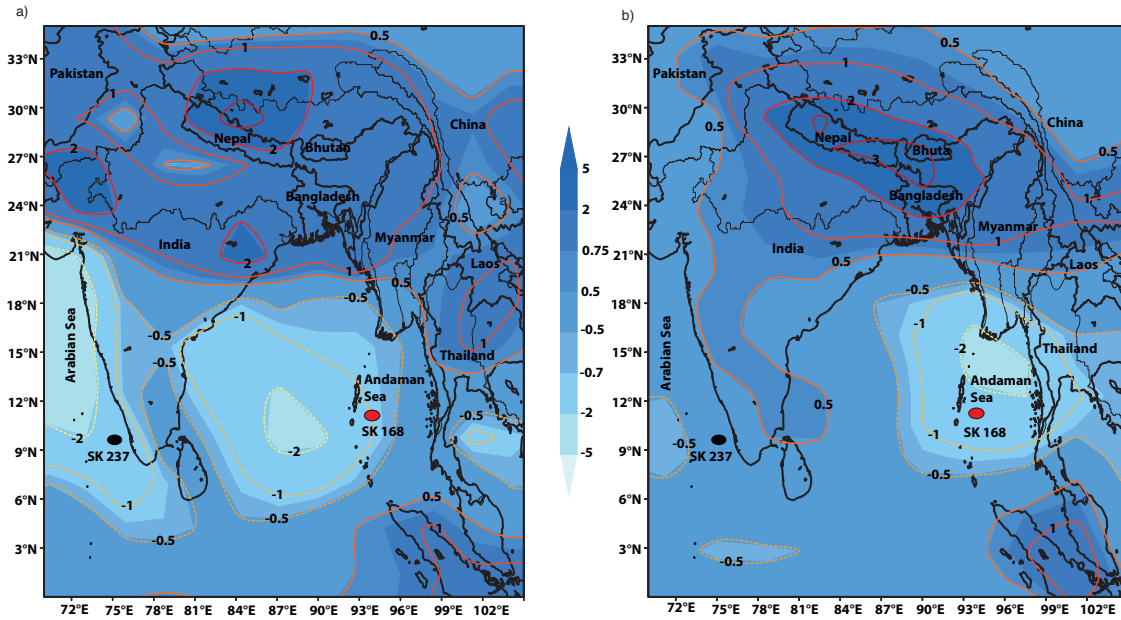


Figure 7. Mid-Holocene JJAS mean precipitation anomalies derived from PMIP3/CMIP5 model output (color shaded) over South Asia (Braconnot et al., 2012). Dark blue (light blue) shaded areas correspond to wetter (drier) mid-Holocene conditions compared to the Pre-Industrial control run, and are expressed in millimeters per day (mm/day). a) MIROC-ESM b) Ensemble mean.

5. Conclusions

This study demonstrates that SAM climate has undergone abrupt and strong changes due to a complex interplay of orbitally induced insolation forcing and interhemispheric and regional variability. Our $\Delta\delta^{18}\text{O}_{\text{sw}}$ time series reveals that upper ocean salinity stratification did not change significantly throughout the glacial indicating a limited influence of NH insolation changes. The SAM was significantly weaker during the LGM, which is supported by heavily reduced river runoff and high SSS estimates. Deglacial Ba/Ca and $\delta^{18}\text{O}_{\text{sw}}$ trends indicate a gradual monsoon strengthening with the exception of HS1. $\delta^{18}\text{O}_{\text{sw}}$ values indicate abrupt mixed layer freshening during HS1 consistent with other studies from the Arabian Sea that reported major intensification of the southwest monsoon around 15.5 ka. However, the onset of the last deglaciation shows a gradual SAM strengthening with river

runoff increasing beginning ~18 kyr and lead observed Ba/Ca increases the Arabian Sea by ~2–3 kyr. This indicates South Asian Monsoon climate dynamics are more complex than the simple N-S displacement of the ITCZ following insolation changes. Early to mid-Holocene SAM variability is characterized by a gradual intensification of monsoon rainfall while upper ocean stratification remained relatively constant. Peak monsoon strength during the mid-Holocene in the Andaman Sea is in agreement with records obtained from other monsoon regions and was most likely linked to combined precession and obliquity forcing, which is consistent with model simulations.

Acknowledgments

Part of this work was funded by the German Science Foundation, DFG, grant [HA 5751/3-1](#). B.N. Nath thanks the Director, CSIR-National Institute of Oceanography, Goa, for the permission to publish this paper and Ministry of Earth Sciences (Government of India) for the ship time. Support from CSIR Networked Projects GEOSINKS and GENIAS is acknowledged. This is NIO contribution No. 5861. We thank Nadine Gehre for laboratory assistance for Mg/Ca cleaning and Fynn Wulf for stable isotopes measurements. We thank the two anonymous reviewers for their constructive comments, which helped us to improve the manuscript.

References

- Ali, S., Hathorne, E.C., Frank, M., Gebregiorgis, D., Statterger, K., Stumpf, R., Kutterolf, S., Johnson, J.E. and Giosan, L., 2015. South Asian monsoon history over the past 60 kyr recorded by radiogenic isotopes and clay mineral assemblages in the Andaman Sea. *Geochemistry, Geophysics, Geosystems*, 16(2): 505-521.
- Anand, P., Elderfield, H. and Conte, M.H., 2003. Calibration of Mg/Ca thermometry in planktonic foraminifera from a sediment trap time series. *Paleoceanography*, 18(2).
- Andersen, K.K., Svensson, A., Johnsen, S.J., Rasmussen, S.O., Bigler, M., Röthlisberger, R., Ruth, U., Siggaard-Andersen, M.-L., Steffensen, J.P. and Dahl-Jensen, D., 2006. The Greenland ice core chronology 2005, 15–42ka. Part 1: Constructing the time scale. *Quaternary Science Reviews*, 25(23): 3246-3257.
- Bahr, A., Schönfeld, J., Hoffmann, J., Voigt, S., Aurahs, R., Kucera, M., Flögel, S., Jentzen, A. and Gerdes, A., 2013. Comparison of Ba/Ca and as freshwater proxies: A

- multi-species core-top study on planktonic foraminifera from the vicinity of the Orinoco River mouth. *Earth and Planetary Science Letters*, 383(0): 45-57.
- Barbante, C., Barnola, J.-M., Becagli, S., Beer, J., Bigler, M., Boutron, C., Blunier, T., Castellano, E., Cattani, O. and Chappellaz, J., 2006. One-to-one coupling of glacial climate variability in Greenland and Antarctica. *Nature*, 444(7116): 195-198.
- Barker, S., Greaves, M. and Elderfield, H., 2003. A study of cleaning procedures used for foraminiferal Mg/Ca paleothermometry. *Geochemistry, Geophysics, Geosystems*, 4(9).
- Bemis, E., Spero, H.J., Bijma, J. and Lea, D.W., 1998. Reevaluation of the oxygen isotopic composition of planktonic foraminifera: Experimental results and revised paleotemperature equations. *Paleoceanography*, 13(2): 150-160.
- Bevington, P.R., Robinson, D.K., 2003. Data reduction and error analysis, third ed. McGraw-Hill, New York, p. 320.
- Bolton, C.T., Chang, L., Clemens, S.C., Kodama, K., Ikehara, M., Medina-Elizalde, M., Paterson, G.A., Roberts, A.P., Rohling, E.J. and Yamamoto, Y., 2013. A 500,000 year record of Indian summer monsoon dynamics recorded by eastern equatorial Indian Ocean upper water-column structure. *Quaternary Science Reviews*, 77: 167-180.
- Boyle, E.A., 1981. Cadmium, zinc, copper, and barium in foraminifera tests. *Earth and Planetary Science Letters*, 53(1): 11-35.
- Braconnot, P., Harrison, S.P., Kageyama, M., Bartlein, P.J., Masson-Delmotte, V., Abe-Ouchi, A., Otto-Bliesner, B. and Zhao, Y., 2012. Evaluation of climate models using palaeoclimatic data. *Nature Climate Change*, 2(6): 417-424.
- Braconnot, P., Otto-Bliesner, B., Kageyama, M., Kitoh, A., Laîné, A., Loutre, M.-F., Marti, O., Merkel, U., Ramstein, G. and Valdes, P., 2007. Results of PMIP2 coupled simulations of the Mid-Holocene and Last Glacial Maximum—Part 1: experiments and large-scale features.
- Bryson, R.A. and Swain, A., 1981. Holocene variations of monsoon rainfall in Rajasthan. *Quaternary Research*, 16(2): 135-145.
- Butzin, M., Prange, M. and Lohmann, G., 2005. Radiocarbon simulations for the glacial ocean: the effects of wind stress, Southern Ocean sea ice and Heinrich events. *Earth and Planetary Science Letters*, 235(1): 45-61.
- Caley, T., Malaizé, B., Zaragosi, S., Rossignol, L., Bourget, J., Eynaud, F., Martinez, P., Giraudeau, J., Charlier, K. and Ellouzi-Zimmermann, N., 2011. New Arabian Sea records help decipher orbital timing of Indo-Asian monsoon. *Earth and Planetary Science Letters*, 308(3): 433-444.
- Chapman, H., Bickle, M., Thaw, S.H. and Thiam, H.N., 2015. Chemical fluxes from time series sampling of the Irrawaddy and Salween Rivers, Myanmar. *Chemical Geology*, 401: 15-27.
- Chen, T.-C., 2003. Maintenance of Summer Monsoon Circulations: A Planetary-Scale Perspective. *Journal of Climate*, 16(12): 2022-2037.
- Clemens, S., Prell, W., Murray, D., Shimmield, G. and Weedon, G., 1991. Forcing mechanisms of the Indian Ocean monsoon. *Nature*, 353(6346): 720-725.

- Clemens, S.C., Prell, W.L. and Sun, Y., 2010. Orbital - scale timing and mechanisms driving Late Pleistocene Indo - Asian summer monsoons: Reinterpreting cave speleothem $\delta^{18}\text{O}$. *Paleoceanography*, 25(4).
- Clemens, S.C., Murray, D.W. and Prell, W.L., 1996. Nonstationary phase of the Pliocene Pleistocene Asian monsoon. *Science*, 274(5289): 943-948.
- Clemens, S.C. and Prell, W.L., 2003. A 350,000 year summer-monsoon multi-proxy stack from the Owen Ridge, Northern Arabian Sea. *Marine Geology*, 201(1): 35-51.
- Clemens, S.C., Prell, W.L., Sun, Y., Liu, Z. and Chen, G., 2008. Southern Hemisphere forcing of Pliocene $\delta^{18}\text{O}$ and the evolution of Indo - Asian monsoons. *Paleoceanography*, 23(4).
- Cullen, J.L., 1981. Microfossil evidence for changing salinity patterns in the Bay of Bengal over the last 20 000 years. *Palaeogeography, Palaeoclimatology, Palaeoecology*, 35: 315-356.
- Curry, W., Thunell, R. and Honjo, S., 1983. Seasonal changes in the isotopic composition of planktonic foraminifera collected in Panama Basin sediment traps. *Earth and Planetary Science Letters*, 64(1): 33-43.
- Dickson, R.R., 1984. Eurasian snow cover versus Indian monsoon rainfall-An extension of the Hahn-Shukla results. *Journal of Climate and Applied Meteorology*, 23(1): 171-173.
- Elderfield, H., Vautravers, M. and Cooper, M., 2002. The relationship between shell size and Mg/Ca, Sr/Ca, $\delta^{18}\text{O}$, and $\delta^{13}\text{C}$ of species of planktonic foraminifera. *Geochemistry, Geophysics, Geosystems*, 3(8): 1-13.
- Fairbanks, R.G., Sverdrup, M., Free, R., Wiebe, P.H. and Bé, A.W., 1982. Vertical distribution and isotopic fractionation of living planktonic foraminifera from the Panama Basin.
- Fairbanks, R.G., Sverdrup, M., Free, R., Wiebe, P.H. and Bé, A.W., 1982. Vertical distribution and isotopic fractionation of living planktonic foraminifera from the Panama Basin.
- Fairbanks, R.G., Wiebe, P.H. and Bé, A.W., 1980. Vertical distribution and isotopic composition of living planktonic foraminifera in the western North Atlantic. *Science*, 207(4426): 61-63.
- Fang, X.-M., Ono, Y., Fukusawa, H., Bao-Tian, P., Li, J.-J., Dong-Hong, G., Oi, K., Tsukamoto, S., Torii, M. and Mishima, T., 1999. Asian summer monsoon instability during the past 60,000 years: magnetic susceptibility and pedogenic evidence from the western Chinese Loess Plateau. *Earth and Planetary Science Letters*, 168(3): 219-232.
- Field, D.B., 2004. Variability in vertical distributions of planktonic foraminifera in the California Current: Relationships to vertical ocean structure. *Paleoceanography*, 19(2).
- Fleitmann, D., Burns, S.J., Mangini, A., Mudelsee, M., Kramers, J., Villa, I., Neff, U., Al-Subary, A.A., Buettner, A. and Hippler, D., 2007. Holocene ITCZ and Indian monsoon dynamics recorded in stalagmites from Oman and Yemen (Socotra). *Quaternary Science Reviews*, 26(1): 170-188.

- Fleitmann, D., Burns, S.J., Mudelsee, M., Neff, U., Kramers, J., Mangini, A. and Matter, A., 2003. Holocene Forcing of the Indian Monsoon Recorded in a Stalagmite from Southern Oman. *Science*, 300(5626): 1737-1739.
- Fleitmann, D., Burns, S.J., Pekala, M., Mangini, A., Al-Subbary, A., Al-Aowah, M., Kramers, J. and Matter, A., 2011. Holocene and Pleistocene pluvial periods in Yemen, southern Arabia. *Quaternary Science Reviews*, 30(7): 783-787.
- Foerster, V., Junginger, A., Langkamp, O., Gebru, T., Asrat, A., Umer, M., Lamb, H.F., Wennrich, V., Rethemeyer, J. and Nowaczyk, N., 2012. Climatic change recorded in the sediments of the Chew Bahir basin, southern Ethiopia, during the last 45,000 years. *Quaternary International*, 274: 25-37.
- Garcia-Solsona, E., Jeandel, C., Labatut, M., Lacan, F., Vance, D., Chavagnac, V. and Pradoux, C., 2014. Rare Earth Elements and Nd isotopes tracing water mass mixing and particle-seawater interactions in the SE Atlantic. *Geochimica et Cosmochimica Acta*, 125: 351-372.
- Gasse, F., Arnold, M., Fontes, J.C., Fort, M., Gibert, E., Huc, A., Bingyan, L., Yuanfang, L., Qing, L. and Melieres, F., 1991. A 13, 000-year climate record from western Tibet. *Nature*, 353(6346): 742-745.
- Gasse, F. and Van Campo, E., 1994. Abrupt post-glacial climate events in West Asia and North Africa monsoon domains. *Earth and Planetary Science Letters*, 126(4): 435-456.
- Govil, P. and Divakar Naidu, P., 2011. Variations of Indian monsoon precipitation during the last 32kyr reflected in the surface hydrography of the Western Bay of Bengal. *Quaternary Science Reviews*, 30(27): 3871-3879.
- Greaves, M., Caillon, N., Rebaubier, H., Bartoli, G., Bohaty, S., Cacho, I., Clarke, L., Cooper, M., Daunt, C. and Delaney, M., 2008. Interlaboratory comparison study of calibration standards for foraminiferal Mg/Ca thermometry. *Geochemistry, Geophysics, Geosystems*, 9(8).
- Guptha, M., Curry, W., Ittekkot, V. and Muralinath, A., 1997. Seasonal variation in the flux of planktic Foraminifera; sediment trap results from the Bay of Bengal, northern Indian Ocean. *The Journal of Foraminiferal Research*, 27(1): 5-19.
- Hahn, D.G. and Shukla, J., 1976. An apparent relationship between Eurasian snow cover and Indian monsoon rainfall. *Journal of the Atmospheric Sciences*, 33(12): 2461-2462.
- Hall, J.M. and Chan, L.H., 2004. Ba/Ca in *Neogloboquadrina pachyderma* as an indicator of deglacial meltwater discharge into the western Arctic Ocean. *Paleoceanography*, 19(1): PA1017.
- Hönisch, B., Allen, K.A., Russell, A.D., Eggins, S.M., Bijma, J., Spero, H.J., Lea, D.W. and Yu, J., 2011. Planktic foraminifers as recorders of seawater Ba/Ca. *Marine Micropaleontology*, 79(1-2): 52-57.
- Kakade, S. and Dugam, S., 2000. The simultaneous effect of NAO and SO on the monsoon activity over India. *Geophysical research letters*, 27(21): 3501-3504.
- Kessarkar, P.M., Purnachandra Rao, V., Naqvi, S., Chivas, A.R. and Saino, T., 2010. Fluctuations in productivity and denitrification in the southeastern Arabian Sea during the Late Quaternary. *Current Science*, 99(4): 485-491.

- Kudrass, H., Hofmann, A., Doose, H., Emeis, K. and Erlenkeuser, H., 2001. Modulation and amplification of climatic changes in the Northern Hemisphere by the Indian summer monsoon during the past 80 ky. *Geology*, 29(1): 63-66.
- Kumar, K.K., Rajagopalan, B. and Cane, M.A., 1999. On the weakening relationship between the Indian monsoon and ENSO. *Science*, 284(5423): 2156-2159.
- Laepfle, T. and Huybers, P., 2013. Reconciling discrepancies between Uk37 and Mg/Ca reconstructions of Holocene marine temperature variability. *Earth and Planetary Science Letters*, 375: 418-429.
- Laskar, J., Robutel, P., Joutel, F., Gastineau, M., Correia, A. and Levrard, B., 2004. A long-term numerical solution for the insolation quantities of the Earth. *Astronomy & Astrophysics*, 428(1): 261-285.
- Lau, K.M., Kim, K.M. and Yang, S., 2000. Dynamical and Boundary Forcing Characteristics of Regional Components of the Asian Summer Monsoon. *Journal of Climate*, 13(14): 2461-2482.
- Lea, D.W. and Boyle, E.A., 1991. Barium in planktonic foraminifera. *Geochimica et Cosmochimica Acta*, 55(11): 3321-3331.
- Lea, D.W. and Spero, H.J., 1992. Experimental determination of barium uptake in shells of the planktonic foraminifera *Orbulina universa* at 22°C. *Geochimica et Cosmochimica Acta*, 56(7): 2673-2680.
- Lea, D.W. and Spero, H.J., 1994. Assessing the reliability of paleochemical tracers: Barium uptake in the shells of planktonic foraminifera. *Paleoceanography*, 9(3): 445-452.
- Li, C. and Yanai, M., 1996. The Onset and Interannual Variability of the Asian Summer Monsoon in Relation to Land–Sea Thermal Contrast. *Journal of Climate*, 9(2): 358-375.
- Liu, D., Wang, Y., Cheng, H., Edwards, R.L., Kong, X., Wang, X., Hardt, B., Wu, J., Chen, S. and Jiang, X., 2010. Sub-millennial variability of Asian monsoon intensity during the early MIS 3 and its analogue to the ice age terminations. *Quaternary Science Reviews*, 29(9): 1107-1115.
- Locarnini, R. A., A. V. Mishonov, J. I. Antonov, T. P. Boyer, H. E. Garcia, O. K. Baranova, M. M. Zweng, C. R. Paver, J. R. Reagan, D. R. Johnson, M. Hamilton, and D. Seidov, 2013. *World Ocean Atlas 2013, Volume 1: Temperature*. S. Levitus, Ed., A. Mishonov Technical Ed.; NOAA Atlas NESDIS 73, 40 pp.
- Mark, B., Harrison, S., Spessa, A., New, M., Evans, D. and Helmens, K., 2005. Tropical snowline changes at the last glacial maximum: a global assessment. *Quaternary International*, 138: 168-201.
- Martinson, D.G., Pisias, N.G., Hays, J.D., Imbrie, J., Moore Jr, T.C. and Shackleton, N.J., 1987. Age dating and the orbital theory of the ice ages: development of a high-resolution 0 to 300,000-year chronostratigraphy. *Quaternary Research*, 27(1): 1-29.
- Meehl, G.A., 1994. Coupled Land-Ocean-Atmosphere Processes and South Asian Monsoon Variability. *Science*, 266(5183): 263-267.
- Mohtadi, M., Prange, M., Oppo, D.W., De Pol-Holz, R., Merkel, U., Zhang, X., Steinke, S. and Luckge, A., 2014. North Atlantic forcing of tropical Indian Ocean climate. *Nature*, 509(7498): 76-80.

- Murty, V., Gupta, G., Sarma, V., Rao, B., Jyothi, D., Shastri, P. and Supraveena, Y., 2000. Effect of vertical stability and circulation on the depth of the chlorophyll maximum in the Bay of Bengal during May–June, 1996. *Deep Sea Research Part I: Oceanographic Research Papers*, 47(5): 859-873.
- Naqvi, W.A. and Fairbanks, R.G., 1996. A 27,000 year record of Red Sea outflow: Implication for timing of post - glacial monsoon intensification. *Geophysical research letters*, 23(12): 1501-1504.
- Neff, U., Burns, S., Mangini, A., Mudelsee, M., Fleitmann, D. and Matter, A., 2001. Strong coherence between solar variability and the monsoon in Oman between 9 and 6 kyr ago. *Nature*, 411(6835): 290-293.
- Ni, Y., Foster, G.L., Bailey, T., Elliott, T., Schmidt, D.N., Pearson, P., Haley, B. and Coath, C., 2007. A core top assessment of proxies for the ocean carbonate system in surface - dwelling foraminifers. *Paleoceanography*, 22(3).
- Overpeck, J., Anderson, D., Trumbore, S. and Prell, W., 1996. The southwest Indian Monsoon over the last 18 000 years. *Climate Dynamics*, 12(3): 213-225.
- Pant, G. and Parthasarathy, S.B., 1981. Some aspects of an association between the Southern Oscillation and Indian summer monsoon. *Archives for meteorology, geophysics, and bioclimatology, Series B*, 29(3): 245-252.
- Partin, J.W., Cobb, K.M., Adkins, J.F., Clark, B. and Fernandez, D.P., 2007. Millennial-scale trends in west Pacific warm pool hydrology since the Last Glacial Maximum. *Nature*, 449(7161): 452-455.
- Ramesh Babu, V. and Sastry, J., 1976. Hydrography of the Andaman Sea during late winter. *Ind J Mar. Sci*, 5: 179-189.
- Randel, W.J. and Park, M., 2006. Deep convective influence on the Asian summer monsoon anticyclone and associated tracer variability observed with Atmospheric Infrared Sounder (AIRS). *Journal of Geophysical Research: Atmospheres*, 111(D12): D12314.
- Rao, L.G. and Jayaraman, R., 1968. Hydrographical features of the southern and central Bay of Bengal during the transition period between winter and summer. *Bulletin of the National Institute of Sciences of India*, 38: 123-147.
- Rashid, H., England, E., Thompson, L. and Polyak, L., 2011. Late glacial to Holocene Indian summer monsoon variability based upon sediment. *Terr. Atmos. Ocean. Sci*, 22(2): 215-228.
- Rashid, H., Flower, B., Poore, R. and Quinn, T., 2007. A ~ 25ka Indian Ocean monsoon variability record from the Andaman Sea. *Quaternary Science Reviews*, 26(19): 2586-2597.
- Rasmussen, S.O., Andersen, K.K., Svensson, A., Steffensen, J.P., Vinther, B.M., Clausen, H.B., Siggaard - Andersen, M.L., Johnsen, S.J., Larsen, L.B. and Dahl - Jensen, D., 2006. A new Greenland ice core chronology for the last glacial termination. *Journal of Geophysical Research: Atmospheres (1984-2012)*, 111(D6).
- Rasmusson, E.M. and Carpenter, T.H., 1983. The relationship between eastern equatorial Pacific sea surface temperatures and rainfall over India and Sri Lanka. *Monthly Weather Review*, 111(3): 517-528.

- Ravelo, A. and Shackleton, N., 1995. Evolution of surface water circulation in the east equatorial Pacific over the past 2.0 Ma: isotopic measurements from ODP Site 851, *Proceeding of the Ocean Drilling Program, Scientific Results*, pp. 50.
- Riser, S., Nystuen, J. and Rogers, A., 2008. Monsoon effects in the Bay of Bengal inferred from profiling float - based measurements of wind speed and rainfall. *Limnology and Oceanography*, 53(5part2): 2080-2093.
- Rohling, E., Sprovieri, M., Cane, T., Casford, J., Cooke, S., Bouloubassi, I., Emeis, K., Schiebel, R., Rogerson, M. and Hayes, A., 2004. Reconstructing past planktic foraminiferal habitats using stable isotope data: a case history for Mediterranean sapropel S5. *Marine Micropaleontology*, 50(1): 89-123.
- Rosenthal, Y., Field, M.P. and Sherrell, R.M., 1999. Precise determination of element/calcium ratios in calcareous samples using sector field inductively coupled plasma mass spectrometry. *Analytical Chemistry*, 71(15): 3248-3253.
- Ruddiman, W.F., 1997. Tropical Atlantic terrigenous fluxes since 25,000 yrs BP. *Marine Geology*, 136(3): 189-207.
- Saraswat, R., Lea, D.W., Nigam, R., Mackensen, A. and Naik, D.K., 2013. Deglaciation in the tropical Indian Ocean driven by interplay between the regional monsoon and global teleconnections. *Earth and Planetary Science Letters*, 375: 166-175.
- Sarkar, A., Ramesh, R., Bhattacharya, S.K. and Rajagopalan, G., 1990. Oxygen isotope evidence for a stronger winter monsoon current during the last glaciation. *Nature*, 343(6258): 549-551.
- Sarkar, A., Ramesh, R., Somayajulu, B., Agnihotri, R., Jull, A. and Burr, G., 2000. High resolution Holocene monsoon record from the eastern Arabian Sea. *Earth and Planetary Science Letters*, 177(3): 209-218.
- Sarma, V.V.S.S. and Narvekar, P.V., 2001. A study on inorganic carbon components in the Andaman Sea during the post monsoon season. *Oceanologica Acta*, 24(2): 125-134.
- Schmidt, M.W. and Lynch-Stieglitz, J., 2011. Florida Straits deglacial temperature and salinity change: Implications for tropical hydrologic cycle variability during the Younger Dryas. *Paleoceanography*, 26(4): PA4205.
- Schulz, H., von Rad, U., Erlenkeuser, H. and von Rad, U., 1998. Correlation between Arabian Sea and Greenland climate oscillations of the past 110,000 years. *Nature*, 393(6680): 54-57.
- Sengupta, D., Bharath Raj, G.N. and Shenoi, S.S.C., 2006. Surface freshwater from Bay of Bengal runoff and Indonesian Throughflow in the tropical Indian Ocean. *Geophysical Research Letters*, 33(22): L22609.
- Sengupta, R., Moraes, C., George, M., Kureishy, T., Noronha, R. and Fondekar, S., 1981. Chemistry and hydrography of the Andaman Sea. *Indian Journal of Marine Sciences*, 10(3): 228-233.
- Sharmila, S., Joseph, S., Sahai, A., Abhilash, S. and Chattopadhyay, R., 2015. Future projection of Indian summer monsoon variability under climate change scenario: An assessment from CMIP5 climate models. *Global and Planetary Change*, 124: 62-78.

- Shi, Y., 2002. Characteristics of late Quaternary monsoonal glaciation on the Tibetan Plateau and in East Asia. *Quaternary International*, 97: 79-91.
- Sijinkumar, A., Nath, B.N. and Guptha, M., 2010. Late Quaternary record of pteropod preservation from the Andaman Sea. *Marine Geology*, 275(1): 221-229.
- Sijinkumar, A., Clemens, S., Nath, B.N., Prell, W., Benschila, R. and Lengaigne, M., 2016. $\delta^{18}\text{O}$ and salinity variability from the Last Glacial Maximum to Recent in the Bay of Bengal and Andaman Sea. *Quaternary Science Reviews*, 135: 79-91.
- Singh, S.P., Singh, S.K. and Bhushan, R., 2013. Internal cycling of dissolved barium in water column of the Bay of Bengal. *Marine Chemistry*, 154: 12-23.
- Sirocko, F., Garbe-Schönberg, D., McIntyre, A. and Molino, B., 1996. Teleconnections between the subtropical monsoons and high-latitude climates during the last deglaciation. *Science*, 272(5261): 526-529.
- Sirocko, F., Sarnthein, M., Erlenkeuser, H., Lange, H., Arnold, M. and Duplessy, J.C., 1993. Century-scale events in monsoonal climate over the past 24,000 years. *Nature*, 364(6435): 322-324.
- Steinke, S., Mohtadi, M., Groeneveld, J., Lin, L.C., Löwemark, L., Chen, M.T. and Rendle - Bühring, R., 2010. Reconstructing the southern South China Sea upper water column structure since the Last Glacial Maximum: Implications for the East Asian winter monsoon development. *Paleoceanography*, 25(2).
- Steph, S., Regenber, M., Tiedemann, R., Mulitza, S. and Nürnberg, D., 2009. Stable isotopes of planktonic foraminifera from tropical Atlantic/Caribbean core-tops: Implications for reconstructing upper ocean stratification. *Marine Micropaleontology*, 71(1): 1-19.
- Stott, L., Cannariato, K., Thunell, R., Haug, G.H., Koutavas, A. and Lund, S., 2004. Decline of surface temperature and salinity in the western tropical Pacific Ocean in the Holocene epoch. *Nature*, 431(7004): 56-59.
- Svensson, A., Andersen, K.K., Bigler, M., Clausen, H.B., Dahl-Jensen, D., Davies, S., Johnsen, S.J., Muscheler, R., Parrenin, F. and Rasmussen, S.O., 2008. A 60 000 year Greenland stratigraphic ice core chronology. *Climate of the Past*, 4(1): 47-57.
- Swain, A.M., Kutzbach, J. and Hastenrath, S., 1983. Estimates of Holocene precipitation for Rajasthan, India, based on pollen and lake-level data. *Quaternary Research*, 19(1): 1-17.
- Trenberth, K.E., Stepaniak, D.P. and Caron, J.M., 2000. The Global Monsoon as Seen through the Divergent Atmospheric Circulation. *Journal of Climate*, 13(22): 3969-3993.
- Uddin, M.M., Chowdhury, M., Rahman, Z., Ahammed, S. and Basak, S.C., 2014. Seasonal variability of mixed layer depth (MLD) in the Bay of Bengal. *Indian Journal of Geo-Marine Sciences*, 43(3): 400-407.
- Viswambharan, N. and Mohanakumar, K., 2014. Modulation of Indian summer monsoon through northern and southern hemispheric extra-tropical oscillations. *Climate Dynamics*: 1-14.
- von Rad, U., Schulz, H., Riech, V., den Dulk, M., Berner, U. and Sirocko, F., 1999. Multiple monsoon-controlled breakdown of oxygen-minimum conditions during the past 30,000 years documented in laminated sediments off

- Pakistan. *Palaeogeography, Palaeoclimatology, Palaeoecology*, 152(1): 129-161.
- Waelbroeck, C., Labeyrie, L., Michel, E., Duplessy, J.C., McManus, J., Lambeck, K., Balbon, E. and Labracherie, M., 2002. Sea-level and deep water temperature changes derived from benthic foraminifera isotopic records. *Quaternary Science Reviews*, 21(1): 295-305.
- Wang, B. and Ding, Q., 2008. Global monsoon: Dominant mode of annual variation in the tropics. *Dynamics of Atmospheres and Oceans*, 44(3-4): 165-183.
- Wang, P., Clemens, S., Beaufort, L., Braconnot, P., Ganssen, G., Jian, Z., Kershaw, P. and Sarnthein, M., 2005. Evolution and variability of the Asian monsoon system: state of the art and outstanding issues. *Quaternary Science Reviews*, 24(5): 595-629.
- Webster, P.J., Magana, V.O., Palmer, T., Shukla, J., Tomas, R., Yanai, M.u. and Yasunari, T., 1998. Monsoons: Processes, predictability, and the prospects for prediction. *Journal of Geophysical Research: Oceans (1978-2012)*, 103(C7): 14451-14510.
- Webster, P.J. and Yang, S., 1992. Monsoon and ENSO: Selectively interactive systems. *Quarterly Journal of the Royal Meteorological Society*, 118(507): 877-926.
- Weldeab, S., Lea, D.W., Schneider, R.R. and Andersen, N., 2007. 155,000 Years of West African Monsoon and Ocean Thermal Evolution. *Science*, 316(5829): 1303-1307.
- Weldeab, S., Menke, V. and Schmiedl, G., 2014. The pace of East African monsoon evolution during the Holocene. *Geophysical Research Letters*, 41(5): 1724-1732.
- Wu, G. and Zhang, Y., 1998. Tibetan Plateau Forcing and the Timing of the Monsoon Onset over South Asia and the South China Sea. *Monthly Weather Review*, 126(4): 913-927.
- Yadava, M. and Ramesh, R., 2005. Monsoon reconstruction from radiocarbon dated tropical Indian speleothems. *The Holocene*, 15(1): 48-59.
- Yanai, M., Li, C. and Song, Z., 1992. Seasonal heating of the Tibetan Plateau and its effects on the evolution of the Asian summer monsoon. *Journal of the Meteorological Society of Japan*, 70(1B): 319-351.
- Yihui, D., Chongyin, L. and Yanju, L., 2004. Overview of the South China Sea monsoon experiment. *Advances in Atmospheric Sciences*, 21(3): 343-360.
- Yuan, D., Cheng, H., Edwards, R.L., Dykoski, C.A., Kelly, M.J., Zhang, M., Qing, J., Lin, Y., Wang, Y. and Wu, J., 2004. Timing, duration, and transitions of the last interglacial Asian monsoon. *Science*, 304(5670): 575-578.
- Zweng, M., Reagan, J., Antonov, J., Locarnini, R., Mishonov, A., Boyer, T., Garcia, H., Baranova, O., Johnson, D. and Seidov, D., 2013. *World Ocean Atlas 2013, Volume 2: Salinity*. NOAA Atlas NESDIS, 74: 39.
- Ziegler, M., Lourens, L.J., Tuenter, E., Hilgen, F., Reichert, G.J. and Weber, N., 2010. Precession phasing offset between Indian summer monsoon and Arabian Sea productivity linked to changes in Atlantic overturning circulation. *Paleoceanography*, 25(3).

Supplement material

South Asian Summer Monsoon variability during the last ~54kyrs inferred from surface water salinity and river run off proxies

D. Gebregiorgis¹, E.C. Hathorne¹, A.V. Sijinkumar², B. Nagender Nath³, D. Nürnberg and M. Frank¹

¹GEOMAR Helmholtz Centre for Ocean Research Kiel, Wischhofstraße 1-3, 24148 Kiel, Germany

²Govt. College Kasaragod, Vidyanagar P.O, Kasaragod Dist., Kasaragod, 671123, Kerala, India

³ CSIR-National Institute of Oceanography, Dona Paula, Goa, 403004, India

Age model

The age model for core SK 168/GC 1 was developed using Accelerator Mass Spectrometer (AMS) ¹⁴C dates of planktic foraminiferal tests (mixed *Globigerinoides ruber* and *Globigerinoides sacculifer*) and correlation of the oxygen isotopic values of *G. ruber* with the standard oxygen isotopic curve of Martinson et al. (1987). AMS ¹⁴C ages were determined at five different intervals at NOSAMS facility at WHOI, USA and converted to calendar age using CalPal 2007 Programme (Weninger et al., 2007; <http://www.calpal.de>). The AMS ¹⁴C ages were corrected assuming a reservoir age of 460 years following Butzin et al. (2005). Assuming constant sedimentation rates between the calibrated ages, calendar ages have been assigned by interpolation/extrapolation. The average sedimentation rate for the core is 7.79 cm/ka and vary between ~3.65 and ~10.20 cm/kyr during the MIS3/MIS 2 and the Pleistocene-Holocene transitions respectively. Further comparison of *G. ruber* oxygen isotopic record of core SK 168/GC with LR04 tuned (Lisiecki and Raymo, 2005) published benthic records from the eastern Indian Ocean (Bolton et al., 2013) and the Andaman Sea (Ali et al., 2015) confirm the accuracy of the age model (Figure S1).

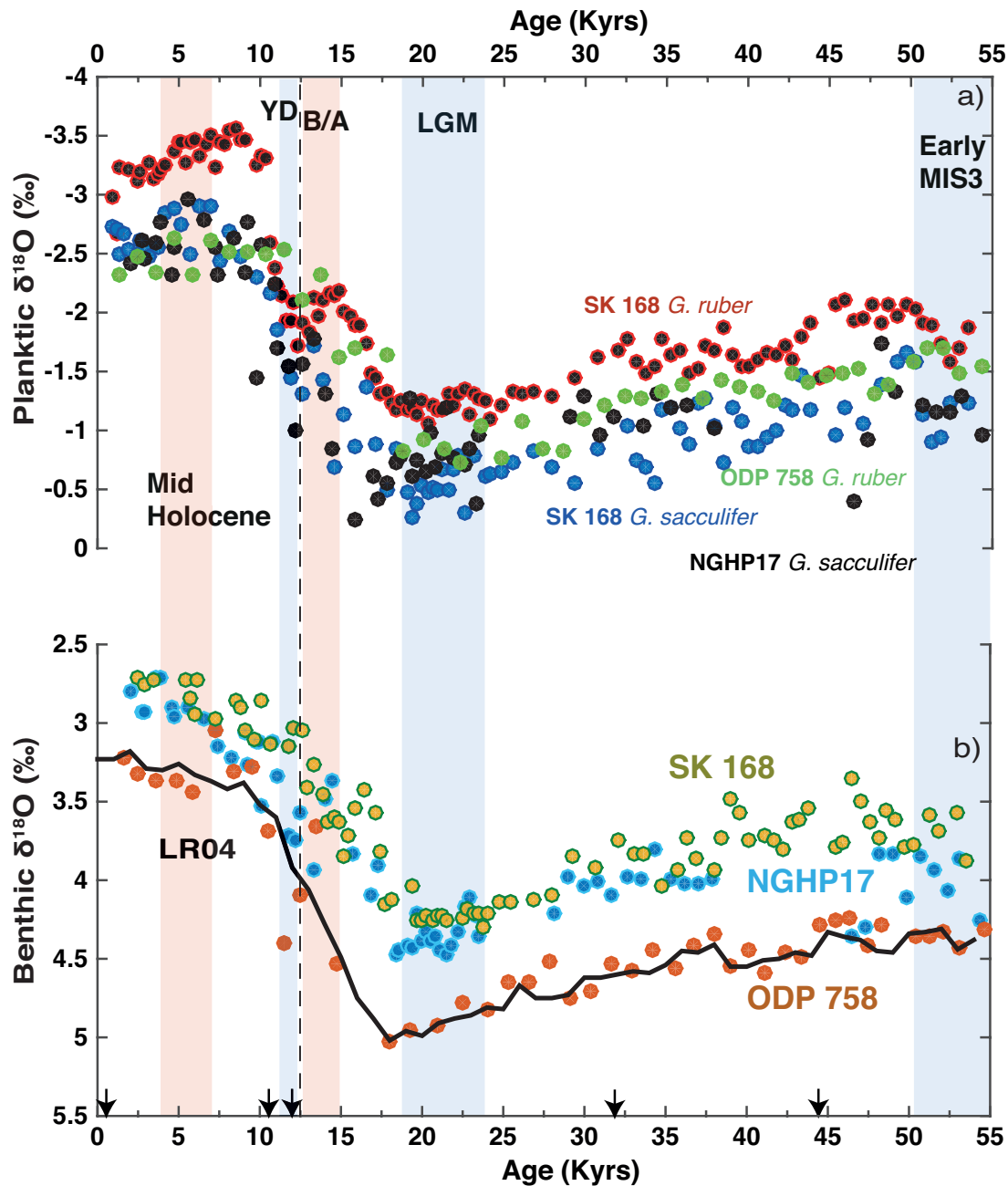


Figure S1. a) SK 168 oxygen isotopic record of *G.ruber* (dark red) and *G. sacculifer* (blue) with *G. ruber* (green) and *G.sacculifer* (black) records from from ODP 758 (Bolton et al., 2013) and NGHP 17 (Ali et al., 2015) respectively; b) Benthic oxygen isotopic records from SK 168 (Sijinkumar et al., 2016, in press QSR), NGHP 17 (Ali et al., 2015), ODP 758 (Bolton et al., 2013) and LR04 stack (Lisiecki and Raymo, 2005).

Planktic foraminiferal Ba/Ca and SSS estimations

Ba/Ca ratio of planktic foraminiferal *tests* provides a useful proxy to assess past river water discharge in to the Ocean and infer paleosalinity changes (e.g. Weldeab

et al., 2007). This is based on the fact that dissolved Ba is high in riverine water relative to sea water (Bahr et al., 2013; Hall and Chan, 2004; Schmidt and Lynch-Stieglitz, 2011) and Ba incorporation into foraminiferal shells varies linearly with seawater Ba concentration (Ba_{sw}) (Lea and Spero, 1992; Lea and Spero, 1994), independent of environmental changes including PH, temperature, salinity and symbiont photosynthesis (Hönisch et al., 2011). Consequently, foraminifera Ba/Ca (Ba/Ca_{foram}) depends only on seawater Ba concentration, and its temporal variation can be used to infer changes in riverine freshwater input. To estimate past SSS change from Ba/Ca_{foram} , we use Ba_{sw} and salinity data obtained from the Bay of Bengal (Singh et al., 2013) and calculate Ba/Ca in sea water (Ba/Ca_{sw}). Ba/Ca_{sw} is calculated considering the conservative behavior of Ca and linear relationship of Ca with salinity based on the assumption that a salinity of 35 psu corresponds to 10.2 mmol/kg (Weldeab et al., 2007). Ba/Ca_{foram} is calculated from Ba/Ca_{sw} ($\mu\text{mol/mol}$) using the partition coefficient of $D_{Ba} = 0.19$ (Lea and Boyle, 1991) and is given us:

$$Ba/Ca_{foram} = D_{Ba} * Ba/Ca_{sw}$$

We estimate past sea surface salinity (SSS) using Ba/Ca_{foram} and the modern SSS- Ba/Ca_{foram} relationship using 7 data points from a North – South transect in the Bay of Bengal (Figure S2). Six stations from the northern tip of the Bay of Bengal appear to overestimate SSS values and were excluded from the equation. Thus, SSS is calculated from Ba/Ca_{sw} ($\mu\text{mol/mol}$) and is given us:

$$SSS = -3.7 * Ba/Ca_{foram} + 36.2$$

The Ba-salinity relationship in the Bay of Bengal – Andaman Sea appears complex with two possible slopes (Fig S2) and six stations from the northern tip of the Bay of Bengal appear to overestimate SSS values in the Andaman Sea and were excluded for our purposes.

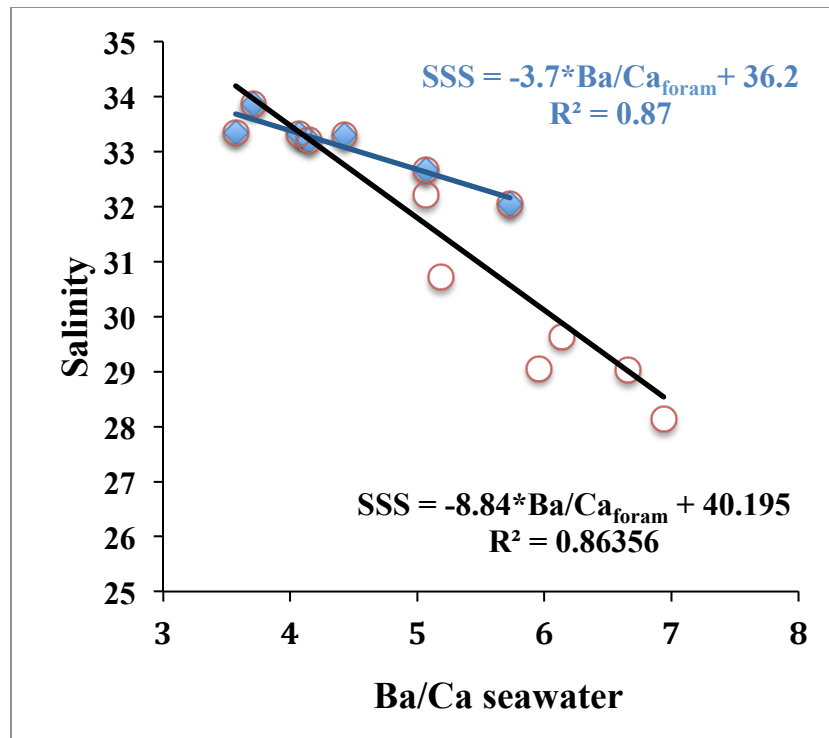


Figure S1. Relationship SSS and Ba/Ca in sea water from the Bay of Bengal (Singh et al., 2013).

References

- Ali, S., Hathorne, E.C., Frank, M., Gebregiorgis, D., Stattegger, K., Stumpf, R., Kutterolf, S., Johnson, J.E. and Giosan, L., 2015. South Asian monsoon history over the past 60 kyr recorded by radiogenic isotopes and clay mineral assemblages in the Andaman Sea. *Geochemistry, Geophysics, Geosystems*, 16(2): 505-521.
- Bahr, A., Schönfeld, J., Hoffmann, J., Voigt, S., Aurahs, R., Kucera, M., Flögel, S., Jentzen, A. and Gerdes, A., 2013. Comparison of Ba/Ca and as freshwater proxies: A multi-species core-top study on planktonic foraminifera from the vicinity of the Orinoco River mouth. *Earth and Planetary Science Letters*, 383(0): 45-57.
- Bolton, C.T., Chang, L., Clemens, S.C., Kodama, K., Ikehara, M., Medina-Elizalde, M., Paterson, G.A., Roberts, A.P., Rohling, E.J. and Yamamoto, Y., 2013. A 500,000 year record of Indian summer monsoon dynamics recorded by eastern equatorial Indian Ocean upper water-column structure. *Quaternary Science Reviews*, 77: 167-180.
- Butzin, M., Prange, M. and Lohmann, G., 2005. Radiocarbon simulations for the glacial ocean: the effects of wind stress, Southern Ocean sea ice and Heinrich events. *Earth and Planetary Science Letters*, 235(1): 45-61.
- Hall, J.M. and Chan, L.H., 2004. Ba/Ca in *Neogloboquadrina pachyderma* as an indicator of deglacial meltwater discharge into the western Arctic Ocean. *Paleoceanography*, 19(1): PA1017.

- Hönisch, B., Allen, K.A., Russell, A.D., Eggins, S.M., Bijma, J., Spero, H.J., Lea, D.W. and Yu, J., 2011. Planktic foraminifers as recorders of seawater Ba/Ca. *Marine Micropaleontology*, 79(1-2): 52-57.
- Lea, D.W. and Boyle, E.A., 1991. Barium in planktonic foraminifera. *Geochimica et Cosmochimica Acta*, 55(11): 3321-3331.
- Lea, D.W. and Spero, H.J., 1994. Assessing the reliability of paleochemical tracers: Barium uptake in the shells of planktonic foraminifera. *Paleoceanography*, 9(3): 445-452.
- Lisiecki, L.E., Raymo, M.E., 2005. A Pliocene-Pleistocene stack of 57 globally distributed benthic $\delta^{18}\text{O}$ records. *Paleoceanography*, 20, PA1003.
- Martinson, D.G., Pisias, N.G., Hays, J.D., Imbrie, J., Moore Jr, T.C. and Shackleton, N.J., 1987. Age dating and the orbital theory of the ice ages: development of a high-resolution 0 to 300,000-year chronostratigraphy. *Quaternary Research*, 27(1): 1-29.
- Schmidt, M.W. and Lynch-Stieglitz, J., 2011. Florida Straits deglacial temperature and salinity change: Implications for tropical hydrologic cycle variability during the Younger Dryas. *Paleoceanography*, 26(4): PA4205.
- Singh, S.P., Singh, S.K. and Bhushan, R., 2013. Internal cycling of dissolved barium in water column of the Bay of Bengal. *Marine Chemistry*, 154: 12-23.
- Weldeab, S., Lea, D.W., Schneider, R.R. and Andersen, N., 2007. 155,000 years of West African monsoon and ocean thermal evolution. *science*, 316(5829): 1303-1307.
- Weninger B., Jöris O., Danzeglocke U., 2007. CalPal-2007 Cologne Radiocarbon Calibration & Palaeoclimate Research Package, <http://www.calpal.de>.

IV. Summary and outlook

IV.1 Summary

Our current knowledge of the South Asian summer monsoon dynamics remains limited due to scarcity of high-resolution monsoon precipitation records across timescales. To date, most information regarding the past variability of SAM precipitation comes from numerous wind-based and upwelling records from the Arabian Sea, although the degree of coupling between the continental scale winds over the Arabian Sea and SAM precipitation across timescales is not well understood. Very little is known about the variability of monsoon precipitation over the Indian subcontinent and directly over the ocean despite the fact that this is the variable that defines the SAM. Consequently, our understanding of the response mechanism of SAM precipitation even to the most basic changes in insolation remains very poor. The overall goal of this PhD thesis was to provide first insights in to the insolation forcing mechanisms of SAM precipitation on orbital and sub-orbital timescales. To accomplish this goal, I employed various geochemical proxies that are independently connected to SAM precipitation changes through certain physical and chemical pathways and performed statistical analysis of SAM proxy data spanning the last ~1 million years. Within the framework of this PhD work, the major findings are summarized below:

- 1) Reconstructed surface water $\delta^{18}\text{O}$ and temperature records from site 17 in the Andaman Sea provide clear evidence in to various forcing mechanism of the monsoon and address the fundamental divergence in opinion that has long persisted in how the monsoon responds to insolation forcing. Our results show that the mean phasing and timing of SAM precipitation is driven by several factors. Over the precession band, seasonal cross-hemispherical thermal/pressure contrast controls the timing and pace of SAM precipitation and accounts for a roughly ~30 % of the total variance in SAM precipitation inferred from $\delta^{18}\text{O}_{\text{sw}}$. This provides the clearest evidence that precession

forcing cannot be considered as a primary forcing mechanism driving the monsoon system. Large amounts of variance in $\delta^{18}\text{O}_{\text{sw}}$ are also contained at heterodyne frequencies (non-primary orbital frequencies) and suggest a combined insolation (precession and obliquity driven) and ice-volume forcing (eccentricity driven). This indicates that monsoon dynamics is strongly non-linear and responds to different forcing mechanisms operating distinctly over a range of frequency bands. Taken together our records provide direct and clear evidence that precession driven variability in the Bay of Bengal is consistent with that observed in the Arabian Sea and demonstrates that monsoon circulation is primarily a response to cross equatorial transport of latent heat and ice-volume changes. More importantly, our finding suggests that obliquity forcing plays an important role pacing SAM precipitation via enhanced cross-hemispherical atmospheric moisture flux. In view of this narrative, obliquity forcing plays a role in way of monsoon intensification than previously considered through enhanced cross-hemispherical atmospheric moisture flux as obliquity decreases and NH cools and SH warms. On the other hand, speleothem $\delta^{18}\text{O}$ records from the East Asian and South Asian monsoon domain cannot be interpreted as standalone proxies of summer monsoon precipitation.

- 2) Analysis of high-resolution XRF proxy records of the monsoon provides direct and independent evidence regarding the forcing mechanisms of SAM precipitation. Consistent with $\delta^{18}\text{O}_{\text{sw}}$ records from site 17 in the Andaman Sea, these records from a nearby core provide supporting evidence that precession driven Arabian Sea productivity changes are primarily indicative of strong summer monsoon over the precession band alone. In line with $\delta^{18}\text{O}_{\text{sw}}$ records from site 17, our results suggest that obliquity forcing plays a dominant role in controlling the pace of the summer monsoon in ways that are fundamentally different than precession pacing of the monsoon. XRF proxy records further validate our hypothesis that obliquity controls the pace of the summer monsoon through enhanced cross-hemispherical

atmospheric moisture following obliquity minima in line with $\delta^{18}\text{O}_{\text{sw}}$ records from the nearby Andaman Sea sediments at site 17. This demonstrates that basin scale winds over the Arabian Sea are decoupled from continental precipitation over this frequency band.

- 3) The coupling between the mixed layer and thermocline and the forcing mechanisms driving orbital scale deeper upper ocean salinity and thermal structures is still poorly understood. Reconstructed $\delta^{18}\text{O}_{\text{MW}}$ and $\delta^{18}\text{O}_{\text{TW}}$, which approximate estimates of seawater salinity at the mixed layer and thermocline respectively, indicate the prevalence a persistent 'top-bottom' propagation of salinity to depth and common forcing of the mixed layer and thermocline over the precession band, similar to published phases of wind-based monsoon proxy records from the Arabian Sea. However, much of the variability in $\delta^{18}\text{O}_{\text{ML}}$ and $\delta^{18}\text{O}_{\text{TL}}$ records is contained at other primary and non-primary frequency bands. This also demonstrates that the link between insolation and, surface and deeper ocean variability cannot be assumed to be linear. The phase relationship between $\delta^{18}\text{O}_{\text{MW}}$ and $\delta^{18}\text{O}_{\text{TW}}$, and ETP over the obliquity band is sharply in contrast with precession timing where both $\delta^{18}\text{O}_{\text{MW}}$ and $\delta^{18}\text{O}_{\text{TW}}$ lead/lag maximum latent heat export and NH insolation respectively and reveals that both $\delta^{18}\text{O}_{\text{ML}}$ and $\delta^{18}\text{O}_{\text{TL}}$ lead maximum obliquity by $\sim 19\text{Kyr}$ s. This indicates a dominant SH influence and suggests that obliquity controls the upper ocean salinity structures via enhanced cross-hemispherical atmospheric moisture following obliquity minima.
- 4) High resolution Ba/Ca and paired Mg/Ca and $\delta^{18}\text{O}$ records demonstrate that SAM climate has undergone abrupt and strong changes during the last deglaciation due to a complex interplay of orbitally induced insolation changes and regional variability. Ba/Ca and $\delta^{18}\text{O}_{\text{sw}}$ records demonstrate that the SAM was significantly weaker during the LGM and is characterized by heavily reduced river runoff and high SSS estimates and a gradual monsoon strengthening throughout the last deglaciation. The onset of the last

deglaciation shows a gradual SAM strengthening beginning ~18 kyrs and leads the onset of deglacial monsoon strengthening inferred from Arabian Sea Ba/Ca records by ~2–3 kyrs. This demonstrates that South Asian Monsoon climate dynamics cannot be assumed to be a mere response to a simple N-S displacement of the ITCZ following insolation changes. Peak monsoon strength during the mid-Holocene in the Andaman Sea is in agreement with records obtained from other monsoon regions and is consistent with model simulations. The mid-Holocene pacing of the monsoon is linked to combined precession and obliquity forcing.

IV.2 Outlook

The present thesis investigated the forcing mechanisms of the SAM and its role in driving deeper upper ocean variability at orbital and sub-orbital scales and provides new insights into orbitally controlled monsoon dynamics. However, the study also leaves some important questions and raises new issues that should be subject of future research. Below, a list of important questions and suggestions are outlined in descending order of relevance.

- 1) Palaeo-monsoon evidence presented here demonstrates that the forcing mechanisms of the SAM during the late Quaternary period are far more complex than a direct insolation response and are strongly non-linear due to internal climate processes and feedback mechanisms. These internal climate processes can only be fully understood within the global monsoon framework and require detailed comparison of global monsoon records across timescales. In this regard, additional efforts are required to gain further understanding into possible tropical-extra tropical forcing mechanisms of the monsoon and necessities expanding the spatial network of high-resolution long-term records of both monsoon precipitation (land and ocean) and SST across both hemispheres. This would allow regional responses to be identified and understood with in

the context of the global monsoon and will lead to a better understanding of the physical processes driving the monsoon across timescales.

- 2) Our finding also suggest that the obliquity forcing might play a significant role in way of monsoon intensification than previously considered via enhanced cross-hemispherical atmospheric moisture flux as obliquity decreases and NH cools and SH warms. However, it is currently not clear how the monsoon winds would react following obliquity minima and what the exact moisture pathways are. In view of this narrative, the role of atmospheric moisture flux triggered by hemispheric insolation gradients and the feedback processes should be examined using transient model simulations.

- 3) Age model development and stratigraphy is a vital part of paleoceanographic research. Often age models are constructed based on the $\delta^{18}\text{O}$ of calcite from benthic foraminifera and aligning the records with a global benthic stack typically the LR04 (Lisiecki and Raymo, 2004). The accuracy of the tuning approach is also dependent on the resolution of the benthic records generated. Consequently, detailed analysis of the terminations is not always possible due to potential age model artifacts despite the fact that orbital scale phase relationships are estimated with great accuracy. To overcome this challenge and analyze the terminations in greater detail, an age model free of orbital assumptions such as a depth-derived age model is should be considered for further comparison.

- 4) Paleo-monsoon evidence suggests that SAM intensity has undergone abrupt changes due to insolation forcing and internal feedback mechanisms. It's also known that the monsoon was generally weaker during the LGM and stronger during the mid-Holocene. However, the

exact mechanisms driving these abrupt changes in SAM precipitation are a matter of speculation. In this regard, individual foraminiferal analysis offer unique prospects to better understand the interseasonal and interannual changes in SAM precipitation. Further studies along this line are recommended and will hopefully shade vital insights in to the various forcing mechanisms of the monsoon.

Appendix

* Published data for Chapter IV is available at
<https://doi.pangaea.de/10.1594/PANGAEA.859177>

* Unpublished XRF data (Chapter III) is attached in a CD and submitted together with this thesis.

Table S1. Benthic isotope data generated from NGHP 17 and tuned to the LR04 stack (Lisiecki and Raymo, 2005) to construct the Age model stratigraphy for NGHP 17.

Core	Depth (m)	Age Model	Foram species	$\delta^{18}\text{O}_{\text{foram}}$	Adjusted $\delta^{18}\text{O}_{\text{foram}}$
NGHP17	0.00	2.20	<i>C. wullerstorfi</i>	2.16	2.80
NGHP17	0.08	3.00	<i>C. mundulus</i>	2.29	2.93
NGHP17	0.10	3.20	<i>C.wullerstorfi</i>	2.29	2.93
NGHP17	0.18	4.00	<i>C.wullerstorfi</i>	2.07	2.71
NGHP17	0.20	4.20	<i>C.wullerstorfi</i>	2.07	2.71
NGHP17	0.28	5.00	<i>C. mundulus</i>	2.26	2.90
NGHP17	0.30	5.20	<i>C.wullerstorfi</i>	2.33	2.97
NGHP17	0.40	6.20	<i>C. mundulus</i>	2.26	2.90
NGHP17	0.50	7.20	<i>C.wullerstorfi</i>	2.34	2.98
NGHP17	0.58	8.00	<i>C.wullerstorfi</i>	2.41	3.05
NGHP17	0.60	8.15	<i>C. mundulus</i>	2.51	3.15
NGHP17	0.68	8.75	<i>C.wullerstorfi</i>	3.07	3.71
NGHP17	0.70	8.90	<i>C. mundulus</i>	2.58	3.22
NGHP17	0.78	9.50	<i>C.wullerstorfi</i>	2.42	3.06
NGHP17	0.80	9.65	<i>C.wullerstorfi</i>	2.62	3.26
NGHP17	0.86	10.10	<i>C. mundulus</i>	2.48	3.12
NGHP17	0.88	10.25	<i>C.wullerstorfi</i>	2.48	3.12
NGHP17	0.90	10.40	<i>C.wullerstorfi</i>	2.89	3.53
NGHP17	0.98	11.00	<i>C.wullerstorfi</i>	2.49	3.13
NGHP17	1.00	11.18	<i>C.wullerstorfi</i>	2.70	3.34
NGHP17	1.08	11.91	<i>C.wullerstorfi</i>	3.08	3.72
NGHP17	1.12	12.27	<i>C.wullerstorfi</i>	3.11	3.75
NGHP17	1.16	12.64	<i>C.wullerstorfi</i>	2.93	3.57
NGHP17	1.24	13.36	<i>C.wullerstorfi</i>	3.29	3.93
NGHP17	1.32	14.09	<i>C.wullerstorfi</i>	2.84	3.48
NGHP17	1.36	14.45	<i>C.wullerstorfi</i>	2.72	3.36
NGHP17	1.48	15.55	<i>C.wullerstorfi</i>	3.19	3.83
NGHP17	1.60	16.64	<i>C.wullerstorfi</i>	3.46	4.10
NGHP17	1.64	17.00	<i>C. mundulus</i>	3.27	3.91
NGHP17	1.72	17.57	<i>C.wullerstorfi</i>	2.87	3.51
NGHP17	1.80	18.14	<i>C.wullerstorfi</i>	3.83	4.47
NGHP17	1.84	18.43	<i>C.wullerstorfi</i>	3.81	4.45
NGHP17	1.92	19.00	<i>C.wullerstorfi</i>	3.77	4.41
NGHP17	1.96	19.33	<i>C.wullerstorfi</i>	3.79	4.43
NGHP17	2.00	19.67	<i>C.wullerstorfi</i>	3.57	4.21
NGHP17	2.04	20.00	<i>C.wullerstorfi</i>	3.75	4.39
NGHP17	2.08	20.33	<i>C.wullerstorfi</i>	3.69	4.33
NGHP17	2.12	20.67	<i>C.wullerstorfi</i>	3.75	4.39
NGHP17	2.16	21.00	<i>C.wullerstorfi</i>	3.72	4.36

Core	Depth (m)	Age Model	Foram species	$\delta^{18}\text{O}_{\text{foram}}$	Adjusted $\delta^{18}\text{O}_{\text{foram}}$
NGHP17	2.20	21.36	<i>C.wullerstorfi</i>	3.81	4.45
NGHP17	2.24	21.72	<i>C.wullerstorfi</i>	3.83	4.47
NGHP17	2.32	22.43	<i>C.wullerstorfi</i>	3.69	4.33
NGHP17	2.36	22.79	<i>C.wullerstorfi</i>	3.52	4.16
NGHP17	2.40	23.15	<i>C.wullerstorfi</i>	3.47	4.11
NGHP17	2.44	23.50	<i>C.wullerstorfi</i>	3.59	4.23
NGHP18	2.46	23.68	<i>C. mundulus</i>	3.72	4.36
NGHP17	2.95	28.06	<i>C.wullerstorfi</i>	3.57	4.21
NGHP17	3.05	28.96	<i>C.wullerstorfi</i>	3.33	3.97
NGHP17	3.15	29.85	<i>C.wullerstorfi</i>	3.40	4.04
NGHP17	3.25	30.74	<i>C.wullerstorfi</i>	3.37	4.01
NGHP17	3.35	31.64	<i>C. mundulus</i>	3.46	4.10
NGHP17	3.45	32.53	<i>C.wullerstorfi</i>	3.34	3.98
NGHP17	3.55	33.42	<i>C.wullerstorfi</i>	3.35	3.99
NGHP17	3.65	34.32	<i>C.wullerstorfi</i>	3.16	3.80
NGHP17	3.75	35.21	<i>C.wullerstorfi</i>	3.35	3.99
NGHP17	3.85	36.11	<i>C.wullerstorfi</i>	3.38	4.02
NGHP17	3.95	37.00	<i>C.wullerstorfi</i>	3.39	4.03
NGHP17	4.05	37.82	<i>C.wullerstorfi</i>	3.35	3.99
NGHP17	5.10	46.48	<i>C.wullerstorfi</i>	3.72	4.36
NGHP17	5.20	47.30	<i>C.wullerstorfi</i>	3.66	4.30
NGHP17	5.30	48.12	<i>C.wullerstorfi</i>	3.19	3.83
NGHP17	5.40	48.95	<i>C.wullerstorfi</i>	3.19	3.83
NGHP17	5.50	49.77	<i>C.wullerstorfi</i>	3.47	4.11
NGHP17	5.60	50.60	<i>C.wullerstorfi</i>	3.20	3.84
NGHP17	5.70	51.42	<i>C.wullerstorfi</i>	3.29	3.93
NGHP17	5.80	52.24	<i>C.wullerstorfi</i>	3.43	4.07
NGHP17	5.88	52.90	<i>C.wullerstorfi</i>	3.22	3.86
NGHP17	5.92	53.23	<i>C.wullerstorfi</i>	3.62	4.26
NGHP17	6.02	54.06	<i>C.wullerstorfi</i>	3.24	3.88
NGHP17	6.12	54.88	<i>C.wullerstorfi</i>	3.36	4.00
NGHP17	6.22	55.70	<i>C.wullerstorfi</i>	3.39	4.03
NGHP17	6.32	56.53	<i>C.wullerstorfi</i>	3.15	3.79
NGHP17	6.42	57.35	<i>C.wullerstorfi</i>	3.33	3.97
NGHP17	6.52	58.18	<i>C.wullerstorfi</i>	3.28	3.92
NGHP17	6.62	59.00	<i>C. wullerstorfi</i>	3.01	3.65
NGHP17	6.72	59.99	<i>C. mundulus</i>	3.11	3.75
NGHP17	6.82	60.98	<i>C.mundulus</i>	3.15	3.79
NGHP17	7.02	61.96	<i>C. mundulus</i>	3.11	3.75
NGHP17	7.12	63.94	<i>C. wullerstorfi</i>	2.69	3.33
NGHP17	7.22	64.43	<i>C. wullerstorfi</i>	3.01	3.65
NGHP17	7.28	64.93	<i>C. mundulus</i>	3.03	3.67
NGHP17	7.34	66.11	<i>C.wuellerstorfi</i>	3.35	3.99
NGHP17	7.44	67.10	<i>C. wullerstorfi</i>	3.10	3.74
NGHP17	7.54	68.09	<i>C.wuellerstorfi</i>	3.34	3.98
NGHP17	7.64	69.07	<i>C.wuellerstorfi</i>	3.29	3.93
NGHP17	7.74	70.06	<i>C. mundulus</i>	3.22	3.86
NGHP17	7.84	71.05	<i>C. mundulus</i>	3.22	3.86
NGHP17	7.94	72.04	<i>C.wuellerstorfi</i>	3.21	3.85
NGHP17	8.04	73.02	<i>C.mundulus</i>	2.94	3.58
NGHP17	8.14	74.01	<i>C.wuellerstorfi</i>	2.78	3.42
NGHP17	8.24	75.00	<i>C. wullerstorfi</i>	3.19	3.83
NGHP17	8.34	76.47	<i>C.wuellerstorfi</i>	2.81	3.45
NGHP17	8.42	77.65	<i>C. wullerstorfi</i>	2.94	3.58
NGHP17	8.76	82.66	<i>C.wuellerstorfi</i>	2.63	3.27
NGHP17	8.86	84.13	<i>C.wuellerstorfi</i>	2.57	3.21

Core	Depth (m)	Age Model	Foram species	$\delta^{18}\text{O}_{\text{foram}}$	Adjusted $\delta^{18}\text{O}_{\text{foram}}$
NGHP17	8.96	85.60	<i>C. mundulus</i>	2.93	3.57
NGHP17	9.06	87.18	<i>C.wuellerstorfi</i>	3.01	3.65
NGHP17	9.16	89.55	<i>C.wuellerstorfi</i>	2.92	3.56
NGHP17	9.26	91.92	<i>C. mundulus</i>	2.71	3.35
NGHP17	9.36	94.30	<i>C.wuellerstorfi</i>	2.65	3.29
NGHP17	9.56	99.04	<i>C.wuellerstorfi</i>	2.78	3.42
NGHP17	9.76	103.79	<i>C.wuellerstorfi</i>	2.71	3.35
NGHP17	9.86	106.16	<i>C.wuellerstorfi</i>	2.78	3.42
NGHP17	9.96	108.55	<i>C. wuellerstorfi</i>	2.94	3.58
NGHP17	10.06	121.05	<i>C.wuellerstorfi</i>	2.19	2.83
NGHP17	10.16	124.05	<i>C.wuellerstorfi</i>	2.17	2.81
NGHP17	10.18	124.36	<i>C. wuellerstorfi</i>	2.19	2.83
NGHP17	10.28	125.91	<i>C.mundulus</i>	2.25	2.89
NGHP17	10.38	127.45	<i>C. mundulus</i>	2.51	3.15
NGHP17	10.48	129.00	<i>C. mundulus</i>	2.74	3.38
NGHP17	10.58	131.88	<i>C.wuellerstorfi</i>	3.07	3.71
NGHP17	10.68	134.76	<i>C. wuellerstorfi</i>	3.54	4.18
NGHP17	10.78	137.02	<i>C. wuellerstorfi</i>	3.57	4.21
NGHP17	10.88	139.22	<i>C.wuellerstorfi</i>	3.76	4.40
NGHP17	10.98	141.68	<i>C. mundulus</i>	3.53	4.17
NGHP17	11.08	144.14	<i>C.mundulus</i>	2.62	3.26
NGHP17	11.18	146.60	<i>C.wuellerstorfi</i>	3.55	4.19
NGHP17	11.60	156.95	<i>C.wuellerstorfi</i>	3.53	4.17
NGHP17	11.70	158.63	<i>C.wuellerstorfi</i>	3.34	3.98
NGHP17	11.80	160.32	<i>C. wuellerstorfi</i>	2.94	3.58
NGHP17	11.90	162.01	<i>C.wuellerstorfi</i>	3.41	4.05
NGHP17	12.10	165.38	<i>C. mundulus</i>	3.34	3.98
NGHP17	12.30	168.76	<i>C.wuellerstorfi</i>	3.34	3.98
NGHP17	12.40	170.44	<i>C. wuellerstorfi</i>	3.34	3.98
NGHP17	12.60	173.82	<i>C.wuellerstorfi</i>	3.13	3.77
NGHP17	12.70	175.95	<i>C. mundulus</i>	3.29	3.93
NGHP17	12.80	178.16	<i>C.mundulus</i>	3.40	4.04
NGHP17	12.90	180.36	<i>C.mundulus</i>	3.07	3.71
NGHP17	13.00	182.56	<i>C. mundulus</i>	3.26	3.90
NGHP17	13.02	183.00	<i>C.wuellerstorfi</i>	3.25	3.89
NGHP17	13.12	185.12	<i>C. mundulus</i>	3.40	4.04
NGHP17	13.22	186.08	<i>C. wuellerstorfi</i>	3.00	3.64
NGHP17	13.32	187.04	<i>C.wuellerstorfi</i>	3.22	3.86
NGHP17	13.42	188.00	<i>C. mundulus</i>	3.25	3.89
NGHP17	13.52	191.83	<i>C. wuellerstorfi</i>	2.93	3.57
NGHP17	13.62	195.68	<i>C.wuellerstorfi</i>	2.99	3.63
NGHP17	14.30	221.82	<i>C.wuellerstorfi</i>	3.07	3.71
NGHP17	14.40	225.67	<i>C. wuellerstorfi</i>	3.02	3.66
NGHP17	14.50	229.23	<i>C. mundulus</i>	2.82	3.46
NGHP17	14.60	230.23	<i>C.wuellerstorfi</i>	3.00	3.64
NGHP17	14.70	232.04	<i>C.mundulus</i>	2.95	3.59
NGHP17	14.80	233.86	<i>C. mundulus</i>	2.71	3.35
NGHP17	14.90	235.68	<i>C.wuellerstorfi</i>	2.53	3.17
NGHP17	15.00	237.50	<i>C. wuellerstorfi</i>	2.32	2.96
NGHP17	15.10	239.16	<i>C. wuellerstorfi</i>	2.14	2.78
NGHP17	15.20	240.52	<i>C. mundulus</i>	2.35	2.99
NGHP17	15.30	241.87	<i>C.wuellerstorfi</i>	2.43	3.07
NGHP17	15.44	243.77	<i>C.wuellerstorfi</i>	2.62	3.26
NGHP17	15.54	245.12	<i>C. mundulus</i>	3.07	3.71
NGHP17	15.64	246.48	<i>C. wuellerstorfi</i>	3.10	3.74
NGHP17	15.74	247.83	<i>C.wuellerstorfi</i>	2.72	3.36

Core	Depth (m)	Age Model	Foram species	$\delta^{18}\text{O}_{\text{foram}}$	Adjusted $\delta^{18}\text{O}_{\text{foram}}$
NGHP17	15.84	249.18	<i>C. wullerstorfi</i>	3.20	3.84
NGHP17	15.94	250.54	<i>C. mundulus</i>	3.03	3.67
NGHP17	16.04	251.89	<i>C.wuellerstorfi</i>	3.39	4.03
NGHP17	16.14	255.87	<i>C. wullerstorfi</i>	3.39	4.03
NGHP17	16.24	260.04	<i>C. wullerstorfi</i>	3.32	3.96
NGHP17	16.34	264.21	<i>C.wuellerstorfi</i>	3.20	3.84
NGHP17	16.54	272.55	<i>C. mundulus</i>	3.24	3.88
NGHP17	16.64	276.72	<i>C.wuellerstorfi</i>	3.25	3.89
NGHP17	16.74	282.08	<i>C. mundulus</i>	2.92	3.56
NGHP17	16.84	286.46	<i>C. wullerstorfi</i>	2.90	3.54
NGHP17	16.88	287.19	<i>C.wuellerstorfi</i>	3.23	3.87
NGHP17	16.98	289.02	<i>C. mundulus</i>	3.01	3.65
NGHP17	17.08	290.85	<i>C. wullerstorfi</i>	3.14	3.78
NGHP17	17.18	292.69	<i>C.wuellerstorfi</i>	2.99	3.63
NGHP17	17.28	294.52	<i>C. wullerstorfi</i>	3.40	4.04
NGHP17	17.38	296.00	<i>C. wullerstorfi</i>	3.30	3.94
NGHP17	17.48	297.20	<i>C.wuellerstorfi</i>	3.13	3.77
NGHP17	17.58	298.40	<i>C.mundulus</i>	2.82	3.46
NGHP17	17.78	300.80	<i>C.wuellerstorfi</i>	2.87	3.51
NGHP17	17.88	302.00	<i>C. wullerstorfi</i>	2.89	3.53
NGHP17	18.33	307.40	<i>C.wuellerstorfi</i>	2.94	3.58
NGHP17	18.43	308.60	<i>C. mundulus</i>	2.91	3.55
NGHP17	18.53	309.80	<i>C. wullerstorfi</i>	2.76	3.40
NGHP17	18.63	311.00	<i>C.wuellerstorfi</i>	2.66	3.30
NGHP17	18.73	317.00	<i>C. wullerstorfi</i>	2.78	3.42
NGHP17	18.83	320.50	<i>C. wullerstorfi</i>	2.65	3.29
NGHP17	18.93	324.00	<i>C.wuellerstorfi</i>	2.40	3.04
NGHP17	19.13	329.00	<i>C. wullerstorfi</i>	2.44	3.08
NGHP17	19.23	330.81	<i>C.wuellerstorfi</i>	2.60	3.24
NGHP17	19.33	332.62	<i>C.mundulus</i>	2.67	3.31
NGHP17	19.43	334.43	<i>C.mundulus</i>	2.71	3.35
NGHP17	19.53	336.24	<i>C.wuellerstorfi</i>	2.79	3.43
NGHP17	19.63	338.05	<i>C. mundulus</i>	3.16	3.80
NGHP17	19.73	339.86	<i>C. mundulus</i>	3.17	3.81
NGHP17	19.77	340.59	<i>C.wuellerstorfi</i>	3.67	4.31
NGHP17	19.97	346.14	<i>C. wullerstorfi</i>	3.32	3.96
NGHP17	20.07	349.13	<i>C.wuellerstorfi</i>	3.39	4.03
NGHP17	20.17	352.11	<i>C. mundulus</i>	3.07	3.71
NGHP17	20.27	355.09	<i>C. wullerstorfi</i>	3.03	3.67
NGHP17	20.37	358.07	<i>C.wuellerstorfi</i>	3.08	3.72
NGHP17	20.47	361.05	<i>C. wullerstorfi</i>	3.21	3.85
NGHP17	20.57	364.03	<i>C. wullerstorfi</i>	3.28	3.92
NGHP17	20.67	367.01	<i>C.wuellerstorfi</i>	3.21	3.85
NGHP17	21.21	383.10	<i>C.wuellerstorfi</i>	2.91	3.55
NGHP17	21.31	386.08	<i>C. mundulus</i>	2.97	3.61
NGHP17	21.41	389.06	<i>C. mundulus</i>	2.72	3.36
NGHP17	21.51	392.04	<i>C.wuellerstorfi</i>	2.78	3.42
NGHP17	21.61	395.02	<i>C. wullerstorfi</i>	2.69	3.33
NGHP17	21.71	398.00	<i>C. wullerstorfi</i>	2.86	3.50
NGHP17	21.81	405.05	<i>C.wuellerstorfi</i>	2.55	3.19
NGHP17	21.91	414.54	<i>C. wullerstorfi</i>	2.62	3.26
NGHP17	22.01	420.80	<i>C. wullerstorfi</i>	2.93	3.57
NGHP17	22.11	427.06	<i>C.wuellerstorfi</i>	3.26	3.90
NGHP17	22.17	430.81	<i>C.wuellerstorfi</i>	3.68	4.32
NGHP17	22.27	432.93	<i>C. mundulus</i>	3.66	4.30
NGHP17	22.37	434.77	<i>C. wullerstorfi</i>	3.38	4.02

Core	Depth (m)	Age Model	Foram species	$\delta^{18}\text{O}_{\text{foram}}$	Adjusted $\delta^{18}\text{O}_{\text{foram}}$
NGHP17	22.47	435.47	<i>C.mundulus</i>	3.80	4.44
NGHP17	22.57	436.16	<i>C. mundulus</i>	3.87	4.51
NGHP17	22.67	438.20	<i>C. wullerstorfi</i>	3.55	4.19
NGHP17	22.77	440.24	<i>C.wuellerstorfi</i>	3.17	3.81
NGHP17	23.50	455.14	<i>C.wuellerstorfi</i>	3.25	3.89
NGHP17	23.80	461.26	<i>C. wullerstorfi</i>	2.64	3.28
NGHP17	23.90	463.30	<i>C.wuellerstorfi</i>	3.04	3.68
NGHP17	24.00	465.34	<i>C. wullerstorfi</i>	2.73	3.37
NGHP17	24.10	467.38	<i>C.wuellerstorfi</i>	3.11	3.75
NGHP17	24.20	469.42	<i>C. mundulus</i>	2.91	3.55
NGHP17	24.30	471.46	<i>C. wullerstorfi</i>	2.65	3.29
NGHP17	24.40	473.50	<i>C.wuellerstorfi</i>	3.19	3.83
NGHP17	24.50	477.99	<i>C. wullerstorfi</i>	3.30	3.94
NGHP17	24.60	488.73	<i>C. mundulus</i>	2.79	3.43
NGHP17	24.70	494.44	<i>C.wuellerstorfi</i>	2.86	3.50
NGHP17	24.80	498.45	<i>C. mundulus</i>	2.90	3.54
NGHP17	24.95	504.46	<i>C.mundulus</i>	2.96	3.60
NGHP17	25.05	508.47	<i>C. mundulus</i>	3.15	3.79
NGHP17	25.25	515.23	<i>C.wuellerstorfi</i>	3.16	3.80
NGHP17	25.45	520.12	<i>C. mundulus</i>	3.01	3.65
NGHP17	25.55	522.57	<i>C.mundulus</i>	2.97	3.61
NGHP17	25.75	527.46	<i>C. wullerstorfi</i>	2.84	3.48
NGHP17	25.85	529.90	<i>C.wuellerstorfi</i>	2.90	3.54
NGHP17	25.95	532.35	<i>C. mundulus</i>	3.07	3.71
NGHP17	26.05	534.79	<i>C. wullerstorfi</i>	2.71	3.35
NGHP17	26.15	537.24	<i>C.wuellerstorfi</i>	3.14	3.78
NGHP17	26.25	539.93	<i>C. wullerstorfi</i>	3.42	4.06
NGHP17	26.35	543.28	<i>C. wullerstorfi</i>	3.07	3.71
NGHP17	26.40	544.96	<i>C.wuellerstorfi</i>	3.16	3.80
NGHP17	26.50	548.31	<i>C. mundulus</i>	3.31	3.95
NGHP17	26.60	551.67	<i>C. wullerstorfi</i>	3.16	3.80
NGHP17	26.70	555.02	<i>C.wuellerstorfi</i>	3.13	3.77
NGHP17	26.80	558.38	<i>C. wullerstorfi</i>	2.96	3.60
NGHP17	26.90	561.73	<i>C.mundulus</i>	2.64	3.28
NGHP17	27.00	565.08	<i>C.wuellerstorfi</i>	2.55	3.19
NGHP17	27.10	568.44	<i>C. wullerstorfi</i>	2.64	3.28
NGHP17	27.20	571.79	<i>C. wullerstorfi</i>	2.58	3.22
NGHP17	27.30	575.15	<i>C.wuellerstorfi</i>	2.33	2.97
NGHP17	27.40	579.52	<i>C. wullerstorfi</i>	2.44	3.08
NGHP17	27.85	600.38	<i>C. wullerstorfi</i>	3.05	3.69
NGHP17	28.05	611.66	<i>C.wuellerstorfi</i>	2.41	3.05
NGHP17	28.25	614.49	<i>C. wullerstorfi</i>	2.70	3.34
NGHP17	28.45	617.32	<i>C.wuellerstorfi</i>	3.26	3.90
NGHP17	28.65	620.15	<i>C. wullerstorfi</i>	2.87	3.51
NGHP17	28.85	622.98	<i>C.mundulus</i>	2.85	3.49
NGHP17	29.05	625.82	<i>C.wuellerstorfi</i>	3.51	4.15
NGHP17	29.25	628.65	<i>C. wullerstorfi</i>	3.76	4.40
NGHP17	29.40	632.56	<i>C.wuellerstorfi</i>	3.50	4.14
NGHP17	29.60	637.89	<i>C. wullerstorfi</i>	3.49	4.13
NGHP17	29.80	643.22	<i>C. wullerstorfi</i>	3.33	3.97
NGHP17	30.20	653.89	<i>C.mundulus</i>	3.01	3.65
NGHP17	30.80	669.89	<i>C.mundulus</i>	3.23	3.87
NGHP17	31.00	675.23	<i>C. wullerstorfi</i>	3.12	3.76
NGHP17	31.20	680.56	<i>C.wuellerstorfi</i>	2.71	3.35
NGHP17	31.40	685.89	<i>C. mundulus</i>	2.92	3.56
NGHP17	31.60	691.23	<i>C.wuellerstorfi</i>	2.74	3.38

Core	Depth (m)	Age Model	Foram species	$\delta^{18}\text{O}_{\text{foram}}$	Adjusted $\delta^{18}\text{O}_{\text{foram}}$
NGHP17	31.71	694.16	<i>C.mundulus</i>	2.38	3.02
NGHP17	31.91	698.60	<i>C.wuellerstorfi</i>	2.50	3.14
NGHP17	32.11	701.65	<i>C. mundulus</i>	2.82	3.46
NGHP17	32.31	704.71	<i>C.mundulus</i>	2.79	3.43
NGHP17	33.00	715.25	<i>C.mundulus</i>	2.98	3.62
NGHP17	33.20	718.46	<i>C.mundulus</i>	3.23	3.87
NGHP17	33.40	723.21	<i>C.wuellerstorfi</i>	2.90	3.54
NGHP17	33.60	727.96	<i>C. wuellerstorfi</i>	2.99	3.63
NGHP17	33.80	732.70	<i>C.wuellerstorfi</i>	2.88	3.52
NGHP17	34.00	737.45	<i>C. mundulus</i>	3.06	3.70
NGHP17	34.20	742.20	<i>C.mundulus</i>	2.91	3.55
NGHP17	34.40	746.94	<i>C. wuellerstorfi</i>	3.24	3.88
NGHP17	34.58	750.96	<i>C.wuellerstorfi</i>	3.20	3.84
NGHP17	34.78	755.42	<i>C. wuellerstorfi</i>	2.93	3.57
NGHP17	34.98	759.88	<i>C.mundulus</i>	3.07	3.71
NGHP17	35.38	768.79	<i>C. wuellerstorfi</i>	2.94	3.58
NGHP17	35.58	773.25	<i>C. wuellerstorfi</i>	2.80	3.44
NGHP17	35.71	776.15	<i>C.wuellerstorfi</i>	2.67	3.31
NGHP17	35.96	781.72	<i>C.wuellerstorfi</i>	2.74	3.38
NGHP17	36.16	786.18	<i>C. mundulus</i>	2.81	3.45
NGHP17	36.36	790.64	<i>C.wuellerstorfi</i>	2.95	3.59
NGHP17	36.56	795.10	<i>C. wuellerstorfi</i>	3.32	3.96
NGHP17	36.76	799.55	<i>C.mundulus</i>	3.39	4.03
NGHP17	36.96	808.91	<i>C. wuellerstorfi</i>	3.28	3.92
NGHP17	37.16	818.37	<i>C.wuellerstorfi</i>	3.10	3.74
NGHP17	37.36	827.83	<i>C.mundulus</i>	2.90	3.54
NGHP17	37.53	835.87	<i>C.mundulus</i>	2.83	3.47
NGHP17	37.73	845.33	<i>C.mundulus</i>	2.51	3.15
NGHP17	37.93	849.34	<i>C.wuellerstorfi</i>	2.54	3.18
NGHP17	38.13	853.01	<i>C. wuellerstorfi</i>	2.66	3.30
NGHP17	38.33	856.67	<i>C.wuellerstorfi</i>	2.48	3.12
NGHP17	38.53	860.22	<i>C.mundulus</i>	2.43	3.07
NGHP17	38.73	862.59	<i>C.wuellerstorfi</i>	2.65	3.29
NGHP17	38.91	864.72	<i>C.mundulus</i>	2.41	3.05
NGHP17	39.31	869.45	<i>C. mundulus</i>	2.91	3.55
NGHP17	39.51	871.81	<i>C.wuellerstorfi</i>	3.30	3.94
NGHP17	39.71	874.18	<i>C. mundulus</i>	3.29	3.93
NGHP17	39.84	875.71	<i>C. wuellerstorfi</i>	3.45	4.09
NGHP17	40.59	890.10	<i>C. mundulus</i>	2.84	3.48
NGHP17	40.79	891.96	<i>C. wuellerstorfi</i>	2.93	3.57
NGHP17	40.99	892.88	<i>C.mundulus</i>	3.20	3.84
NGHP17	41.19	893.80	<i>C. wuellerstorfi</i>	3.00	3.64
NGHP17	41.39	894.72	<i>C. mundulus</i>	2.91	3.55
NGHP17	41.59	895.65	<i>C.mundulus</i>	2.96	3.60
NGHP17	41.79	896.57	<i>C. wuellerstorfi</i>	2.97	3.61
NGHP17	41.87	898.85	<i>C. wuellerstorfi</i>	2.81	3.45
NGHP17	42.07	900.19	<i>C.wuellerstorfi</i>	3.21	3.85
NGHP17	42.20	901.07	<i>C. wuellerstorfi</i>	3.24	3.88
NGHP17	42.50	903.08	<i>C.wuellerstorfi</i>	2.37	3.01
NGHP17	42.90	905.77	<i>C. mundulus</i>	2.95	3.59
NGHP17	43.30	908.46	<i>C. wuellerstorfi</i>	2.60	3.24
NGHP17	43.50	909.81	<i>C. wuellerstorfi</i>	2.62	3.26
NGHP17	43.70	911.15	<i>C.wuellerstorfi</i>	2.70	3.34
NGHP17	43.90	912.50	<i>C. wuellerstorfi</i>	2.61	3.25
NGHP17	43.95	912.84	<i>C. wuellerstorfi</i>	2.58	3.22
NGHP17	44.35	915.53	<i>C. mundulus</i>	2.84	3.48

Core	Depth (m)	Age Model	Foram species	$\delta^{18}\text{O}_{\text{foram}}$	Adjusted $\delta^{18}\text{O}_{\text{foram}}$
NGHP17	44.55	916.87	<i>C. mundulus</i>	2.76	3.40
NGHP17	44.75	918.22	<i>C. wuellerstorfi</i>	2.77	3.41
NGHP17	45.36	922.32	<i>C. wuellerstorfi</i>	3.17	3.81
NGHP17	45.96	935.82	<i>C. mundulus</i>	2.50	3.14
NGHP17	46.16	940.38	<i>C. wuellerstorfi</i>	2.61	3.25
NGHP17	46.56	951.49	<i>C. mundulus</i>	2.50	3.14

Table S2. *G. sacculifer* Mg/Ca and $\delta^{18}\text{O}_{\text{foram}}$ data generated from core NGHP 17. The sea level (SL) records are from Rohling et al. (2014). Details of the calibration equations used to estimate $\delta^{18}\text{O}_{\text{sw}}$ and associated errors are provided in Chapter I.

Depth	Age	Mg/Ca	Temp	$\delta^{18}\text{O}_{\text{foram}}$	$\delta^{18}\text{O}_{\text{sw}}$	SL	$\delta^{18}\text{O}_{\text{sw}} - \text{SL}$ (VPDP)
8	3.00	4.45	27.33	-2.61	-0.35	0.00	-0.35
10	3.20	4.35	27.08	-2.45	-0.25	0.00	-0.25
18	4.00	4.48	27.41	-2.59	-0.32	0.02	-0.34
38	6.00	3.97	26.06	-2.55	-0.56	0.05	-0.61
40	6.20	4.00	26.15	-2.96	-0.94	0.06	-1.00
58	8.00	4.88	28.36	-2.56	-0.09	0.08	-0.17
60	8.15	4.84	28.27	-2.32	0.14	0.08	0.05
70	8.90	4.85	28.31	-2.63	-0.17	0.10	-0.27
78	9.50	4.56	27.61	-2.33	-0.02	0.12	-0.13
100	11.18	4.15	26.56	-1.69	0.40	0.20	0.20
108	11.91	4.78	28.14	-1.54	0.89	0.25	0.64
112	12.27	4.70	27.94	-1.00	1.38	0.28	1.10
124	13.36	4.24	26.80	-1.78	0.37	0.37	-0.01
132	14.09	4.00	26.14	-1.31	0.69	0.43	0.26
136	14.45	3.85	25.73	-0.85	1.07	0.47	0.60
148	15.55	3.58	24.91	-0.24	1.51	0.60	0.91
172	17.57	3.49	24.64	-0.56	1.14	0.84	0.30
184	18.43	3.27	23.92	-0.79	0.76	0.93	-0.18
188	18.71	3.89	25.86	-0.94	1.01	0.96	0.05
192	19.00	4.07	26.34	-1.28	0.77	0.99	-0.22
196	19.33	3.85	25.73	-0.62	1.30	1.00	0.30
200	19.67	4.14	26.53	-0.75	1.34	1.01	0.32
212	20.67	3.59	24.97	-0.98	0.78	1.06	-0.27
220	21.36	4.21	26.71	-0.81	1.32	1.08	0.25
224	21.72	3.86	25.75	-1.20	0.73	1.08	-0.35
236	22.79	3.69	25.26	-0.71	1.12	1.08	0.04
240	23.15	3.88	25.81	-0.84	1.10	1.08	0.03
305	28.96	4.02	26.22	-1.11	0.91	1.00	-0.09
315	29.85	3.55	24.83	-1.30	0.44	1.02	-0.58
335	31.64	3.65	25.13	-1.11	0.69	0.99	-0.30
355	33.42	3.58	24.93	-1.04	0.72	0.92	-0.20
365	34.32	4.22	26.74	-1.31	0.83	0.87	-0.04
375	35.21	3.73	25.37	-1.19	0.66	0.85	-0.19
385	36.11	3.92	25.93	-1.21	0.76	0.86	-0.10
405	37.82	3.84	25.71	-1.01	0.91	0.91	-0.01
450	41.53	3.98	26.10	-1.20	0.80	0.79	0.01
530	48.12	3.58	24.91	-1.74	0.01	0.53	-0.51
560	50.60	4.05	26.30	-1.21	0.83	0.55	0.28
570	51.42	4.10	26.44	-1.16	0.91	0.56	0.35
580	52.24	3.64	25.12	-1.15	0.65	0.56	0.08
588	52.90	3.61	25.01	-1.28	0.49	0.57	-0.08
602	54.06	3.88	25.81	-0.94	1.00	0.59	0.41
622	55.70	4.15	26.55	-1.36	0.74	0.63	0.10

Depth	Age	Mg/Ca	Temp	$\delta^{18}\text{O}_{\text{foram}}$	$\delta^{18}\text{O}_{\text{sw}}$	SL	$\delta^{18}\text{O}_{\text{sw}} - \text{SL}$ (VPDP)
632	56.53	3.64	25.12	-1.49	0.30	0.65	-0.35
662	59.00	3.74	25.40	-1.55	0.31	0.67	-0.36
672	59.99	4.03	26.23	-1.54	0.49	0.67	-0.18
682	60.98	3.74	25.41	-1.45	0.40	0.68	-0.27
692	61.47	3.42	24.43	-1.80	-0.15	0.69	-0.84
702	61.96	4.01	26.17	-1.73	0.28	0.70	-0.42
712	63.94	3.64	25.12	-1.16	0.64	0.71	-0.08
722	64.43	3.55	24.83	-0.99	0.75	0.71	0.03
728	64.93	3.49	24.63	-1.08	0.61	0.71	-0.10
734	66.11	3.47	24.56	-1.14	0.54	0.66	-0.13
744	67.10	3.53	24.76	-1.25	0.48	0.63	-0.16
754	68.09	3.37	24.24	-1.01	0.60	0.61	-0.01
764	69.07	3.39	24.32	-1.00	0.63	0.59	0.04
774	70.06	3.51	24.71	-1.32	0.39	0.60	-0.21
784	71.05	3.54	24.79	-1.23	0.50	0.60	-0.10
794	72.04	3.52	24.72	-1.34	0.38	0.61	-0.23
804	73.02	3.74	25.41	-1.42	0.43	0.58	-0.15
814	74.01	3.40	24.35	-1.25	0.38	0.50	-0.12
824	75.00	3.94	25.98	-2.29	-0.31	0.45	-0.76
834	76.47	3.41	24.37	-1.74	-0.10	0.33	-0.43
842	77.65	3.72	25.34	-1.93	-0.09	0.25	-0.34
876	82.66	3.69	25.26	-1.57	0.26	0.37	-0.11
896	85.60	3.84	25.70	-1.81	0.11	0.42	-0.31
916	89.55	3.76	25.45	-1.55	0.32	0.46	-0.15
926	91.92	3.92	25.94	-1.80	0.17	0.40	-0.24
936	94.30	3.88	25.82	-1.90	0.04	0.32	-0.28
946	96.67	3.82	25.63	-2.22	-0.31	0.16	-0.47
956	99.04	4.11	26.44	-2.08	-0.01	0.10	-0.10
976	103.79	4.01	26.18	-1.82	0.20	0.09	0.10
986	106.16	3.84	25.70	-1.56	0.36	0.17	0.19
996	108.55	4.54	27.57	-1.34	0.96	0.34	0.63
1006	121.05	4.15	26.57	-2.70	-0.60	0.06	-0.66
1016	124.05	4.23	26.78	-2.27	-0.12	0.12	-0.24
1018	124.36	4.38	27.17	-1.63	0.59	0.13	0.46
1028	125.91	4.04	26.25	-1.06	0.97	0.16	0.81
1038	127.45	4.19	26.66	-1.04	1.08	0.19	0.89
1048	129.00	4.19	26.67	-0.88	1.24	0.22	1.02
1058	131.88	3.76	25.46	-0.73	1.14	0.37	0.77
1068	134.76	4.08	26.38	-0.91	1.14	0.69	0.46
1078	137.02	4.01	26.17	-1.08	0.94	0.86	0.08
1088	139.22	3.65	25.13	-0.80	1.00	0.79	0.21
1118	146.60	3.68	25.21	-0.90	0.91	0.61	0.30
1170	158.63	3.65	25.13	-1.42	0.38	0.55	-0.17
1180	160.32	4.09	26.41	-0.91	1.15	0.50	0.65
1190	162.01	3.62	25.06	-1.16	0.62	0.52	0.10
1210	165.38	4.33	27.03	-0.65	1.54	0.42	1.12
1230	168.76	3.76	25.46	-0.85	1.02	0.48	0.54
1240	170.44	3.87	25.78	-0.92	1.01	0.46	0.56
1250	172.13	3.63	25.07	-1.19	0.59	0.41	0.19
1260	173.82	3.49	24.62	-0.79	0.90	0.36	0.54
1280	178.16	3.79	25.56	-0.86	1.03	0.31	0.72
1290	180.36	3.51	24.69	-0.82	0.89	0.38	0.50
1300	182.56	3.70	25.28	-1.28	0.55	0.46	0.09
1302	183.00	3.41	24.39	-1.94	-0.30	0.46	-0.76
1312	185.12	3.47	24.58	-1.47	0.21	0.43	-0.22
1322	186.08	3.38	24.28	-1.71	-0.09	0.40	-0.48

Depth	Age	Mg/Ca	Temp	$\delta^{18}\text{O}_{\text{foram}}$	$\delta^{18}\text{O}_{\text{sw}}$	SL	$\delta^{18}\text{O}_{\text{sw}} - \text{SL}$ (VPDP)
1332	187.04	3.46	24.56	-1.38	0.30	0.37	-0.07
1342	188.00	3.75	25.44	-1.99	-0.13	0.35	-0.48
1352	191.83	3.65	25.12	-1.58	0.22	0.22	0.00
1430	221.82	3.46	24.54	-1.10	0.58	-0.10	0.68
1440	225.67	3.54	24.78	-1.25	0.47	0.17	0.30
1450	229.23	3.78	25.53	-1.48	0.40	0.39	0.01
1460	230.23	3.87	25.80	-1.15	0.79	0.40	0.39
1470	232.04	3.96	26.03	-1.22	0.76	0.33	0.43
1480	233.86	3.70	25.29	-1.76	0.07	0.19	-0.12
1490	235.68	3.52	24.72	-1.70	0.02	0.06	-0.04
1500	237.50	4.09	26.41	-2.51	-0.45	-0.01	-0.44
1510	239.16	4.07	26.36	-2.67	-0.61	0.05	-0.66
1530	241.87	3.90	25.88	-1.92	0.03	0.22	-0.18
1544	243.77	3.79	25.54	-1.28	0.60	0.27	0.34
1554	245.12	3.84	25.71	-1.29	0.63	0.27	0.37
1564	246.48	3.94	25.98	-1.23	0.75	0.32	0.43
1574	247.83	3.78	25.53	-0.88	1.01	0.40	0.61
1584	249.18	3.95	26.01	-1.12	0.87	0.47	0.40
1594	250.54	3.85	25.73	-1.02	0.90	0.55	0.35
1604	251.89	3.70	25.28	-0.81	1.02	0.59	0.43
1614	255.87	3.74	25.42	-0.94	0.91	0.56	0.36
1624	260.04	3.55	24.84	-1.30	0.44	0.53	-0.09
1634	264.21	3.51	24.70	-1.35	0.36	0.63	-0.27
1644	268.38	3.77	25.50	-1.49	0.39	0.73	-0.35
1654	272.55	3.61	25.01	-1.23	0.55	0.79	-0.25
1664	276.72	3.50	24.68	-1.31	0.39	0.67	-0.28
1674	282.08	3.68	25.22	-1.24	0.57	0.37	0.20
1684	286.46	3.83	25.68	-1.13	0.78	0.11	0.68
1688	287.19	3.42	24.42	-1.02	0.64	0.10	0.53
1708	290.85	3.77	25.49	-0.88	0.99	0.31	0.68
1718	292.69	3.77	25.50	-0.72	1.16	0.43	0.73
1728	294.52	4.11	26.46	-1.25	0.82	0.47	0.35
1738	296.00	3.66	25.16	-0.87	0.93	0.43	0.50
1748	297.20	3.40	24.35	-1.19	0.45	0.38	0.07
1758	298.40	3.42	24.42	-1.48	0.17	0.35	-0.18
1768	299.60	3.85	25.72	-1.74	0.18	0.33	-0.15
1778	300.80	3.61	25.01	-1.56	0.22	0.33	-0.11
1788	302.00	3.64	25.10	-2.12	-0.33	0.30	-0.62
1833	307.40	3.51	24.71	-1.49	0.22	0.29	-0.07
1843	308.60	3.69	25.25	-1.54	0.29	0.30	-0.01
1853	309.80	3.76	25.47	-1.24	0.63	0.32	0.32
1863	311.00	3.72	25.34	-1.58	0.27	0.32	-0.06
1873	317.00	3.77	25.48	-1.86	0.02	0.36	-0.35
1883	320.50	3.64	25.12	-1.66	0.13	0.28	-0.15
1893	324.00	3.57	24.89	-1.96	-0.21	0.06	-0.27
1913	329.00	4.05	26.29	-2.05	-0.01	0.06	-0.07
1923	330.81	4.15	26.57	-2.13	-0.04	0.08	-0.11
1933	332.62	3.80	25.59	-1.76	0.13	0.09	0.04
1943	334.43	3.82	25.63	-1.04	0.86	0.11	0.75
1953	336.24	3.89	25.84	-0.72	1.23	0.21	1.01
1973	339.86	3.69	25.26	-0.58	1.25	0.44	0.80
1977	340.59	3.85	25.73	-0.71	1.22	0.46	0.75
1987	343.37	3.72	25.35	-1.07	0.78	0.51	0.26
1997	346.14	3.41	24.38	-1.16	0.48	0.56	-0.07
2007	349.13	3.59	24.94	-1.05	0.71	0.56	0.15
2017	352.11	3.91	25.91	-1.17	0.80	0.63	0.17

Depth	Age	Mg/Ca	Temp	$\delta^{18}\text{O}_{\text{foram}}$	$\delta^{18}\text{O}_{\text{sw}}$	SL	$\delta^{18}\text{O}_{\text{sw}} - \text{SL}$ (VPDP)
2027	355.09	3.66	25.18	-1.09	0.72	0.69	0.03
2037	358.07	3.66	25.17	-0.89	0.92	0.68	0.24
2047	361.05	3.54	24.78	-0.71	1.02	0.57	0.45
2057	364.03	3.56	24.85	-1.22	0.52	0.47	0.05
2067	367.01	3.52	24.72	-1.28	0.44	0.40	0.03
2121	383.10	3.69	25.26	-2.00	-0.17	0.32	-0.49
2131	386.08	3.79	25.57	-1.31	0.58	0.40	0.18
2141	389.06	3.99	26.13	-2.10	-0.09	0.31	-0.40
2151	392.04	3.87	25.79	-1.90	0.04	0.14	-0.10
2161	395.02	4.10	26.43	-1.72	0.35	0.08	0.28
2171	398.00	4.63	27.78	-2.10	0.25	0.05	0.20
2181	405.05	4.49	27.44	-1.59	0.69	0.18	0.51
2191	414.54	4.53	27.55	-1.41	0.89	-0.10	0.99
2201	420.80	4.49	27.43	-1.42	0.86	-0.09	0.95
2211	427.06	4.15	26.57	-0.95	1.14	0.06	1.09
2217	430.81	3.87	25.78	-0.50	1.43	0.18	1.25
2227	432.93	4.30	26.95	-1.45	0.73	0.21	0.52
2237	434.77	4.13	26.50	-1.00	1.08	0.20	0.88
2247	435.47	3.76	25.47	-0.55	1.32	0.18	1.14
2257	436.16	3.80	25.57	-0.62	1.27	0.14	1.13
2267	438.20	3.66	25.16	-0.79	1.02	0.00	1.01
2277	440.24	3.83	25.67	-0.89	1.02	-0.12	1.13
2350	455.14	3.74	25.40	-1.04	0.81	0.58	0.23
2360	457.18	3.77	25.50	-1.36	0.51	0.46	0.05
2370	459.22	3.92	25.93	-2.42	-0.46	0.49	-0.94
2390	463.30	3.96	26.04	-1.33	0.66	0.65	0.01
2410	467.38	3.80	25.58	-1.98	-0.09	0.66	-0.75
2440	473.50	4.19	26.66	-1.96	0.15	0.28	-0.12
2470	494.44	3.60	24.97	-2.27	-0.50	0.07	-0.57
2480	498.45	3.92	25.92	-2.41	-0.45	0.07	-0.52
2495	504.46	3.62	25.04	-2.05	-0.27	0.08	-0.35
2505	508.47	4.29	26.94	-2.00	0.18	0.17	0.00
2515	511.85	3.78	25.54	-2.02	-0.13	0.23	-0.37
2525	515.23	3.92	25.93	-1.64	0.33	0.27	0.06
2535	517.68	3.85	25.74	-1.87	0.06	0.20	-0.15
2555	522.57	3.59	24.97	-1.60	0.16	0.15	0.01
2575	527.46	4.25	26.82	-1.76	0.39	-0.05	0.44
2595	532.35	4.41	27.25	-1.26	0.98	-0.11	1.10
2615	537.24	3.50	24.67	-1.38	0.33	-0.05	0.37
2640	544.96	3.33	24.12	-1.63	-0.04	0.29	-0.33
2650	548.31	3.84	25.71	-1.77	0.15	0.05	0.10
2660	551.67	4.39	27.18	-1.39	0.84	0.02	0.81
2700	565.08	3.88	25.83	-1.73	0.22	0.05	0.17
2730	575.15	4.57	27.63	-2.65	-0.33	-0.03	-0.30
2785	600.38	3.92	25.92	-1.55	0.42	-0.01	0.42
2805	611.66	4.02	26.20	-1.53	0.49	-0.11	0.60
2825	614.49	4.48	27.41	-2.41	-0.14	-0.11	-0.03
2845	617.32	4.14	26.53	-2.19	-0.10	-0.11	0.00
2885	622.98	4.26	26.86	-0.87	1.28	-0.08	1.37
2905	625.82	4.06	26.31	-0.55	1.49	0.09	1.40
2925	628.65	3.86	25.76	-0.89	1.04	0.25	0.79
2940	632.56	3.78	25.52	-0.51	1.37	0.28	1.09
2980	643.22	3.56	24.86	-1.33	0.41	-0.19	0.59
3020	653.89	3.69	25.27	-1.11	0.72	0.15	0.57
3080	669.89	3.72	25.34	-1.61	0.23	0.47	-0.25
3120	680.56	4.39	27.18	-1.58	0.64	0.45	0.19

Depth	Age	Mg/Ca	Temp	$\delta^{18}\text{O}_{\text{foram}}$	$\delta^{18}\text{O}_{\text{sw}}$	SL	$\delta^{18}\text{O}_{\text{sw}} - \text{SL}$ (VPDP)
3160	691.23	4.72	27.99	-2.38	0.01	0.05	-0.04
3171	694.16	4.31	26.98	-2.39	-0.20	0.20	-0.40
3191	698.60	4.15	26.58	-2.10	0.00	0.14	-0.14
3231	704.71	4.43	27.28	-2.20	0.05	0.05	0.00
3300	715.25	4.18	26.63	-1.33	0.78	0.43	0.35
3320	718.46	3.59	24.94	-1.40	0.35	0.59	-0.24
3340	723.21	3.97	26.07	-1.80	0.19	0.44	-0.24
3360	727.96	3.78	25.53	-0.95	0.93	0.11	0.82
3380	732.70	4.07	26.35	-1.56	0.49	0.03	0.45
3420	742.20	3.80	25.57	-0.70	1.19	0.48	0.71
3440	746.94	3.47	24.57	-1.20	0.49	0.51	-0.02
3458	750.96	3.50	24.67	-1.26	0.44	0.49	-0.05
3478	755.42	3.44	24.47	-1.27	0.39	0.48	-0.09
3498	759.88	3.87	25.80	-1.62	0.32	0.45	-0.14
3518	764.34	3.95	26.01	-1.79	0.19	0.31	-0.12
3558	773.25	4.13	26.51	-1.77	0.32	0.05	0.27
3571	776.15	3.78	25.53	-2.02	-0.14	0.03	-0.16
3596	781.72	3.89	25.85	-1.44	0.51	-0.01	0.52
3616	786.18	3.77	25.50	-1.13	0.74	-0.04	0.79
3636	790.64	3.69	25.25	-0.70	1.12	-0.07	1.18
3656	795.10	3.57	24.90	-1.02	0.73	0.15	0.58
3676	799.55	3.63	25.07	-1.10	0.68	0.55	0.13
3736	827.83	3.55	24.84	-1.49	0.25	0.03	0.21
3753	835.87	3.74	25.40	-1.52	0.33	0.30	0.04
3773	845.33	4.10	26.43	-1.87	0.20	0.05	0.14
3793	849.34	3.86	25.75	-1.54	0.39	-0.07	0.46
3833	856.67	4.01	26.17	-1.35	0.66	-0.01	0.67
3853	860.22	4.07	26.36	-2.16	-0.11	0.02	-0.13
3873	862.59	4.54	27.56	-2.18	0.13	0.08	0.05
3911	867.08	4.62	27.77	-2.06	0.28	0.47	-0.19
3951	871.81	4.56	27.60	-1.32	1.00	0.85	0.15
3971	874.18	4.38	27.17	-0.82	1.41	0.81	0.59
3984	875.71	4.28	26.90	-0.96	1.20	0.69	0.51
4039	886.26	3.53	24.77	-0.86	0.86	0.66	0.20
4059	890.10	3.72	25.36	-0.55	1.30	0.77	0.53
4079	891.96	3.58	24.92	-0.97	0.78	0.73	0.05
4099	892.88	3.60	24.98	-1.20	0.56	0.71	-0.15
4119	893.80	3.91	25.91	-1.46	0.50	0.70	-0.20
4159	895.65	3.96	26.05	-1.91	0.08	0.70	-0.62
4179	896.57	4.02	26.22	-1.68	0.35	0.71	-0.37
4187	898.85	3.80	25.57	-0.86	1.03	0.63	0.41
4207	900.19	3.76	25.48	-1.11	0.76	0.50	0.25
4310	907.12	4.03	26.22	-1.28	0.74	0.25	0.49
4330	908.46	4.35	27.09	-1.36	0.85	0.36	0.49
4370	911.15	4.12	26.49	-2.36	-0.28	0.48	-0.76
4455	916.87	4.28	26.90	-1.96	0.21	0.51	-0.30
4475	918.22	3.85	25.72	-2.23	-0.31	0.51	-0.82
4536	922.32	3.39	24.33	-1.53	0.11	0.49	-0.39
4596	935.82	4.14	26.55	-1.96	0.13	0.16	-0.03
4636	946.27	3.99	26.12	-2.08	-0.07	0.04	-0.11
4656	951.49	4.05	26.30	-2.59	-0.55	-0.05	-0.50

Table S3. *N. dutertrei* Mg/Ca and $\delta^{18}\text{O}_{\text{foram}}$ data generated from core NGHP 17. The sea level (SL) records are from Rohling et al. (2014). Details of the calibration equations used to estimate $\delta^{18}\text{O}_{\text{sw}}$ and associated errors are provided in Chapter III.

Depth	Age	Mg/Ca	Temp (TT)	$\delta^{18}\text{O}_{\text{foram}}$	$\delta^{18}\text{O}_{\text{sw}}$ (TL)	SL	$\delta^{18}\text{O}_{\text{TL}} - \text{SL}$ (VPDP)
8.00	3.00	2.83	23.49	-1.99	-0.54	0.00	-0.54
10.00	3.20	2.84	23.53	-2.07	-0.61	0.00	-0.61
18.00	4.00	3.03	24.23	-1.97	-0.36	0.02	-0.39
20.00	4.20	3.19	24.80	-1.95	-0.22	0.03	-0.25
28.00	5.00	2.92	23.85	-1.72	-0.19	0.04	-0.23
30.00	5.20	2.54	22.30	-1.79	-0.58	0.05	-0.63
38.00	6.00	2.60	22.56	-1.71	-0.45	0.06	-0.51
40.00	6.20	2.19	20.62	-1.81	-0.95	0.07	-1.02
50.00	7.20	2.35	21.40	-1.82	-0.80	0.09	-0.89
60.00	8.15	2.31	21.21	-1.65	-0.67	0.10	-0.77
68.00	8.75	2.58	22.45	-1.74	-0.50	0.12	-0.62
70.00	8.90	2.32	21.28	-1.85	-0.85	0.12	-0.97
88.00	10.25	2.25	20.91	-1.54	-0.63	0.18	-0.81
90.00	10.40	2.55	22.32	-1.69	-0.47	0.19	-0.67
98.00	11.00	2.67	22.84	-0.95	0.37	0.23	0.14
100.00	11.18	2.21	20.72	-0.62	0.26	0.25	0.01
112.00	12.27	2.71	23.01	-0.82	0.54	0.36	0.18
116.00	12.64	2.36	21.46	-0.84	0.19	0.39	-0.20
132.00	14.09	2.06	19.97	-0.47	0.26	0.54	-0.28
160.00	16.64	2.75	23.18	0.17	1.56	0.91	0.65
172.00	17.57	2.63	22.65	-0.45	0.83	1.05	-0.22
184.00	18.43	3.26	25.07	0.08	1.86	1.17	0.69
188.00	18.71	2.64	22.72	0.02	1.32	1.20	0.12
192.00	19.00	3.02	24.21	-0.10	1.51	1.24	0.27
200.00	19.67	2.76	23.21	-0.02	1.37	1.27	0.11
204.00	20.00	2.82	23.44	0.00	1.45	1.28	0.16
208.00	20.33	2.73	23.10	0.10	1.47	1.30	0.17
212.00	20.67	2.40	21.63	-0.05	1.02	1.32	-0.30
220.00	21.36	3.18	24.78	0.03	1.76	1.34	0.41
224.00	21.72	2.57	22.43	-0.06	1.17	1.35	-0.17
228.00	22.07	2.73	23.10	-0.18	1.19	1.35	-0.16
232.00	22.43	2.58	22.43	0.10	1.33	1.35	-0.01
236.00	22.79	3.16	24.71	0.01	1.72	1.34	0.38
244.00	23.50	2.60	22.54	0.09	1.35	1.35	0.00
246.00	23.68	3.27	25.08	-0.22	1.57	1.35	0.22
305.00	28.96	2.61	22.57	-0.37	0.89	1.26	-0.36
315.00	29.85	2.71	22.99	-0.47	0.88	1.28	-0.40
325.00	30.74	2.80	23.38	-0.41	1.02	1.26	-0.24
345.00	32.53	2.76	23.21	-0.63	0.77	1.21	-0.44
375.00	35.21	2.47	21.99	-0.85	0.29	1.06	-0.77
395.00	37.00	2.60	22.55	-0.67	0.59	1.13	-0.54
530.00	48.12	2.63	22.65	-0.25	1.03	0.66	0.37
540.00	48.95	2.69	22.92	-0.46	0.88	0.65	0.23
550.00	49.77	2.92	23.81	-0.49	1.03	0.67	0.36
560.00	50.60	2.54	22.26	-0.58	0.62	0.68	-0.06
570.00	51.42	2.84	23.52	-0.94	0.52	0.70	-0.17
580.00	52.24	2.83	23.49	-0.68	0.77	0.71	0.07
588.00	52.90	3.02	24.19	-0.84	0.77	0.72	0.05
592.00	53.23	3.27	25.09	-0.38	1.41	0.72	0.69
622.00	55.70	2.51	22.15	-1.06	0.12	0.79	-0.67
642.00	57.35	2.94	23.91	-1.31	0.23	0.83	-0.60
652.00	58.18	2.15	20.40	-1.56	-0.75	0.84	-1.59
662.00	59.00	1.99	19.59	-0.92	-0.28	0.83	-1.12
672.00	59.99	2.57	22.39	-0.84	0.38	0.84	-0.46

Depth	Age	Mg/Ca	Temp (TT)	$\delta^{18}\text{O}_{\text{foram}}$	$\delta^{18}\text{O}_{\text{sw}}(\text{TL})$	SL	$\delta^{18}\text{O}_{\text{TL}} - \text{SL}(\text{VPDP})$
682.00	60.98	2.15	20.41	-0.84	-0.02	0.85	-0.87
692.00	61.47	3.12	24.57	-0.89	0.79	0.86	-0.07
712.00	63.94	3.80	26.74	-0.34	1.79	0.89	0.90
722.00	64.43	3.59	26.14	-0.38	1.63	0.89	0.73
728.00	64.93	3.19	24.81	-0.51	1.22	0.89	0.33
734.00	66.11	3.06	24.36	-0.50	1.14	0.83	0.31
744.00	67.10	1.89	18.99	-0.33	0.19	0.79	-0.61
754.00	68.09	2.24	20.88	-0.70	0.21	0.77	-0.56
764.00	69.07	2.19	20.61	-0.65	0.20	0.74	-0.53
774.00	70.06	2.01	19.67	-0.52	0.14	0.74	-0.60
794.00	72.04	2.00	19.60	-0.69	-0.04	0.76	-0.80
814.00	74.01	2.00	19.63	-0.55	0.10	0.63	-0.53
834.00	76.47	1.97	19.47	-1.26	-0.64	0.41	-1.04
842.00	77.65	3.37	25.42	-1.38	0.48	0.31	0.17
876.00	82.66	2.52	22.20	-1.17	0.02	0.46	-0.44
886.00	84.13	2.50	22.08	-0.87	0.30	0.50	-0.20
896.00	85.60	3.23	24.94	-1.11	0.64	0.52	0.12
906.00	87.18	2.49	22.07	-1.02	0.14	0.57	-0.43
916.00	89.55	2.50	22.09	-1.10	0.07	0.58	-0.51
926.00	91.92	3.21	24.87	-1.55	0.20	0.50	-0.31
936.00	94.30	2.43	21.81	-1.45	-0.34	0.41	-0.75
946.00	96.67	2.57	22.39	-2.04	-0.81	0.20	-1.01
956.00	99.04	2.61	22.58	-1.69	-0.43	0.12	-0.55
976.00	103.79	3.08	24.43	-1.45	0.20	0.12	0.08
986.00	106.16	3.16	24.72	-1.43	0.28	0.22	0.07
996.00	108.55	2.73	23.08	-1.69	-0.31	0.42	-0.73
1006.00	121.05	3.26	25.05	-1.65	0.13	0.07	0.06
1016.00	124.05	3.70	26.47	-1.55	0.53	0.15	0.38
1028.00	125.91	3.80	26.76	-0.99	1.15	0.20	0.95
1058.00	131.88	3.13	24.61	-0.28	1.41	0.47	0.94
1068.00	134.76	3.77	26.65	-0.38	1.73	0.86	0.87
1088.00	139.22	3.05	24.31	-0.49	1.13	0.98	0.15
1118.00	146.60	2.69	22.90	-0.27	1.07	0.76	0.31
1170.00	158.63	3.26	25.06	-0.51	1.27	0.69	0.58
1190.00	162.01	2.89	23.70	-0.11	1.39	0.65	0.74
1230.00	168.76	3.15	24.68	-0.41	1.29	0.60	0.69
1240.00	170.44	2.80	23.35	-0.30	1.13	0.57	0.56
1250.00	172.13	2.99	24.07	-0.34	1.24	0.51	0.73
1260.00	173.82	3.33	25.28	-0.54	1.29	0.45	0.84
1270.00	175.95	2.45	21.87	-0.34	0.77	0.40	0.37
1280.00	178.16	2.92	23.83	-0.51	1.02	0.39	0.62
1290.00	180.36	2.75	23.15	-0.33	1.05	0.48	0.57
1300.00	182.56	2.49	22.07	-0.61	0.55	0.58	-0.03
1302.00	183.00	2.65	22.74	-0.83	0.48	0.58	-0.10
1312.00	185.12	2.56	22.38	-1.29	-0.06	0.54	-0.60
1332.00	187.04	2.66	22.78	-0.89	0.42	0.47	-0.05
1342.00	188.00	3.26	25.05	-1.18	0.60	0.43	0.17
1352.00	191.83	2.53	22.25	-1.47	-0.28	0.27	-0.55
1362.00	195.68	2.95	23.94	-0.87	0.68	0.13	0.55
1430.00	221.82	3.00	24.11	-0.75	0.83	-0.13	0.96
1440.00	225.67	2.59	22.50	-0.99	0.26	0.21	0.05
1460.00	230.23	3.39	25.48	-0.86	1.02	0.50	0.52
1470.00	232.04	2.35	21.40	-1.13	-0.11	0.41	-0.52
1480.00	233.86	2.31	21.24	-1.18	-0.19	0.24	-0.43
1490.00	235.68	3.23	24.94	-1.38	0.38	0.08	0.30
1500.00	237.50	3.14	24.63	-1.86	-0.16	-0.01	-0.16
1510.00	239.16	2.62	22.64	-1.92	-0.64	0.06	-0.70

Depth	Age	Mg/Ca	Temp (TT)	$\delta^{18}\text{O}_{\text{foram}}$	$\delta^{18}\text{O}_{\text{sw}} \text{ (TL)}$	SL	$\delta^{18}\text{O}_{\text{TL}} - \text{SL} \text{ (VPDP)}$
1530.00	241.87	3.11	24.54	-1.70	-0.03	0.27	-0.30
1544.00	243.77	3.04	24.28	-0.53	1.09	0.33	0.76
1574.00	247.83	2.99	24.08	-0.78	0.80	0.49	0.31
1604.00	251.89	2.81	23.42	-0.64	0.80	0.74	0.06
1624.00	260.04	3.08	24.42	-0.55	1.11	0.66	0.44
1634.00	264.21	3.04	24.26	-0.70	0.92	0.79	0.13
1644.00	268.38	3.63	26.25	-0.91	1.12	0.92	0.21
1664.00	276.72	3.40	25.52	-0.70	1.18	0.84	0.33
1684.00	286.46	3.25	25.02	-0.43	1.34	0.13	1.21
1688.00	287.19	3.33	25.29	-0.52	1.31	0.13	1.18
1698.00	289.02	2.97	24.03	-0.31	1.26	0.20	1.06
1708.00	290.85	3.08	24.41	-0.59	1.06	0.39	0.67
1718.00	292.69	3.08	24.43	-0.49	1.16	0.53	0.63
1728.00	294.52	3.19	24.82	-0.60	1.14	0.59	0.55
1738.00	296.00	2.86	23.62	-0.69	0.79	0.54	0.25
1758.00	298.40	2.71	22.99	-0.91	0.44	0.44	0.00
1768.00	299.60	2.68	22.88	-1.42	-0.09	0.41	-0.51
1778.00	300.80	3.08	24.42	-1.37	0.28	0.41	-0.13
1833.00	307.40	2.87	23.64	-1.18	0.31	0.36	-0.05
1843.00	308.60	2.97	24.01	-0.98	0.58	0.37	0.21
1853.00	309.80	2.93	23.88	-0.97	0.57	0.39	0.18
1863.00	311.00	3.01	24.17	-1.01	0.59	0.40	0.18
1873.00	317.00	3.15	24.66	-1.10	0.60	0.45	0.14
1883.00	320.50	3.14	24.64	-1.33	0.37	0.35	0.02
1893.00	324.00	2.94	23.90	-1.41	0.13	0.08	0.05
1923.00	330.81	3.58	26.08	-1.26	0.74	0.10	0.64
1933.00	332.62	3.35	25.34	-0.85	1.00	0.11	0.88
1943.00	334.43	3.65	26.31	-0.58	1.46	0.14	1.32
1953.00	336.24	3.13	24.59	-0.25	1.44	0.26	1.17
1963.00	338.05	3.62	26.23	-0.13	1.90	0.42	1.47
1973.00	339.86	3.38	25.44	0.15	2.01	0.56	1.46
1977.00	340.59	3.69	26.42	-0.45	1.62	0.58	1.04
1987.00	343.37	3.15	24.66	-0.67	1.03	0.64	0.39
1997.00	346.14	3.03	24.22	-0.85	0.76	0.70	0.06
2007.00	349.13	3.03	24.26	-0.66	0.96	0.70	0.26
2017.00	352.11	3.52	25.92	-0.50	1.46	0.79	0.67
2027.00	355.09	3.50	25.85	-0.64	1.31	0.87	0.45
2037.00	358.07	3.28	25.11	-0.60	1.20	0.84	0.35
2047.00	361.05	2.95	23.94	-0.69	0.86	0.71	0.15
2057.00	364.03	3.61	26.18	-0.63	1.39	0.59	0.80
2067.00	367.01	2.87	23.62	-0.71	0.78	0.50	0.27
2121.00	383.10	2.86	23.62	-1.26	0.23	0.41	-0.18
2131.00	386.08	2.95	23.95	-1.00	0.56	0.51	0.05
2141.00	389.06	2.78	23.26	-1.23	0.17	0.38	-0.21
2151.00	392.04	2.80	23.37	-1.09	0.34	0.18	0.17
2161.00	395.02	3.29	25.15	-1.07	0.73	0.10	0.63
2171.00	398.00	3.39	25.49	-1.18	0.70	0.06	0.63
2181.00	405.05	3.26	25.06	-1.13	0.65	0.22	0.43
2191.00	414.54	3.73	26.55	-0.86	1.23	-0.13	1.36
2201.00	420.80	3.29	25.16	-1.32	0.49	-0.11	0.60
2211.00	427.06	2.93	23.86	-1.04	0.49	0.07	0.42
2217.00	430.81	3.17	24.75	-0.53	1.19	0.23	0.96
2227.00	432.93	3.01	24.16	-0.74	0.86	0.26	0.59
2237.00	434.77	3.45	25.67	-0.76	1.15	0.25	0.89
2247.00	435.47	3.02	24.22	-0.44	1.17	0.22	0.95
2257.00	436.16	3.11	24.53	-0.07	1.60	0.18	1.42
2267.00	438.20	2.87	23.62	-0.26	1.22	0.00	1.22

Depth	Age	Mg/Ca	Temp (TT)	$\delta^{18}\text{O}_{\text{foram}}$	$\delta^{18}\text{O}_{\text{sw}}(\text{TL})$	SL	$\delta^{18}\text{O}_{\text{TL}}-\text{SL}(\text{VPDP})$
2277.00	440.24	3.01	24.18	-0.57	1.03	-0.15	1.17
2350.00	455.14	2.82	23.44	-0.77	0.67	0.73	-0.05
2360.00	457.18	2.73	23.10	-0.49	0.89	0.58	0.31
2370.00	459.22	3.27	25.09	-0.59	1.20	0.61	0.59
2390.00	463.30	3.12	24.58	-1.12	0.56	0.81	-0.25
2410.00	467.38	3.06	24.35	-1.31	0.33	0.83	-0.50
2440.00	473.50	3.09	24.45	-1.16	0.50	0.35	0.15
2470.00	494.44	3.07	24.37	-1.06	0.58	0.09	0.49
2495.00	504.46	2.71	23.00	-1.13	0.22	0.09	0.13
2505.00	508.47	2.56	22.35	-0.96	0.26	0.22	0.04
2525.00	515.23	2.99	24.09	-1.06	0.53	0.33	0.19
2535.00	517.68	3.25	25.03	-1.66	0.12	0.25	-0.14
2575.00	527.46	3.16	24.70	-1.30	0.41	-0.06	0.47
2585.00	529.90	3.29	25.17	-1.29	0.52	-0.12	0.64
2595.00	532.35	3.24	24.98	-0.67	1.10	-0.14	1.24
2615.00	537.24	2.89	23.70	-1.01	0.49	-0.06	0.55
2635.00	543.28	3.72	26.52	-0.80	1.28	0.41	0.88
2640.00	544.96	2.73	23.07	-0.81	0.55	0.36	0.19
2650.00	548.31	2.73	23.10	0.21	1.58	0.06	1.52
2660.00	551.67	3.41	25.55	-0.89	1.00	0.03	0.97
2670.00	555.02	3.16	24.72	-1.20	0.51	0.28	0.23
2690.00	561.73	3.53	25.93	-1.96	0.01	0.31	-0.30
2700.00	565.08	3.04	24.29	-1.39	0.24	0.06	0.18
2730.00	575.15	3.36	25.39	-1.82	0.03	-0.03	0.07
2785.00	600.38	3.58	26.10	-0.81	1.19	-0.01	1.21
2805.00	611.66	3.71	26.50	-1.15	0.94	-0.02	0.96
2825.00	614.49	4.15	27.73	-1.93	0.41	-0.07	0.48
2845.00	617.32	3.54	25.98	-1.67	0.30	-0.12	0.42
2885.00	622.98	3.97	27.24	-0.91	1.33	-0.13	1.46
2905.00	625.82	3.43	25.61	-0.13	1.77	-0.13	1.90
2925.00	628.65	3.02	24.20	-0.25	1.35	-0.14	1.49
2940.00	632.56	3.08	24.41	-0.04	1.61	-0.13	1.74
2980.00	643.22	2.85	23.58	-0.48	1.00	-0.12	1.12
3020.00	653.89	3.17	24.75	-0.39	1.33	0.22	1.11
3080.00	669.89	3.10	24.48	-0.66	1.01	0.24	0.77
3120.00	680.56	3.15	24.65	-1.19	0.51	-0.06	0.57
3160.00	691.23	3.11	24.53	-1.31	0.37	-0.28	0.65
3171.00	694.16	3.55	26.00	-1.83	0.15	-0.28	0.43
3191.00	698.60	3.85	26.91	-1.53	0.63	-0.25	0.89
3231.00	704.71	3.00	24.12	-1.65	-0.06	-0.08	0.02
3300.00	715.25	3.01	24.17	-0.33	1.27	0.31	0.96
3320.00	718.46	2.71	22.99	-0.72	0.63	0.39	0.24
3340.00	723.21	3.05	24.32	-1.51	0.12	0.60	-0.48
3380.00	732.70	2.97	24.03	-1.19	0.38	0.61	-0.24
3420.00	742.20	3.23	24.95	-0.86	0.90	0.61	0.29
3440.00	746.94	2.59	22.50	-0.95	0.30	0.65	-0.35
3458.00	750.96	3.05	24.33	-0.92	0.72	0.70	0.02
3478.00	755.42	3.27	25.07	-1.17	0.62	0.67	-0.05
3498.00	759.88	2.98	24.07	-1.10	0.48	0.61	-0.13
3518.00	764.34	3.36	25.38	-1.46	0.39	0.41	-0.02
3558.00	773.25	3.25	25.00	-1.48	0.29	0.01	0.28
3571.00	776.15	2.99	24.09	-1.67	-0.09	-0.02	-0.07
3596.00	781.72	3.44	25.65	-0.87	1.04	0.05	0.99
3616.00	786.18	3.71	26.50	-0.79	1.29	0.17	1.12
3636.00	790.64	3.74	26.58	-0.91	1.19	0.28	0.90
3656.00	795.10	3.20	24.84	-0.57	1.17	0.25	0.92
3676.00	799.55	2.93	23.85	-0.95	0.58	0.10	0.48

Depth	Age	Mg/Ca	Temp (TT)	$\delta^{18}\text{O}_{\text{foram}}$	$\delta^{18}\text{O}_{\text{sw}}(\text{TL})$	SL	$\delta^{18}\text{O}_{\text{TL}}-\text{SL}(\text{VPDP})$
3716.00	818.37	3.07	24.39	-1.03	0.62	0.27	0.35
3736.00	827.83	3.24	24.98	-0.89	0.88	0.45	0.43
3753.00	835.87	3.11	24.54	-1.20	0.48	0.73	-0.25
3773.00	845.33	3.11	24.54	-1.42	0.26	0.61	-0.35
3793.00	849.34	3.20	24.84	-1.56	0.17	0.38	-0.20
3833.00	856.67	3.36	25.40	-1.48	0.38	0.12	0.26
3853.00	860.22	3.67	26.38	-1.37	0.69	0.04	0.65
3911.00	867.08	3.57	26.05	-1.85	0.14	0.07	0.07
3931.00	869.45	3.57	26.05	-0.67	1.32	0.17	1.15
3951.00	871.81	3.46	25.70	-0.80	1.11	0.32	0.79
3971.00	874.18	3.27	25.09	0.08	1.87	0.41	1.46
3984.00	875.71	3.35	25.35	-0.32	1.53	0.46	1.06
4039.00	886.26	3.86	26.93	-0.71	1.47	0.60	0.87
4059.00	890.10	3.38	25.45	-0.13	1.74	0.62	1.12
4079.00	891.96	3.08	24.43	-0.64	1.01	0.63	0.39
4099.00	892.88	2.73	23.10	-0.78	0.60	0.63	-0.03
4119.00	893.80	2.97	24.01	-1.32	0.25	0.63	-0.38
4159.00	895.65	2.83	23.48	-1.42	0.04	0.63	-0.59
4179.00	896.57	3.32	25.26	-1.31	0.52	0.62	-0.11
4187.00	898.85	3.19	24.82	-0.72	1.02	0.62	0.40
4207.00	900.19	3.05	24.30	-1.18	0.45	0.63	-0.18
4310.00	907.12	2.95	23.93	-1.20	0.35	0.58	-0.24
4330.00	908.46	3.30	25.19	-1.02	0.79	0.58	0.21
4370.00	911.15	2.58	22.45	-2.09	-0.85	0.60	-1.45
4390.00	912.50	2.71	23.01	-1.52	-0.16	0.62	-0.78
4395.00	912.84	2.87	23.65	-1.05	0.44	0.62	-0.18
4415.00	914.18	3.19	24.82	-1.33	0.40	0.63	-0.23
4455.00	916.87	3.41	25.56	-1.26	0.63	0.60	0.02
4475.00	918.22	3.11	24.54	-2.14	-0.47	0.59	-1.05
4536.00	922.32	2.96	23.97	-1.22	0.34	0.51	-0.18
4596.00	935.82	2.57	22.43	-1.15	0.08	0.21	-0.13
4636.00	946.27	2.99	24.09	-1.73	-0.14	0.06	-0.21
4656.00	951.49	3.20	24.84	-2.00	-0.26	0.04	-0.29

Table S4. *G. sacculifer* and *N. dutertrei* Mg/Ca and $\delta^{18}\text{O}_{\text{foram}}$ data generated from core NGHP 17. The sea level (SL) records are from Rohling et al. (2014). Details of the calibration equations used to estimate $\delta^{18}\text{O}_{\text{SW}}$ and associated errors are provided in Chapter IV.

Depth	Age	<i>G. sacculifer</i> $\delta^{18}\text{O}$	<i>N. dutertrei</i> $\delta^{18}\text{O}$	Mg/Ca (<i>G. sacculifer</i>)	Mg/Ca (<i>N. dutertrei</i>)	Ba/Ca (<i>G. sacculifer</i>)
0.01	0.88	-2.727	-1.896	3.8528	2.3461	1.7318
0.03	1.14	-2.716		3.5189		1.4309
0.05	1.39	-2.487	-2.061	4.0086	2.2363	
0.07	1.64	-2.662		4.1323		
0.09	1.89	-2.541	-2.025	3.913	2.2079	2.0047
0.13	2.4	-2.488		4.0474		1.4303
0.15	2.65	-2.607	-1.803	4.1075	2.5256	2.4621
0.17	2.91	-2.548				1.6227
0.19	3.16	-2.483	-1.965	3.7069	2.5395	2.2671
0.23	3.66	-2.547	-2.158	4.1353	1.9182	2.0773
0.27	4.17	-2.838	-2.139	4.1808	2.0236	1.9668
0.31	4.67	-2.888	-1.757	3.9247	1.9337	2.4913
0.35	5.18	-2.753	-1.91	4.0828		2.4486
0.39	5.69	-2.49	-1.654	4.1729	2.3944	2.6135
0.43	6.19	-2.898	-2.251	4.7984	2.3344	
0.49	6.95	-2.898	-1.787		2.15	
0.535	7.52	-2.438	-1.973	4.5133	2.5203	1.9414
0.585	8.15	-2.68	-1.813	4.1108	2.509	1.6748
0.635	8.78	-2.469	-1.902	4.256	2.4325	
0.71	9.73	-2.305	-1.324	4.2189	2.5624	1.8132
0.785	10.61	-2.17	-1.297	3.6205	3.0987	1.7864
0.835	11.1	-1.853	-1.199	3.9536	2.5263	1.7643
0.91	11.83	-1.443	-0.956	3.7376	2.4756	1.2965
0.985	12.64	-1.315	-0.65	3.9323	2.5387	
1.035	13.28	-1.722	-0.534	4.5159	2.4212	1.5444
1.085	13.91	-1.427	-1.332	4.6453	2.2736	1.2936
1.135	14.55	-0.68	-0.877	3.6898	2.102	1.7839
1.185	15.19	-1.135		3.621	2.1387	0.958
1.235	15.83	-0.866	-0.424		2.4493	1.37
1.285	16.46	-1.371	-0.257	3.8335	2.9087	1.1912
1.335	17.1	-0.888	-0.129	4.3491		1.2943
1.385	17.74	-0.496	0.153	4.1275	2.5143	1.1581
1.435	18.37	-0.843	0.113	4.109	2.7206	0.8429
1.485	19.01	-0.48	0.253	3.6548	2.6272	0.9717
1.51	19.33	-0.26		3.2303		0.962
1.535	19.65	-0.373	0.129	3.8981	2.4476	
1.56	19.97	-0.525		3.6847		0.8328
1.585	20.29	-0.468	-0.238	4.3636	2.2368	
1.61	20.61	-0.51		3.7438		1.0111
1.635	20.92	-0.491		3.4156	2.5597	1.1452
1.66	21.24	-0.671		3.2922		
1.685	21.56	-0.49	-0.049	3.8466	2.6731	1.0379
1.71	21.88	-0.67				
1.735	22.2	-0.781	0.108	3.5649	2.2116	1.2053
1.76	22.52	-0.297		3.7274		1.8013
1.785	22.84		-0.007		2.4556	
1.81	23.15	-0.789		3.1927		1.0655
1.835	23.47		0.063		2.3134	
1.86	23.79	-0.61		3.8471		1.1551
1.885	24.11	-0.64	0.136	3.2711	2.5204	0.8501
1.91	24.79	-0.652		3.0485		2.1337
1.935	25.48	-0.723	0.191	3.5827	2.3961	0.9242
1.985	26.85	-0.816	0.029	3.5732	2.8612	1.6624
2.025	27.95	-0.687		3.4931		1.8385
2.075	29.32	-0.545	-0.14	3.7509	2.8127	
2.125	30.69	-0.839		3.5701		
2.225	32.59	-1.04	-0.233	3.8905	2.2884	1.4148

Depth	Age	<i>G. sacculifer</i> $\delta^{18}\text{O}$	<i>N. dutertrei</i> $\delta^{18}\text{O}$	Mg/Ca (<i>G.sacculifer</i>)	Mg/Ca (<i>N.dutertrei</i>)	Ba/Ca (<i>G.sacculifer</i>)
2.275	33.13	-0.745		3.4174		1.0864
2.325	33.66	-0.68	0.169	3.7616	2.9728	1.547
2.375	34.2	-0.561		3.5607		1.0533
2.425	34.73	-1.178	-0.125	3.15	2.6045	0.8672
2.475	35.27	-1.196		3.2703		1.0813
2.525	35.8	-1.02	-0.2	4.1553	2.3012	1.9484
2.575	36.34	-0.891		3.0426		0.8153
2.625	36.87	-1.234	-0.193		2.2969	
2.675	37.41	-1.276		3.6295		1.1792
2.725	37.94	-1.041	-0.496		2.2461	
2.775	38.48	-0.723				
2.825	39.01	-1.193	-0.6		3.0886	
2.875	39.55	-1.084		3.3745		1.3793
2.925	40.08	-0.869	-0.267		2.4143	
2.975	40.62	-0.864		3.5554		1.1753
3.025	41.15	-0.935	-0.275	4.075	2.6749	1.6015
3.075	41.69	-1.009		3.813		1.0483
3.125	42.22	-1.217	-0.691	3.8226	2.4318	2.0187
3.175	42.76	-1.169		3.6542		1.0814
3.225	43.29	-1.46	-0.755		2.6308	
3.275	43.83	-1.17		3.8947		
3.425	45.43	-0.967	-0.621		2.3837	
3.475	45.97	-1.186		3.2955		1.0947
3.525	46.5		-0.994		2.1333	
3.575	47.04	-1.066		4.2161		
3.625	47.57		-0.995			
3.675	48.11	-1.397				
3.725	48.64		-1.093		2.1309	
3.775	49.18	-1.576		3.5076		1.1105
3.825	49.71	-1.669	-1.18	3.6062	2.483	1.6734
3.875	50.25	-1.584		3.6252		1.498
3.925	50.78	-1.137	-1.279	3.4868	2.3984	1.2116
3.975	51.32	-0.901				1.8694
4.025	51.85	-0.949	-0.56	4.6455	2.6283	2.3028
4.075	52.39	-1.233				
4.125	52.93		-0.956		2.2002	
4.175	53.46	-1.235		3.241		1.1132

Acknowledgment

I would like to express my deepest appreciation to my mentor Dr. Ed Hathorne for his guidance, consistent encouragement and pushing me to the limits at times, which I felt, was very helpful. Without him, this dissertation would have taken a different trajectory, one that I wouldn't even want to spare a thought now. I couldn't ask for a better supervisor in my right mind.

I would also very much like to thank Prof. Dr. Martin Frank for his endless support and encouragement, giving me all the time I need even to discuss non-work related issues.

I also want to thank Prof. Dr. Dirk Nürnberg for his support over the past three years and for always letting me in whenever I knock his office, which I did far too many times. I thank the entire team paleo for the extra hand in the labs. I am thinking of you here Nadine and I am most grateful for all the things that you have done in the lab.

Also, thanks for being there Jutta and for keeping the work place as pleasant as it is. Team paleo owes you a great deal.

Imke, Julia and Ingmar- thanks so much for picking the forams and letting me focus on the other parts of my research. I am truly grateful!

This was as much about you: A'aba, Medihine, Haile. I will forever cherish the beautiful memories.

Daniel Gebregiorgis

Blitzstrasse 31

24143 Kiel, Germany

Office +49 431600 2310

Office +49 17684194959

dyirgaw@geomar.de

Birth date- 07-Nov- 1983

EDUCATION

Nov/2002 –Aug/2006

Bachelor of Science (BSc) in Earth Science, Addis Ababa University, Ethiopia

Aug /2009 –June/2011

Master of Science in Atmospheric Science, University of Gothenburg, Sweden

Feb 2013 – Present

Phd Candidate, GEOMAR – Helmholtz Center for Ocean Research, Kiel

WORK EXPERIENCE

Sep 2011 – Dec 2012

Research Assistant, GULD - RCG group, University of Gothenburg

Honors and Awards

Addis Ababa City Administration Award for top grade in the national University entrance examination (ESLCE) (2002).

Study scholarship (EVTEK University of Applied Sciences, Helsinki, Finland) (2006)

PUBLICATIONS

Ali, S., Hathorne, E.C., Frank, M., **Gebregiorgis, D.**, Stattegger, K., Stumpf, R., Johnson, J.E., and Giosan, L., (2015). South Asian monsoon history over the past 60 kyr recorded by radiogenic isotopes and clay mineral assemblages in the Andaman Sea. *Geochemistry, Geophysics, Geosystems*, **16**, 505-521.

D. Gebregiorgis, D., Hathorne, E.C., Sijinkumar, A.V., Nath, B.N., Nürnberg, D. and Frank, M. South Asian summer monsoon variability during the last ~54 kyrs inferred from surface water salinity and river runoff proxies. *Quaternary Science Reviews*, **138**, 6-15

Knutsson, P., and **Gebregiorgis, D.**, (2011). Assessment of frequency and magnitude of extreme rainfall events and flooding in Gothenburg and Falsterbo. (SECOA internal project submitted to the EU)

